AD NUMBER

AD907817

NEW LIMITATION CHANGE

TO

Approved for public release, distribution unlimited

FROM

Distribution authorized to U.S. Gov't. agencies only; Test and Evaluation; 29 DEC 1972. Other requests shall be referred to Air Force Dynamics Laboratory, Attn: PTB, Wright-Patterson AFB, OH 45433.
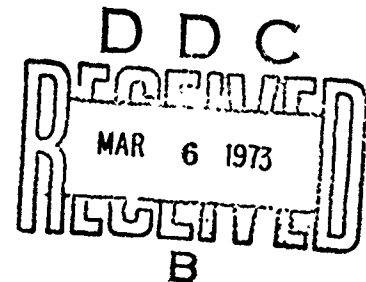
AUTHORITY

AFWAL ltr, 11 Feb 1980

AFFDL-TR-72-147 — VOL. IV

PROPULSION SYSTEM INSTALLATION CORRECTIONS

VOLUME IV:
BOOKKEEPING DEFINITION — DATA CORRELATIONS

W. H. BALL
THE BOEING COMPANY

TECHNICAL REPORT AFFDL-TR-72-147 — VOL IV
DECEMBER 1972

AIR FORCE FLIGHT DYNAMICS LABORATORY
AIR FORCE SYSTEMS COMMAND
WRIGHT-PATTERSON AIR FORCE BASE, OHIO 45433

NOTICE

PROPULSION SYSTEM
INSTALLATION CORRECTIONS

VOLUME IV:

BOOKKEEPING DEFINITION – DATA CORRELATIONS

W. H. BALL

FOREWORD

This report was prepared by the Research and Engineering Division, Aerospace Group, of The Boeing Company under Air Force Contract F33615-72-C-1580, "Propulsion System Installation Corrections", Project 1366. The program was conducted under the direction of the Prototype Division, Air Force Flight Dynamics Laboratory, Air Force Systems Command. Mr. Gordon Tamplin was the Air Force Program Monitor.

The program was initiated on 31 December 1971 and draft copies of the final reports were submitted for approval on 31 October 1972.

Dr. P. A. Ross was Program Manager and Mr. W. H. Ball was principal investigator during the program. Significant contributions to the program were made by the following individuals: Mr. Joe Zeeben, engine performance; Dr. Franklin Marshall, inlet and exhaust system technology; Mr. John Petit, nozzle internal performance and nozzle/afterbody drag; and Mr. Gary Shurtleff, programming.

This report contains no classified information extracted from other classified reports.

Publication of this report does not constitute Air Force approval of the report's findings or conclusions. It is published only for the exchange and stimulation of ideas.

Lt. Col. Ernest J. Cross, Jr.
Chief, Prototype Division
Air Force Flight Dynamics Laboratory

ABSTRACT

This report presents the results of a research program to develop a procedure for calculating propulsion system installation losses. These losses include inlet and nozzle internal losses and external drag losses for a wide variety of subsonic and supersonic aircraft configurations up to Mach 4.5. The calculation procedure, which was largely developed from existing engineering procedures and experimental data, is suitable for preliminary studies of advanced aircraft configurations. Engineering descriptions, equations, and flow charts are provided to help in adapting the calculation procedures to digital computer routines. Many of the calculation procedures have already been programmed on the CDC 6600 computer. Program listings and flow charts are provided for the calculation procedures that have been programmed. The work accomplished during the program is contained in four separate volumes. Volume I contains an engineering description of the calculation procedures. Volume II is a programmer's manual containing flow charts, listings, and subroutine descriptions. Volume III contains sample calculations and sample input data. Volume IV contains bookkeeping definitions and data correlations.

TABLE OF CONTENTS

TABLE OF CONTENTS (Continued)

LIST OF ILLUSTRATIONS

LIST OF ILLUSTRATIONS (Continued)

LIST OF ILLUSTRATIONS (Continued)

LIST OF ILLUSTRATIONS (Continued)

SYMBOLS AND NOMENCLATURE

A	Area, in^2
A_C	Inlet capture area, in^2
A_O	Local stream tube area ahead of the inlet, in^2
A_{O_I}	Free-stream tube area of air entering the inlet, in^2
$\mathcal{R}$	Aspect ratio, dimensionless
B	Velocity decay exponent, dimensionless
C	Sonic velocity, ft/sec.
C_D	Drag coefficient, $\dfrac{D}{qA_{REF}}$, dimensionless
C-D	Convergent-divergent
$C_{D_{ADD}}$	Additive drag coefficient, $C_{D_{ADD}} = \dfrac{D_{ADD}}{qA_C}$, dimensionless
$C_{D_{A_{MAX}}}$	Afterbody drag coefficient, $\dfrac{DRAG}{q\,A_{MAX}}$, dimensionless
$C_{D_{Base}}$	Base drag coefficient $\dfrac{(P_b-P_\infty)A_{BASE}}{qA_{MAX}}$, dimensionless
C_{D_S}	Scrubbing drag coefficient, $\dfrac{DRAG}{qA_{MAX}}$, dimensionless
C_{f_g}	Thrust coefficient, $\dfrac{F_g}{\dfrac{\dot{w}}{g}(V_{cp})}$, dimensionless
C_S	Stream thrust coefficient, dimensionless, (defined by Figure 48 of Volume IV)
C_V	Nozzle velocity coefficient, dimensionless
Conv.	Convergent
D	Drag, lb.; Hydraulic Diameter, $\dfrac{4A}{P}$, in., diameter, in.

F Thrust, lb.

F_{g_i} Ideal gross thrust (fully expanded), lb.

f/a Fuel/air ratio, dimensionless

g Gravitational constant, ft/sec^2

h Enthalpy per unit mass, BTU/lb.; height, in.

h_{fan} Enthalpy of fan discharge flow, BTU/lb

h_{pri} Enthalpy of primary exhaust flow after heat addition BTU/lb

h_t Throat height, in^2

K Velocity decay coefficient, dimensionless

L Length, in.

M Mach number, dimensionless

P Pressure, lb/in^2

P_r Relative pressure; the ratio of the pressures p_a and p_b corresponding to the temperatures T_a and T_b, respectively, along a given sentrope, dimensionless

P_T Total pressure, lb/in^2

Q Effective heating value of fuel, BTU/lb.

q Dynamic pressure, lb/in^2

R, r Radius, in.

S Nozzle centerline spacing, in.

T Temperature, °R

V Velocity, ft/sec

W	Mass flow, lb/sec
W_{BX}	Bleed air removed from engine, lb/sec.
W_C, $\dfrac{W\sqrt{\theta}}{\delta}$	Corrected airflow, lb/sec.
W_f	Weight flow rate of fuel, lb/sec.
W_2	Weight flow rate of air, primary plus secondary, lb/sec.
W_8	Primary nozzle airflow rate, lb/sec.
x	Length, in.
α	Angle of attack; convergence angle of nozzle, degrees
γ	Ratio of specific heats, dimensionless
ε	Diffuser loss coefficient, $\dfrac{\Delta P_T}{q}$, dimensionless
η_B	Burner efficiency, dimensionless
ν	Kinematic viscosity, ft^2/sec.
ρ	Density, lb/ft^3

SUBSCRIPTS

B	Burner
b, base	Base flow region
BP	Bypass
BLC	Boundary layer bleed
btail	Boattail
c	Core (nozzle); capture (inlet)
DES	Design conditions

SYMBOLS AND NOMENCLATURE (Continued)

<u>SUBCRIPTS</u>

e	Boattail trailing edge
EFF	Based on effective area
ENG	Refers to engine demand
f	Fuel
g	gross
GEOM	Based on geometric area
int	Interference; internal
ip	Ideal, primary exhaust flow
jet	Exhaust flow jet
max	Maximum
min	Minimum
s	Scrubbing flow region
SPILL	Spillage
T	Total condition; throat station
t_f	Total condition, fan flow
T/O	Takeoff
t_p	Total condition, primary flow
o	Local conditions ahead of inlet
2	Compressor face station
8	Nozzle throat station
9	Nozzle exit station
18	Fan discharge throat station
∞	Free-stream condition
x	Local

SECTION I

INTRODUCTION

This document presents a detailed discussion of the bookkeeping system used in PITAP to account for aeropropulsion forces. It also presents the data correlations which provide a basis for the generalized data plots used in the PITAP procedure. A catalog of useful inlet data is presented which provides geometric and performance data for several specific configurations. This catalog of data contains a number of sets of data already prepared in the PITAP input format. These data can be used directly to generate installed performance data for inlet configurations which are like those for which data are available.

The purpose of this document is to provide a ready source of reference material that will be useful in understanding and using the PITAP procedure. To achieve this objective, as much information as possible is presented that could be helpful. It is set up in a manner that will make it easy to add additional data as it becomes available.

SECTION II

BOOKKEEPING DEFINITION

2.1 INTRODUCTION

The need for a performance integration system in an airplane
development program arises largely from the inability to
determine the performance of the complete airplane system,
with simultaneous real inlet and exhaust system operation,
in one test or one calculation. Furthermore, it is usually
desirable to optimize the inlet and exhaust system in separate
tests which are independent of the general aerodynamic drag
testing of the basic airplane configuration. Thus, a well-
defined performance integration system is required to insure
that the performance estimated for the various elements (i.e.,
inlet, exhaust system, airframe, turbomachinery) of the air-
plane system are properly integrated to yield an accurate
prediction of overall system performance.

The approaches taken by the major airframe contractors
(References 1 through 9) in treating this problem are all
similar in concept. The aerodynamic drag testing of the basic
airplane configuration is done with some reference inlet and
exhaust system condition. Most commonly this testing is done
with the propulsion system represented by a flow nacelle (i.e.,
flow-through duct). Thus, the reference inlet and exhaust
system simulation on the airplane drag model is that which
is achievable under flow-through conditions. To extrapolate
from this condition to the full scale airplane condition in
flight, separate inlet and exhaust system tests are conducted
with a portion of the airplane geometry and flow properties
duplicated in the region of the inlet or exhaust system being
studied. These separate tests include full engine simulation
so as to allow measurement of drag increments of the operating
condition relative to that which is produced on the airplane
reference flow nacelle. For the nozzle this requires blowing
high pressure air through the exhaust system to produce the
pressure ratios and external nozzle geometry consistent with
the installed engine in flight. For the inlet this requires
varying the mass flow and inlet geometry on the flow-through
nacelle. The inlet and exhaust system drag increments thus
obtained are then combined with the internal propulsion system
thrust and airplane drag to obtain a prediction of overall
thrust-minus-drag performance of the airplane system as depicted
in Figure 1.

2
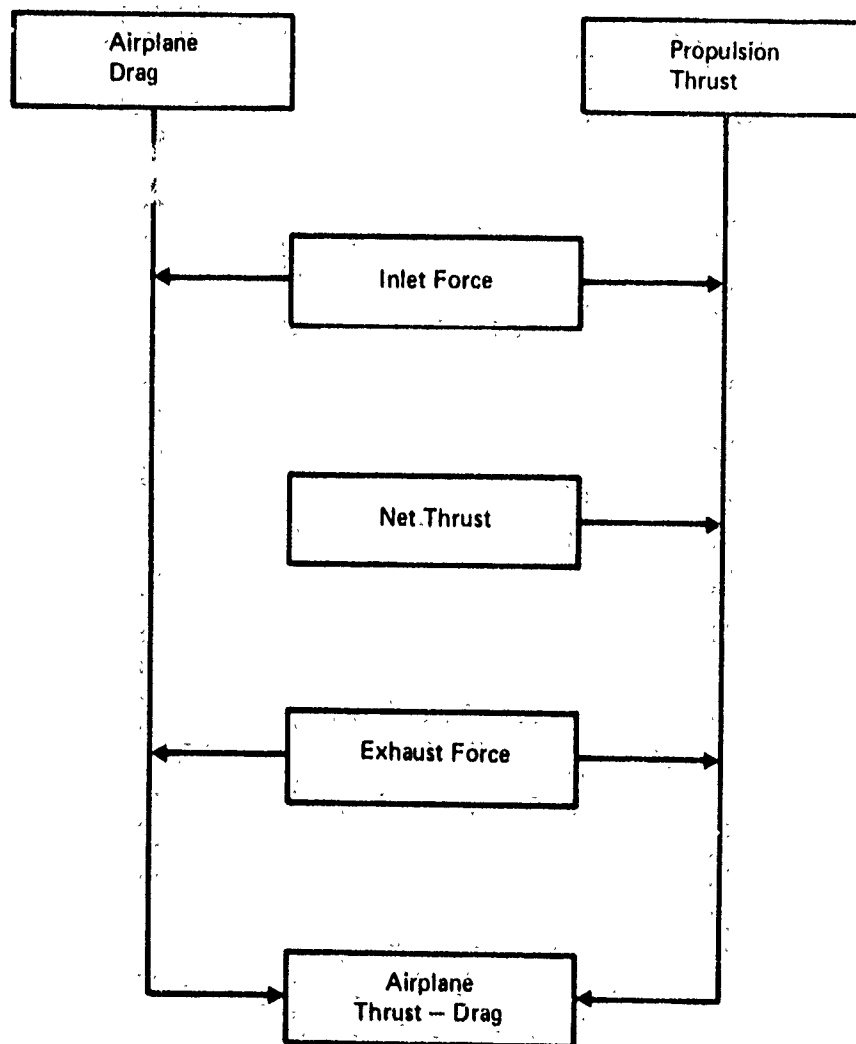
Figure 1 : AIRPLANE THRUST/DRAG BOOKKEEPING

Fundamental to this performance integration is the definition adopted for the thrust and drag forces. Herein lies the controversy or bookkeeping differences that currently afflict the industry. From a performance calculation standpoint it is immaterial how the split is made between thrust and drag provided that all forces exerted on the airplane system are accounted for once and only once as either a drag force or a thrust force. The split defined however, has implications in accuracy, test technique employed, accountability and comparison of component performance between airplanes. These implications can be made evident by considering a specific example. Assume that the split or bookkeeping definition is established by the condition of the flow nacelle on the airplane drag model. Further, assume the reference flow-nacelle condition is one which passes airflow equal to the inlet capture area through the duct for all Mach numbers (i.e., MFR = 1.0).

Both the inlet and nozzle geometry are significantly altered relative to the operating condition of the propulsion system to achieve this condition. Thus, as shown in Figures 2 and 3, the propulsion force increment measured relative to this reference will contain a significant drag increment that is associated with the flow-through simulation of the propulsion system geometry on the reference flow nacelle. These "configuration change" drag increments will ultimately have to be assigned to airplane drag (i.e., scaled from model test data) when comparison is made with flight test data; when evaluating performance of competing airplane configurations or when attempting to develop a technology base for predicting drag of the real airplane in flight. This is completely correct and consistent bookkeeping. However, consider that with this kind of reference significant configuration dependent drag increments for the airplane system are measured on inlet and nozzle component models which are designed to accurately measure external force changes associated with engine flow and pressure/ratio change rather than on the airplane drag model which is used to develop the airplane configuration. Referring to Figure 2, by simply changing the flow nacelle condition then the configuration change drag increment becomes a part of the total measured for the airplane, the airplane drag contains the interference associated with it. Note some small correction to the drag polar may still be required due to differences in the inlet ramp angle. This increment, however, as indicated in the figure will usually be quite small and on a scaled basis will not significantly affect the airplane drag buildup accuracy.

From this brief example it is apparent arbitrary selection of the bookkeeping is not desirable if one strives to meet overall

4
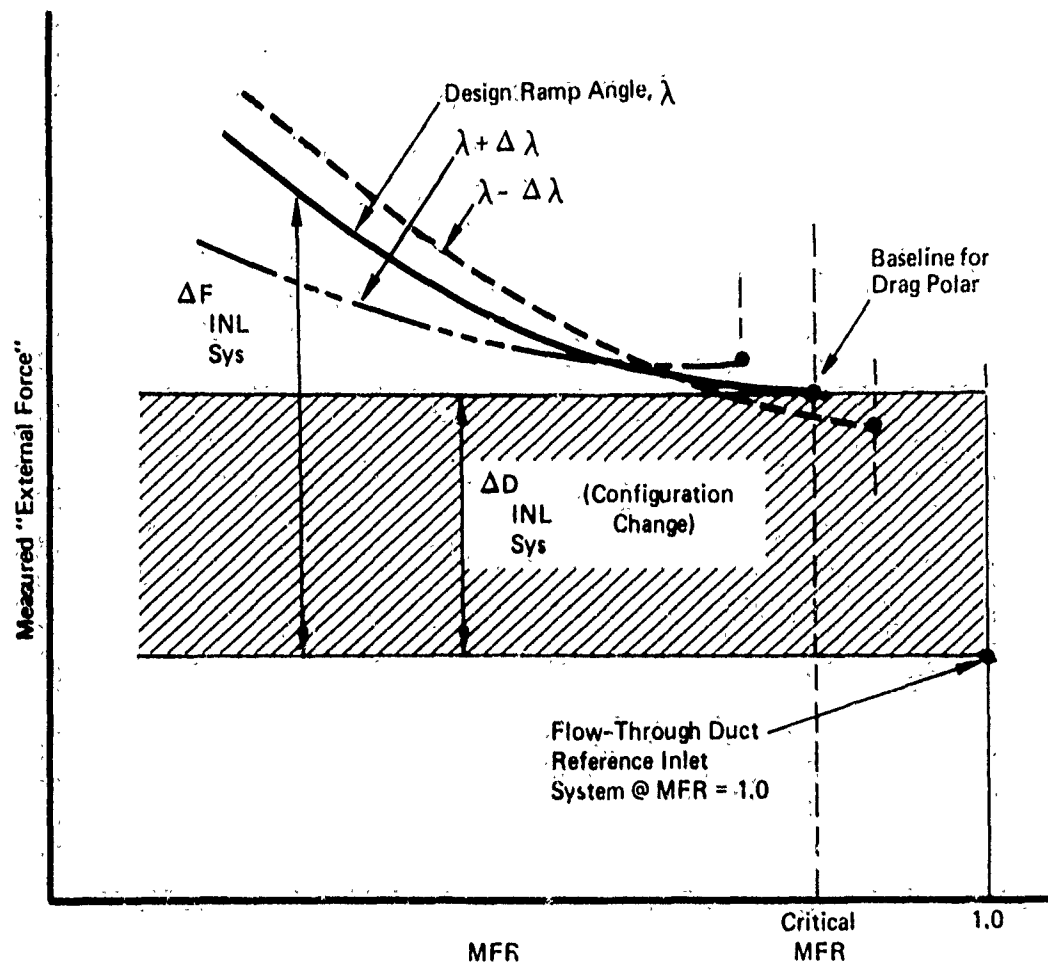
Figure 2 : INLET SYSTEM DRAG RELATIVE TO FLOW NACELLE REFERENCE

5
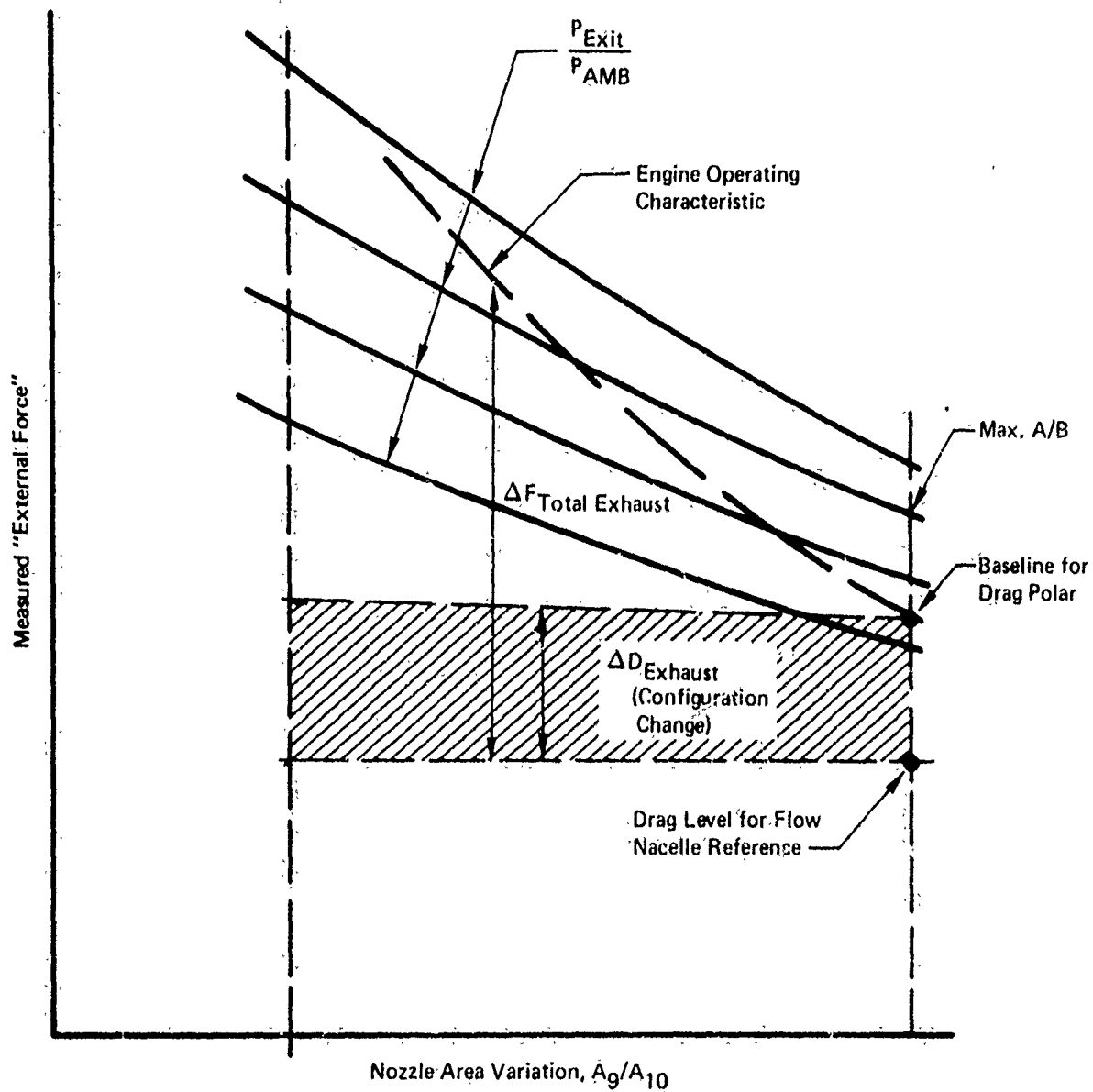
Figure 3: *EXHAUST SYSTEM DRAG DATA RELATIVE TO FLOW NACELLE REFERENCE*

objectives for airplane system performance prediction accuracy. Rather, selection should be based on satisfying criteria derived from the overall objective.

First of all, accuracy of simulation and measurement in the wind tunnel is required, not only for the propulsion system components, but also for the airplane system. Thus, all aspects of the propulsion system such as external geometry and inlet flow that can be obtained with the flow nacelle simulation should be attempted on the airplane drag model provided the reference condition so obtained can be accurately reproduced on the propulsion model. Secondly, the performance integration definition and integration procedure must afford as much visibility as possible of the behavior of the components involved (inlet, nozzle, airframe, engine) consistent with the accuracy requirement, in order to provide a basis for comparison, evaluation and development of component technology. This is best obtained by selecting references for the inlet, nozzle and airplane which not only provide a near operating condition but at the same time are sufficiently general to be adopted for a variety of airplane systems and types.

Finally, it is desirable that a single performance integration system can be found that would be applicable throughout the entire airplane development cycle (e.g., from the initial theoretical design through flight test). This will make it possible to trace the evolution and adequacy of the performance prediction of the airplane system relative to component or subsystems performance over the total life of the program.

With these criteria, and a review of bookkeeping (References 1-9) a performance integration method described below was evolved.

2.2 SYSTEM DEFINITIONS

The basis for a complete accounting of forces acting on the airplane system in flight is to a large extent derived from the test techniques used to simulate the propulsion and airframe subsystems. Hence, the performance integration system definitions are derived from a wind tunnel reference based on the following:

1) Engine thrust is established from a static full scale thrust measurement with inlet internal pressure and exhaust system altitude condition reproduced in the test cell.

2) Airplane drag is derived from a reference full airplane force and moment model having a flow nacelle simulator of the propulsion system at a specified mass flow condition.

3) Inlet drag is derived either from the full airplane model or a partial airplane model using a flow nacelle simulation and the same reference condition as 2).

7

4) Exhaust system drag is derived from a full or partial
   airplane model having faired over inlets and blown
   nacelle simulation for jet effects and the same re-
   ference condition as 2).

The reference condition is established with the airplane model.
It is a measurable repeatable condition which is accurately
duplicated on the inlet and exhaust nozzle models and serves
as the connector for the experimental buildup of the drag
polar for the "baseline" airplane.

The "baseline" for the full scale airplane drag is a specified
inlet and exhaust system geometry and flow condition, where-
in the propulsion system throttle dependent drag is defined to
be zero. All engine throttle conditions different from the
baseline conditions produce a throttle dependent drag which is
charged to the engine net thrust. Thus the "baseline" defini-
tion constitutes the bookkeeping definition for splitting
thrust and drag on the full scale airplane.

With these definitions the total force for the airplane in the
flight direction is given by

$$F_{TOTAL} = \underbrace{\sum_{i=1}^{n} F_{N_{R_i}} + \Delta F_{N_{EXH}} + \Delta F_{N_{INL}}}_{F_{N_A}} \underbrace{- D_{REF} - \Delta D_{EXH}_{A/P} - \Delta D_{INL}_{A/P}}_{D_{A/P}} \quad (1)$$

The first three terms on the right side of equation (1) combine
to form, by definition, the propulsion system net thrust, F_{N_A}.
(There n is the number of engines on the airplane). The
three terms subtracted at the end combine to form the airframe
system drag, which is independent of engine throttle setting,
$D_{A/P}$. All drag variations associated with changes in throttle
setting are included in the inlet and exhaust system force in-
crements, $\Delta F_{N_{INL}}$ and $\Delta F_{N_{EXH}}$, respectively.

All of the terms on the right side of equation (1) are defined
below.

2.2.1 ENGINE NET THRUST, F_{N_R}

The engine net thrust F_{N_R} is defined to be the difference be-
tween the gross thrust of the exhaust system in quiescent air,
at a specified pressure ratio, and the ram drag on the engine

8

streamtube at the specified flight conditions. The engine
streamtube includes by definition all of the airflow demand
at the engine face as well as any secondary airflow captured
by the engine inlet and ducted around the engine to the ex-
haust system. Any additional airflow captured by the inlet
and ducted overboard through bleed or bypass systems, or
simply lost by leakage, is not part of the engine streamtube.

The effects of inlet internal performance, i.e., inlet total
pressure recovery and steady-state and dynamic distortion, are
accounted for in the engine net thrust. Thus, identical
engines in a multi-engine airplane might produce different
engine net thrusts because of different inlet installations.

The effects of engine bleed, engine power extraction, and
exhaust system internal performance are also accounted for in
the engine net thrust.

The term "gross thrust" used in this definition of engine net
thrust is the force that would be measured on the balance in a
blowing test, in quiescent air, if the inlet air were intro-
duced in a direction normal to the thrust direction. For most
exhaust systems the gross thrust equals the integral of total
momentum (axial momentum flux plus pressure increment above
ambient) across the nozzle exit plane. For a plug nozzle it
also includes the force (in quiescent air) on the part of the
plug extending beyond the exit plane.

The "ram drag" used in this definition is the product of the
mass flow in the engine streamtube and the flight velocity.

Thu , the engine net thrust F_{N_R} can be determined in an altitude
chamber with an available engine using conventional techniques.
The effects of inlet internal performance would be simulated,
and the measured thrust would be corrected to the proper ram
drag for the flight conditions being simulated.

2.2.2   Inlet Thrust Increment, $\Delta F_{N_{INL}}$

The inlet thrust increment (inlet throttle dependent drag) is
the drag increment between the inlet at its baseline condition
and its operating condition. It is derived from:

$$\Delta F_{N_{INL}} = \Delta F_{TOTAL\ INL} - \Delta D_{INL-A/P}$$

9

where

$\Delta F_{TOTAL\ INL}$ is the total inlet drag measured relative to the reference flow nacelle condition.

$\Delta D_{INL-A/P}$ is the drag increment between the reference flow nacelle and baseline inlet.

The relationship between the various increments thus defined are shown geometrically in Figure 4. Note that the reference and baseline condition for the inlet is intended to be the same and usually differ only because of difficulty in achieving the full scale baseline condition on the small scale reference airplane model. Thus $\Delta D_{INL-A/P}$ is usually quite small and is used to correct the reference airplane drag to the baseline airplane drag. The inlet baseline condition is defined at each Mach number as shown in Figure 5. These conditions were chosen because:

a) it corresponds to an accurate reference and measurable condition for the real inlet,

b) it corresponds to a condition when inlet spillage drag is minimum (i.e., minimum lip separation and therefore less error in scaling),

c) it is near the operating condition of the inlet (airplane reference model therefore contains major inlet interference effects).

Figure 6 compares theoretical buildup of the total inlet drag with the experimental definition established above. The experimental buildup of the inlet forces from balance and flow nacelle measurements is defined in Figure 7. Figures 8 and 9 show the experimental results schematically for the subsonic and supersonic conditions respectively.

Typical data thus obtained from a full airplane model is shown in Figure 10. The corresponding total inlet drag derived from the data is shown in Figure 11.

2.2.3 Exhaust System Thrust Increment, $\Delta F_{N_{EXH}}$

As for the inlet, the exhaust system thrust increment is the throttle dependent drag increment between the baseline exhaust system condition and its operating condition. It is derived from:

10

Reference (Flow Nacelle)[*]

$A_{O_{Ref.}}$

A_{Cap}

$\Delta D_{inl-A/P}$

$\Delta F_{total\ inl}$

Baseline (Inlet Drag)

Bleed Closed

$A_{O_{Baseline}}$

A_{Cap}

Bypass Closed

$\Delta F_{N_{inl}}$

Operating

A_O

A_{Cap}

* Reference is Intended to be Close
Simulation of Baseline Condition
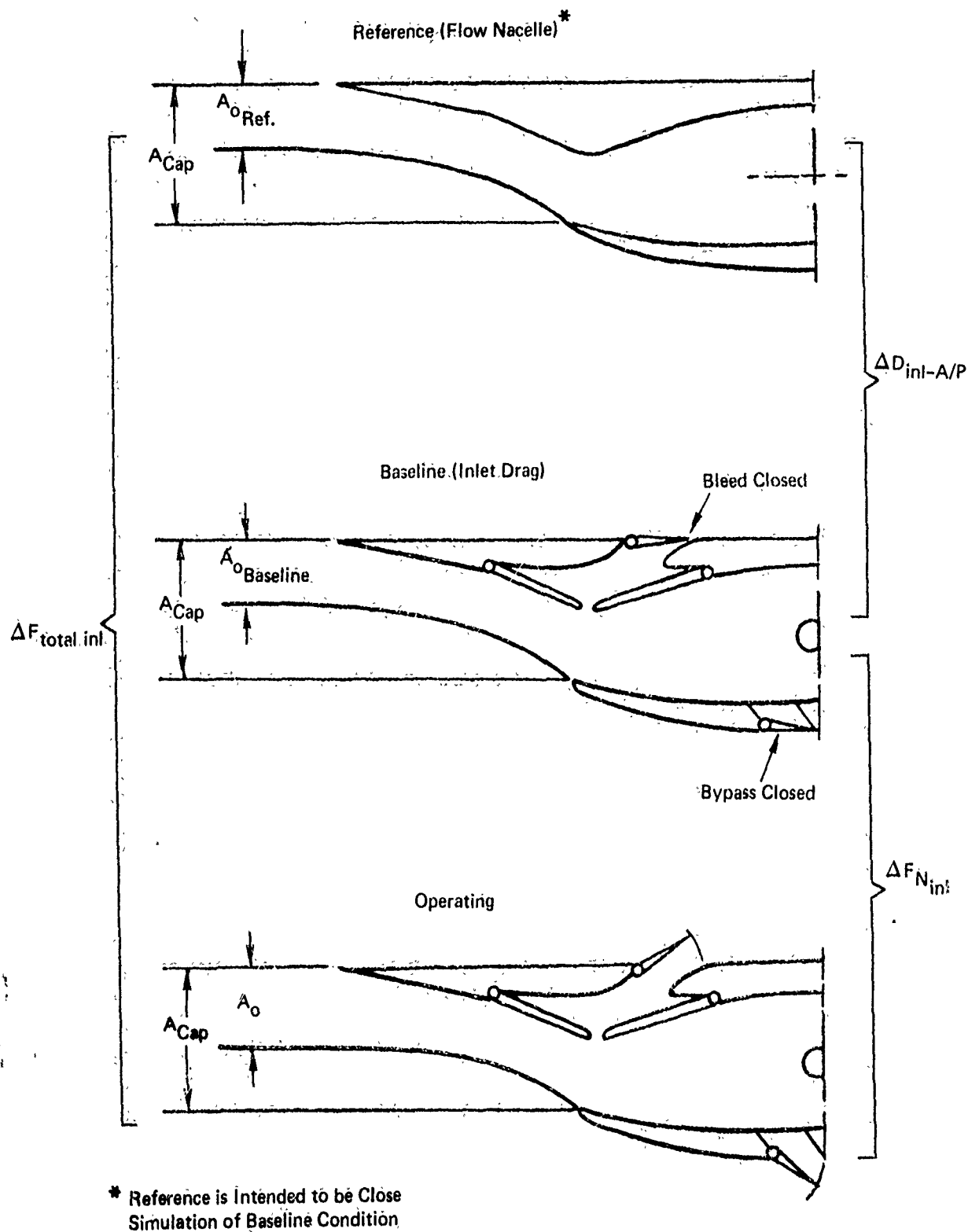
Figure 4 : INLET DRAG DEFINITION

11
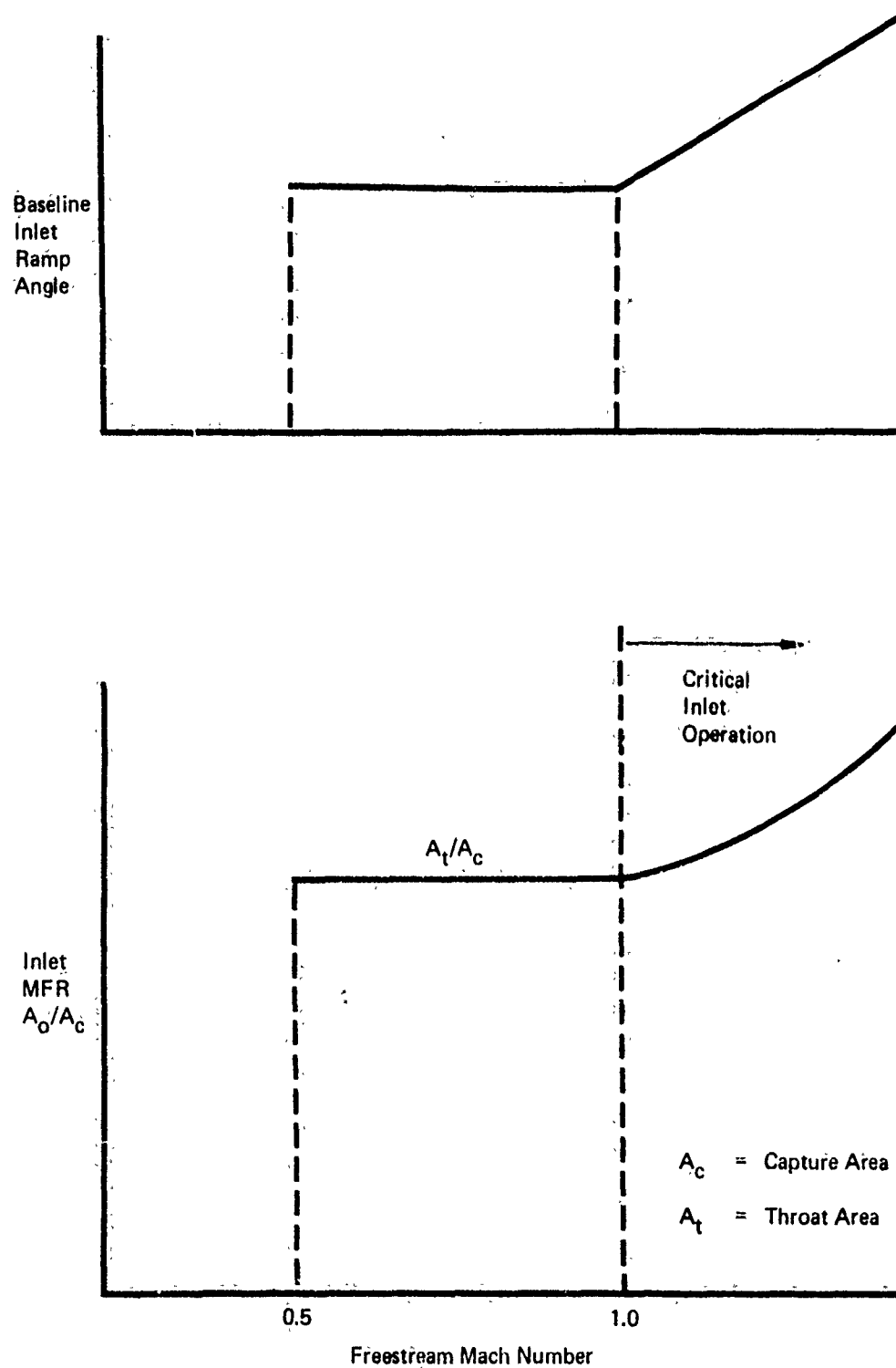
Figure 5 : BASELINE INLET CONDITION VERSUS MACH NUMBER

$$\Delta F^*_{tot\ inl} = \left[\overbrace{D_{Add} + D_{Press\ +\ S.F.}}^{D_{Spill}} + D_{Bleed} + D_{Bypass} \right] - \left[\overbrace{D_{Add} + D_{Press\ +\ S.F.}}^{D_{Spill}} \right] \longleftarrow \text{Theoretical}$$

on Spillage   on Spillage

Surfaces   Surfaces

Real MFR   Ref. MFR

Real Geom   Ref. Geom

$$\Delta F_{tot\ inl} = \overbrace{\left(\begin{array}{c} \text{External Force} \\ \text{For Real} \\ \text{Inlet Condition} \end{array} \right)}^{F_{ext}} - \overbrace{\left(\begin{array}{c} \text{External Force} \\ \text{For Reference} \\ \text{Inlet Operation} \end{array} \right)}^{F_{ext_{ref}}} \longleftarrow \text{Experimental}$$

Where:

D_{Bleed} and D_{Bypass} = Drag associated with momentum loss and exit doors of respective systems.

D_{Add} = Integrated pressure along inlet captured stream tube

$D_{Press\ +\ S.F.}$ = Integrated pressure and skin friction over all surfaces affected by spillage.

* If secondary air is removed from inlet or leakage differences occur between model and full scale then these drag losses must be included as well.

Figure 6:   *TOTAL INLET DRAG BUILDUP*

$$F_{Ext} \equiv F_{Bal\ Corr} - D_{Int}$$

$F_{Bal\ Corr} \equiv$ Balance measurement corrected for tare, mounting effects and base pressure on flow nacelle model.

$D_{int} \equiv$ Internal drag of flow nacelle which is difference in momentum and pressure force in flow nacelle exit jet relative to free stream condition of captured stream tube.

Figure 7 : *EXTERNAL FORCE DETERMINATION FROM FLOW NACELLE/FORCE BALANCE*

14
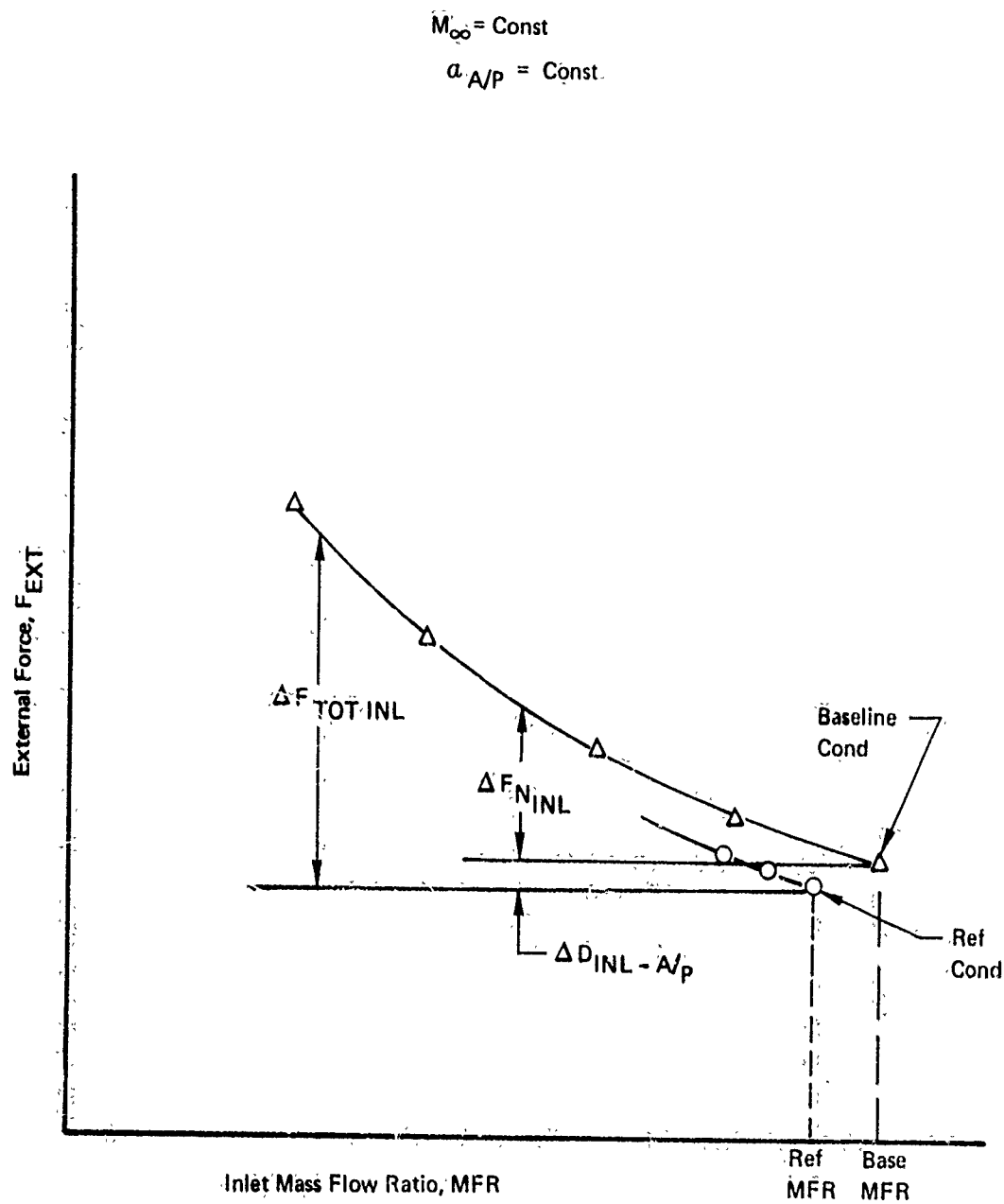
Figure 8: SUBSONIC INLET DRAG

$M_\infty = Const$
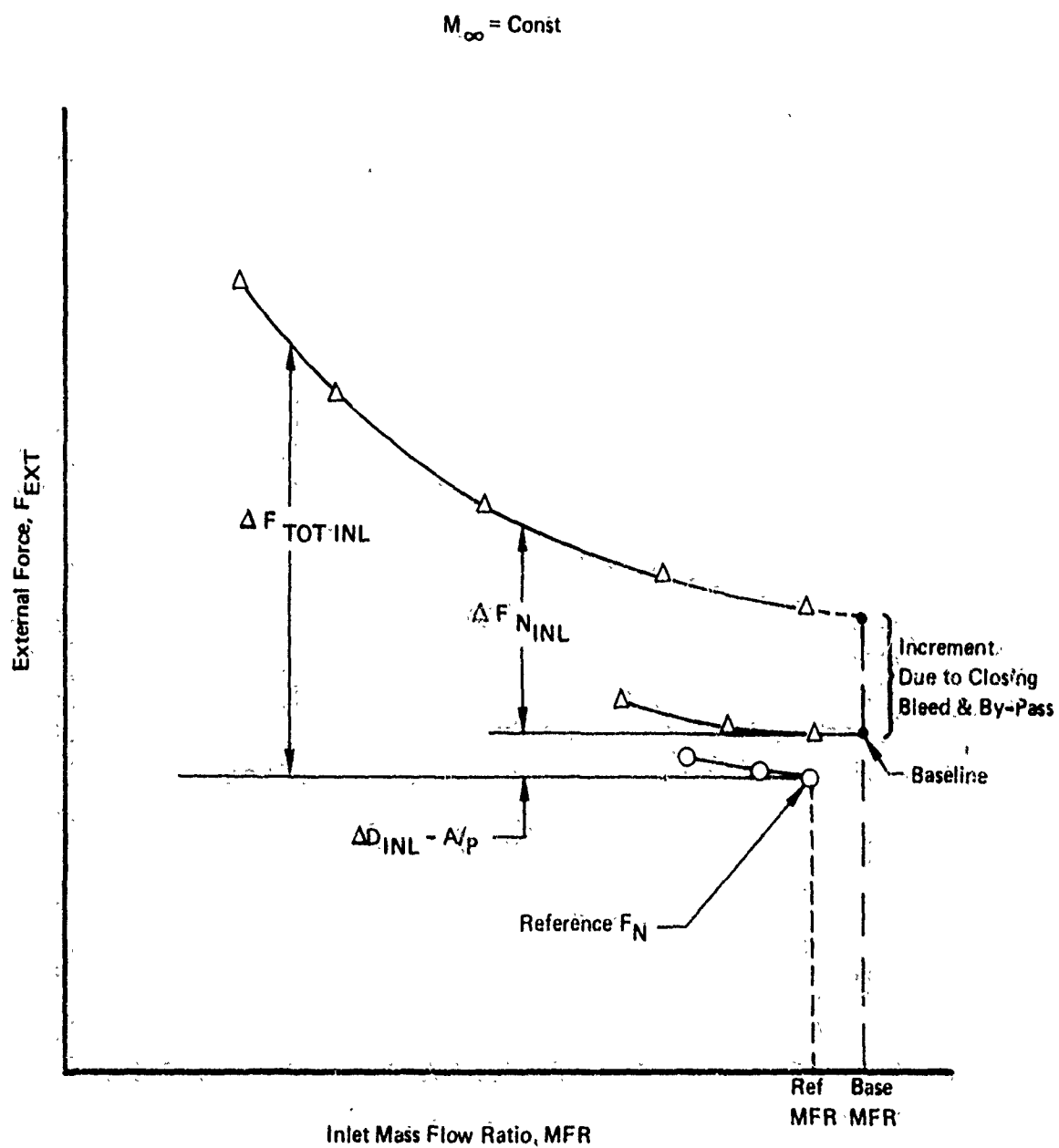
Figure 9: SUPERSONIC INLET DRAG

16
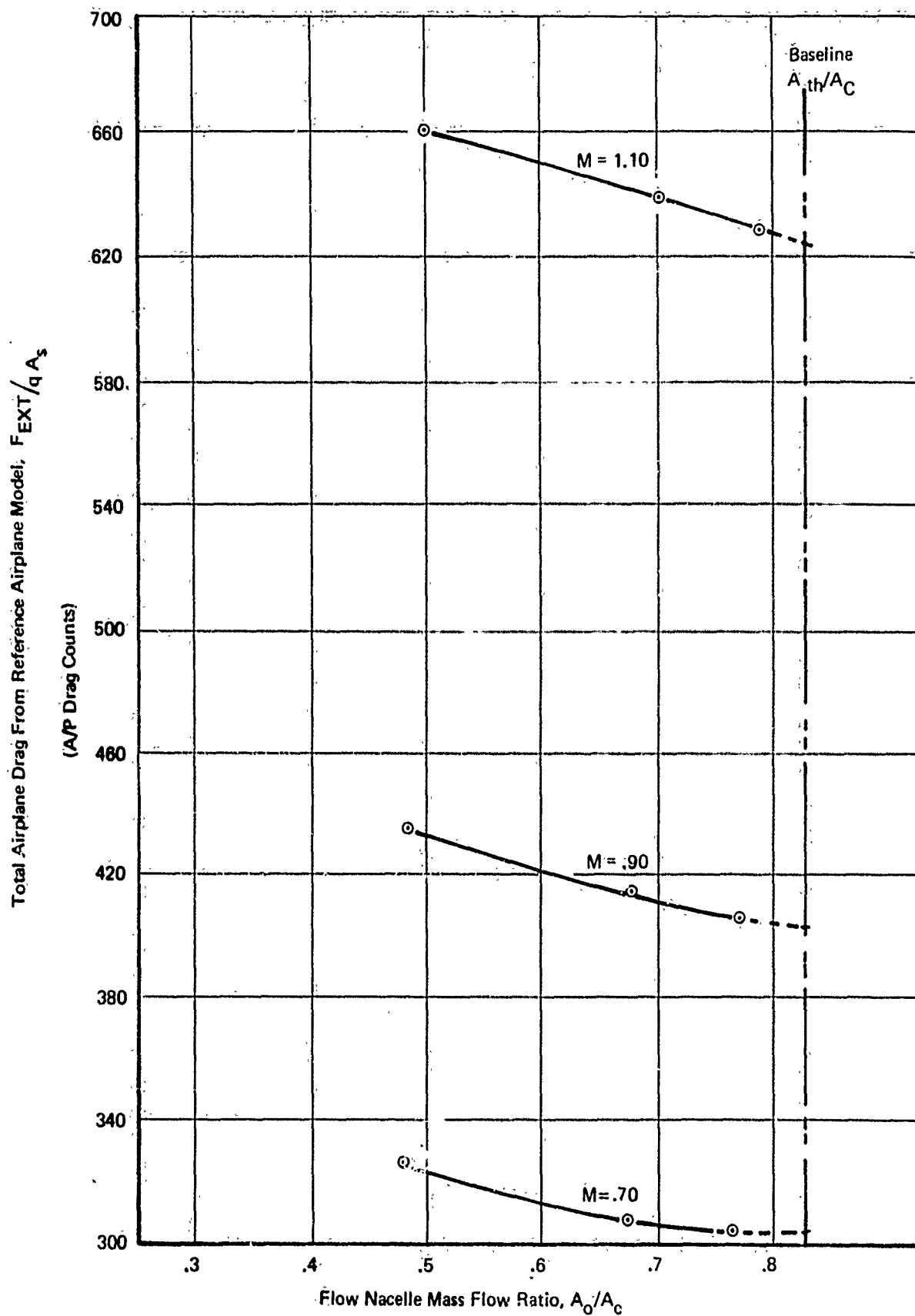
Figure 10: EXTERNAL FORCE MEASUREMENT; AIRPLANE VERSUS
MASS FLOW FOR FULL A/P MODEL

17

$$\frac{A_{th}}{A_c} = .85$$
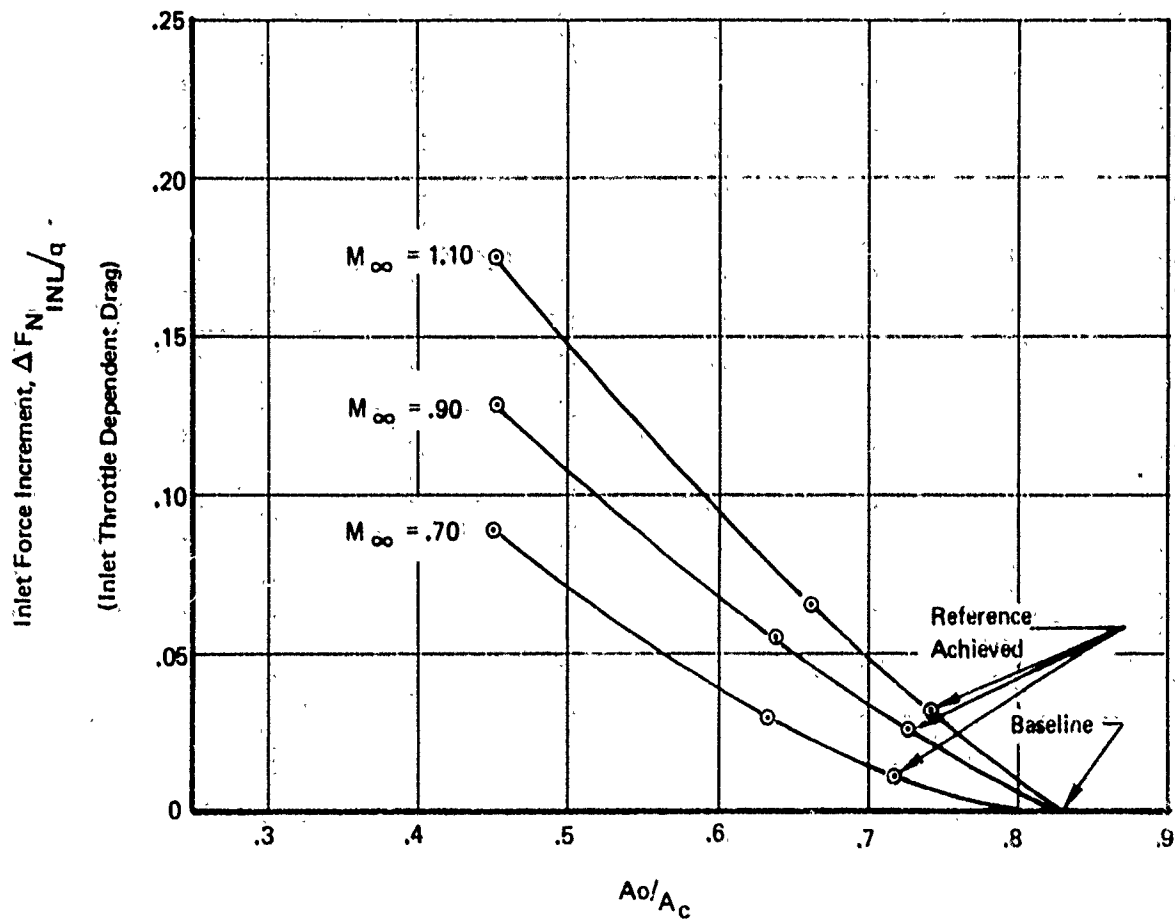
Figure 11:   INLET DATA DERIVED FROM FULL MODEL MEASUREMENTS

18

$$\Delta F_{N_{EXH}} = \Delta F_{TOTAL\ EXH} = \Delta D_{EXH\ SYS}$$

where

$\Delta F_{TOTAL\ EXH}$ is the total exhaust system drag measured relative to the reference flow nacelle nozzle condition

$\Delta D_{EXH-A/P}$ is the drag increment between the reference and baseline nozzle conditions.

The relationship between the various increments thus defined are shown geometrically in Figure 12. The difference between the reference and baseline condition will be greater for the exhaust system because of inability to simulate both inlet and exhaust system baseline condition simultaneously with a flow nacelle. Thus, $\Delta D_{EXH-A/P}$ is the airplane drag correction bridging the gap between the flow nacelle nozzle and real baseline nozzle. The baseline condition selected for the nozzle was maximum afterburning external geometry and a jet exit static pressure ratio of 1.0. This allowed duplication of real external nozzle geometry while at the same time providing sufficient base area for maximum inlet mass flow requirements.

The theoretical buildup of the exhaust system drag is shown in Figure 13 compared to the experimental definition. A schematic of the blown nacelle installation used in the experimental buildup is shown in Figure 14. The blown nacelle is alternately operated with tunnel off (wind-off static thrust) and with wind tunnel on at desired Mach number condition. The measurements thus obtained are combined as shown in Figure 15 to establish the total exhaust system drag. Figure 16 graphically portrays the results. Typical data is shown in Figure 17.

2.2.4 Airplane System Drag, $D_{A/P}$

The airplane drag, $D_{A/P}$, is established for the defined inlet and nozzle baseline condition. It is derived by scaling the model data to full scale. It is made up of these terms, namely:

$$D_{A/P} = D_{REF} + \Delta D_{INL-A/P} + \Delta D_{EXH-A/P}$$

where the inlet and nozzle increments are derived from the propulsion wind tunnel models or theoretical buildup and D_{REF} is derived by scaling the external force measurements of the reference airplane wind tunnel model. Figure 18 and 19 illustrate

Figure 12: EXHAUST SYSTEM DRAG DEFINITION
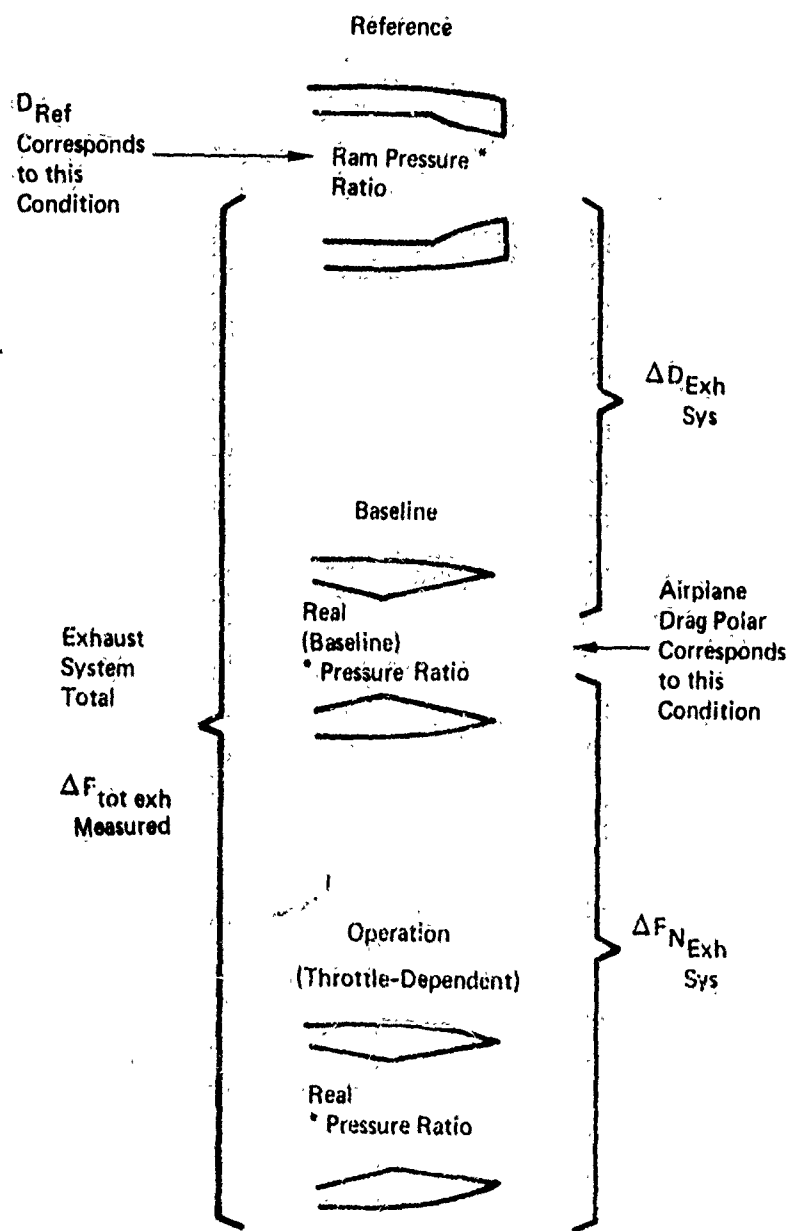
* Pressure Ratio = Jet Exit Static to Free Stream Pressure Ratio

EXHAUST SYSTEM DRAG BUILD-UP

$$\Delta D_{Exh_{Sys}} = \underbrace{\left[\sum_{i=1}^{n} D_{Iso-lated\,Boat-tail_i} + D_{Inter-ference} + D_{Rest\,of\,A/P\,on\,Balance}\right]}_{\text{(Cancels in Theoretical Build-Up)}} + \sum_{i=1}^{n} \Delta F_{G_i} - \underbrace{\left[\sum_{i=1}^{n} D_{Iso-lated\,Boat-tail_i} + D_{Inter-ference} + D_{Rest\,of\,A/P\,on\,Balance}\right]}_{\text{Ref. Geom. \& Pres. Ratio}}$$

Baseline Geom. & Press. Ratio → THEORETICAL BUILD-UP

$$\Delta D_{Exh_{Sys.}} = \left(\text{External Force for Baseline Exhaust System Operation}\right) - \left(\text{External Force for Reference Exhaust System Operation}\right)$$

EXPERIMENTAL BUILD-UP

$$\Delta F_{N_{Exh.\,Sys.}} = \underbrace{\left[\sum_{i=1}^{n} D_{Iso-lated\,Boat-tail_i} + D_{Inter-ference} + D_{Rest\,of\,A/P\,on\,Bal-ance}\right]}_{\text{(Cancels in Theoretical Build-Up)}} + \sum_{i=1}^{n} \Delta F_{G_i} - \underbrace{\left[\sum_{i=1}^{n} D_{Iso-lated\,Boat-tail_i} + D_{Inter-ference} + D_{Rest\,of\,A/P\,on\,Balance}\right]}_{\text{Ref. Geom. \& Pres. Ratio}}$$

Baseline Geom. & Press. Ratio → THEORETICAL BUILD-UP

$$\Delta F_{N_{Exh.\,Sys.}} = \left(\text{External Force for Baseline Exhaust System Operation}\right) - \left(\text{External Force for Specified Real Exhaust System Operation}\right)$$

EXPERIMENTAL BUILD-UP

Figure 13: EXHAUST SYSTEM DRAG BUILD-UP

21
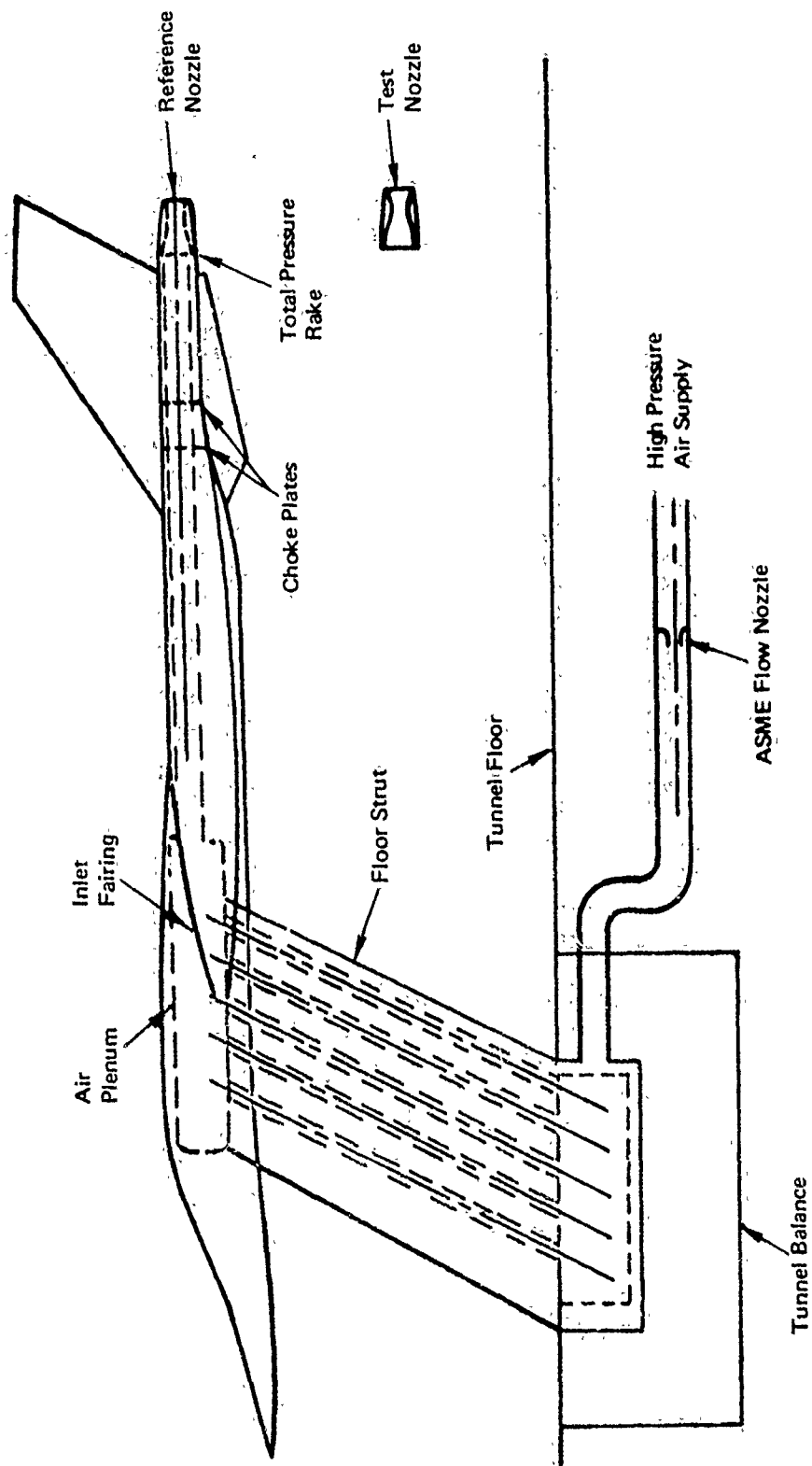
Figure 14 : SCHEMATIC OF BLOWN NACELLE MODEL USING SINGLE BALANCE

- Flow Nacelle Reference Nozzle Installed and Operated

$$F_{Ext\ Ref.} = \left[\frac{\dot{M}_{W.O.}}{\dot{M}_{Static}} \quad \bar{F}_{Bal} \underset{Cor}{(Wind\text{-}Off)} - F_{Bal} \underset{Cor}{(Wind\text{-}On)} \right]_{Ref.\ Noz.}$$

- Replace Flow Nacelle Nozzle with Real Nozzle

$$F_{Ext\ Test} = \left[\frac{\dot{M}_{W.O.}}{\dot{M}_{Static}} \quad \bar{F}_{Bal} \underset{Cor}{(Wind\text{-}Off)} - F_{Bal} \underset{Cor}{(Wind\text{-}On)} \right]_{Test\ Noz.}$$

- Total External Force Increment

$$\Delta F_{Tot\ Exh} = F_{Ext\ Test} - F_{Ext\ Ref.}$$

Note: $C_{V_{Static}} = \bar{F}_{Bal} \underset{Cor}{(Wind\text{-}Off)} / \dot{M}_{Static} \times V_{Ideal}$

Figure 15 :   *EXPERIMENTAL BUILDUP FROM A SINGLE BALANCE MEASUREMENT (BLOWN NACELLE/FORCE BALANCE)*
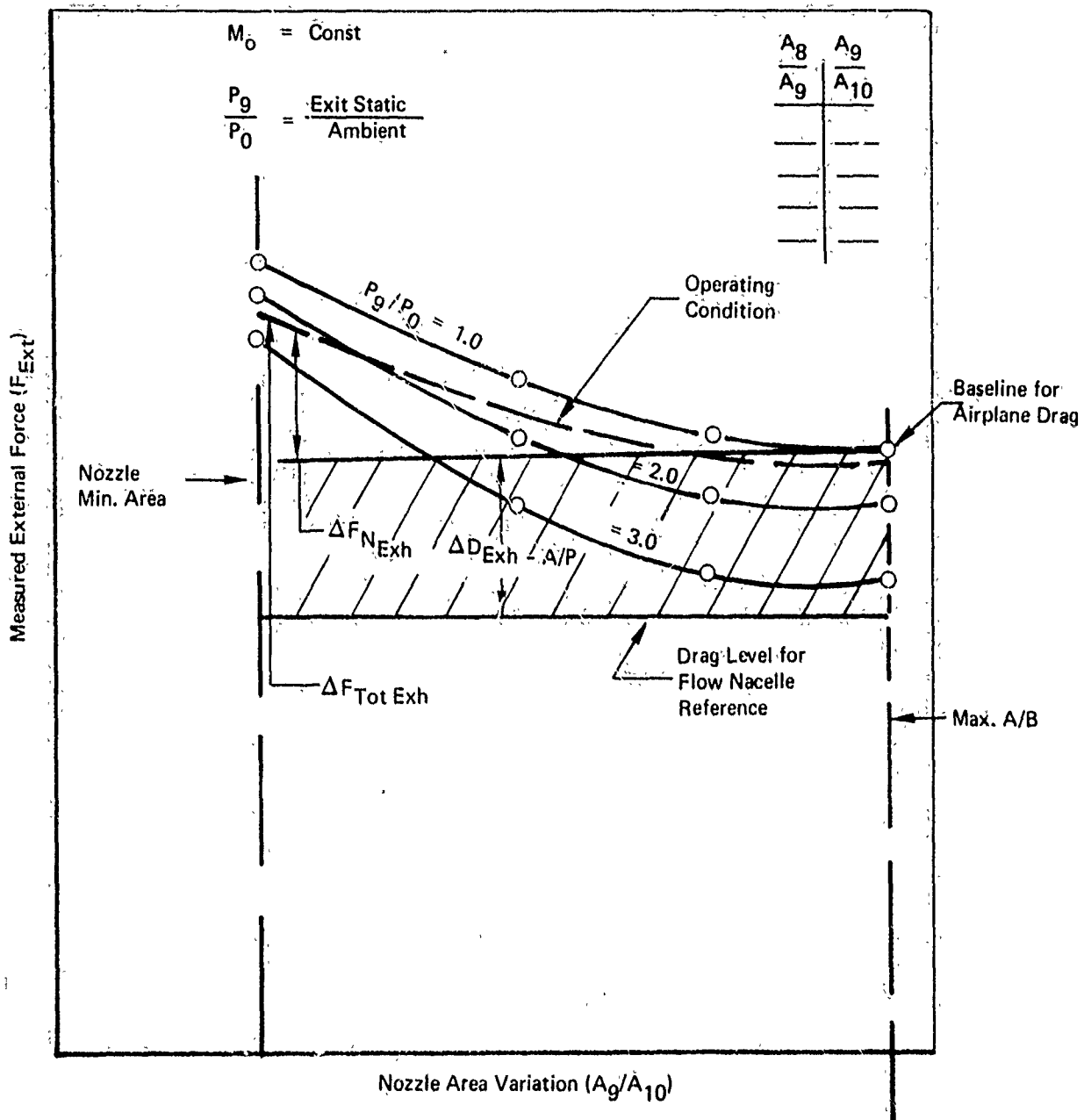
Figure 16:   EXHAUST SYSTEM DRAG SCHEMATIC
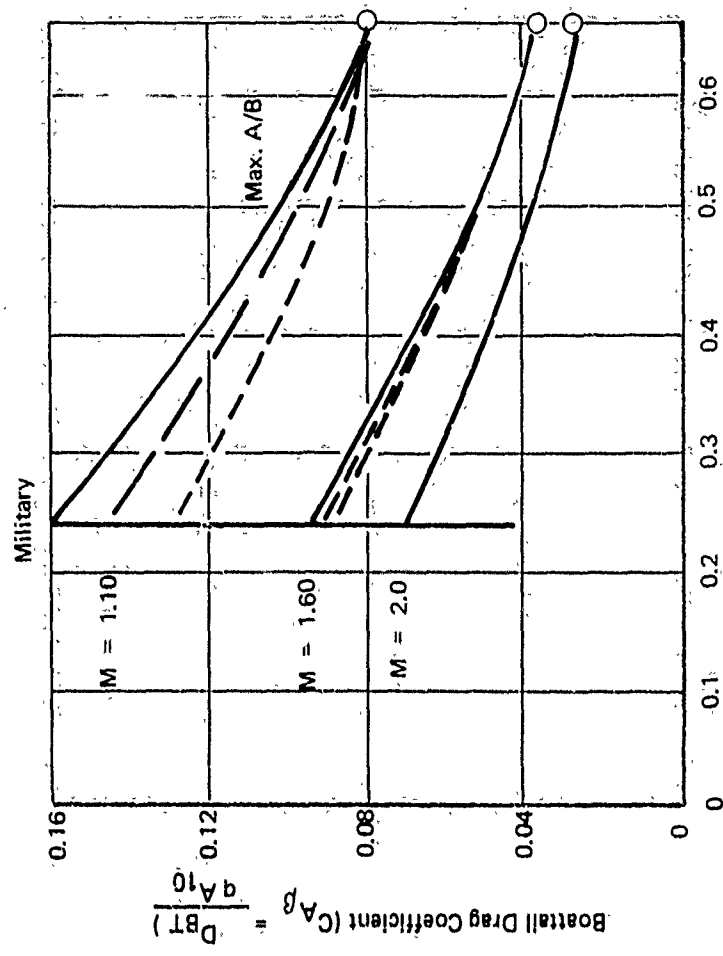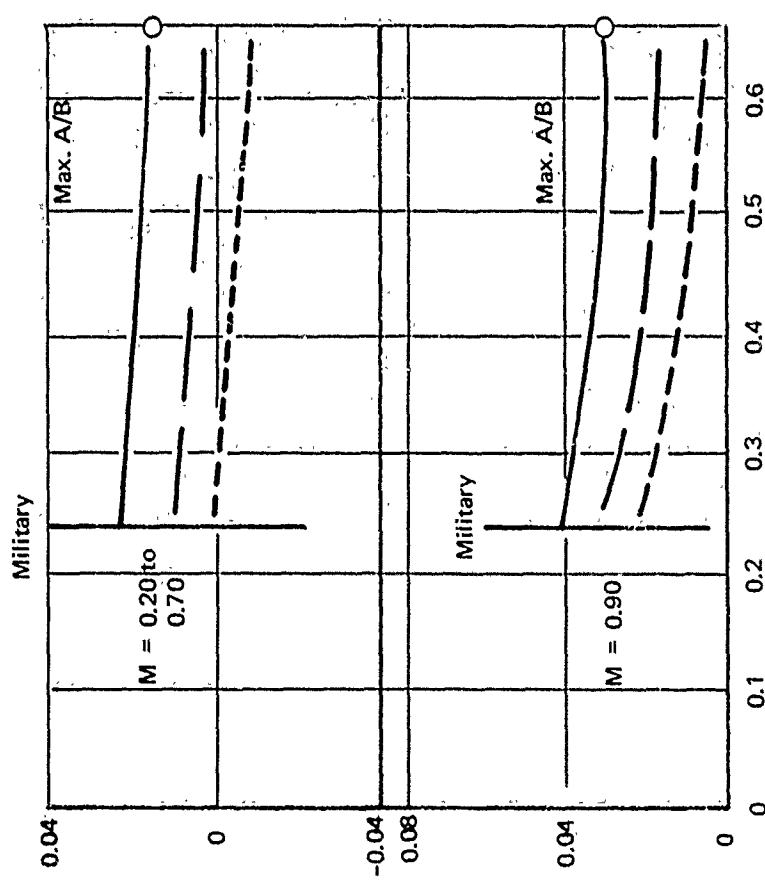
Figure 17: EXHAUST SYSTEM DRAG DATA

Reference Inlet Mass Flow Ratio
Reference Exhaust System Configuration

Drag Coefficient (C_D)

Full Scale Data

Reference Inlet Mass Flow Ratio
Baseline Exhaust System Configuration

Drag Coefficient (C_D)

Figure 18: *SUBSONIC DRAG POLAR BUILDUP FOR BASELINE AIRPLANE*

26

SUPERSONIC AERODYNAMIC DATA
WIND TUNNEL DATA

Reference Inlet Mass Flow Ratio
Reference Exhaust System.
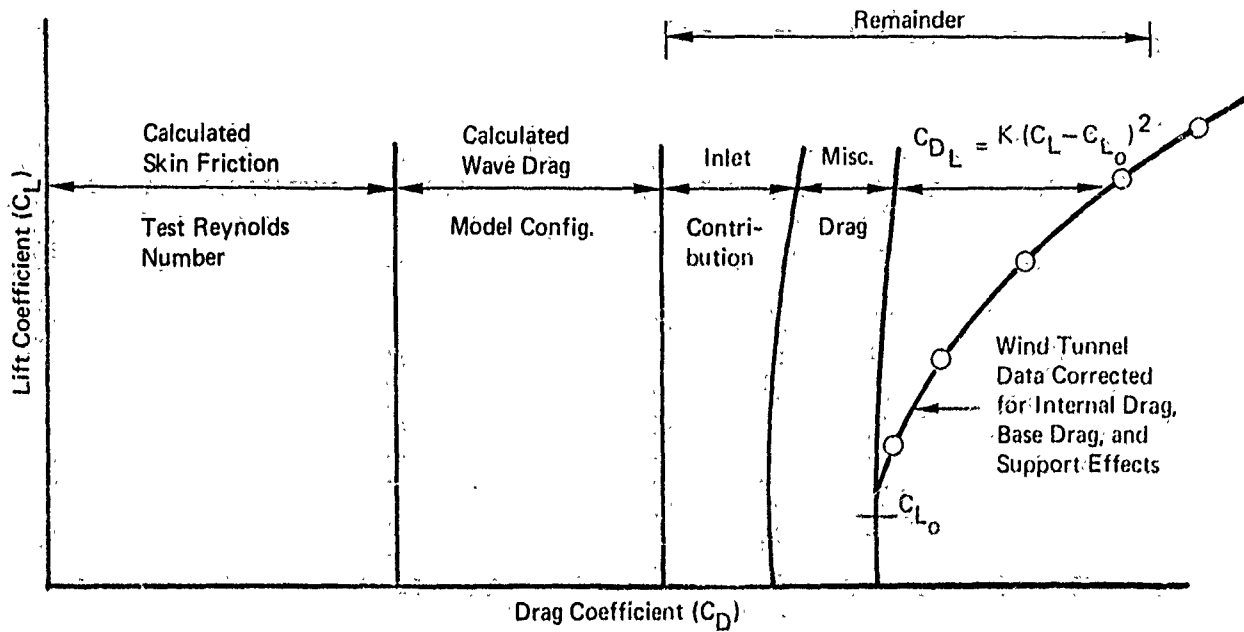
Full Scale Data

Reference Mass Flow Ratio
Baseline Exhaust System
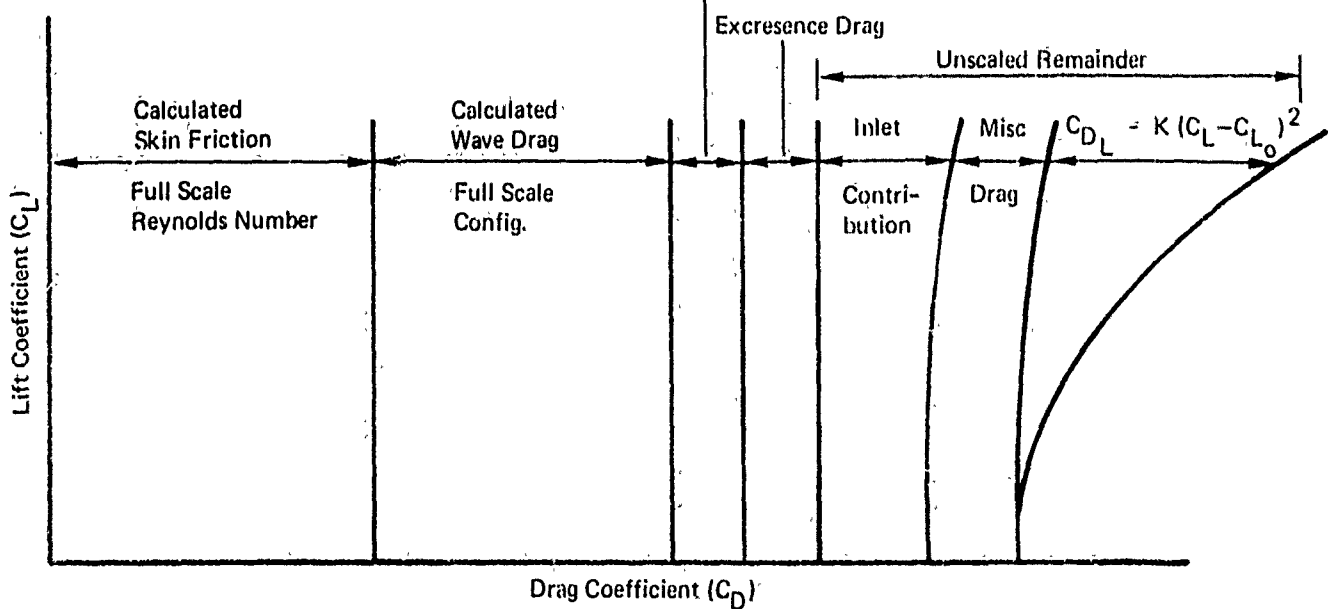
Figure 19: *SUPERSONIC DRAG POLAR BUILDUP FOR BASELINE AIRPLANE*

27

the buildup to the full scale baseline airplane drag polar from model scale data for both the subsonic and supersonic case, respectively.

Note that the flow nacelle reference inlet spillage is reflected in the shape of the measured drag polar which is unchanged in the scaling to full scale. This is a prime reason for attempting to reduce the increment $\Delta C_{D_{INL-A/P}}$ that is added to correct the drag polar from the reference to baseline condition.

SECTION III

GENERAL CORRELATIONS

3.1 TAKEOFF RECOVERY

Inlets designed for high-speed flight usually have sharp cowl lips and ramp leading edges to reduce drag and shock losses at high Mach numbers. These same sharp lips cause flow distortion and losses in total pressure recovery at low speeds (when $A_o/A_{LIP} > 1.00$) due to separation inside the inlet lip. To achieve acceptable inlet performance at these low speed conditions, it is common to employ takeoff doors (sometimes called auxiliary inlets) to provide additional flow passage area into the diffuser. This reduces the flow Mach number around the sharp lips and helps the lip separation problem. The exact benefits to be gained by any given set of takeoff doors depends on their shape, location, size, and distribution around the diffuser periphery. To obtain detailed, thoroughly reliable data to show their effects, then, it is necessary to make wind tunnel tests. For purposes of preliminary studies, however, this is usually not practical. However, some means must be provided to account for the effect of takeoff doors. To accomplish this for the PITAP procedure, a correlation of low-speed test data from Reference 10 was developed as shown in Figure 20. The low speed data, with total pressure recovery, P_{T_2}/P_{T_0}, plotted as a function of the corrected weight flow parameter, $\frac{W_2 \sqrt{\theta_2}}{A_T \delta_2}$, showed a good correlation, regardless of the size of the takeoff doors. In this case, A_T was always equal to the sum of the main inlet throat area plus the area of the take-off doors. Thus it makes a convenient generalization for use in all preliminary estimates of low-speed performance. Simply add the throat area of the takeoff doors to that of the main inlet and calculate the recovery as if the main inlet were operating at a correspondingly lower throat Mach number.

A correlation of experimental data (presented in Figure 21) is used to calculate the effect of lip bluntness on total pressure recovery at takeoff.

This method (Ref. 11) which is used to calculate total pressure recovery at the throat of an inlet with rounded lips, calculates the fraction of the loss for sharp lips that is applicable to rounded lips according to the following equation:

29
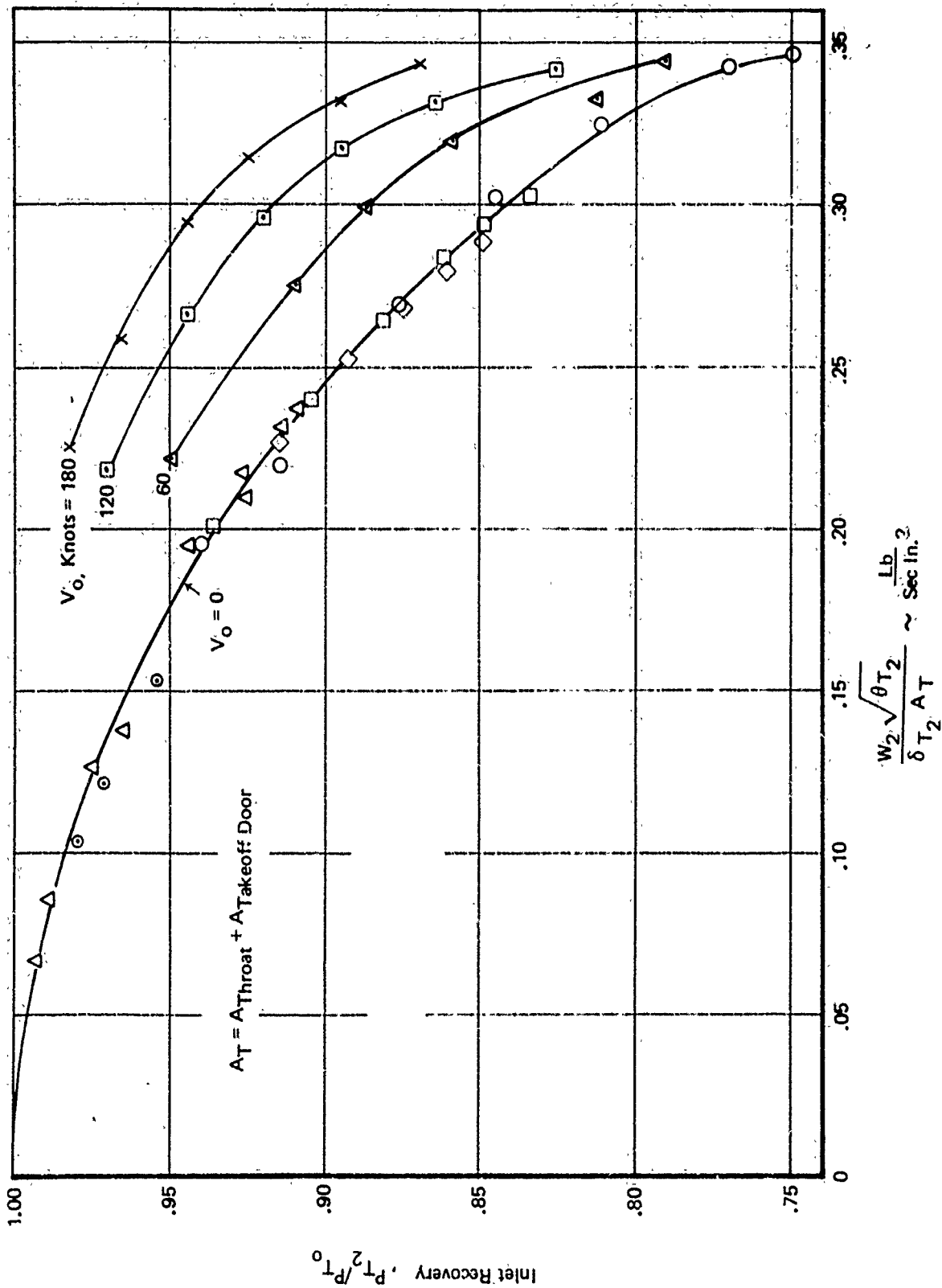
Figure 20: *LOW SPEED INLET RECOVERY CORRELATION*

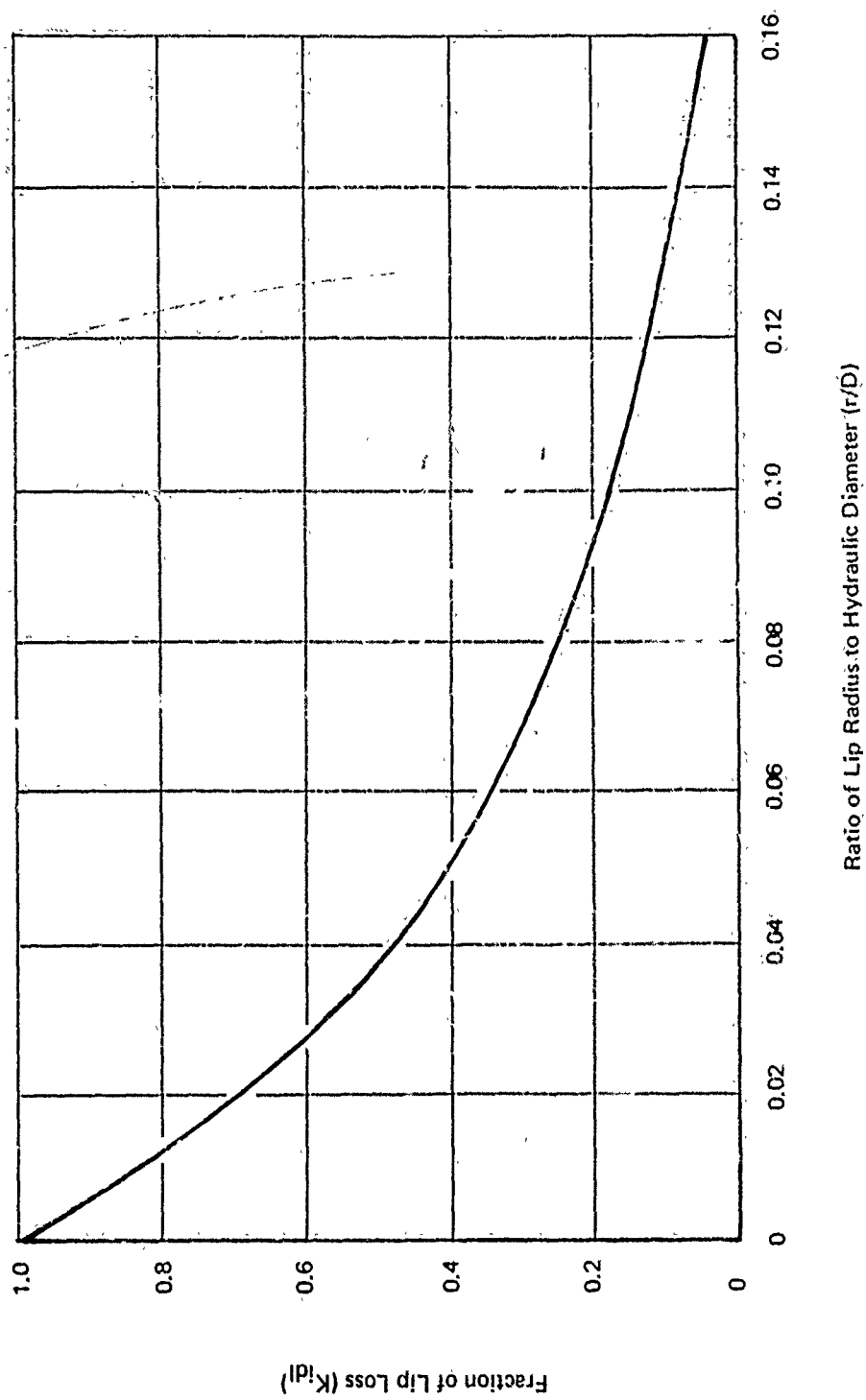$$A_T = A_{Throat} + A_{Takeoff\ Door}$$

$$\frac{W_2 \sqrt{\theta_{T_2}}}{\delta_{T_2} A_T} \sim \frac{Lb}{Sec\ In.^2}$$

Inlet Recovery, P_{T_2}/P_{T_0}

V_0, Knots = 180

120

60

$V_0 = 0$

Figure 21 : VARIATION OF LIP LOSS WITH LIP RADIUS

31

$$\left.\frac{P_T}{P_{T_O}}\right|_{\substack{\text{Rounded Lips,}\\ \text{MFR}_c > 1}} = 1 - \left[1 - \left(\frac{P_T}{P_{T_O}}\right)_{\substack{\text{Sharp Lip,}\\ \text{Same MFR}_c}}\right] \times K_{idl}$$

Where K_{idl} (Figure 21) is based on experimental data.

3.2 SUBSONIC DIFFUSER LOSSES

Subsonic diffuser performance is difficult to predict analytically because it is a function of many interrelated geometric and aerodynamic parameters. Because of this, attempts to simplify the prediction of diffuser performance have met with varying degrees of success. The most reliable diffuser data is that obtained from wind tunnel tests of the specific configuration of interest at realistic operating conditions. This type of data is normally not available, however, during preliminary studies. Therefore, about the best that can be done is to use the existing data, supplemented by theory, to arrive at an estimate for the new diffuser geometry. This section presents some data correlations that can be used to estimate the magnitude of the effect of various geometric and aerodynamic parameters on subsonic diffuser efficiency. Subsonic diffuser efficiency is expressed in terms of total pressure recovery from entrance to exit P_{T_2}/P_{T_1}.

Much of the experimental work shows that, for a given diffuser geometry, the total pressure loss characteristics of a subsonic diffuser can be reasonably well represented by expressing the total pressure loss as a function of the entrance dynamic pressure, where the diffuser loss coefficient is expressed as:

$$\varepsilon = \frac{\Delta P_T}{q_i} \quad \text{and} \quad \frac{P_{T_2}}{P_{T_1}} = 1 - \varepsilon \left[1 - \frac{1}{(1 + .2M_1^2)^{3.5}}\right]$$

Many subsonic diffusers have been experimentally shown to have a nearly constant duct loss factor as a function of throat Mach number, at least until the point is reached where the diffuser throat is nearly choked. Thus, it is possible to calculate directly the total pressure loss through the subsonic diffuser if the duct loss factor, ε, is known or assumed. The relationship between these variables is represented graphically in Figure 31. If the diffuser duct loss coefficient is known or can be estimated from experience, this method provides a convenient way to determine diffuser total pressure losses.

32

The most important factors which influence diffuser total pressure losses are: area ratio, length, entrance conditions (is there a shock ahead of the entrance or not?) and throat Mach number. Although diffuser test data can be presented in many different forms, depending on the geometry of the diffuser tested (for example; ε vs. third ramp angle, ε vs. effective conical diffusion angle, etc.), these parameters can be related to one of the more general parameters described above. This makes it possible to generalize the available data for preliminary analysis purposes. This is the approach used in obtaining the data correlations presented in this section.

Figure 22 presents data showing the effect of variations in the third ramp angle for a subsonic diffuser, for a two-dimensional inlet. The increase in third ramp angle causes a smaller throat size. This effectively increases the area ratio, A_{EXIT}/A_{throat}, and produces higher losses at inlet throat Mach numbers above .65.

Free-stream Mach number has relatively little effect in the diffuser loss coefficient (Figure 23), as long as the flow ahead of the entrance is subsonic.

Figures 24, 25, and 26 present correlations of data which show the effect of subsonic diffuser length on total pressure loss coefficient, ε, and max-minus-min distortion parameter. Another important factor in determining the total pressure loss through the diffuser is the presence of a normal shock ahead of the diffuser entrance. The effect of this shock is easily seen by comparing Figure 25 (no shock) with Figure 26 (shock present). Substantially higher total pressure losses are incurred by the diffuser with the shock ahead of the entrance. The shock also increases the turbulence in the diffuser, an important consideration for engine/inlet compatibility.

The effect of bends in the diffuser is shown in Figure 27.

The increase in diffuser loss due to increasing area ratio is shown in Figures 28 and 30.

Boundary layer effects on diffuser loss are presented in Figure 29. Allowing for scatter in the experimental data, it is difficult to sort out consistent differences due to boundary layer effects which can be consistently explained. It appears that a fairly wide error band must be accepted for the existing data.

Figure 31 presents a curve that can be used to relate the duct loss coefficient, ε, to a pressure recovery, P_{T_2}/P_{T_1}, for any
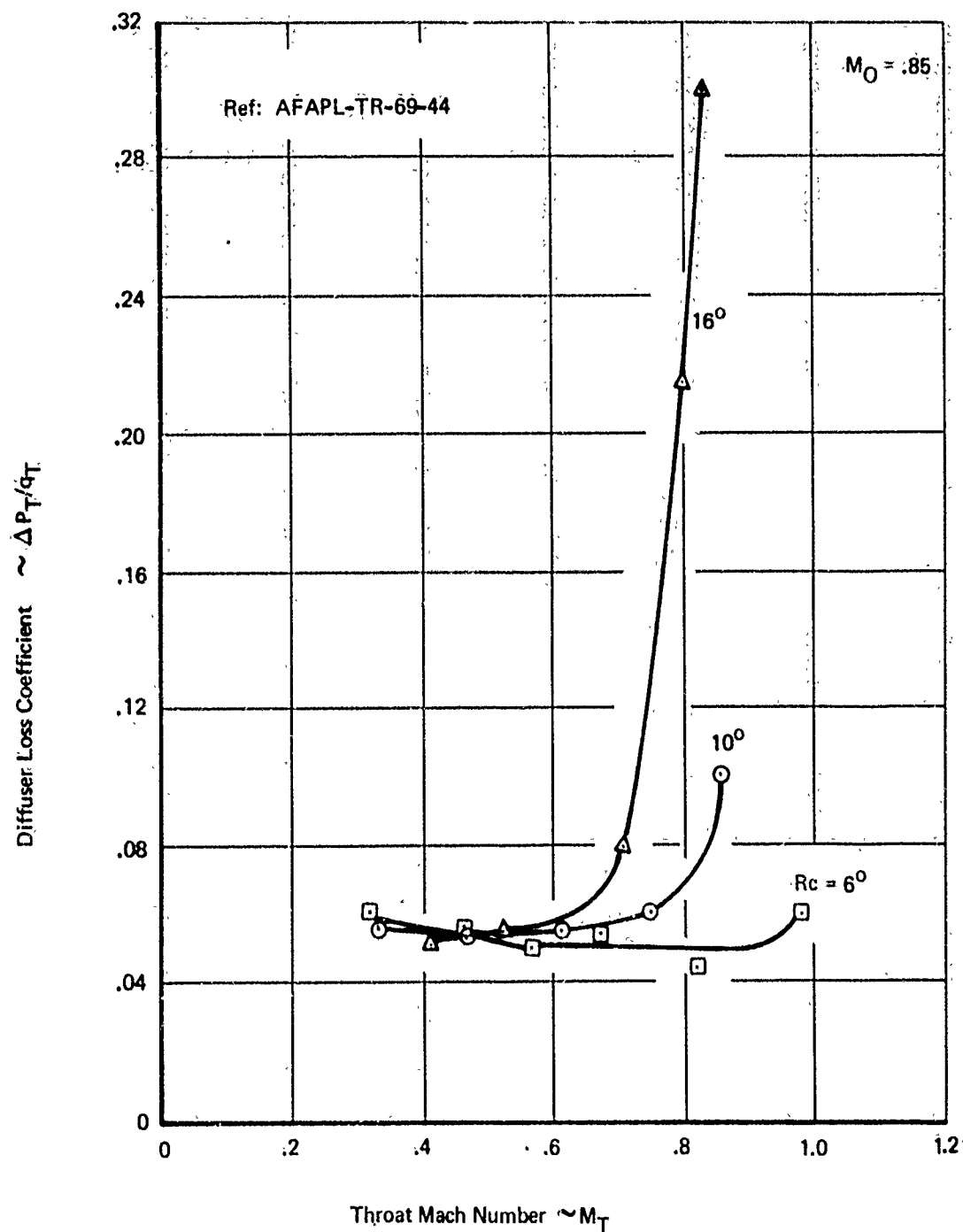
Figure 22: EFFECT OF THIRD RAMP ANGLE ON DIFFUSER EFFICIENCY
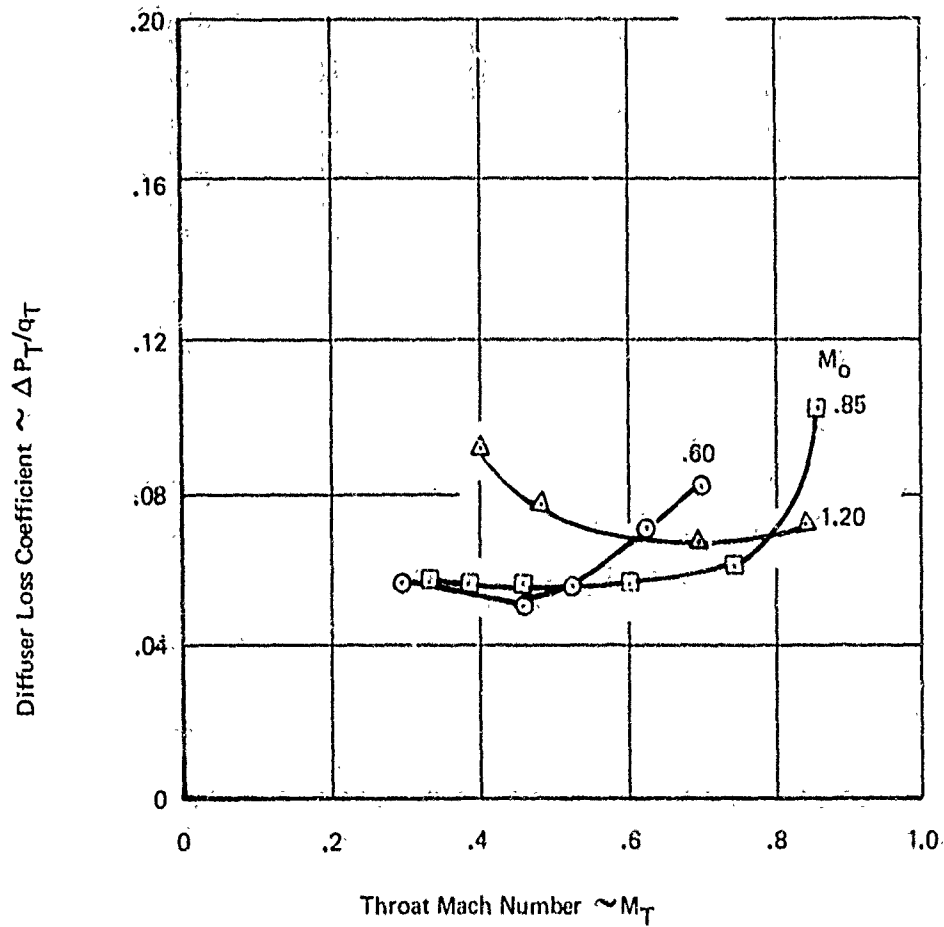
34

Ref: AFAPL-TR-69-44

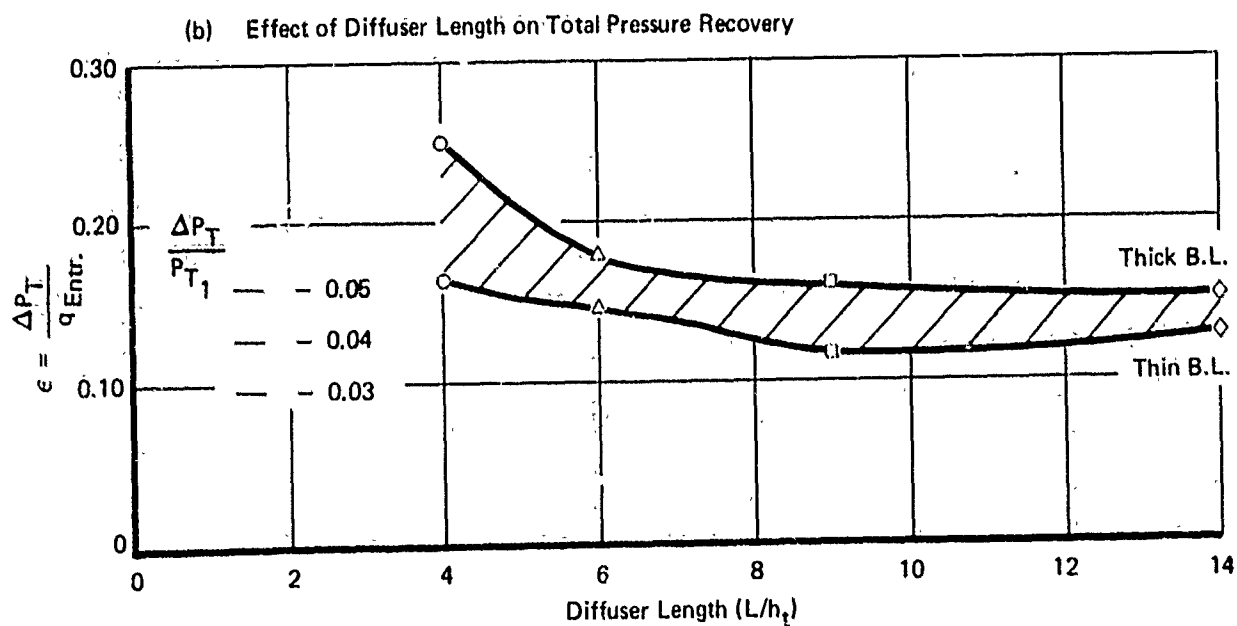Figure 23: EFFECT OF FREE-STREAM MACH NUMBER ON DIFFUSER LOSSES

35

$M_{Entr} = 0.75$ } For Both
$\dfrac{A_{Eng}}{A_{Entr}} = 1.80$ } Figures (a) and (b)

(a) Effect of Diffuser Length on Distortion

Distortion Index $\dfrac{P_{T_{Max}} - P_{T_{Min}}}{P_{T_{Ave.}}}$

0.30
0.20
0.10
0

Thick B.L.
Thin B.L.

Diffuser Length (L/h_t)
0   2   4   6   8   10   12   14

(b) Effect of Diffuser Length on Total Pressure Recovery

$\epsilon = \dfrac{\Delta P_T}{q_{Entr.}}$

0.30
0.20
0.10
0

$\dfrac{\Delta P_T}{P_{T_1}}$
— 0.05
— 0.04
— 0.03

Thick B.L.
Thin B.L.

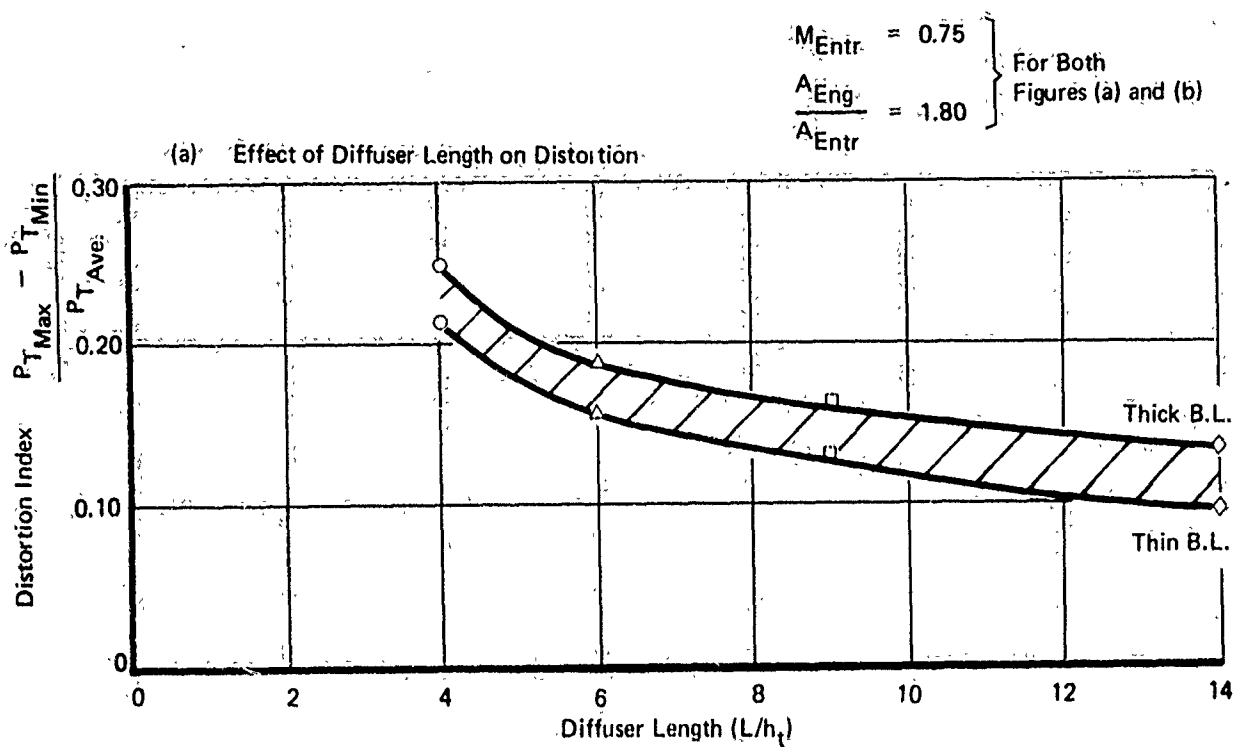Diffuser Length (L/h_t)
0   2   4   6   8   10   12   14

Figure 24 : EFFECT OF DIFFUSER LENGTH ON TOTAL PRESSURE RECOVERY
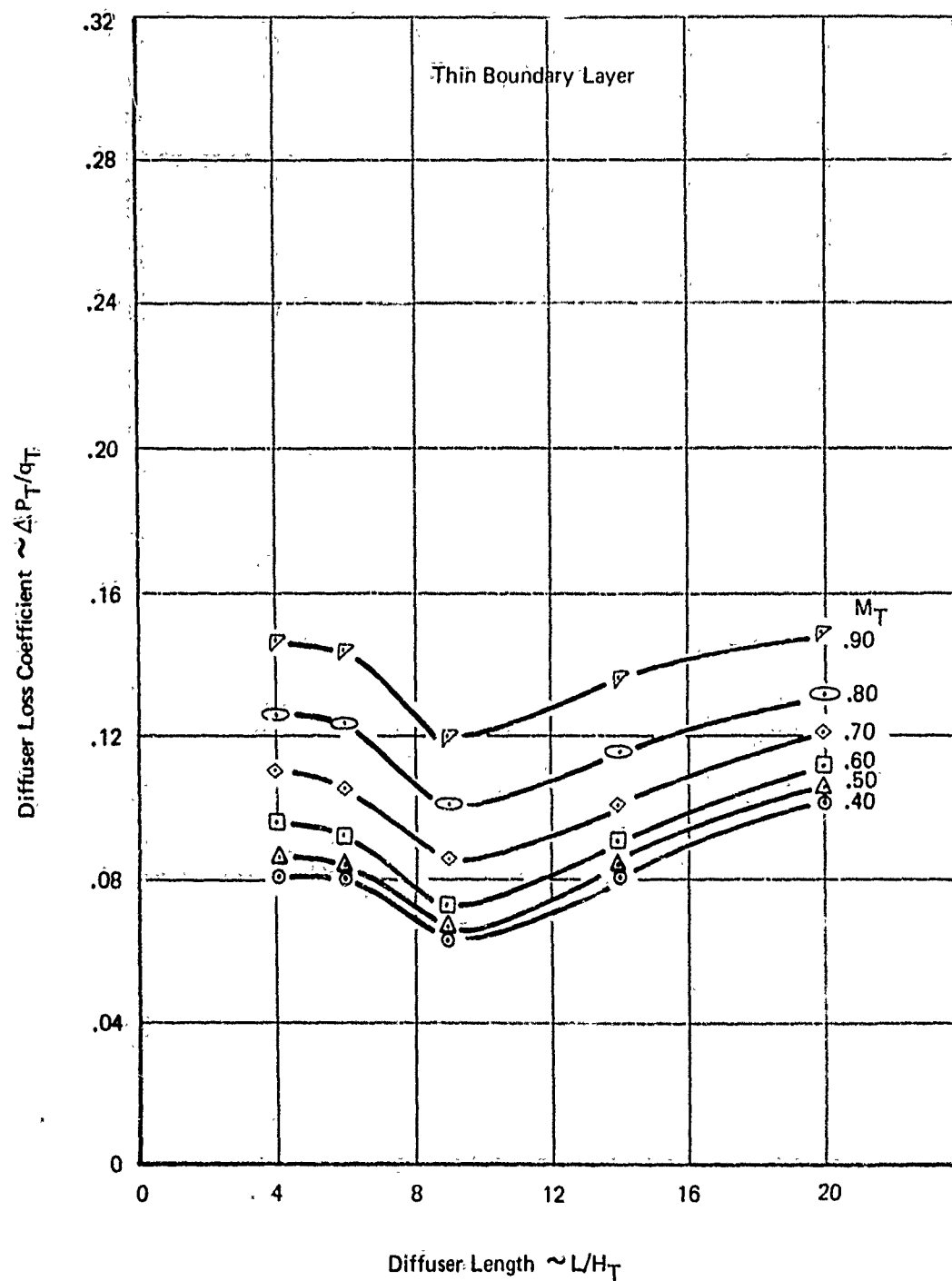AND DISTORTION

36

Figure 25: EFFECT OF DIFFUSER LENGTH ON DIFFUSER LOSS
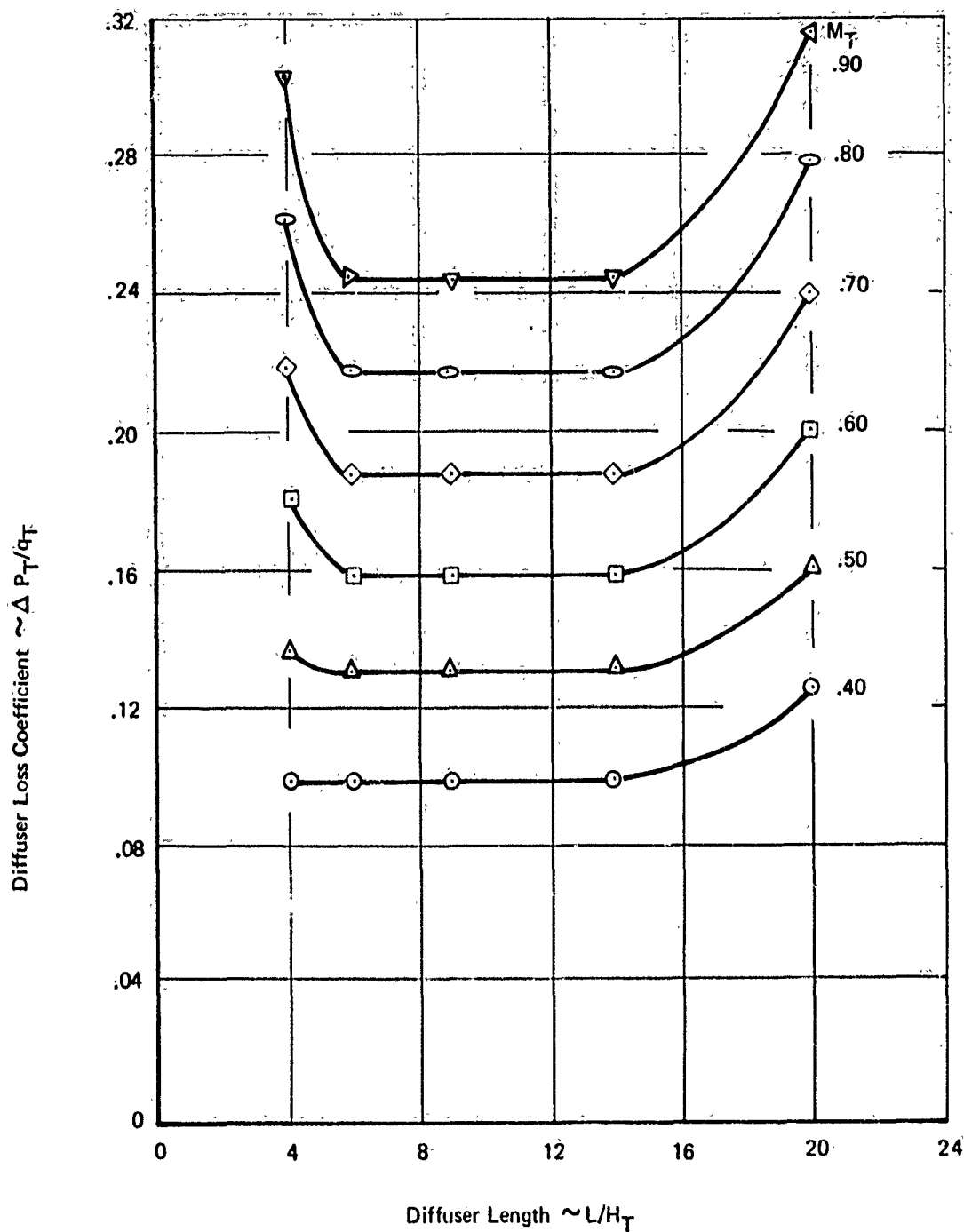COEFFICIENT (SUBSONIC ENTRANCE)

37

Figure 26: EFFECT OF DIFFUSER LENGTH ON DIFFUSER LOSS COEFFICIENT (SHOCK AHEAD OF ENTRANCE)
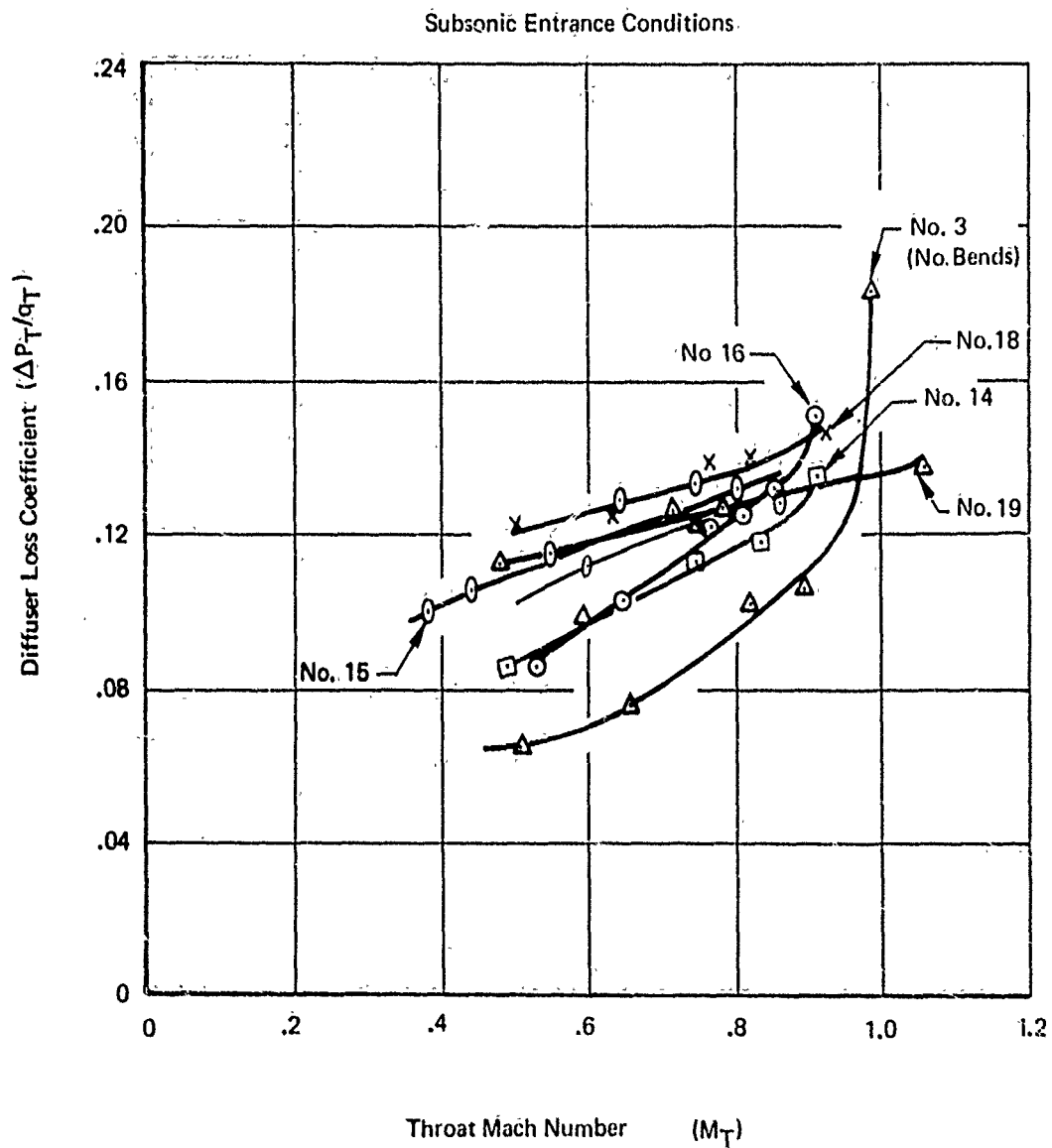
38

Subsonic Entrance Conditions

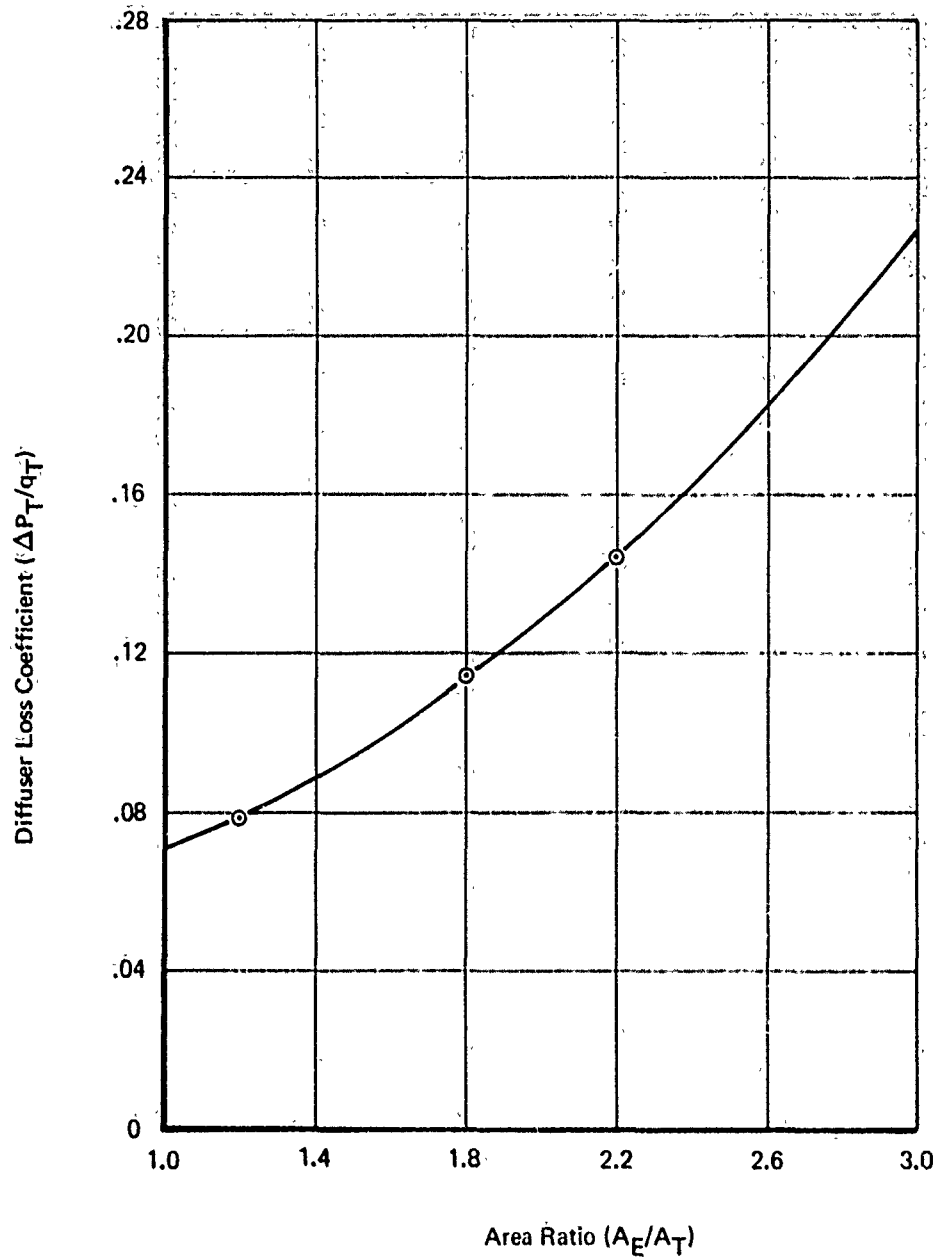Figure 27 : EFFECT OF BENDS ON SUBSONIC DIFFUSER EFFICIENCY

39

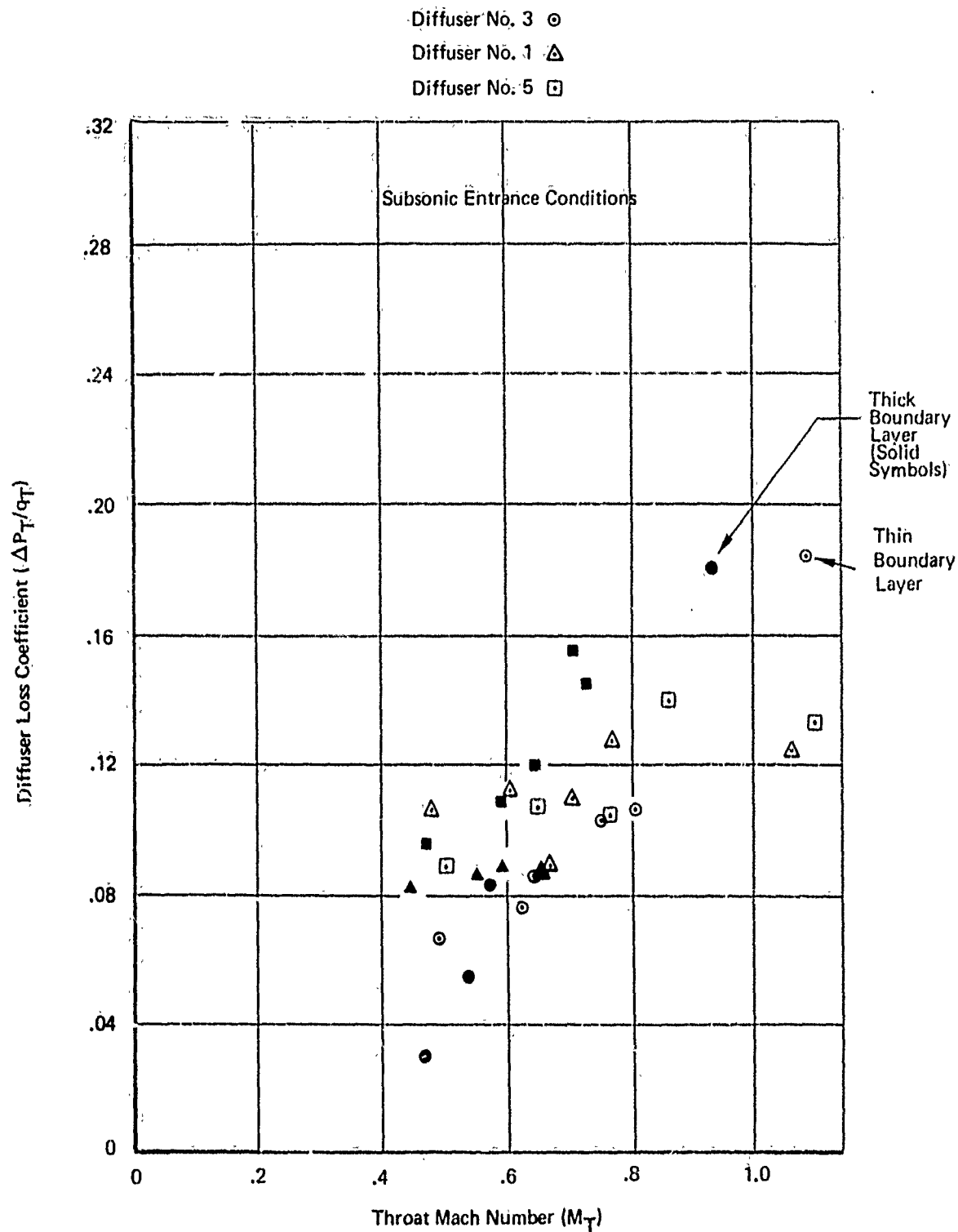Figure 28 : EFFECT OF AREA RATIO ON DIFFUSER LOSS COEFFICIENT

Figure 29 : *EFFECT OF BOUNDARY LAYER THICKNESS ON DIFFUSER LOSS COEFFICIENT*
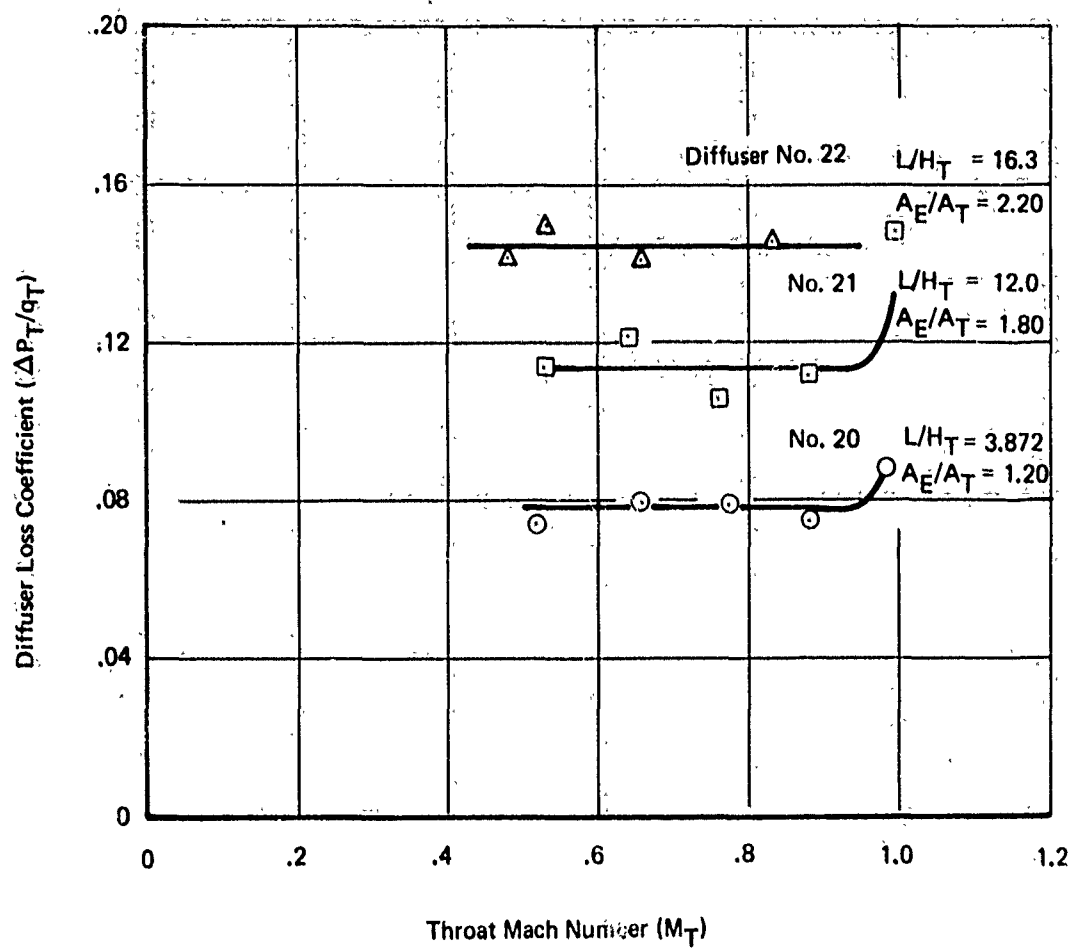
41

Thin Boundary Layer

Figure 30 : EFFECT OF AREA RATIO ON DIFFUSER LOSS COEFFICIENT

42

$$\frac{P_{T_2}}{P_{T_1}} = 1 - \epsilon \left(1 - \frac{1}{(1 + .2 M_1^2)^{3.5}}\right)$$
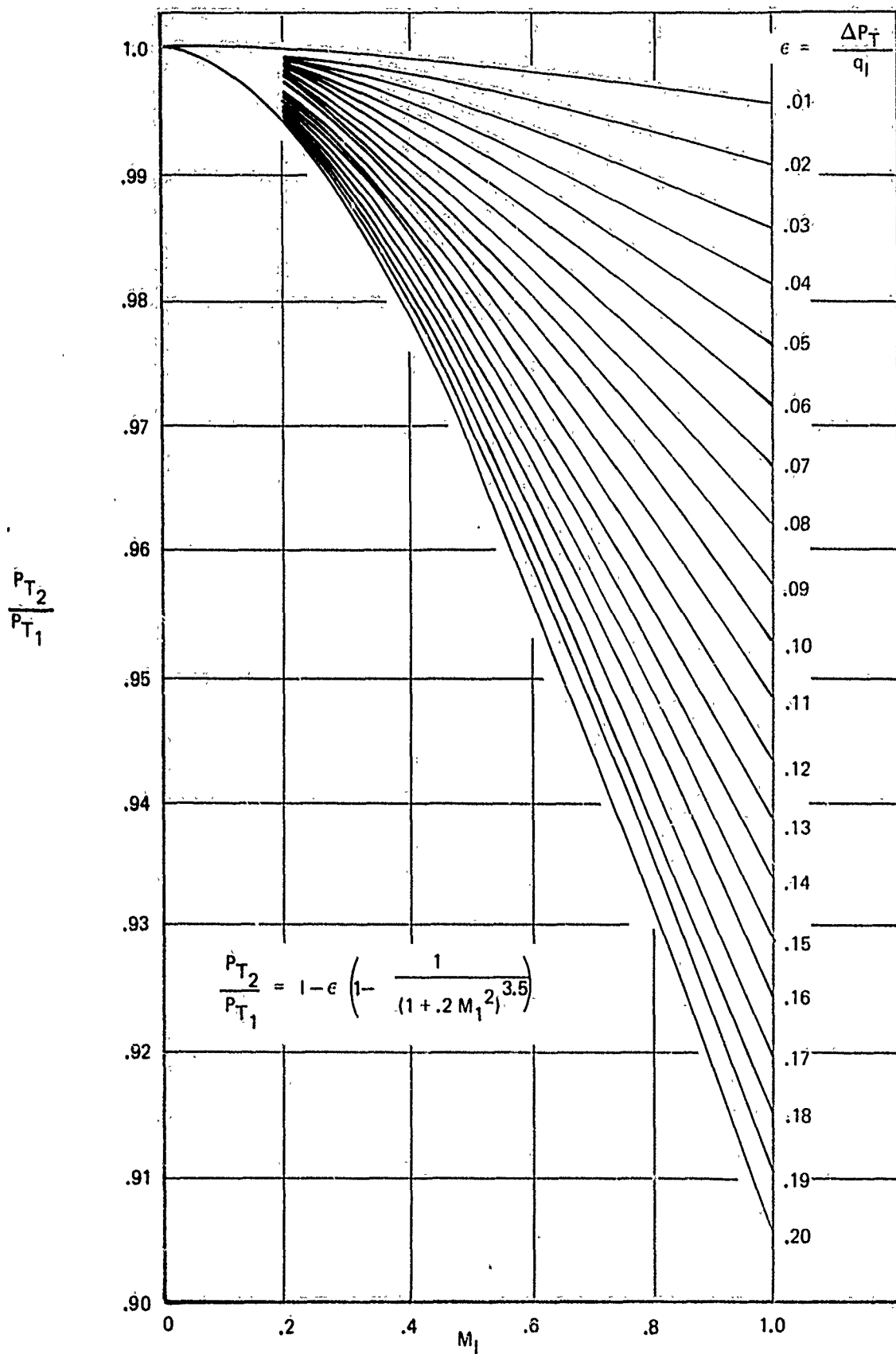
Figure 31 :   TOTAL PRESSURE RECOVERY LOSS FACTORS

43

given throat Mach number, M_1. This curve can be used to estimate
diffuser losses, even if no experimental data are available.
It is necessary to estimate a duct loss coefficient (either a
constant or a variation with M_1). If no other value is available,
use a constant $\varepsilon = .12$ for subsonic entrance conditions and a
constant $\varepsilon = .16$ if a normal shock is ahead of the diffuser
entrance.

3.3 SHOCK LOSSES

Inlet total pressure recovery is a function of many parameters,
and so it is difficult to develop generalized correlations that
are applicable to a wide range of configurations. Nevertheless,
by plotting the operating (engine-matched) total pressure re-
coveries for a large variety of full-scale and small scale inlet
tests for a range of Mach numbers from 0 to 3.0, it is possible
to detect definite trends in the experimental data that are
predictable, according to theory. A plot such as this is pre-
sented in Figure 32. At first glance, the data appear to follow
no particular patterns. However, if the data of Figure 32 are
compared with the theoretical plots shown in Figure 33 it is
seen that the experimental data fall into trends that are to be
expected, based on the factors that are known to cause the
greatest losses for each Mach number regime. Figure 33 was
calculated to show the effect of sharp lip losses, subsonic
diffuser losses, and shock losses. At low speeds, the sharp-
lipped supersonic inlets have large losses in recovery, while
the subsonic inlets with blunt lips have high recovery. At
transonic speeds, the subsonic diffuser losses account for most
of the total pressure losses. As flight Mach number is increased
to higher supersonic speeds, the shock losses increase steadily,
reducing total pressure recovery greatly. The shock losses
depend on the number and strengths of the shocks used to deceler-
ate the flow to subsonic Mach numbers for use by the engine.
By knowing the complexity of the inlet comression scheme (N =
number of shocks), the lip shape (blunt or sharp), and the
approximate subsonic diffuser efficiency (average duct loss
factors can be used when no unusual geometries are required),
calculations can be made of overall inlet recovery that are suit-
able for preliminary performance predictions.

3.4 BOUNDARY LAYER BLEED AIRFLOW

The amount of boundary layer bleed airflow required to make an
inlet operate efficiently depends on several factors: design
Mach number, type of compression scheme, sideplate design,
shock stability required, engine tolerance to distortion, and
the extent to which the inlet performance is optimized. Bleed
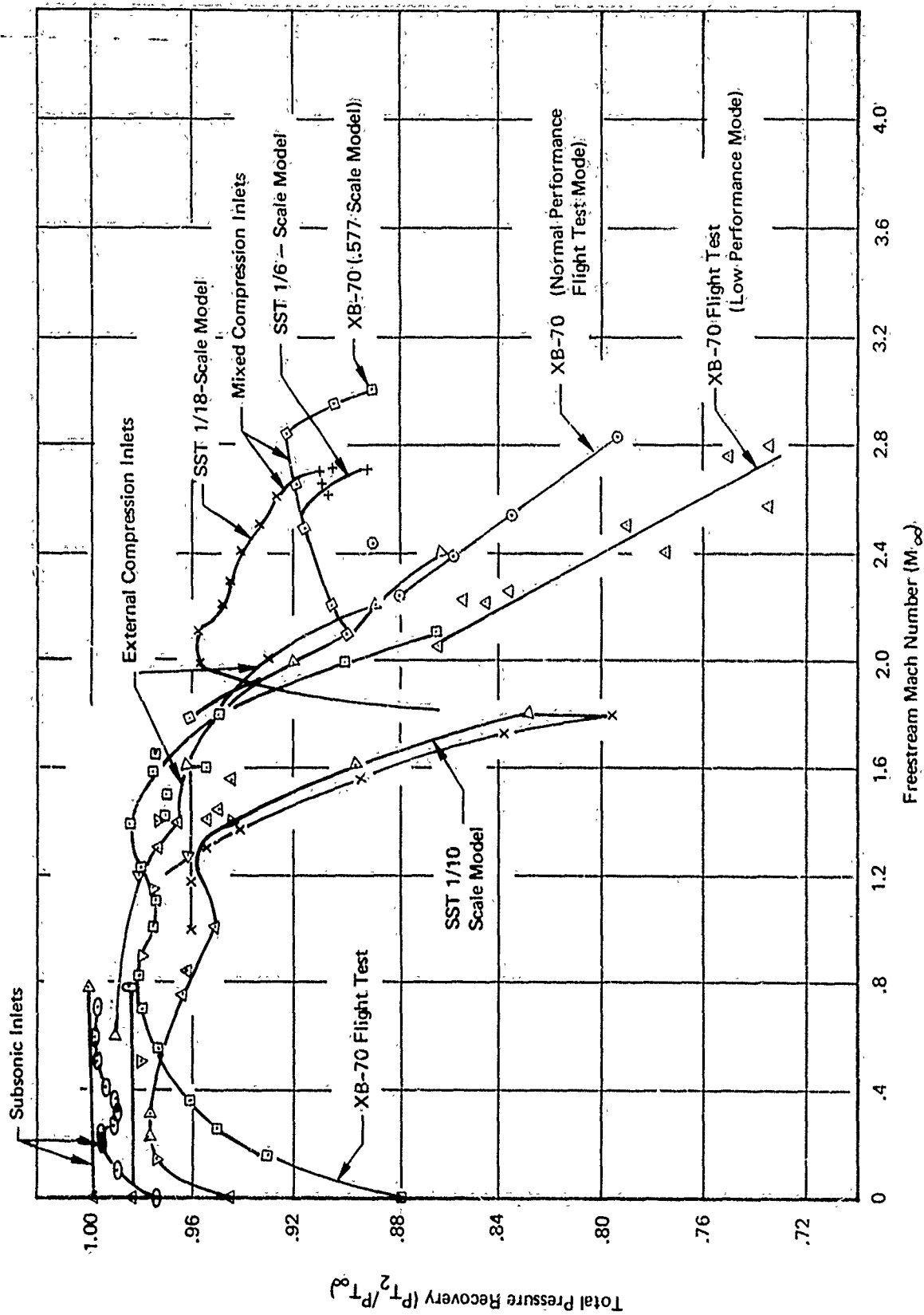system design is a complex analytical and experimental problem,

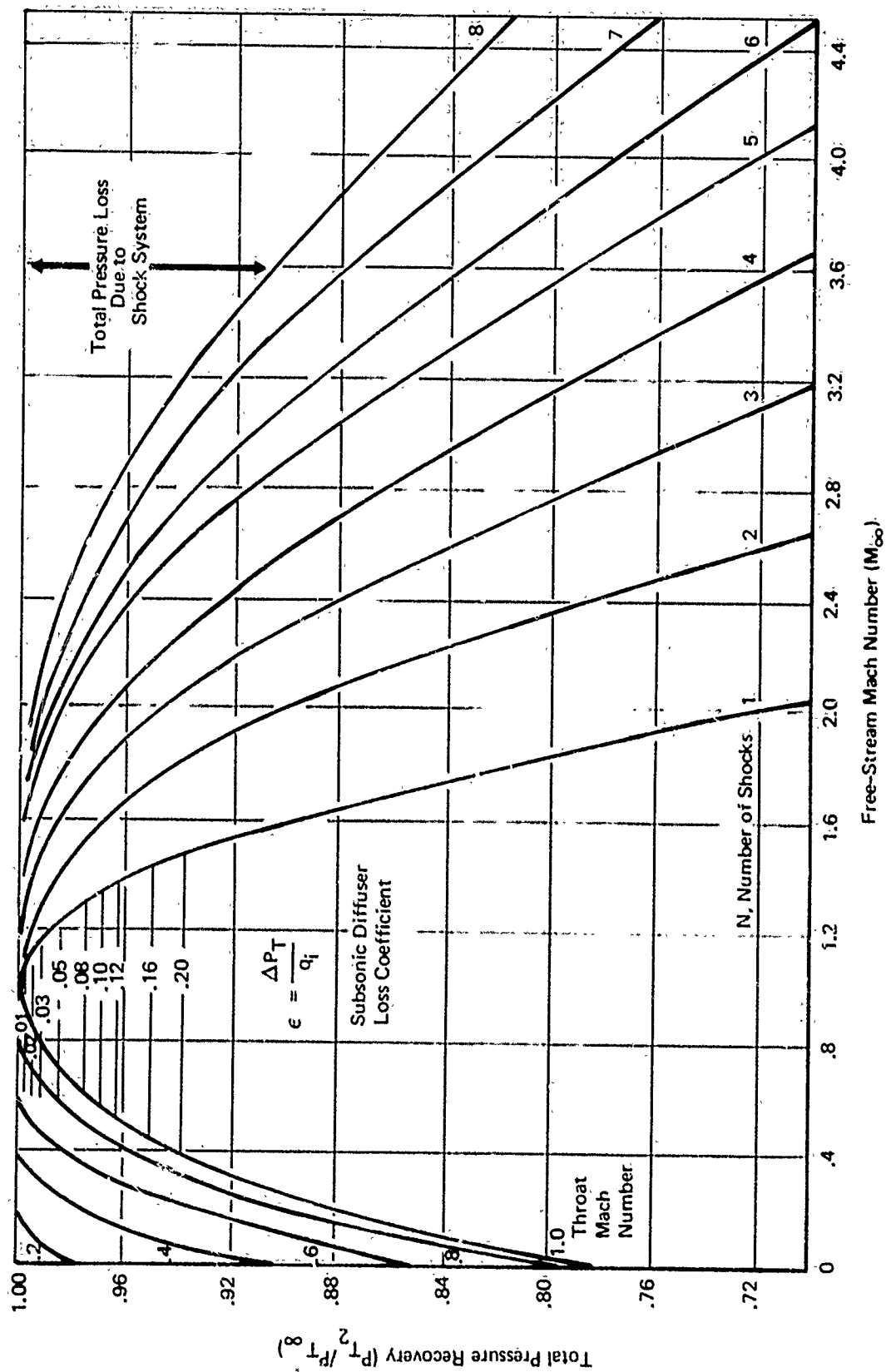Figure 32: COMPILATION OF TOTAL PRESSURE RECOVERY DATA FOR VARIOUS INLETS

45

Figure 23: THEORETICAL INLET LOSSES

requiring much development time to be spent on a relatively small number of specific configurations. The available data have been plotted to obtain the generalized curves shown in Figure 34. These curves can be used to obtain design point bleed airflows for reasonably well-optimized inlet configurations as a function of free-stream Mach number. If more detailed bleed data are desired, refer to Section IV.

3.5 BOUNDARY LAYER PLENUM PRESSURE

The boundary layer plenum pressure depends mainly on the type of bleed removal system used. There are many factors that can have some influence on the total pressure recovery of the bleed air. These factors include: type of scoop or hole geometry (shape, size, angle) used to remove the air, the region of the inlet where bleed air is removed (forward surfaces have high Mach number flow, low static pressures, and hence, low bleed plenum pressures, while the throat region has high local pressures and hence, high plenum pressures), boundary layer thickness, shock position, and number of bleed compartments. It is too difficult to account for all these factors in a preliminary design method which is to be applied to a wide variety of configurations.

As a practical matter, however, either a slot or porous bleed removal system is usually employed, which is optimized through testing until the highest plenum pressure is achieved that is consistent with adequate bleed removal. For preliminary design purposes, a correlation has been made of plenum pressures obtained for each of the two types of bleed systems most commonly used as a function of free-stream Mach number. This correlation is presented in Figure 35.

3.6 NOZZLE BOATTAIL DRAG

The ability to correlate isolated boattail drag is hindered by the fact that there is considerable disagreement in the literature with regard to experimentally determined boattail drag coefficients for similar or identical boattail shapes. Some of the disagreement is attributable to different simulation techniques (e.g., solid jet simulator vs. cold-jet blowing), and some must be assumed the result of tunnel blockage effects or support interference. The subsonic correlation used in PITAP is based on a blown-model test (Ref. 12) run in the Boeing Transonic Wind Tunnel with circular arc boattail nozzles. The drag at a nozzle pressure ratio of 2.5 was correlated as a function of the boattail chord angle from the start of the boattail to the nozzle exit. The data (with calculated skin friction removed) are given in Figure 36.
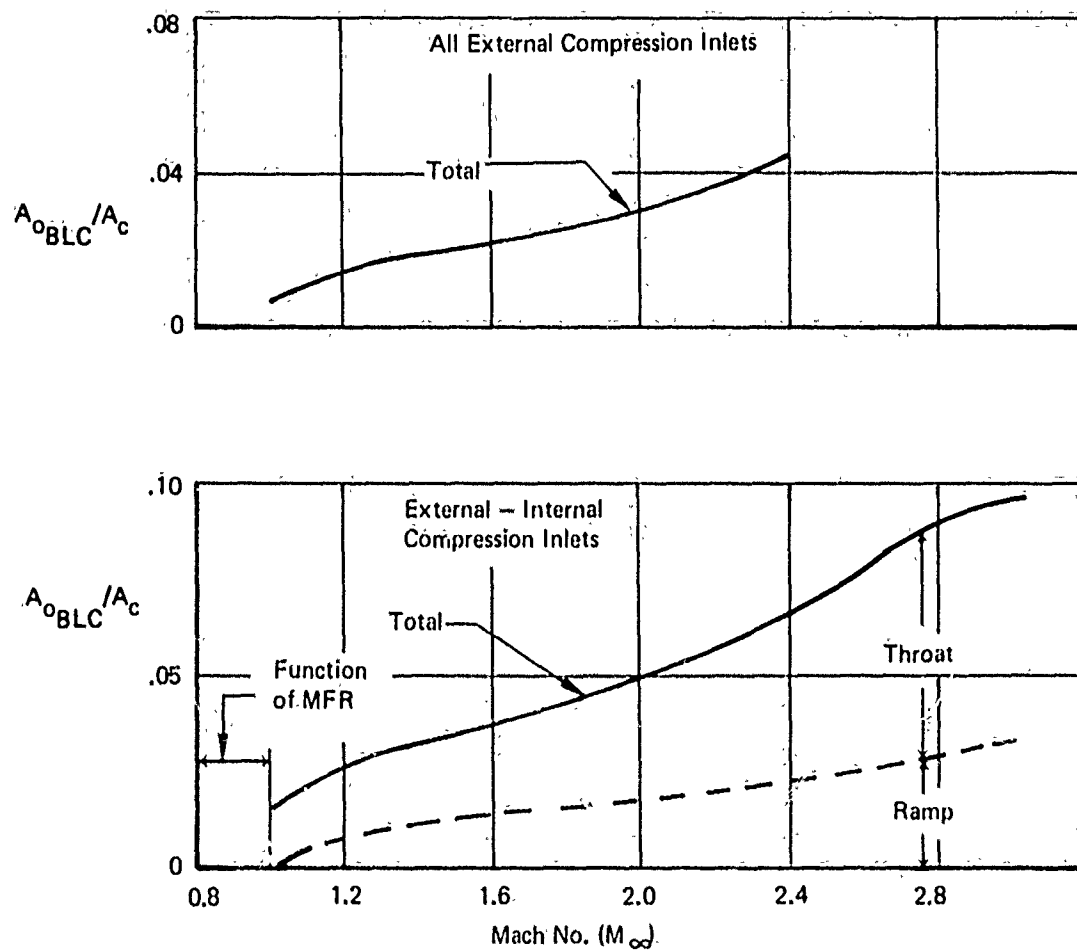
47

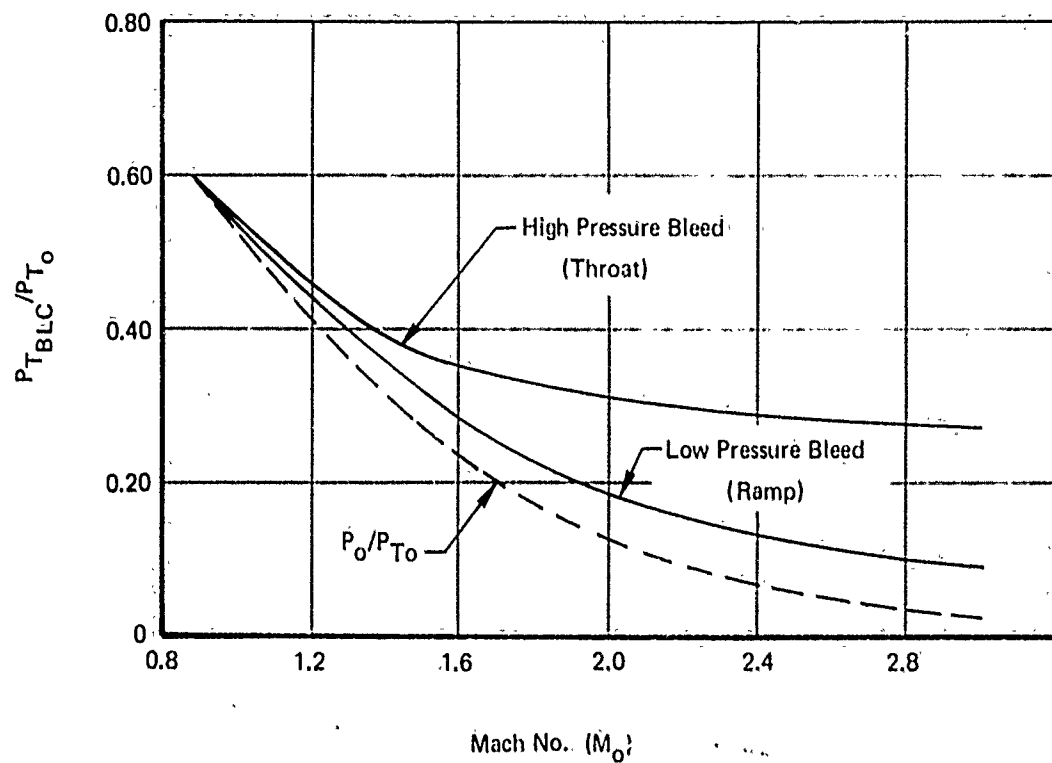Figure 34 : BOUNDARY LAYER CONTROL SYSTEM BLEED FLOW RATES

48
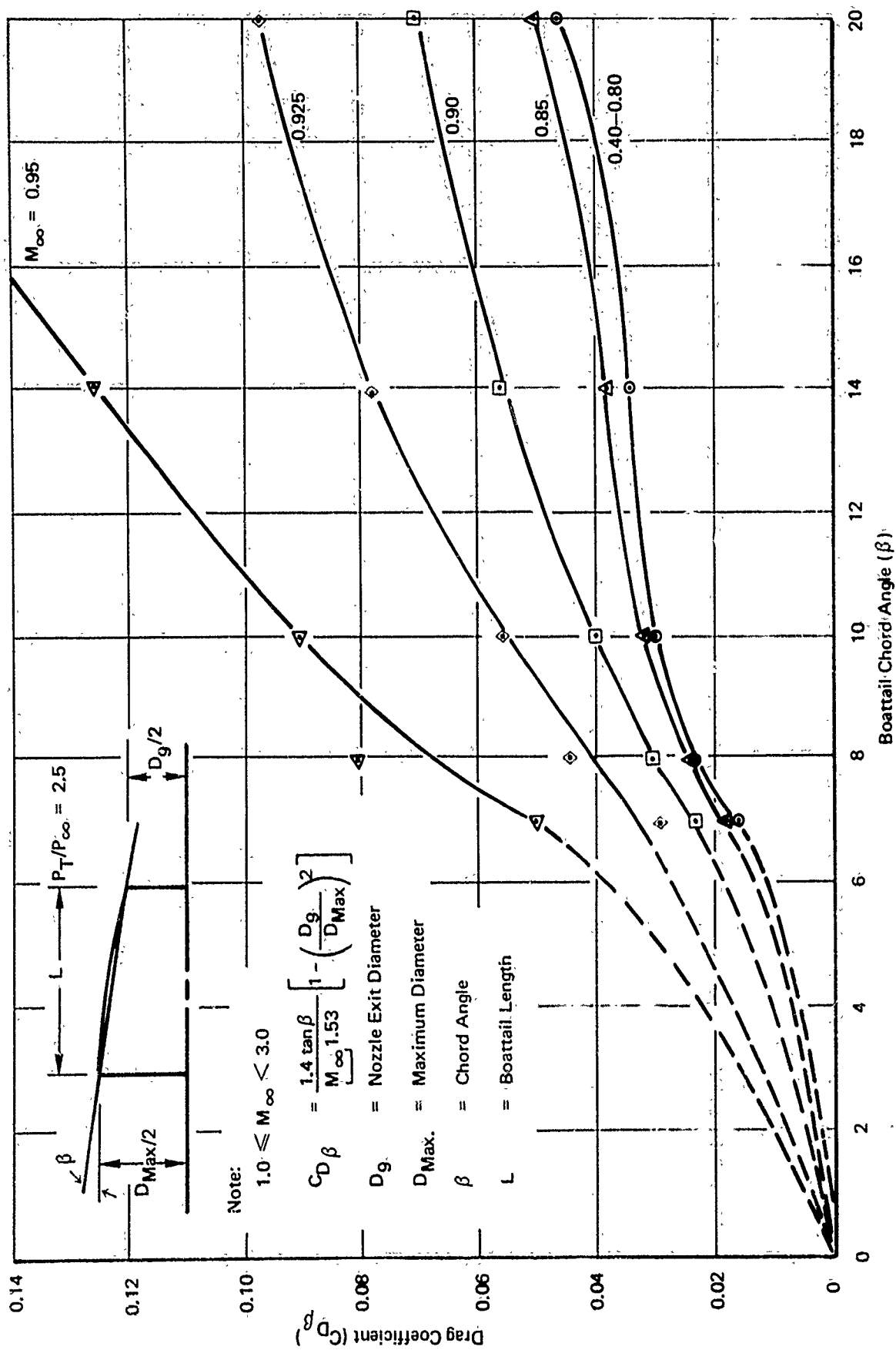
Figure 35: BOUNDARY LAYER CONTROL SYSTEM BLEED PRESSURES

49

Figure 36: NOZZLE BOATTAIL PRESSURE DRAG COEFFICIENTS AS f.(β)

The following labels appear within the figure:

$M_\infty = 0.95$

Vertical axis: Drag Coefficient (C_{D_β}), ranging from 0 to 0.14

Horizontal axis: Boattail Chord Angle (β), ranging from 0 to 20

Curve labels: 0.925, 0.90, 0.85, 0.40–0.80

Note:

$1.0 \leqslant M_\infty < 3.0$

$P_T/P_\infty = 2.5$

$$C_{D_\beta} = \frac{1.4 \tan\beta}{M_\infty^{1.53}} \left[1 - \left(\frac{D_g}{D_{Max}} \right)^2 \right]$$

D_g = Nozzle Exit Diameter

$D_{Max.}$ = Maximum Diameter

β = Chord Angle

L = Boattail Length

50

Although Figure 36 applies strictly to circular arc boattails
only, there is some evidence that a conical boattail with a large
corner radius at the start of the boattail behaves in a similar
fashion. Figure 37, from Ref. 13, shows boattail pressure drag
characteristics for conical boattails with corner radius ratios
(radius over model maximum diameter) varying from zero to 4.84.
All of the open symbols correspond to models with trailing edge
boattail angles (not chord angles) of 15 degrees. For radius
ratios of 1.0 and less, the transonic drag rise characteristics
are clearly affected by the relatively sharp corner. For radius
ratios of 2.5 and 3.5, however, the drag rise characteristics
match those of the model with a radius ratio of 4.84, which is
the limiting case of a circular arc boattail. Also plotted in
Figure 37 is some conical boattail data from Ref. 14 which
correspond to the same nozzle geometry as the open circles.
The disagreement in drag coefficient level of 0.03 to 0.04
apparent in the figure illustrates the difficulties involved in
generating reliable correlations.

In Ref. 13 t. data shown in Figure 37 were also cross-plotted
to show the effect of corner radius at various Mach numbers,
as presented in Fig. 38. The corresponding predictions from
the PITAP correlation are also plotted at Mach 0.9 and 0.8.
PITAP predictions at Mach 0.56 and 0.7 are the same as at Mach
0.8). The PITAP predictions decrease with radius ratio because
the start of the boattail, used to define chord angle, moves
upstream with increasing radius ratio.

Despite a drag coefficient level difference of about 0.02, the
PITAP predictions display the same trends as the conical boat-
tail data for corner radius ratios of 2.5 or more.

It should perhaps be noted that both the PITAP data and the data
of Ref. 14 indicate higher drag levels than the data of Ref. 13.
Both the Boeing test used for PITAP correlations and the test
reported in Ref. 14 used blown models to achieve jet simulation.
The test reported in Ref. 13 used a solid plume simulator instead.

For supersonic Mach numbers up to Mach 3.0 PITAP uses the ex-
pression given in Figure 36. This represents an empirical
correlation of data from several sources, as shown in Figure 37.
The correlation was biased at the lower Mach numbers toward
data obtained with blown jet simulation. The form of the corre-
lation was suggested by supersonic wave drag considerations (Ref.
15), and, as shown in Figure 39 it does a reasonably good job
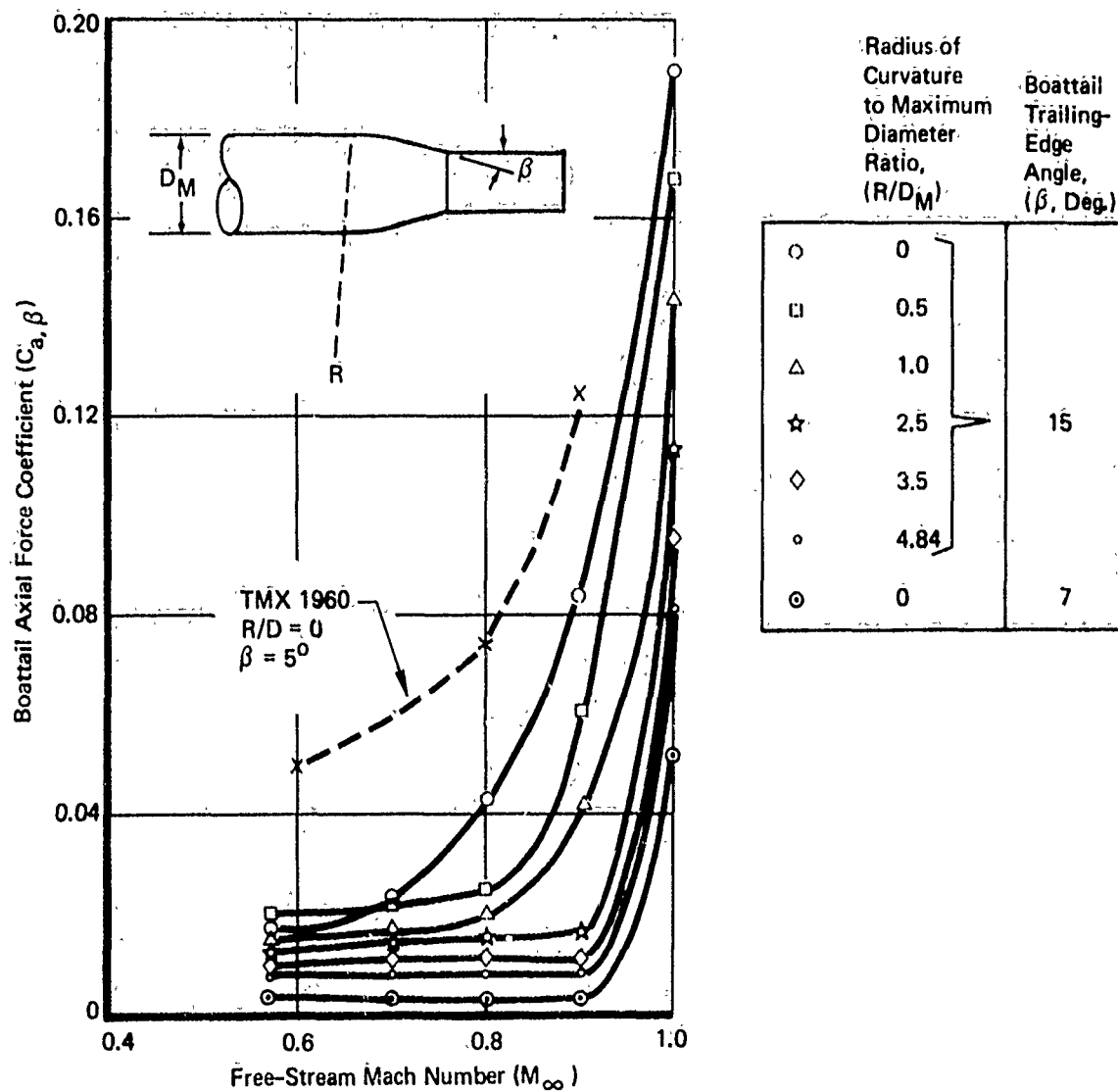of collapsing the data.

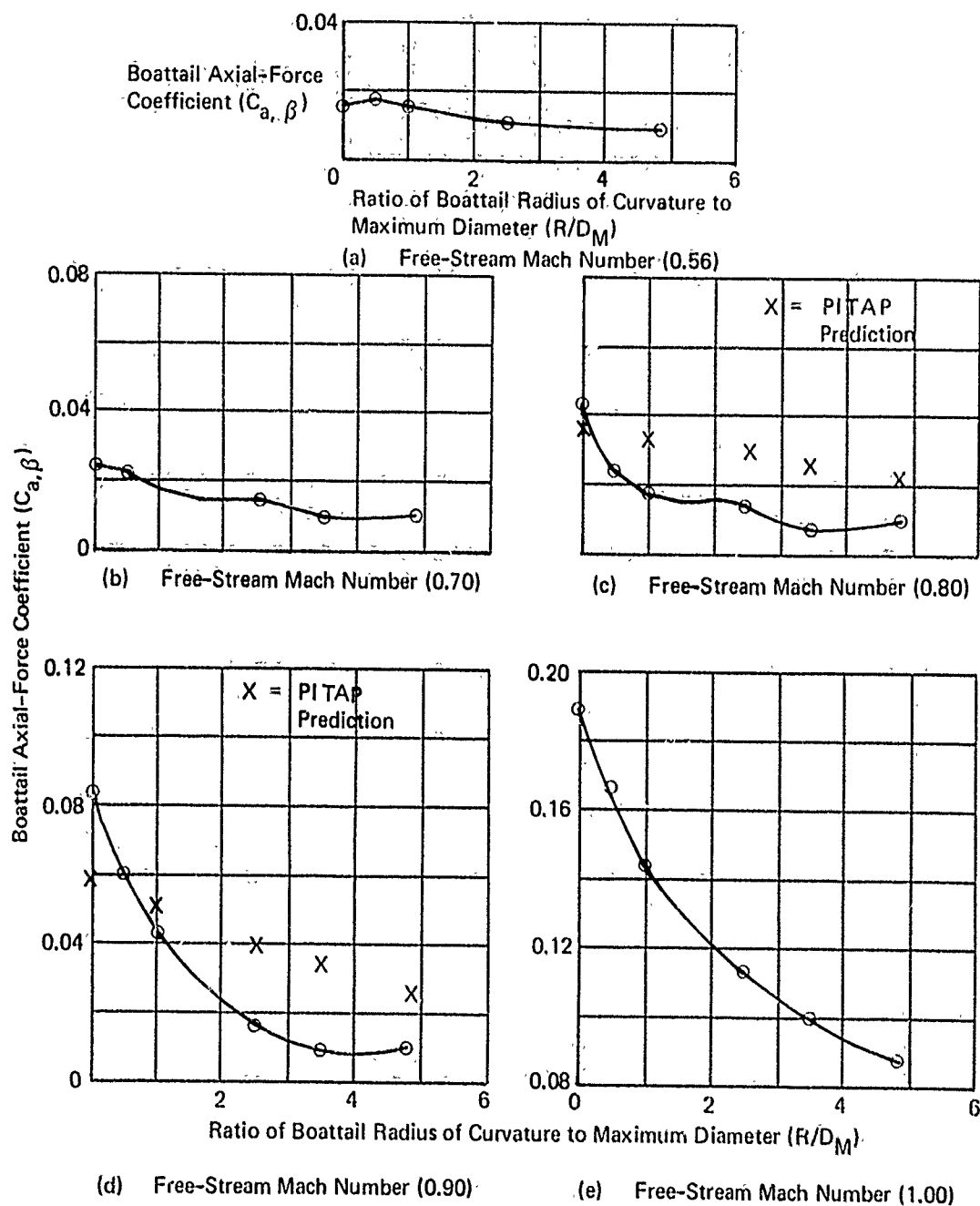*Figure 37: EFFECT OF AFTERBODY SHAPE ON TRANSONIC DRAG RISE*

Figure 38 : **EFFECT OF RADIUS OF CURVATURE TO DIAMETER RATIO ON BOATTAIL AXIAL-FORCE COEFFICIENT. BOATTAIL TRAILING-EDGE ANGLE, 15°; MODEL ANGLE OF ATTACK, 0°; WITH JET SIMULATOR**
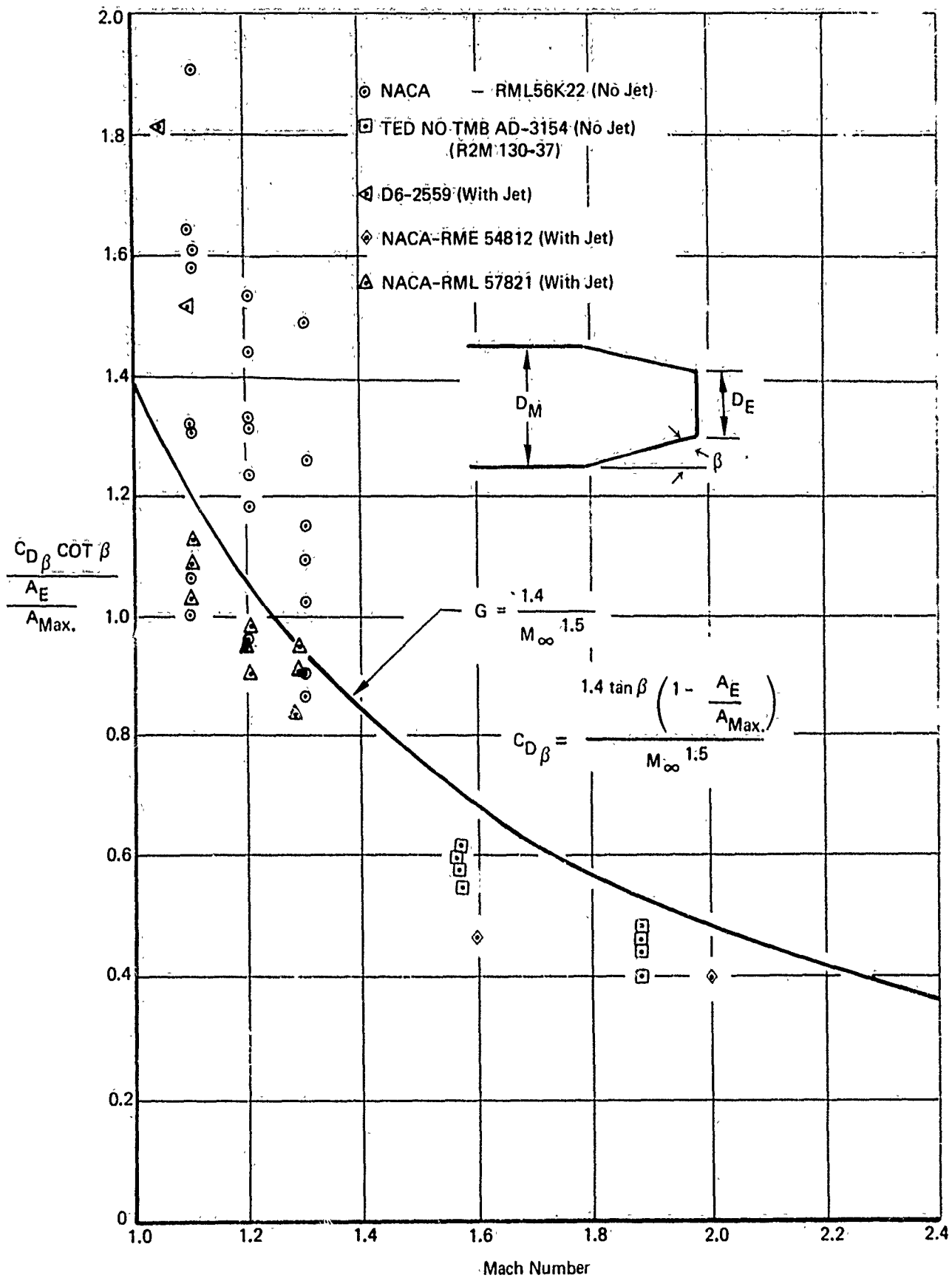
53

Figure 39 : SUPERSONIC BOATTAIL DRAG CORRELATION

54

3.7 BASE PRESSURE

The PITAP method is currently set up to receive an input table of base pressure coefficient versus Mach number for a specified afterbody geometry. It can use the base pressure coefficient from the input table and a specified base area to compute base drag as a function only of freestream Mach number. However, to be throttle-sensitive, the base area must be located where it is also affected by the propulsive jet effects which vary with nozzle pressure ratio. In addition, the base pressure is known to be sensitive to approaching boundary layer conditions. Therefore, methods to account for these effects should be incorporated into the calculation procedure to obtain an improved base pressure prediction.

Subsonically, the effects of the propulsive jet may be accounted for by using correlations obtained by McDonald and Hughes (Ref. 16).

The McDonald and Hughes correlation gives the increment in base pressure coefficient between a base with no jet effects and one with a jet of a given nozzle pressure ratio and a given temperature. The correlation is presented in Ref. 16 for a freestream Mach number of 0.90 and jet total pressure ratios of 2.0 and 3.0. The correlation is seen to work for approach boattail angles from 8 degrees to 24 degrees and specifically treats the case of an annular base around the jet. The key correlating parameter is the jet diameter squared divided by the product of the base diameter and the maximum diameter. Figure 40 presents this correlation for a jet pressure ratio of 2.0. The success of this parameter in correlating the data at Mach 0.90 suggest that it be tried at other subsonic Mach numbers. The method of McDonald and Hughes for Mach 0.90 is programmed into PITAP.

For supersonic Mach numbers, from 1.0 to 2.2, an excellent base pressure correlation has been reported in Ref. 17. Using correlation parameters called B and C which involve a reference base pressure level and known information about nozzle geometry and pressure ratio, a remarkable collapsing of the available data is obtained, as shown in Figure 41.

The parameters B and C are defined below:

$$B = M_\infty \ln^{-1} (.815 - 1.15 \ln K) \left(\frac{P_b}{P_\infty}\right)_M \left(\frac{P_b}{P_\infty}\right)_K$$

where $\left(\frac{P_b}{P_\infty}\right)_M$ = model base pressure ratio

P_{T_J} = Propulsive Jet Total Pressure

P_∞ = Freestream Static Pressure

ΔC_{P_b} = Base Pressure Increment

D_j = Jet Diameter

D_b = Base Diameter

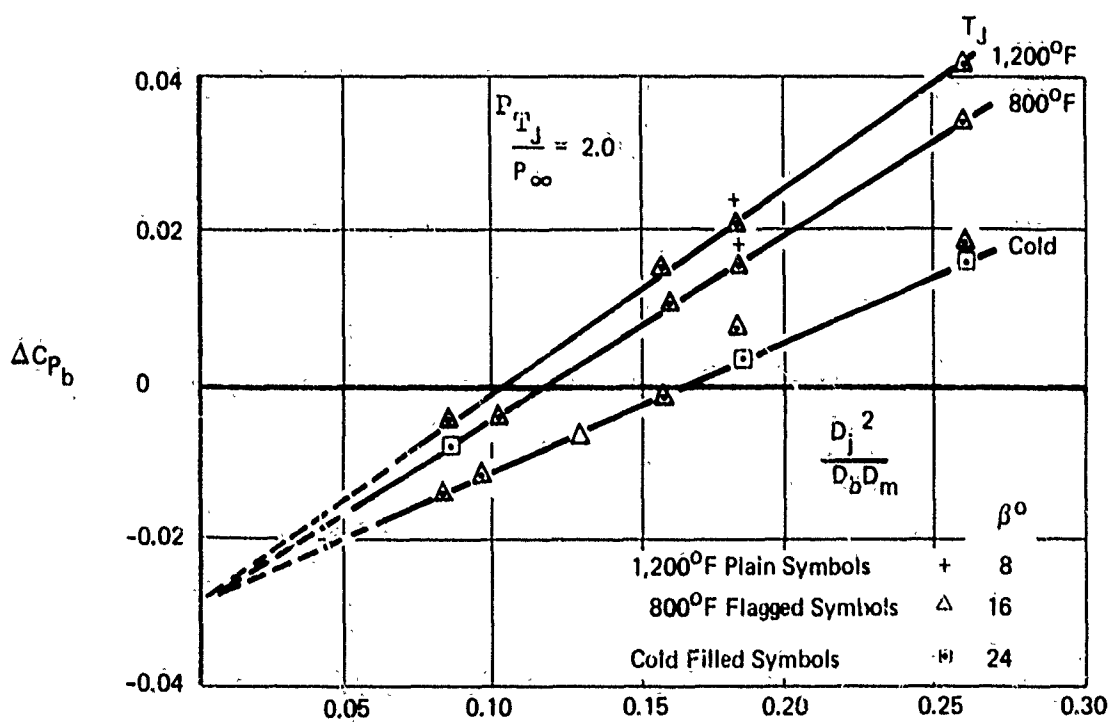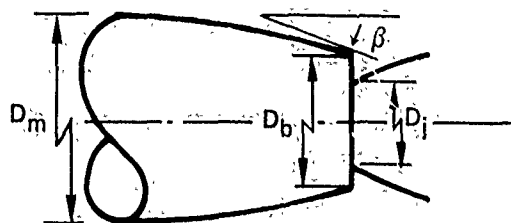D_m = Body Maximum Diameter

β = Boattail Angle

Figure 40 : CORRELATION OF INCREMENTAL BASE PRESSURE DUE TO PROPULSIVE JET AS A FUNCTION OF JET TO BASE-TO-MAXIMUM BODY DIAMETER FUNCTION
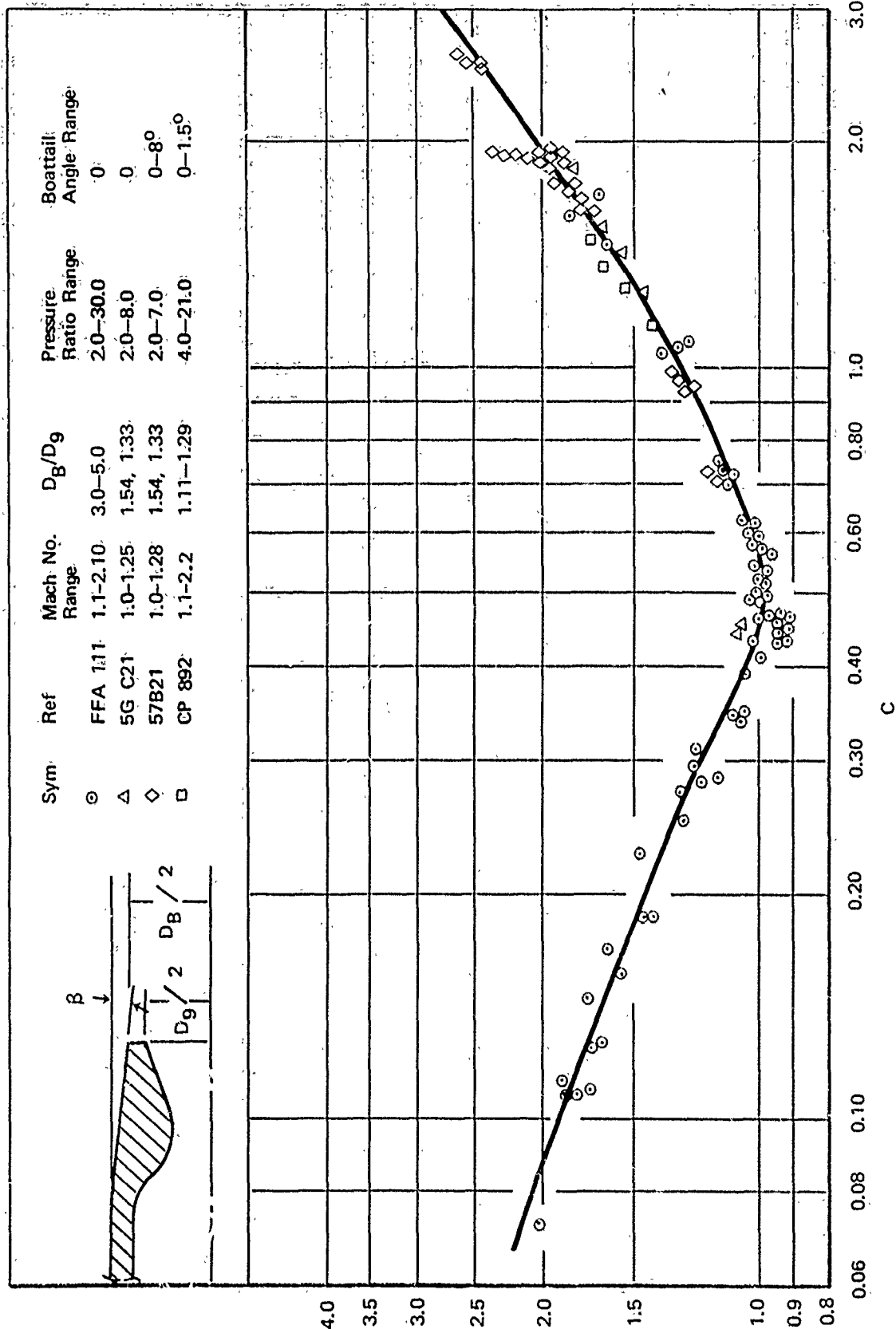
Figure 41 : ANNULAR SUPERSONIC BASE PRESSURE CORRELATION

$$\left(\frac{P_b}{P_\infty}\right)_K = \text{base pressure ratio at K from Figure 42.}$$

$$K = \frac{M_\infty P_B + M_J P_j}{P_e}$$

M_j = Mach number corresponding to nozzle pressure ratio

P_B = base perimeter exposed to freestream

P_j = jet perimeter

P_e = perimeter of circle of area equal to the base area.

$$C = (.37 M_\infty + 0.62) \quad M_{j_{\text{design}}} \frac{2(D_b/D_j) - 1.5}{10} \quad M_{j_{\text{design}}} \frac{A_j}{A_j + A_b} \frac{P_{je}}{P_\infty}$$

where D_b = base diameter

D_j = jet exit diameter

$M_{j_{\text{design}}}$ = nozzle design exit Mach number

A_j = jet exit area

A_B = base area

P_{je} = nozzle exit static pressure (just inside the nozzle)

The parameter $(P_b/P_\infty)_k$ is plotted as a function of k in Figure 42. B is plotted as a function of C in Figure 41.

The procedure for determining base drag is then:

1. Compute C

2. Find the corresponding B from Figure 41.

3. Compute K

4. Find $\left(\frac{P_b}{P_\infty}\right)_K$ from Figure 42.
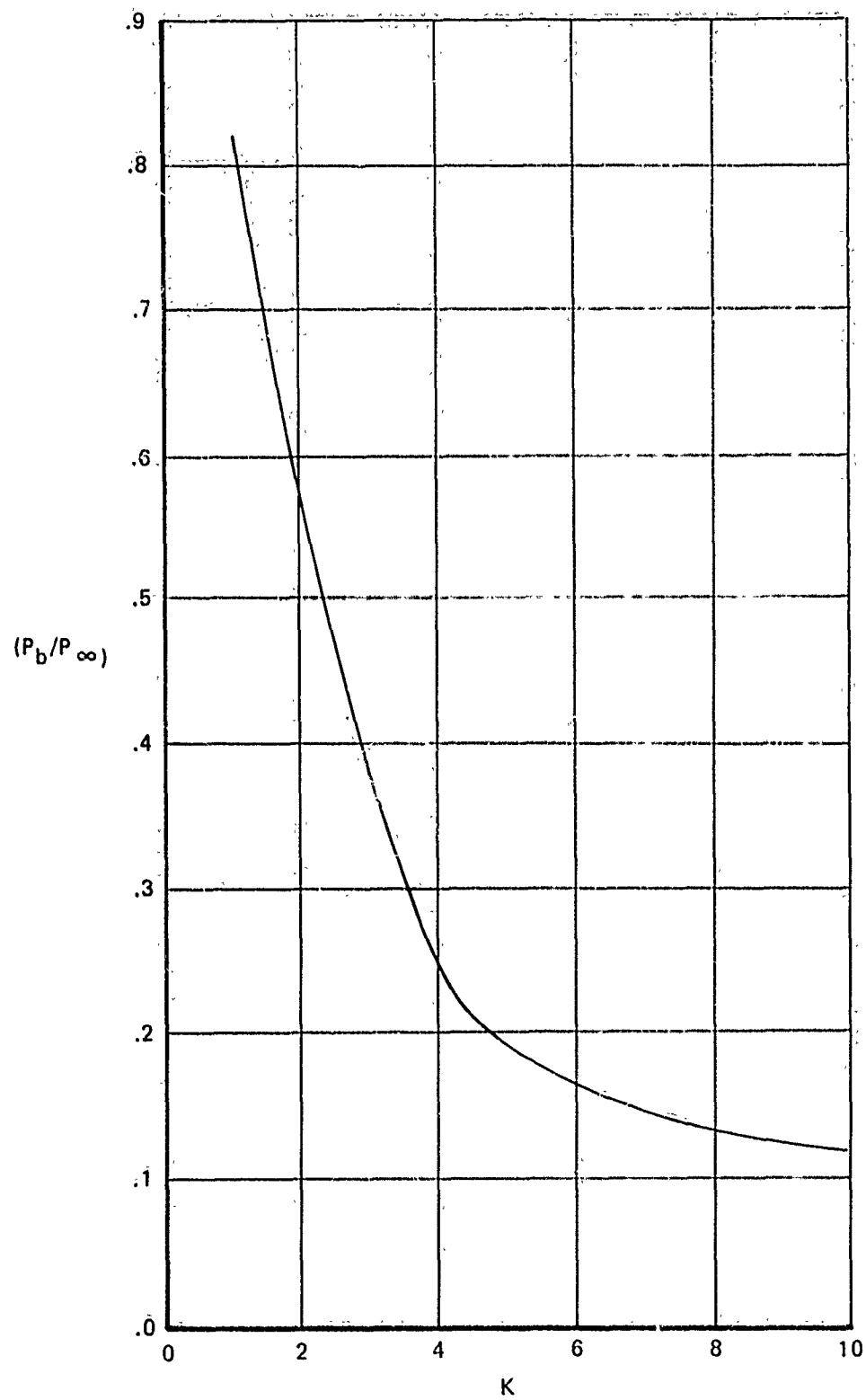
Figure 42 : REFERENCE BASE PRESSURE RATIO

59

5. Compute $\left(\dfrac{P_b}{P_\infty}\right)_M$ from B and $\left(\dfrac{P_b}{P_\infty}\right)_K$

6. $C_{D_{BS}} = \dfrac{2 \, A_B}{\gamma M_\infty^2 \, A_M} \left(1 - \left(\dfrac{P_b}{P_\infty}\right)_M\right)$

A method to account for upstream boundary layer effects has been developed by Nash (Ref. 18). Nash proposed a curve of the limiting value of the base pressure coefficient for zero boundary layer thickness as a function of Mach number. Then he obtained an impressive correlation (Figure 43) for the increment in base pressure coefficient due to a finite momentum thickness θ approaching a base of effective height h. Thus the base pressure coefficient in the absence of jet effects can be estimated. The momentum thickness, θ, to make use of the correlation can be obtained from experimental data, detailed theoretical calculations, or engineering procedures, as time permits.

3.8 INTERFERENCE DRAG

PITAP is programmed to accept an input drag increment table giving "interference" drag. Potentially this slot could be used to account for any discrepancies between the calculated isolated nacelle drag and the actual drag of the nacelle installed in an airplane configration.

At the present time this table is being used solely to account for the twinning penalties associated with putting two nacelles side by side with a clean, sharp-edged interfairing in between. The independent variables are Mach number and spacing ratio, i.e., center line spacing over nozzle exit diameter. (The present version of PITAP, however, can handle any number of side-by-side nozzles in a row, adding n-1 twinning penalties for n nozzles.)

The interference drag coefficients used in the procedure (Fig. 44) at spacing ratios greater than those for which C_{D_I} is a maximum are based on data from Refs. 19 and 20 which are in generally good agreement with recent data reported in Ref. 21. At lower spacing ratios, the curves correspond to completely separated flow on the inside half of the nozzles and on the entire interfairing and base drag has been computed for this region.

Figure 44 has been shown to work quite well when applied to plug nozzles as well as convergent or convergent-divergent nozzles. In this case the equivalent nozzle concept is first
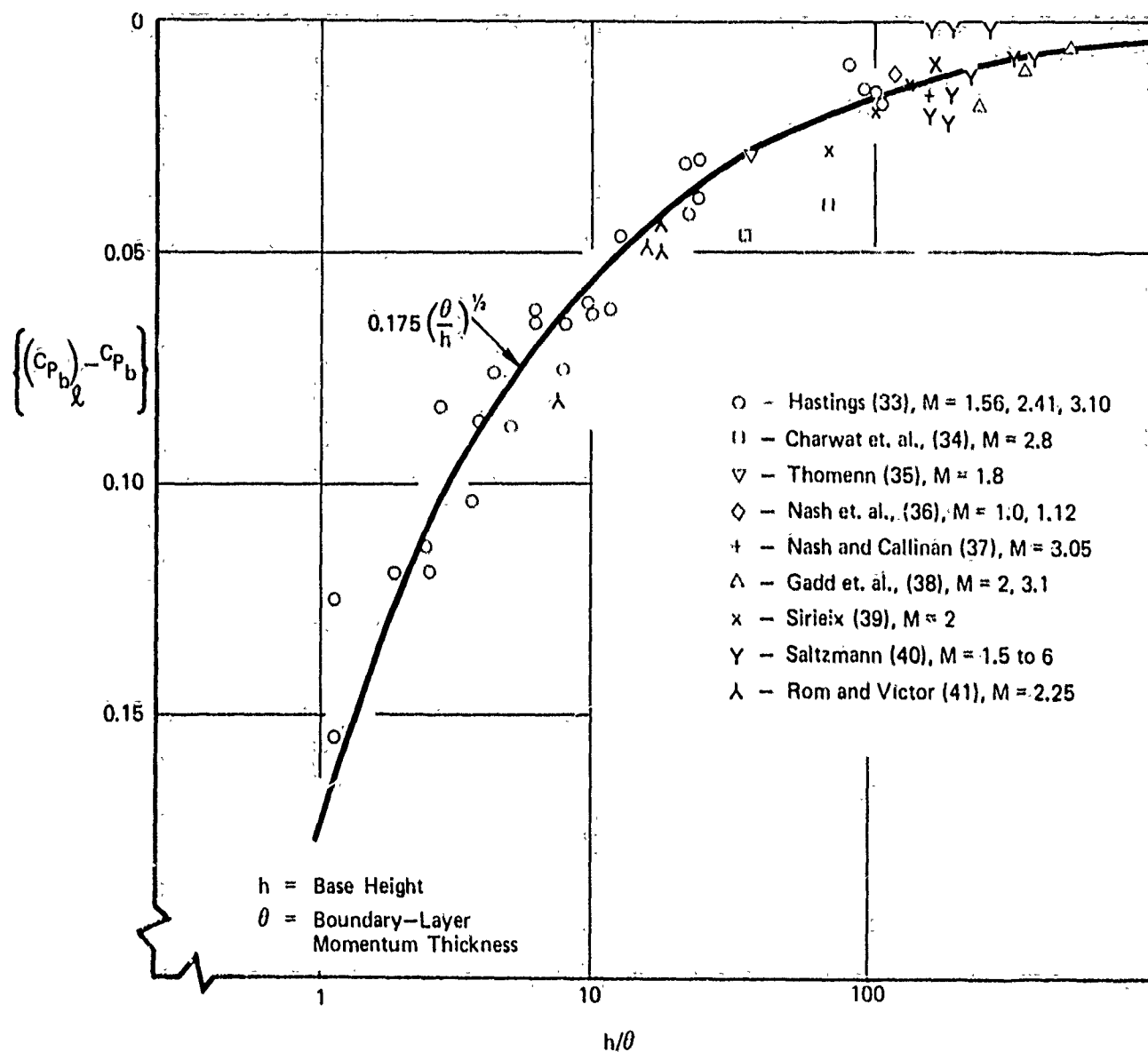
Figure 43 : CORRELATION OF BASE PRESSURE DATA FOR SUPERSONIC FLOW
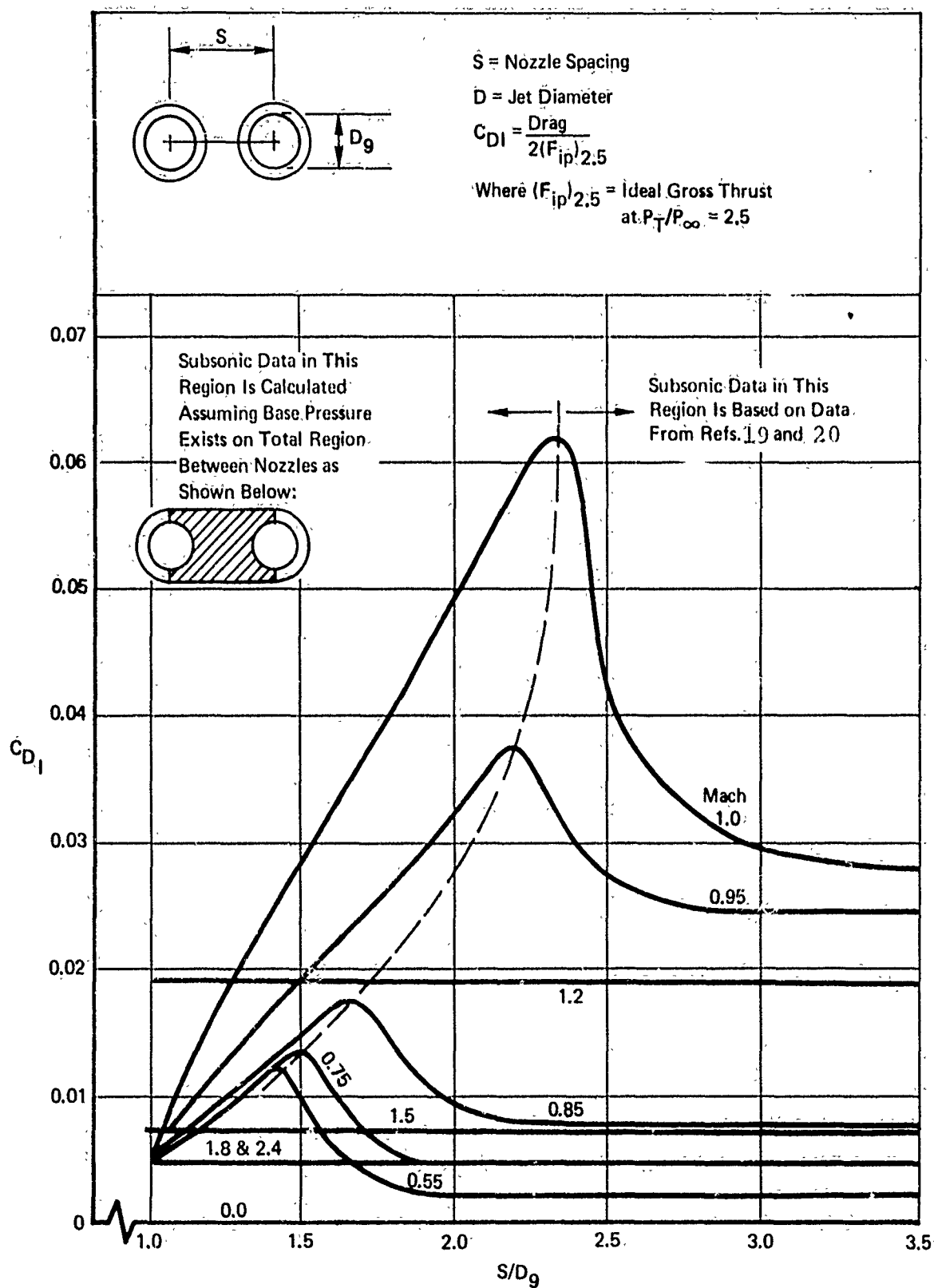
Figure 44: NOZZLE INTERFERENCE DRAG COEFFICIENT

used to estimate isolated nozzle drag, and then Figure 44 is used, with spacing ratio defined to be centerline spacing over fully expanded exit diameters. Figure 45 (from Ref. 22) shows a comparison of twin-nacelle thrust-minus-drag predicted performance and measured performance for both plug and convergent-divergent nozzles. Although the agreement is better for the convergent-divergent nozzles, in both cases the prediction is within about 1% of gross thrust.

For nozzle interfairings that differ from clean sharp-edged fairings, a considerable amount of data (Refs. 19, 21, 23, 24 and 25) is available, but realiable correlations of the interference effects as such do not exist.

3.9 NOZZLE PRESSURE RATIO

The pressure ratio correction used in PITAP is shown in Figure 46. The effect of increasing jet pressure ratio is two-fold. Increasing the size of the exhaust plume tends to force higher pressures on the nozzle surfaces, decreasing drag. Jet entrainment effects tend to pump down the pressure on nozzle surfaces, particularly where separated regions exist, increasing drag. Over a moderate range of pressure ratios these effects tend to cancel out. Reference 26 provides an example where these two opposing effects were isolated. Between jet-off conditions and a particular jet pressure ratio no net effect was observed. Using a solid plume simulator, thus eliminating entrainment effects, it was determined that the jet plume produced a favorable increase in isolated boattail drag coefficient of 0.02, while entrainment had accounted for -0.02.

The relative importance of entrainment and plume effects is a strong function of how much of the flow is separated or in a base region, and thus sensitive to entrainment effects. The Boeing data of Figure 47, (Ref. 27) clearly illustrates this phenomenon. The upper three bands of data represent twin nozzle configurations for which oil flow photographs revealed significant separated regions. Between a pressure ratio of 2 (barely more than ram pressure ratio) and 4 there is little apparent effect of pressure ratio on drag. The dashed line is a single nozzle reference configuration which had no separated flow. For this nozzle, plume effects cause a continuous reduction in drag with increasing pressure ratio.

Similarly, in Figure 46 the highest angle nozzle does not benefit as much from high pressure ratio as the intermediate angle nozzles. (The low-angled nozzles are almost zero drag at the outset.)
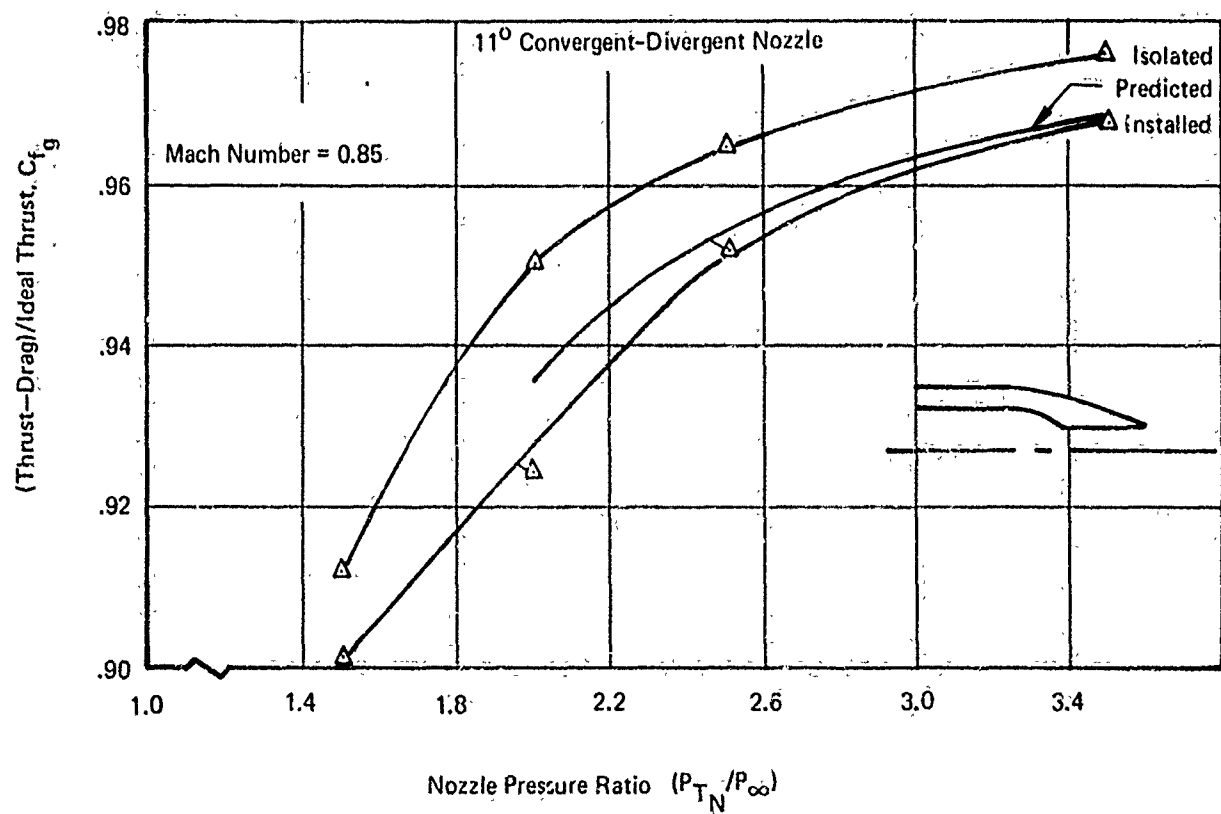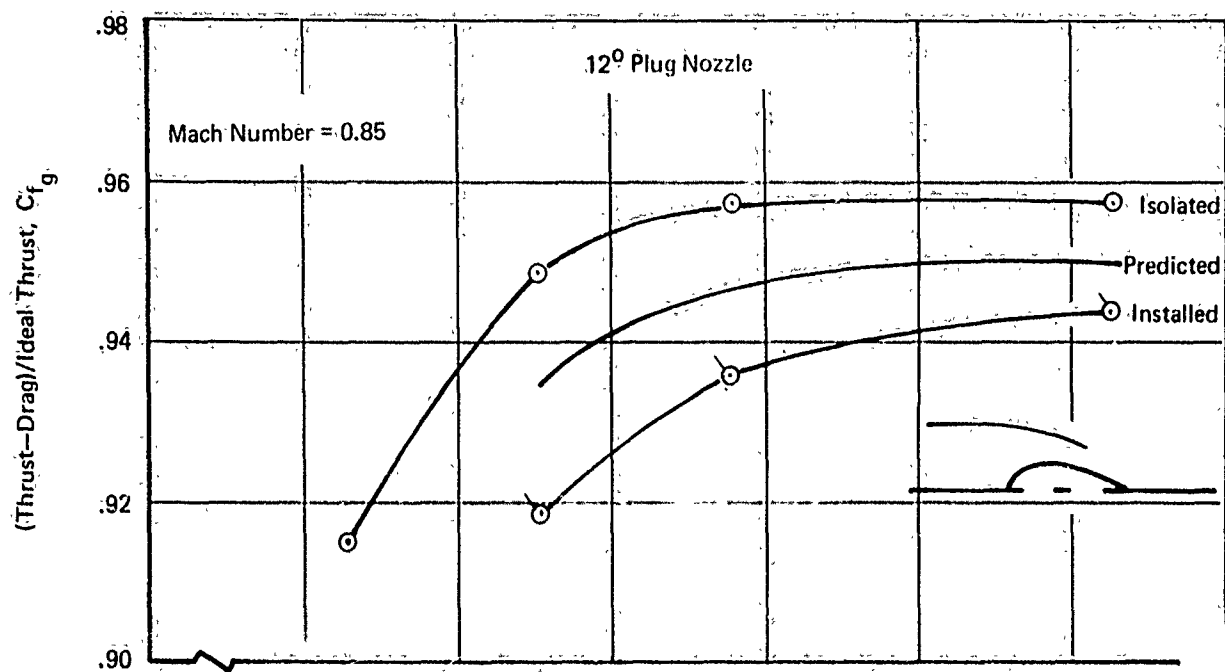
Figure 45 : INSTALLATION EFFECTS FOR PLUG AND CONVERGENT-
DIVERGENT NOZZLES
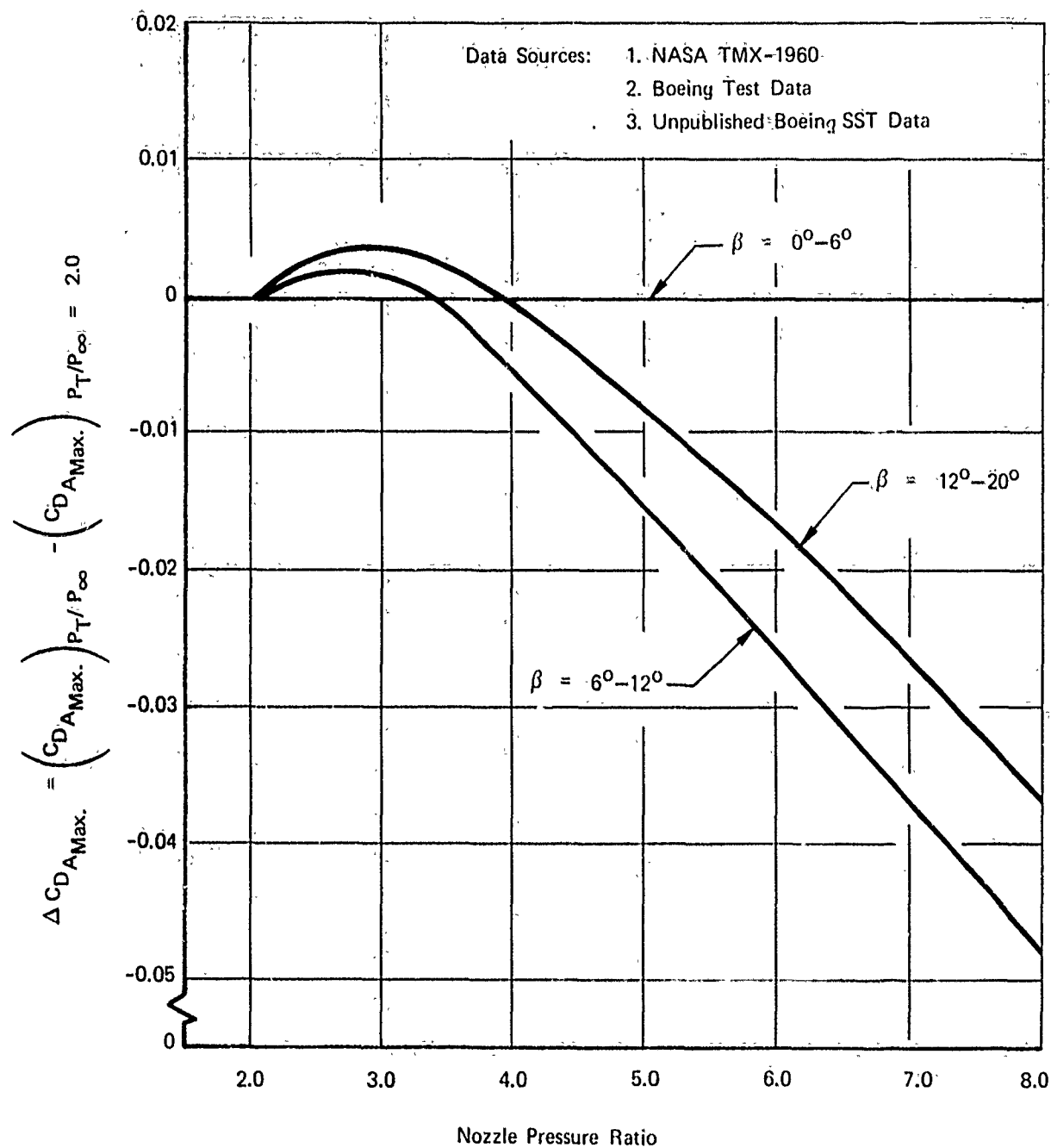
Figure 46 :   BOATTAIL DRAG CORRECTION FOR NOZZLE PRESSURE RATIOS
$> P_T/P = 2.0$
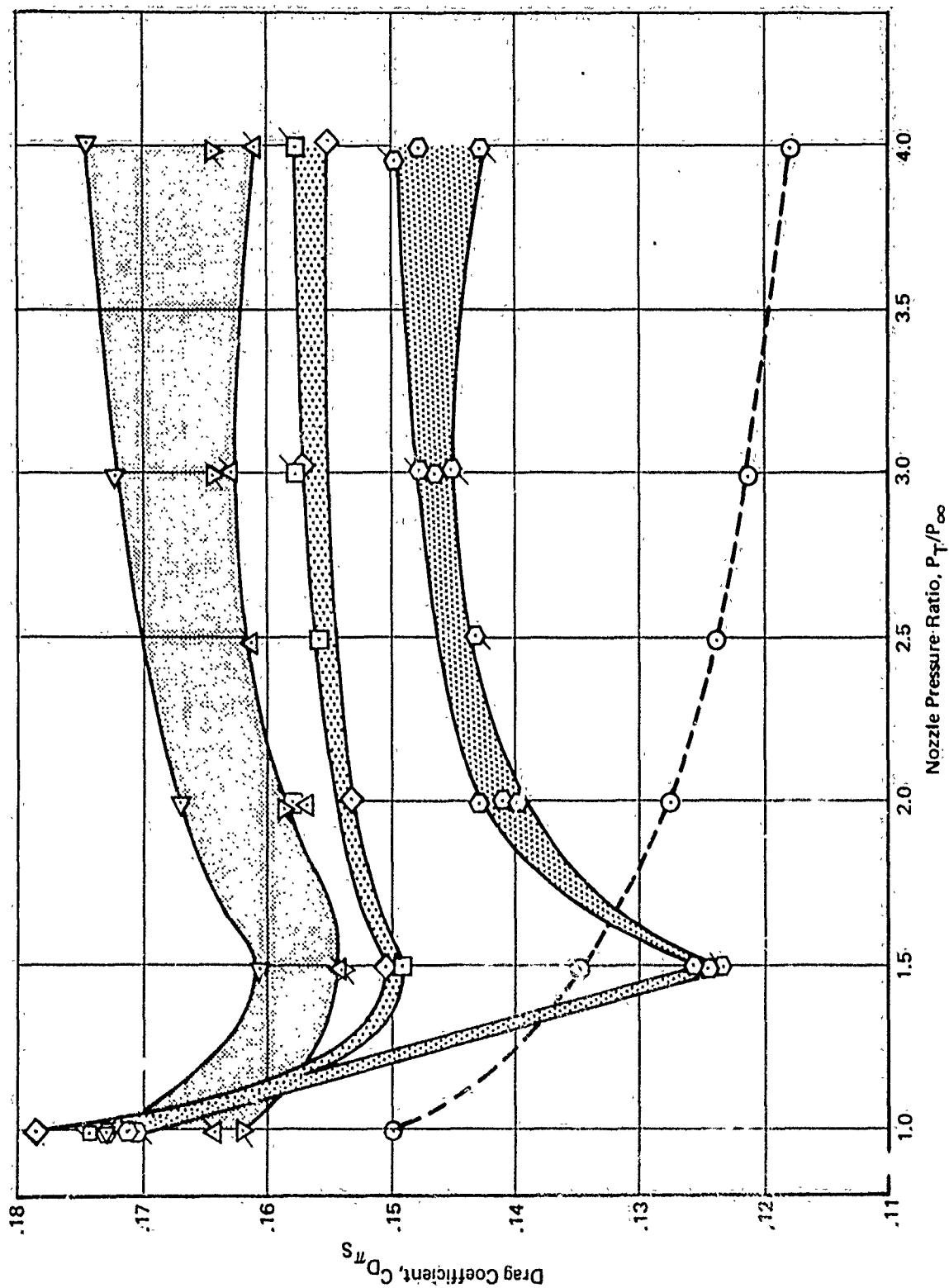
Figure 47: EFFECT OF NOZZLE PRESSURE RATIO ON AFT FUSELAGE DRAG — MACH 0.95

66

Considerations such as these suggest that the pressure ratio
effects might correlate well with the initial drag level
at a reference pressure ratio. If the drag coefficient
were normalized by the projected nozzle/afterbody external
surface area, it represents a measure of how much separation
existed at the reference nozzle pressure ratio.

3.10 CONVERGENT-DIVERGENT NOZZLE NON-ISENTROPIC EXPANSION LOSSES

The convergent-divergent nozzle suffers a non-isentropic
expansion loss unless the internal contours are specifically
designed for isentropic flow. Most C-D nozzles for aircraft
have a simple conical divergent section and therefore
exhibit this loss. The loss was originally called a "cosine"
loss because it can be roughly defined by the expression

$$\Delta C_V = 1/2 \ (1 + \cos \theta)$$

where θ is the nozzle divergence half angle. The above ΔC_V
expression can be derived by finding the loss in momentum
parallel to the nozzle axis as the flow expands in a spherical
manner as sketched below.

Careful experimental determination of the "cosine" loss
for a series of conical convergent-divergent nozzles has
been reported in Reference 39. The data from this report
are summarized in Figure 48 as C_θ, angularity loss coefficient at
design pressure ratio, versus nozzle angle and area ratio.
The loss predicted from the simple cosine loss equation given
above is also shown. At high area ratios the simple expression
is reasonably good. At the lower area ratios typical of
aircraft nozzles, the deviation between the "cosine" loss
and the actual nozzle internal flow loss is significant. It
therefore appears that the loss is due to non-isentropic
expansion and should be predicted from the data of Figure 48.
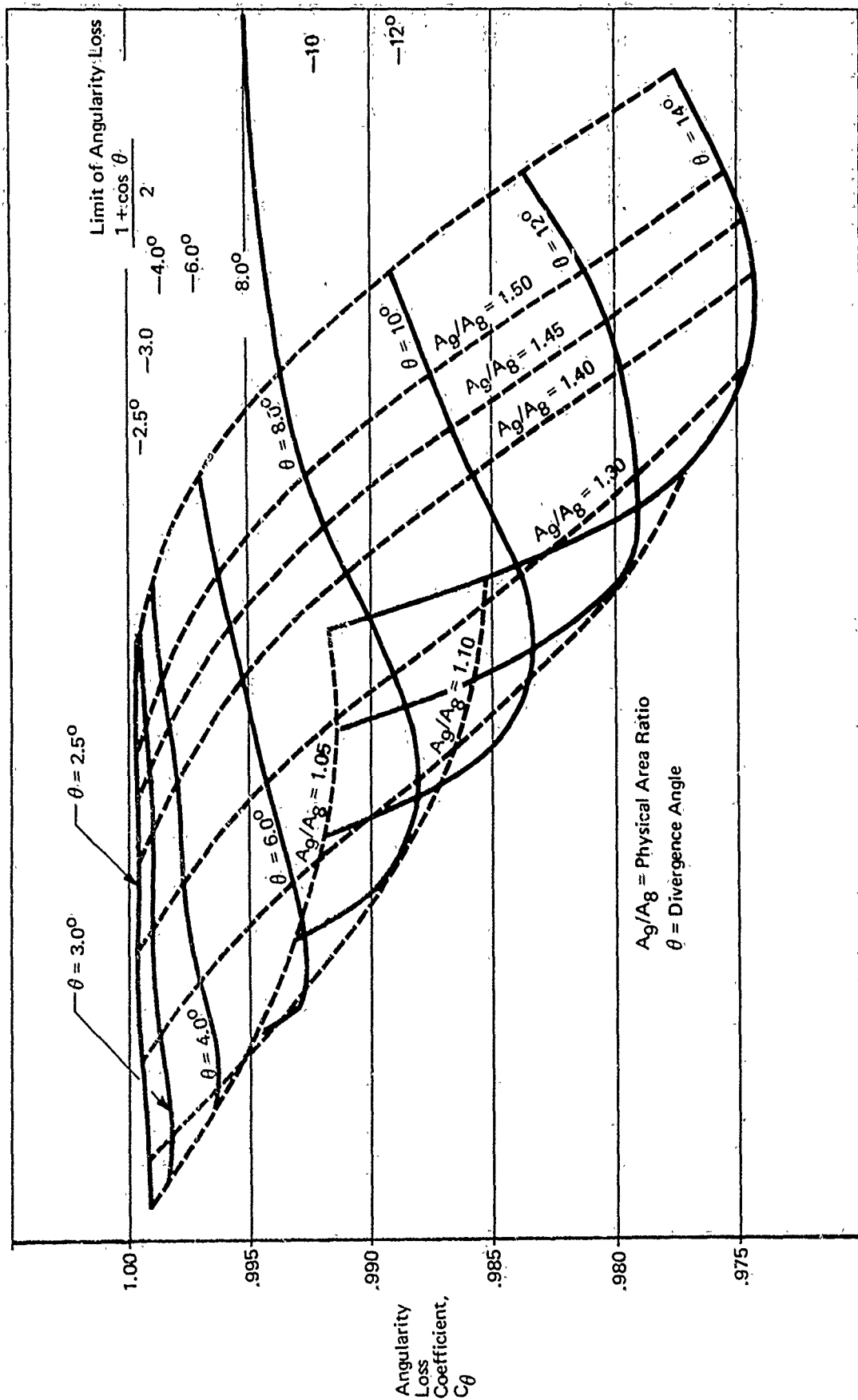
Figure 48: ANGULARITY LOSS COEFFICIENT FOR CONVERGENT-DIVERGENT NOZZLES

68

3.11 VELOCITY COEFFICIENT LOSSES FOR PLUG NOZZLES

For a plug nozzle the ratio of cowl to throat area affects nozzle performance as shown in Figure 49. The ordinate is the peak performance possible from a well-designed plug nozzle. The data shown are from References 22, 29 and 30 and include plug half angles from 10 to 20 degrees and pressure ratios from 1.5 to 4.

The data of Figure 49 are for optimum nozzle designs. As throat angle, the difference between cowl internal angle and plug angle, and plug truncation length are varied, additional losses must be subtracted from the peak C_V's of Figure 49.

No performance loss is suffered if the cowl angle is greater than the plug angle, but if it is less, the losses indicated in Figure 50 will occur. Figure 51 presents truncation loss corrections.

Correlations for blow-in-door ejector nozzle internal performance are not now available. Attempts to derive satisfactory correlations from the available data (e.g., References 31-36) will therefore be necessary.

3.12 VELOCITY COEFFICIENTS FOR CONVERGENT NOZZLES

Results from a parametric test of 16 convergent conical nozzles (Reference 28) are shown in Figures 52 to 55. The data show small but definite effects due to wall angle, α, and diameter ratio D_1/D_2. Penalties due to skin friction and underexpansion losses are charged separately, as shown in Figure 52.

During preliminary design studies, the simplest method of predicting nozzle performance, termed a "Level 1" prediction, is adequate because the nozzle geometry is not well defined. The nozzle is charged with $\Delta C_V = 0.005$ for skin friction losses and underexpansion losses are charged for supercritical pressure ratios.

3.13 NEW ESIP AFT-END DRAG PREDICTION METHOD

3.13.1 Introduction

A parametric wind tunnel investigation of aft-end drag for twin, buried-engine configurations has recently been concluded as part of the Exhaust System Interaction Program (ESIP). A correlation of the data resulting from this test program has been obtained, thus providing the basis for a new drag prediction method which could be readily incorporated into PITAP.
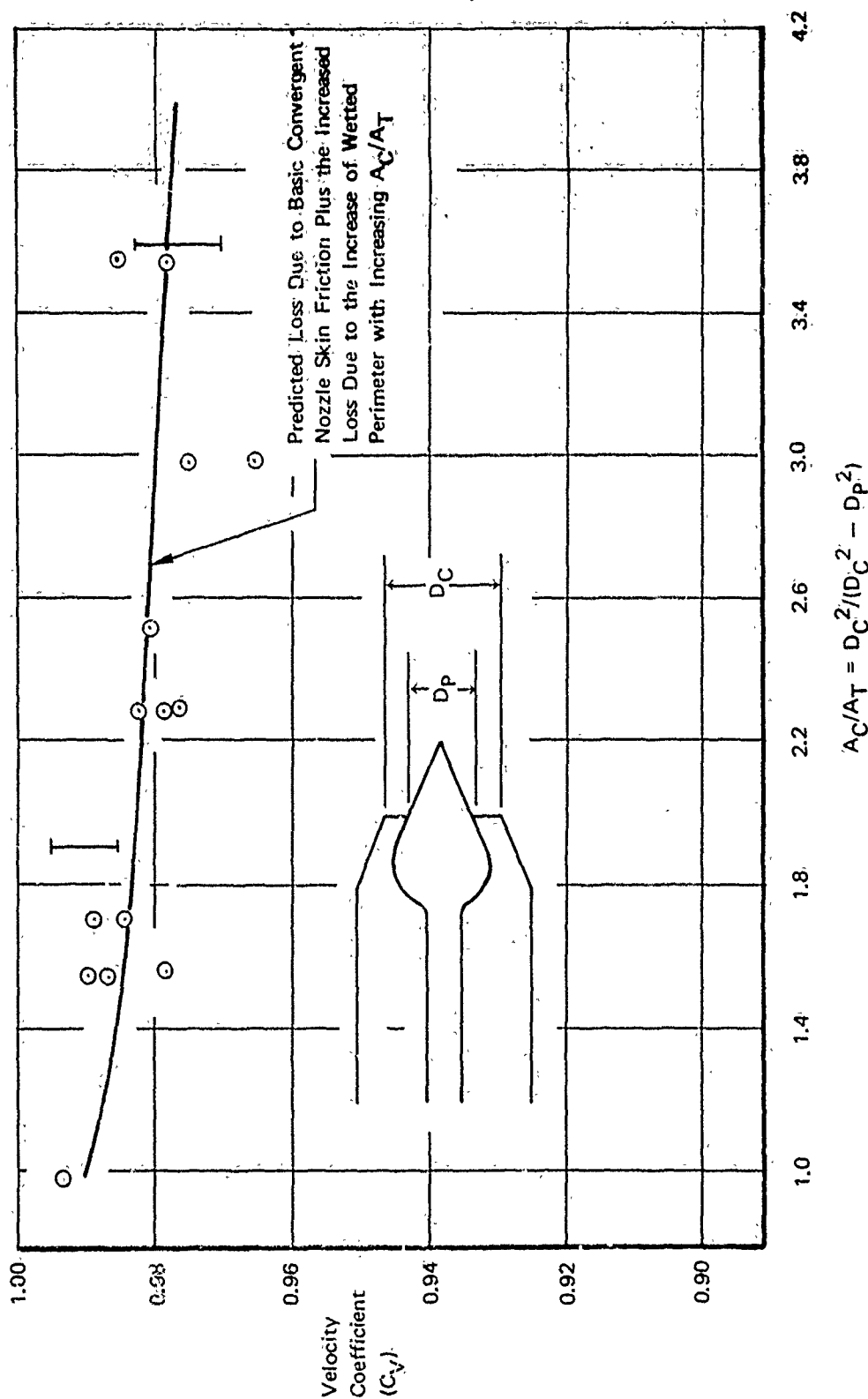
Figure 49 : MAXIMUM POSSIBLE C_V VERSUS A_C/A_T FOR PRESSURE RATIOS FROM 1.5 TO 4.0

Data for $\alpha = \beta = 10^0$ to 20^0
No External Flow

Predicted Loss Due to Basic Convergent Nozzle Skin Friction Plus the Increased Loss Due to the Increase of Wetted Perimeter with Increasing A_C/A_T

$A_C/A_T = D_C^2/(D_C^2 - D_P^2)$

Velocity Coefficient (C_V)

70
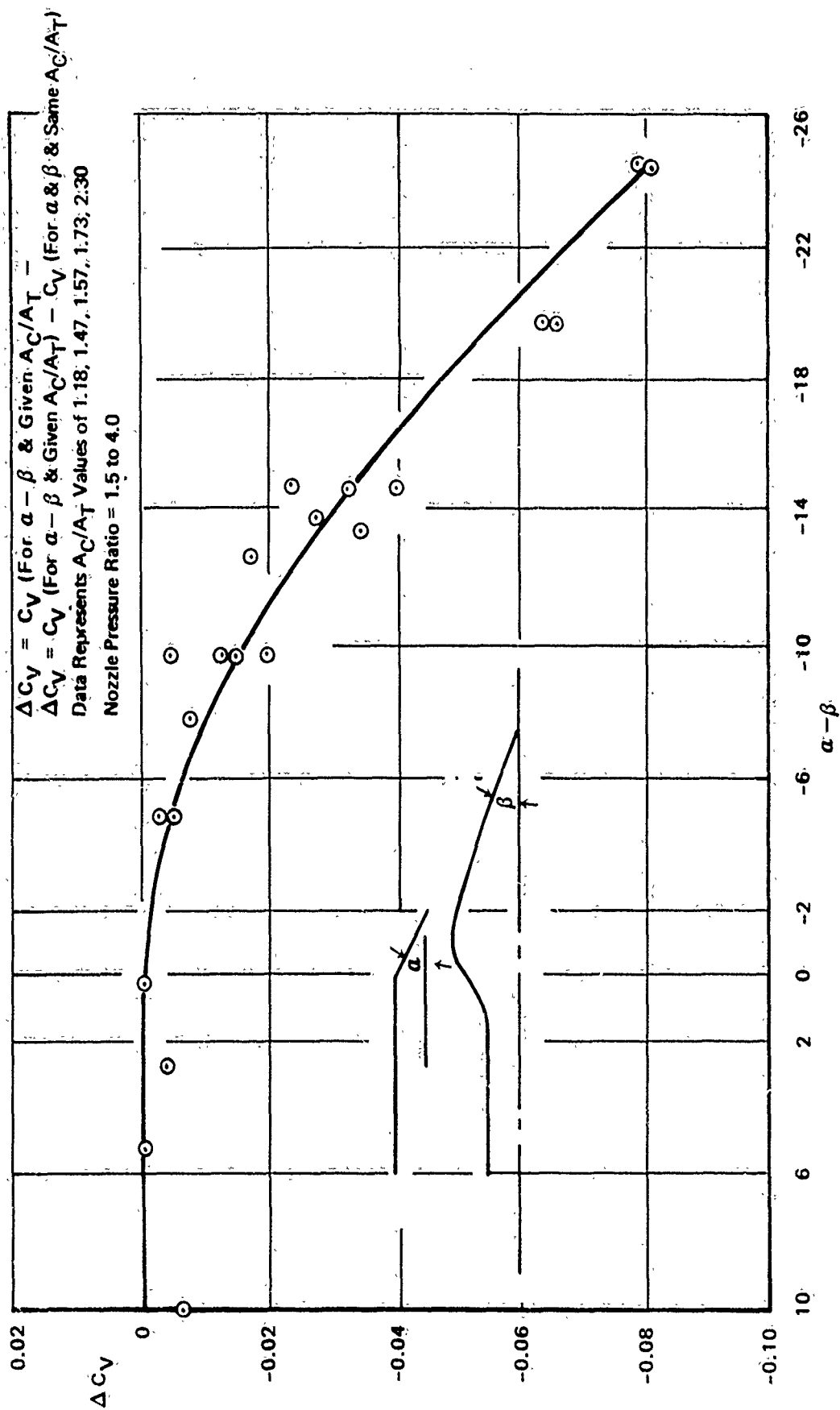
Figure 50: PERFORMANCE LOSS DUE TO DIFFERENCE BETWEEN COWL ANGLE AND PLUG ANGLE

71
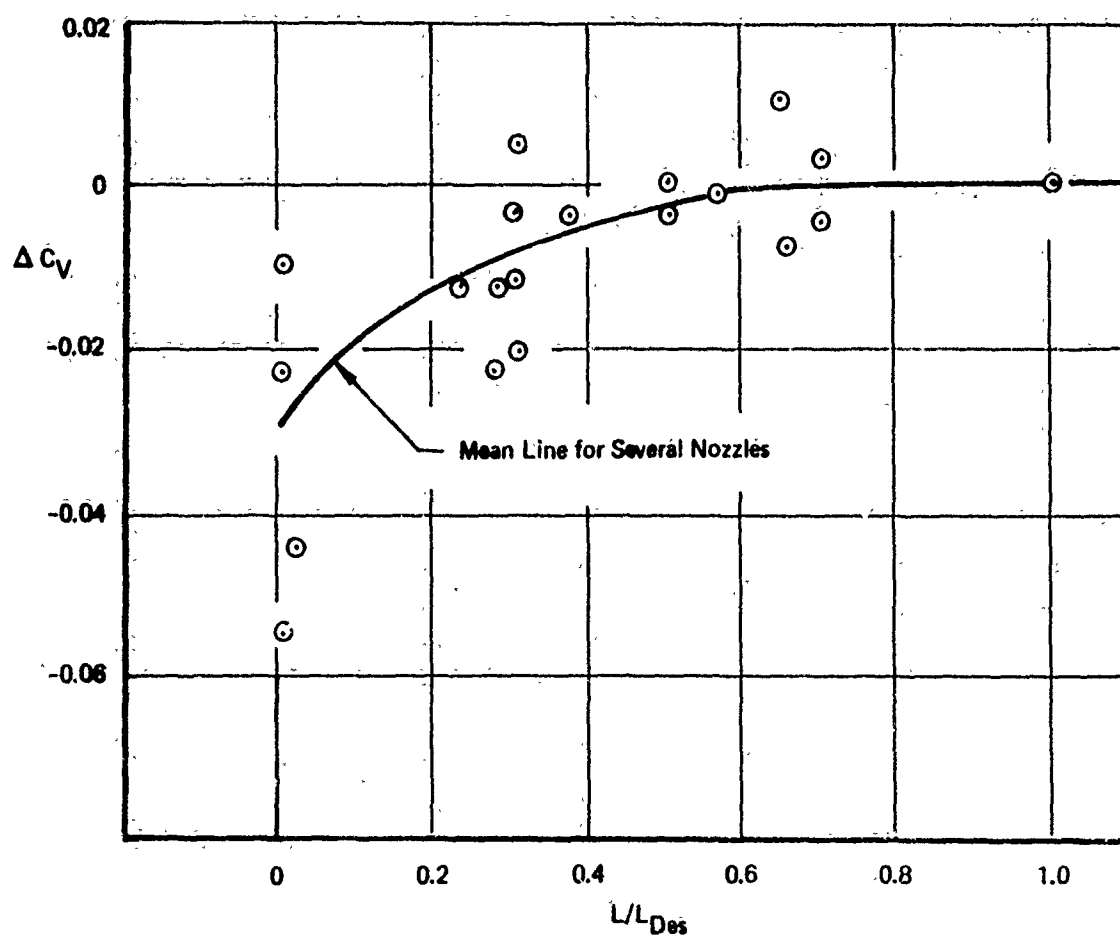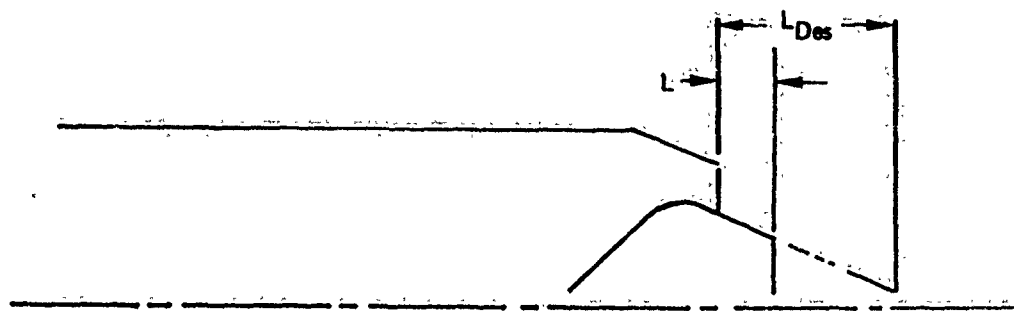
Figure 51 :   THRUST LOSS DUE TO PLUG NOZZLE TRUNCATION

Figure 52: EFFECT OF WALL ANGLE ON VELOCITY COEFFICIENT FOR CONICAL NOZZLES ($D_1/D_2 = 1.1$)

73
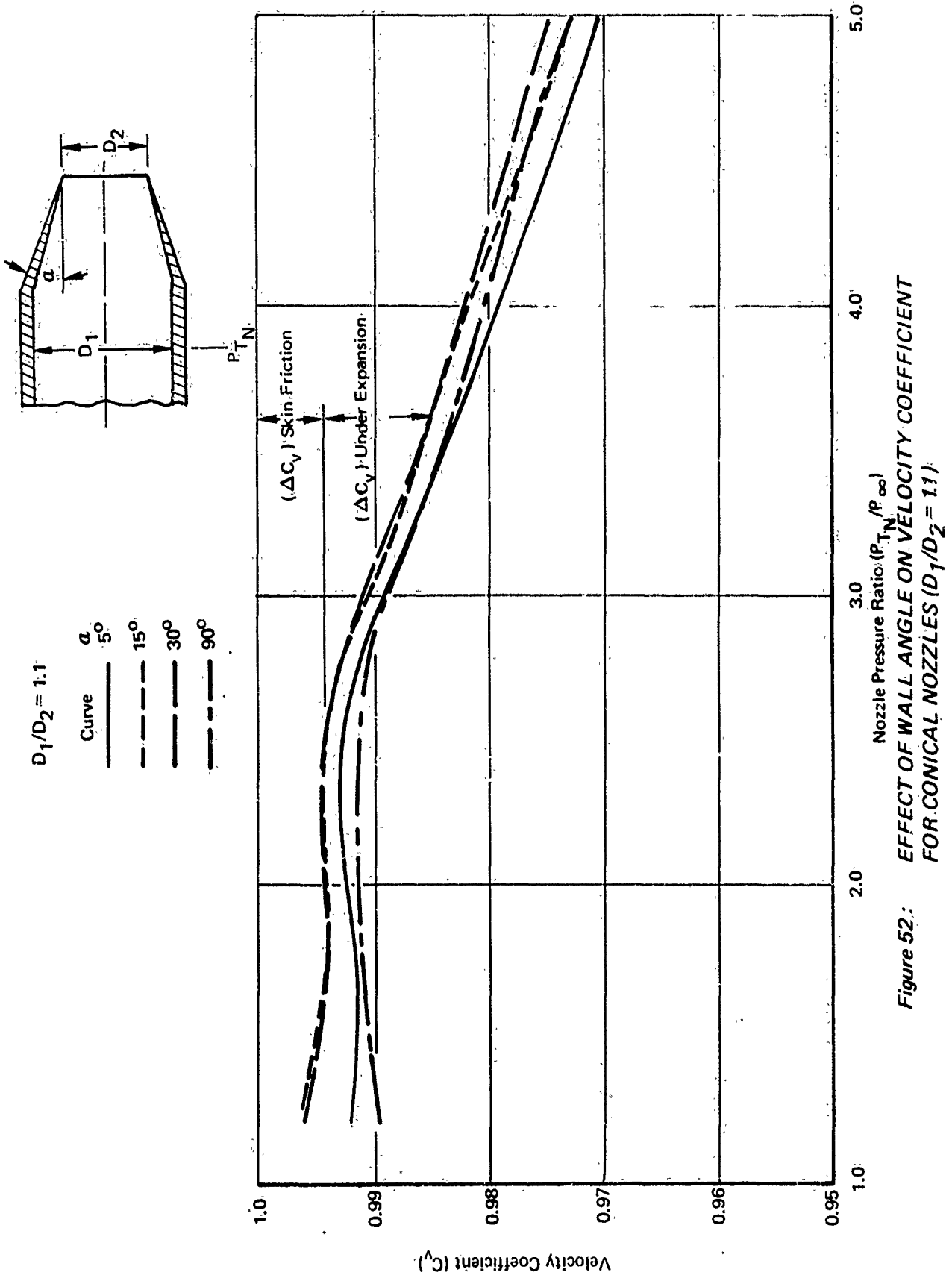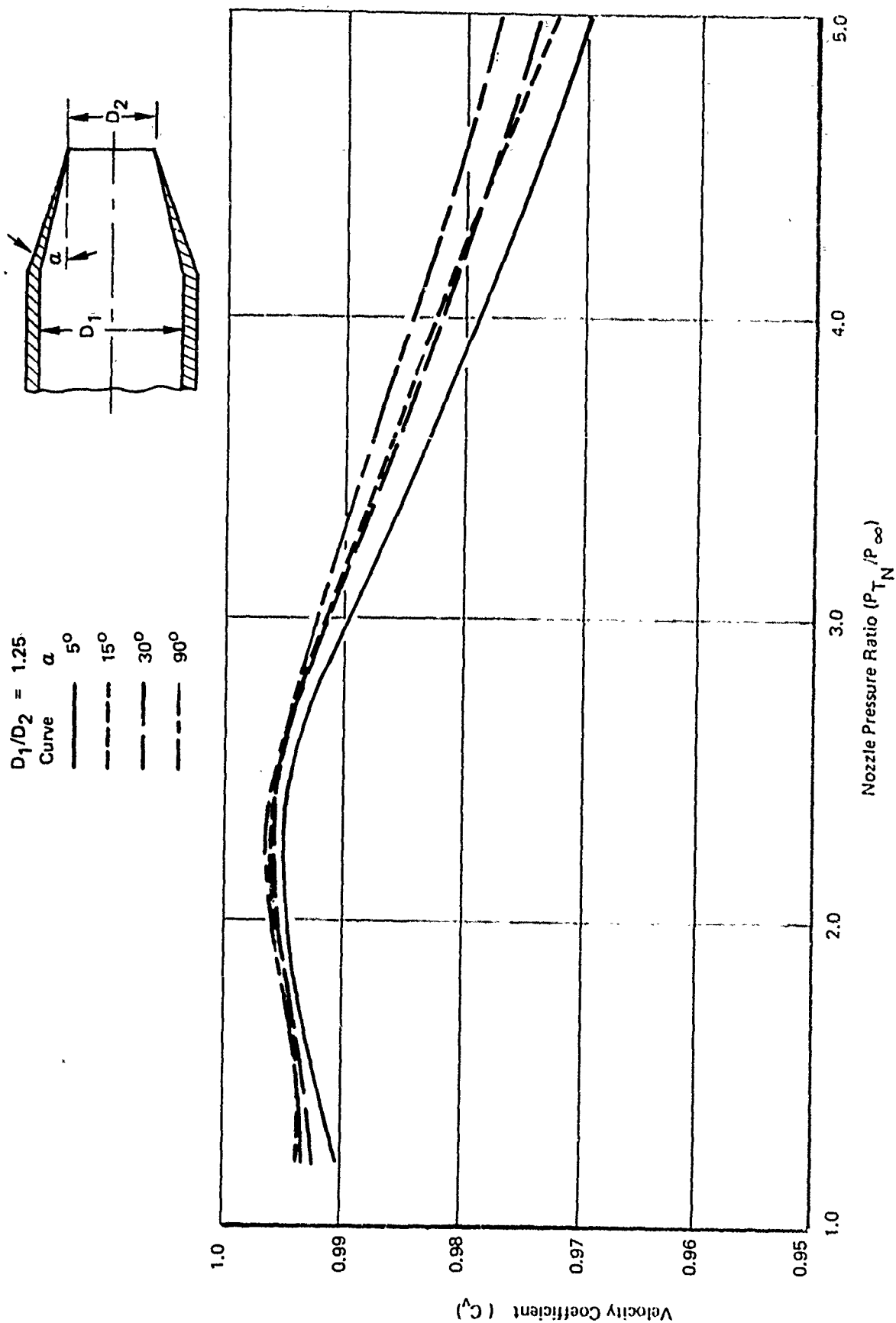
Figure 53 : EFFECT OF WALL ANGLE ON VELOCITY COEFFICIENTS FOR
CONICAL NOZZLES, $D_1/D_2 = 1.25$

Figure 54 : *EFFECT OF WALL ANGLE ON VELOCITY COEFFICIENTS FOR CONICAL NOZZLES, $D_1/D_2 = 1.6$*

$D_1/D_2 = 1.6$

Curve	α
——	5°
- - -	15°
——	30°
—·—	70°

Nozzle Pressure Ratio (P_{T_N}/P_∞)
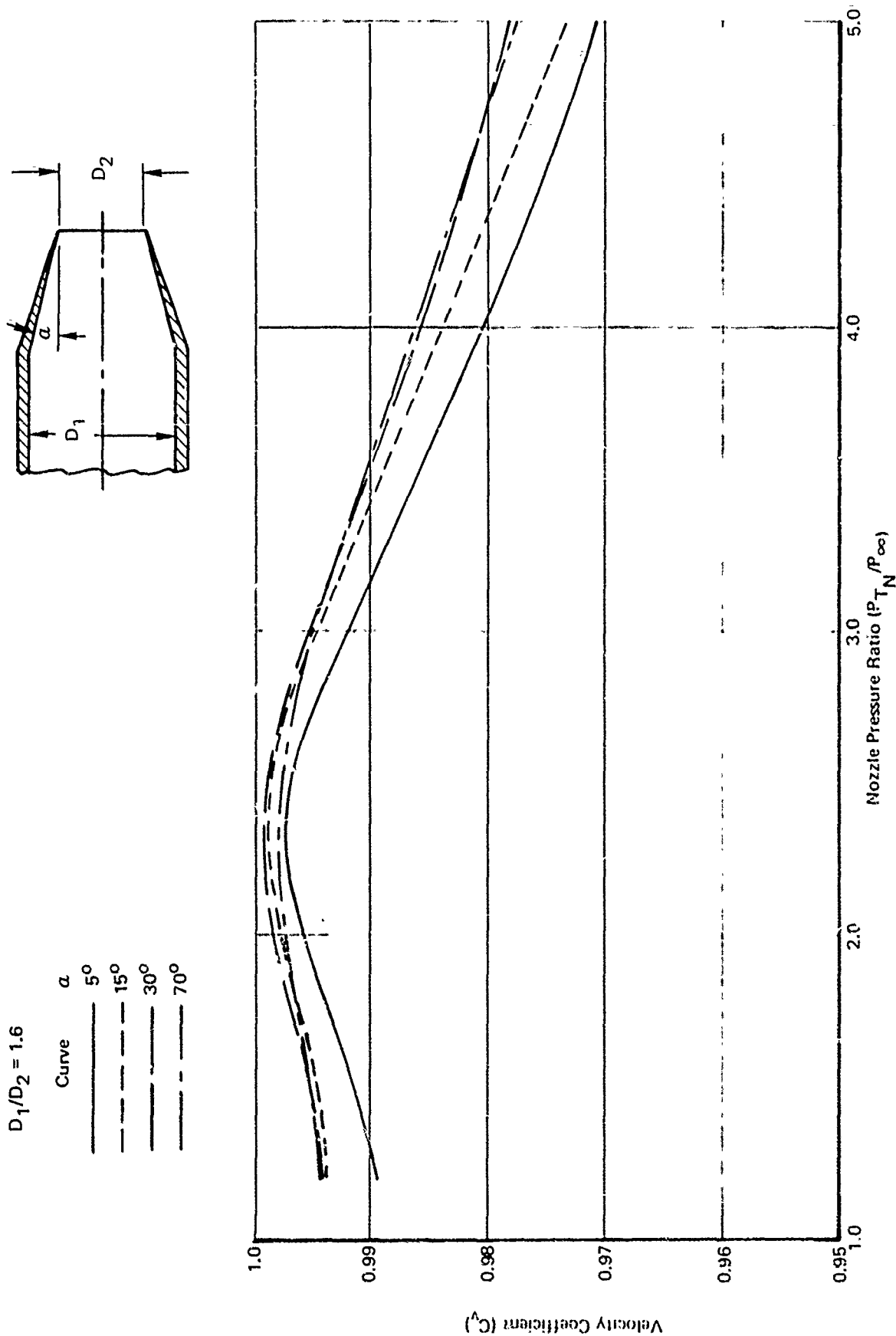
Velocity Coefficient (C_v)
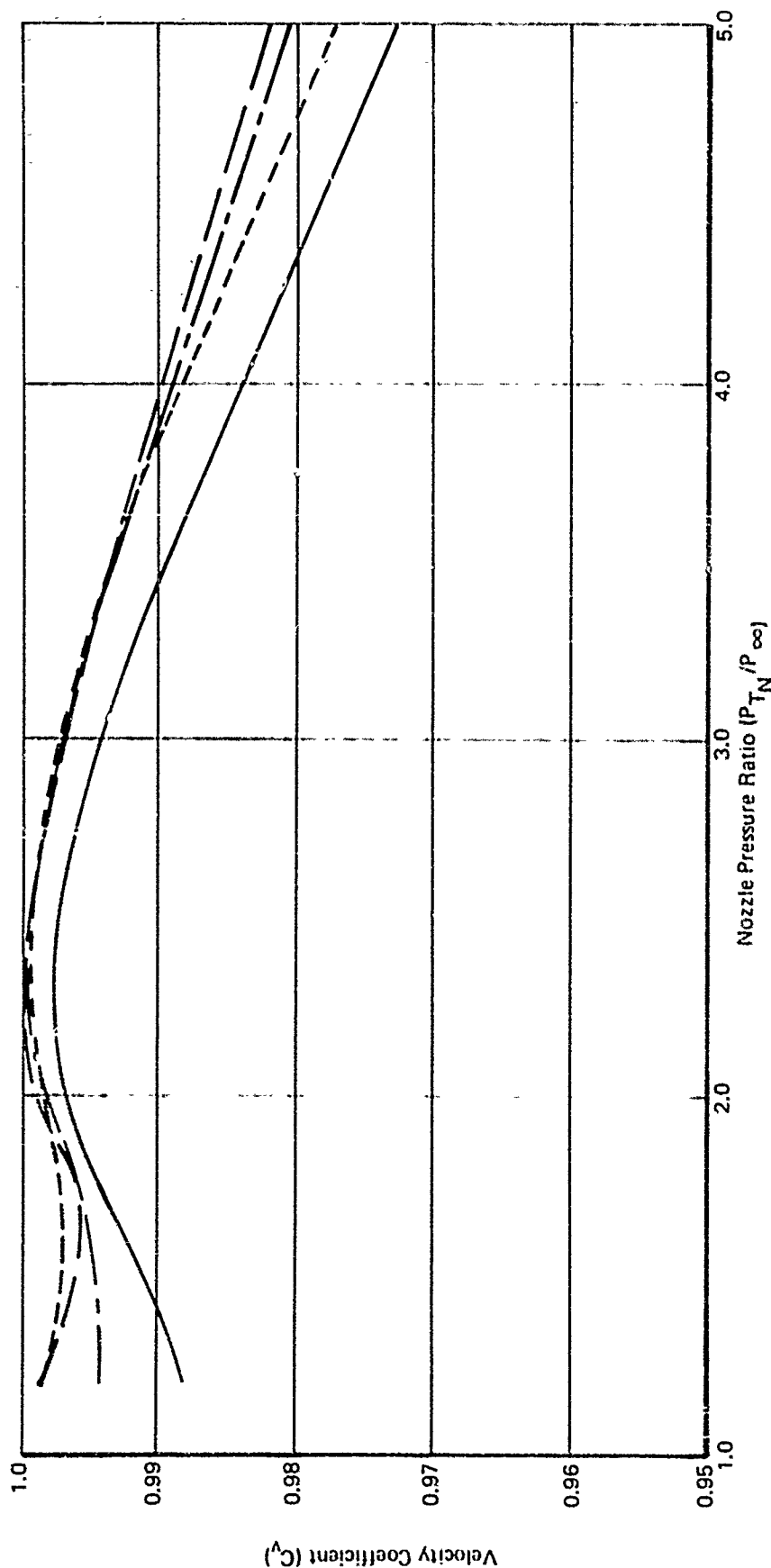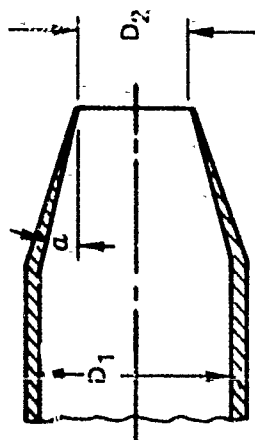
Figure 55 : EFFECT OF WALL ANGLE ON VELOCITY COEFFICIENTS FOR CONICAL NOZZLES, $D_1/D_2 = 1.93$

76

The correlation deals with the pressure drag of the aft
fuselage, from the maximum cross-sectional area point back.
As with present PITAP procedures, the drag polar baseline
conditions must be defined so that the installation loss
correction can be computed as the increment from the baseline
conditions to given operating conditions.

The correlation covers configurations with horizontal
interfairings. (There is reason to suspect it is equally
applicable to other interfairing concepts, or even to single
engine configurations, but data are not now available to
verify this). Subsonic Mach numbers up to 0.95 are covered.
The correlation accounts for the effects of both a single
vertical stabilizer and twin verticals extending radially
from nacelle centerlines.

The correlation treats only the case for which the nozzle
exit static pressure equals freestream ambient pressure.
Pratt and Whitney, as a subcontractor to Boeing on ESIP, is
currently working to develop a "jet plume parameter" to
help handle other off-design conditions.

It is anticipated that if a good jet plume parameter can be
found, accounting for the combined effects of such things as
exit static pressure ratio and nozzle divergence angle, the
present correlation could be easily adapted to account for
different values of the plume parameter.

It should be noted that at this time the correlation
effectively uses exit static pressure ratio as the plume
parameter. Some of the scatter in the correlation is
directly attributable to the fact that the various nozzle
types tested, ranging from convergent nozzles to convergent-
divergent nozzles of area ratios 1.4 and 2.0, and with
divergence angles of 6 degrees and 12 degrees, have a
measureably different effect on drag at the same exit static
pressure ratio. The development of a good plume parameter
is expected to improve this situation, and to permit the
extension of the present correlation approach to off-design
exit pressure ratios.

The Test Summary Section below briefly summarizes the config-
uration variables investigated in the test program. The
Data Correlation and Drag Prediction Sections describe,
respectively, the data correlation that was obtained and
the resulting drag prediction method.

3.13.2 Test Summary

The drag of a variety of afterbodies was measured behind a

common forebody. The area distributions used to define aft-end configurations included first-, second-, and fourth-order polynomials, and a number of elliptical area distribution not representing an analytic function. All models had horizontal interfairings.

Unswept stub tails were used to simulate the pressure drag effects of real tails. (Calculated friction drag was subtracted from the measured drag. The correlation work dealt only with the resulting pressure drags.) Additional testing with full swept tails, and without any tails, established that the stub tails adequately simulated the effects of realistic tails for single-vertical configurations and for configurations with twin verticals positioned radially on nacelle centerlines.

On the other hand the stub tails were found not to represent the effect of twin verticals mounted outboard of the engine nacelles. Consequently, the data for outboard tail locations was not used in the correlation work, and the resulting drag prediction method is not applicable for such configurations.

The configurations tested covered a range of nozzle exit areas, afterbody lengths and nacelle spacing. Exit areas ranged from 10 to 40% of the maximum fuselage cross-sectional area, A_{10}. Afterbody lengths ranged from 1.32 to 3.60 times the equivalent diameter D_{eq} associated with A_{10}. The nacelle spacing was varied from 67% to 128% of D_{eq}.

3.13.3 Data Correlation

The correlation approach was based on improving the basic Integral Mean Slope (IMS) approach developed by Pratt and Whitney. The original IMS parameter represented an area weighted average of the rate of change of area of the non-dimensional afterbody area distribution:

$$ IMS = - \frac{1}{\left(1 - \frac{A_9}{A_{10}}\right)} \int_{A_9/A_{10}}^{1} \frac{d\left(\frac{A}{A_{10}}\right)}{d\left(\frac{X}{D_{eq}}\right)} \; d\left(A/A_{10}\right), $$

where A_9 is the total nozzle exit area and $D_{eq} = \sqrt{\frac{4A_{10}}{\pi}}$. Previous Pratt & Whitney studies indicated the aft-end drag coefficient, normalized by the projected area $(A_{10} - A_9)$, should correlate well with the IMS parameter. The ESIP data, however,

78

showed that the correlation broke down for afterbodies whose area plots involved regions of steep slopes. A modified IMS parameter, called IMS_m, was then developed to avoid a sensitivity to afterbody contours in regions which were likely to be separated. The IMS_m approach is based on specifying a maximum slope of the non-dimensional area distribution which can be used in the IMS calculation. The maximum slope is substituted for the real slope at each step of the IMS calculation for which the real slope exceeds the maximum slope. The resulting improvement in the correlation is illustrated in Figure 56, which compares the IMS and IMS_T approaches. The limiting slope for the IMS_T calculation for this figure was 1.4. This had little effect for some afterbodies, but had a very large effect for others. The solid symbol in Figure 56 represents and extreme case of an afterbody with very steep slopes near the nozzle exit. The original IMS value of 1.06 was substantially reduced to an IMS_T value of 0.68.

The best correlation was obtained by making the maximum slope a function of Mach number. Figure 57 gives the values of the maximum slopes which have been determined to yield the best IMS_T correlations. At low Mach numbers the maximum slope is quite large, and there is very little difference between IMS and IMS_m for most afterbodies. In the drag rise region, where larger portions of a typical afterbody are likely to be separated, the reduced value of the maximum slope means that it comes into play over a larger portion of the projected area in the IMS_m calculation. Here there is likely to be a significant difference between IMS and IMS_T for high drag afterbodies.

The resulting correlation for centered twin vertical configurations (i.e., verticals mounted radially from nacelle centerlines) is given in Figure 58. Here $C_{D_{P_{AP}}}$ indicates the pressure drag coefficient based on projected area $A_{10} - A_9$. As indicated the data represent a wide range of aft-end geometries and nozzle types. Nearly all of the data is correlated to within a scatter band little larger than that estimated to be inherent in the data itself.

A similar correlation for single vertical configurations is shown in Figure 59. The centered twin vertical configuration was considered the primary tail configuration for the ESIP test, and there are consequently fewer data points for the single vertical configurations.

The two sets of correlations were found to be nearly identical except for a level shift of 0.006 in $C_{D_{P_{AP}}}$. Thus the two
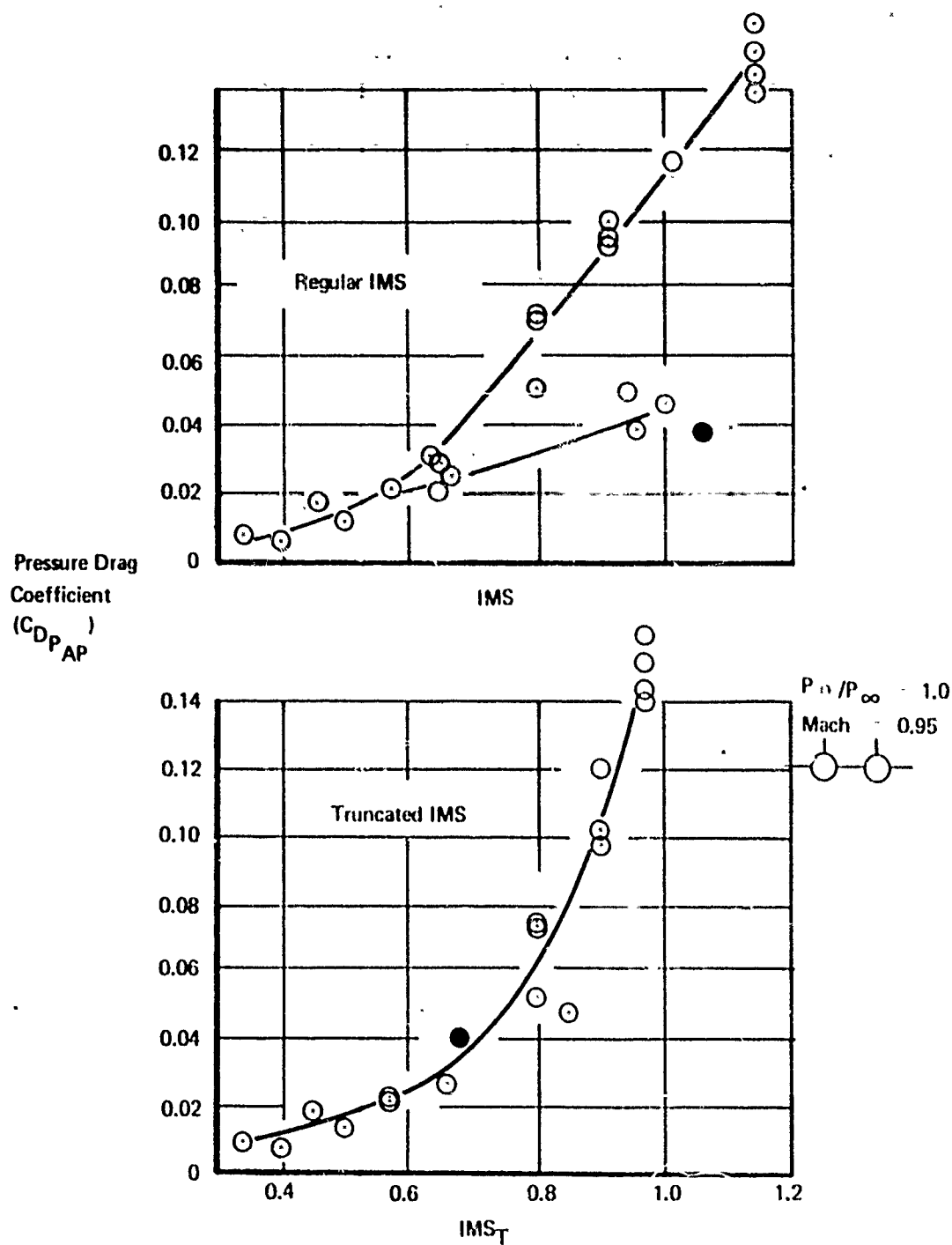
Figure 56 : IMS VERSUS IMS$_T$

IMS Truncation
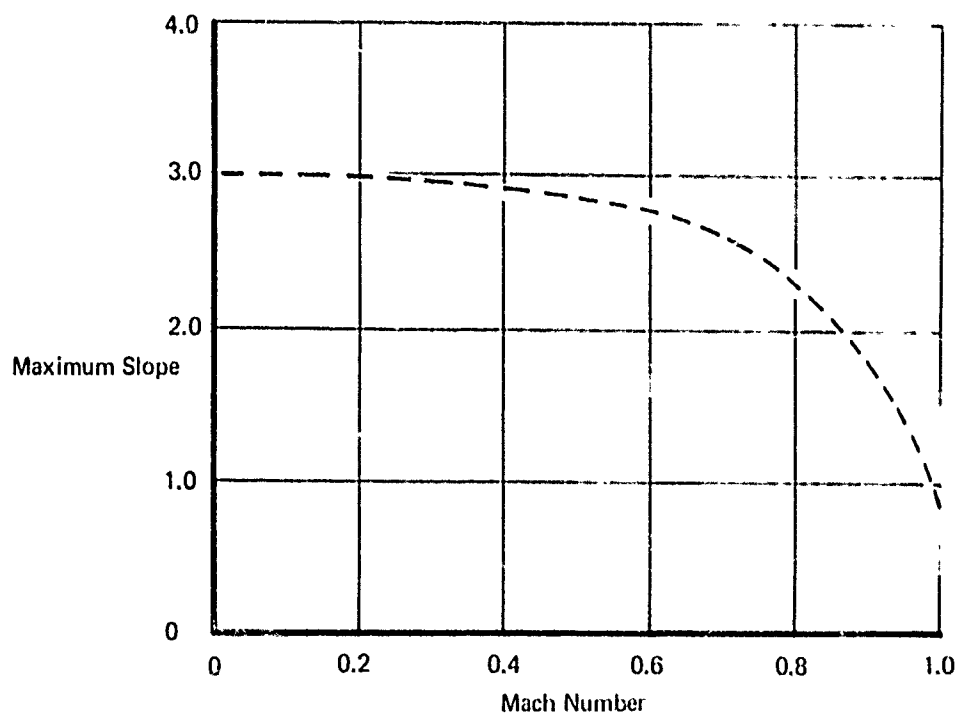
Figure 57 :   MAXIMUM SLOPE AS A FUNCTION OF MACH NUMBER
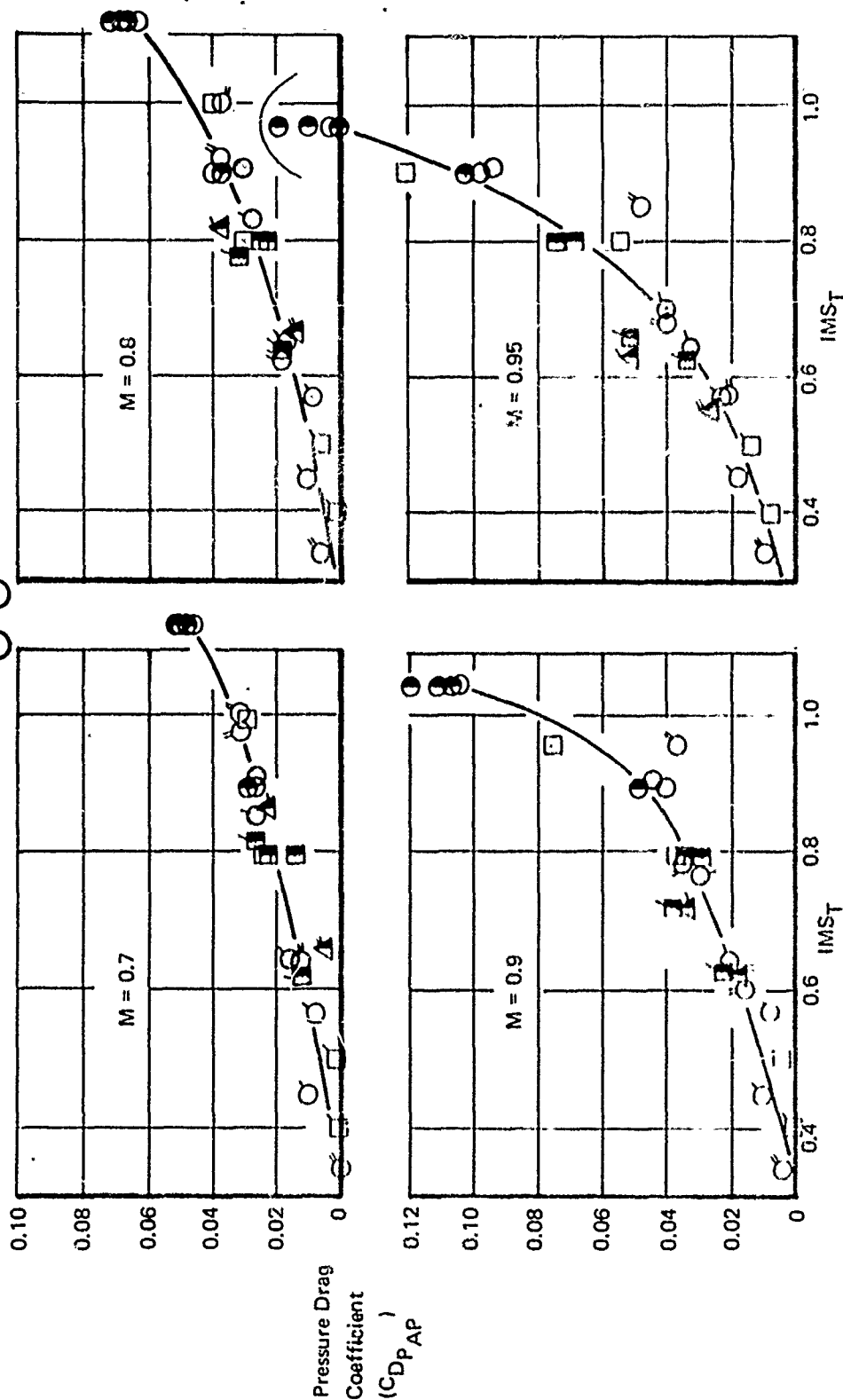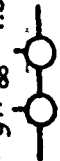
Figure 58: DRAG CORRELATION FOR CENTERED TWIN VERTICAL CONFIGURATIONS
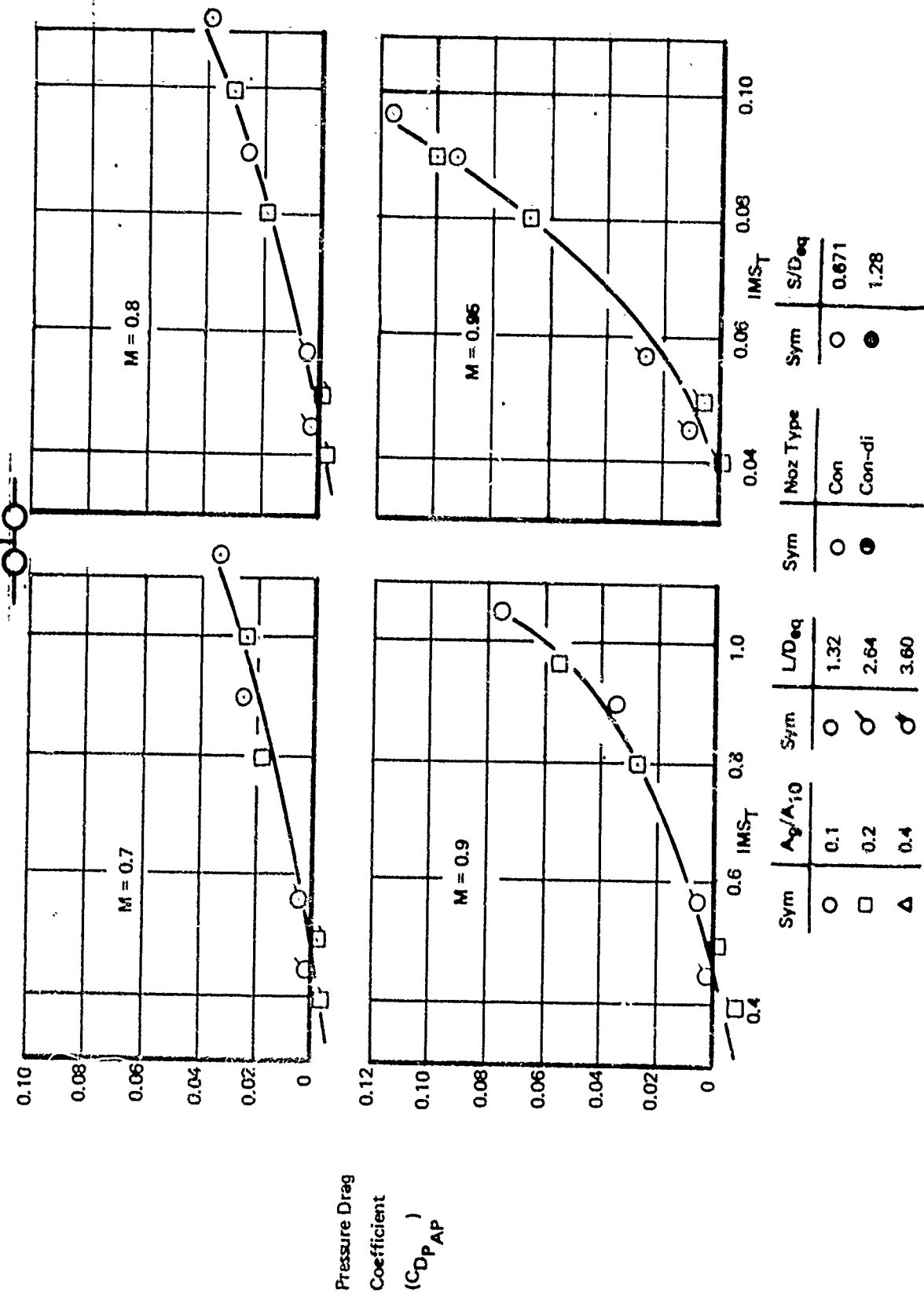
Figure 59: DRAG CORRELATION FOR SINGLE VERTICAL CONFIGURATIONS

83

correlations were combined, as shown in Figure 60 into a single correlation in terms of $C_D + \Delta C_D$. Here ΔC_D equals zero for centered twin vertical configurations and 0.006 for single vertical configurations. That is, the data for single vertical configurations have been raised 0.006 to the level of the centered twin vertical data.

It is always desirable to account analytically for the effects of as many independent variables as possible in a set of correlation curves such as those shown in Figure 60. This minimizes the risk of interpolation errors, particularly when the curves become part of a computerized prediction method.

In the case of Figure 60 it can be shown that all four of the correlation curves vary almost precisely as the IMS_T parameter raised to the 2.77 power. Thus the IMS_T dependence can be divided out to obtain a drag parameter which is a function of Mach number only, as shown in Figure 61. The upper half of the figure shows that the trend lines become flat, i.e., independent of IMS_T, when the drag parameter is defined as described above. Thus the ESIP correlation can be reduced to the single curve shown in the bottom half of the figure.

Figure 61 may give the false impression that the correlation does not work quite as well for models with low IMS_T values, where the apparent scatter is greater, as for models with high IMS_T values. However, the scatter at low IMS_T values is created by the fact that for the low IMS_T (low drag) models a relatively small increment in the absolute value of C_D may represent a sizeable <u>percentage</u> of the initially small value of C_D.

The overall effectiveness of the correlation curve shown in the bottom half of the figure in accounting for all of the data in the data base is shown in Figure 62. This figure compares the value which would be predicted by the correlation for each data point with its actual value. The dashed line represents the locus of perfect agreement. In this figure it is clear that the low drag models are accounted for quite accurately. Nearly all of the data are accounted for within 0.02 in C_D, with the majority of it within 0.01.

3.13.4 Drag Prediction Method

The correlation shown in Figure 61 can easily be built into a computerized prediction method for subsonic afterbody drag of twin buried engine configurations. The overall procedure
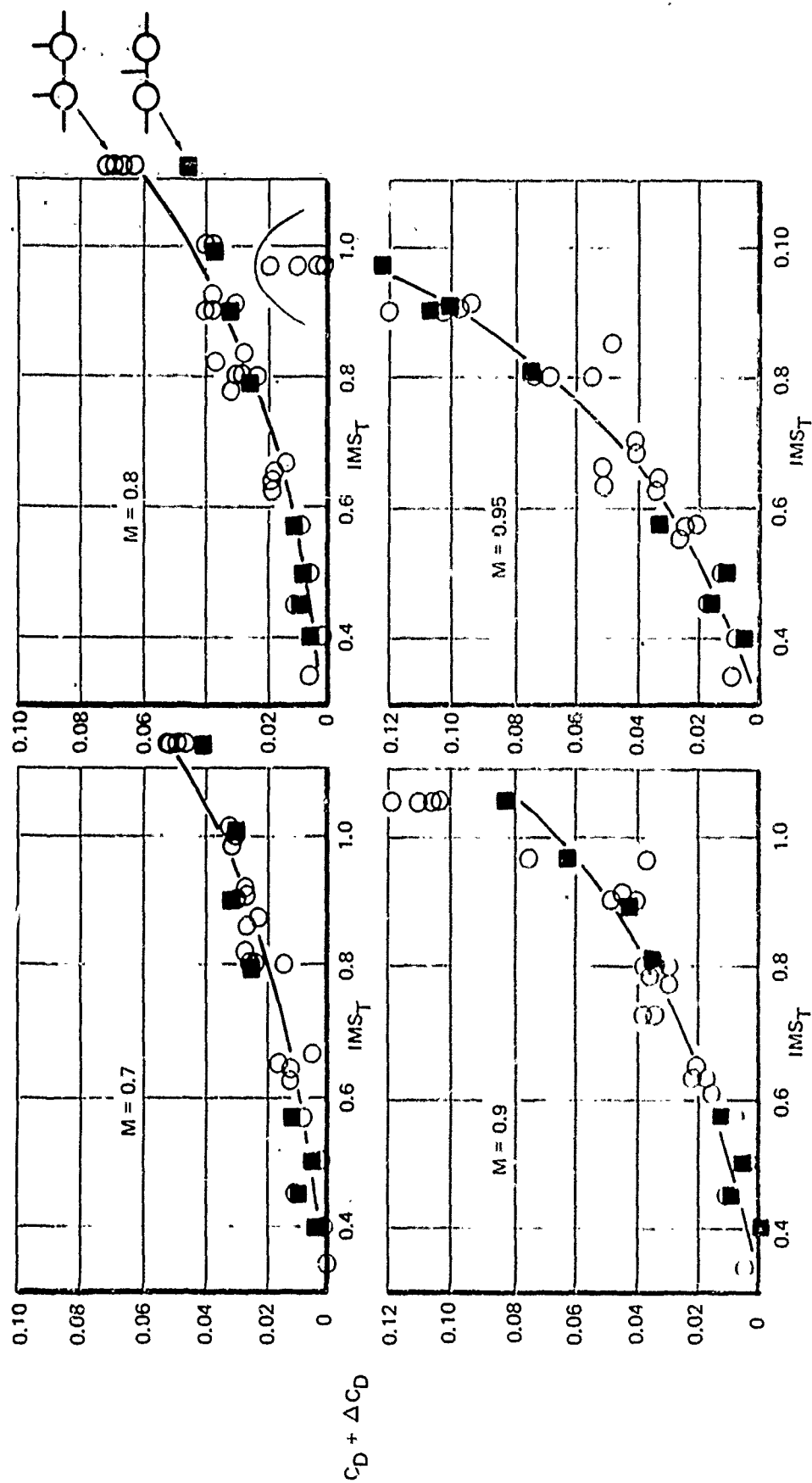
Figure 60: COMBINED DRAG CORRELATION FOR SINGLE AND TWIN VERTICAL CONFIGURATIONS
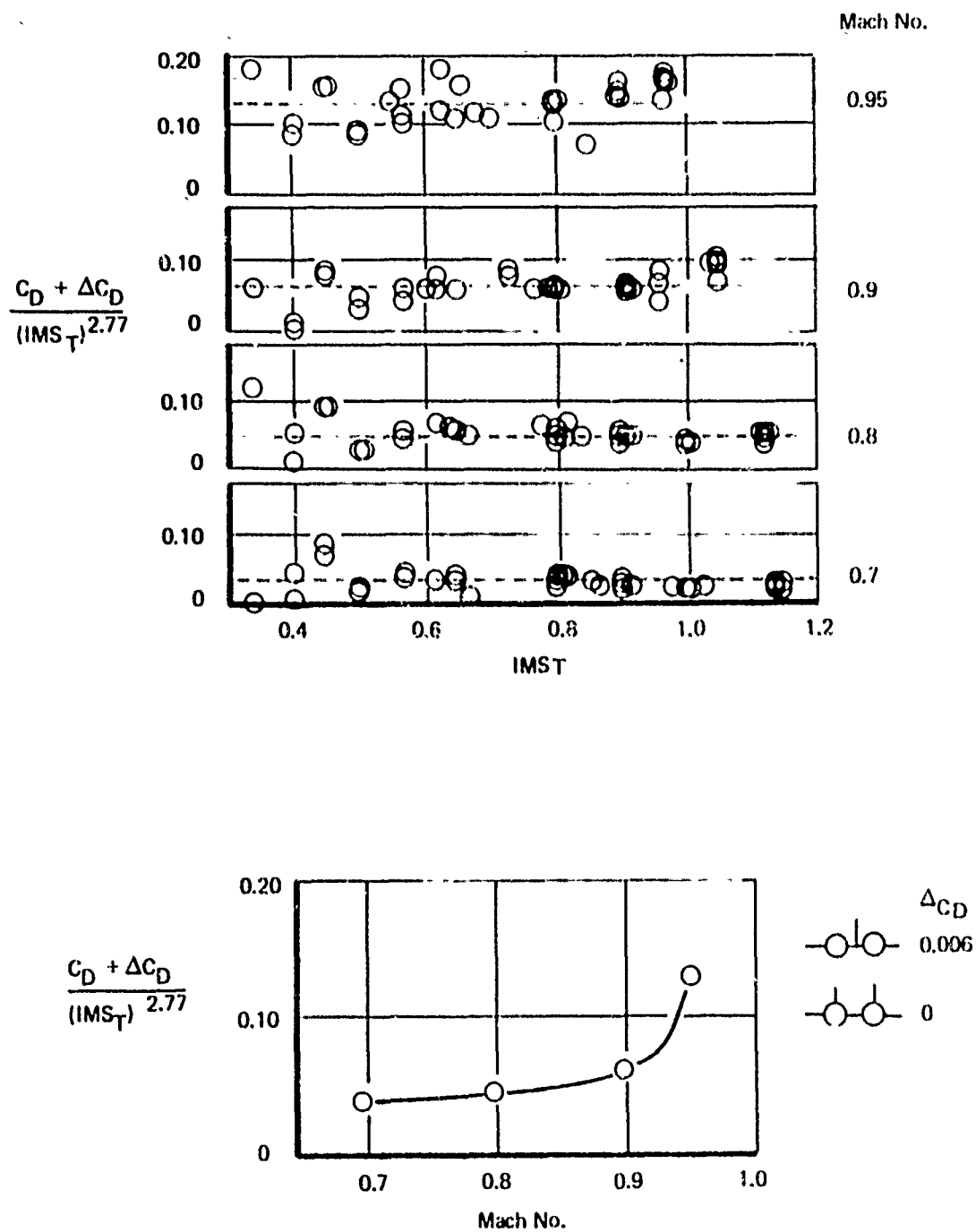
Figure 61 :   FINAL CORRELATION CURVE FOR SINGLE
                AND TWIN VERTICAL CONFIGURATIONS
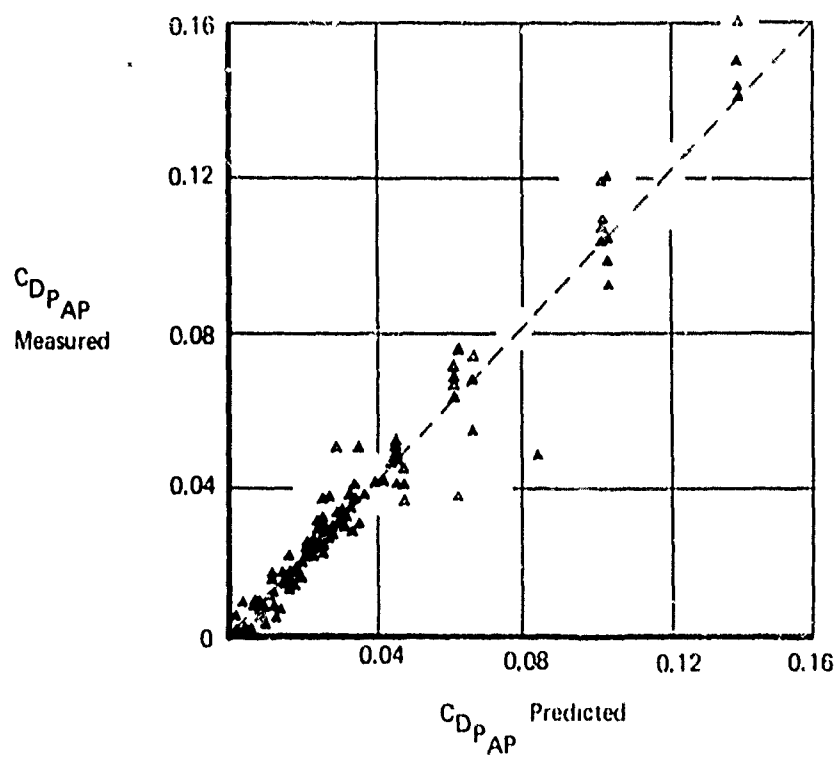
Figure 62 : COMPARISON OF CORRELATION WITH DATA BASE

is illustrated schematically in Figure 63.

The first step would be the inputting of the non-dimensional afterbody area distribution, as shown. The area distribution, together with the maximum slopes given in Figure 57, are then used to calculate the IMS_T values as a function of Mach number. This procedure has already been programmed for the Hewlett Packard 9810A desk-top computers. Thus the curve of IMS_T versus Mach number can be generated within minutes of the receipt of an area distribution.

The remaining calculations are then the obvious ones. The drag parameter from the basic correlation curve (Figure 61) is multiplied by IMS_T to the 2.77 power. The appropriate drag increment for the tail type is then subtracted from the result to obtain the aft end pressure drag coefficient. The same procedure should then be repeated for the drag polar baseline aft-end geometry in order to obtain the drag increment chargeable to the propulsion system.

The correlation curve of Figure 61 does not extend below Mach 0.7, because no data was taken there in the ESIP test program. However, extrapolation to Mach zero along a constant equal to the value at Mach 0.7 appears to be a reasonable approach, since very little in the way of a compressibility effect is evident at Mach 0.7. Extrapolation in the other direction, to Mach numbers greater than 0.95, would, of course, be unwarranted.

Similarly, the data base includes models with IMS_T values as large as about 1.1. The method should not be considered applicable to models with larger values of IMS_T.

$$A/A_{10}$$

$$x/D_{eq}$$

Max.
Slope

Mach No.

Compute $IMS_T = -\dfrac{1}{(1-A_9/A_{10})} \displaystyle\int_{A_9/A_{10}}^{1.0} \dfrac{d\,(A/A_{10})}{d\,(X/D_{eq})}\, d\,(A/A_{10})$

$$\dfrac{d\,(A/A_{10})}{d\,(X/D_{eq})} \leqslant \text{Max. Slope}$$

$$IMS_T$$

Mach No.

Correct for Tail Type

$$\Delta c_D = 0.006 \qquad \Delta c_D = 0$$

Predicted
Drag

Correlation

$$\dfrac{c_D + \Delta c_D}{IMS_T{}^{2.77}}$$

Mach No.
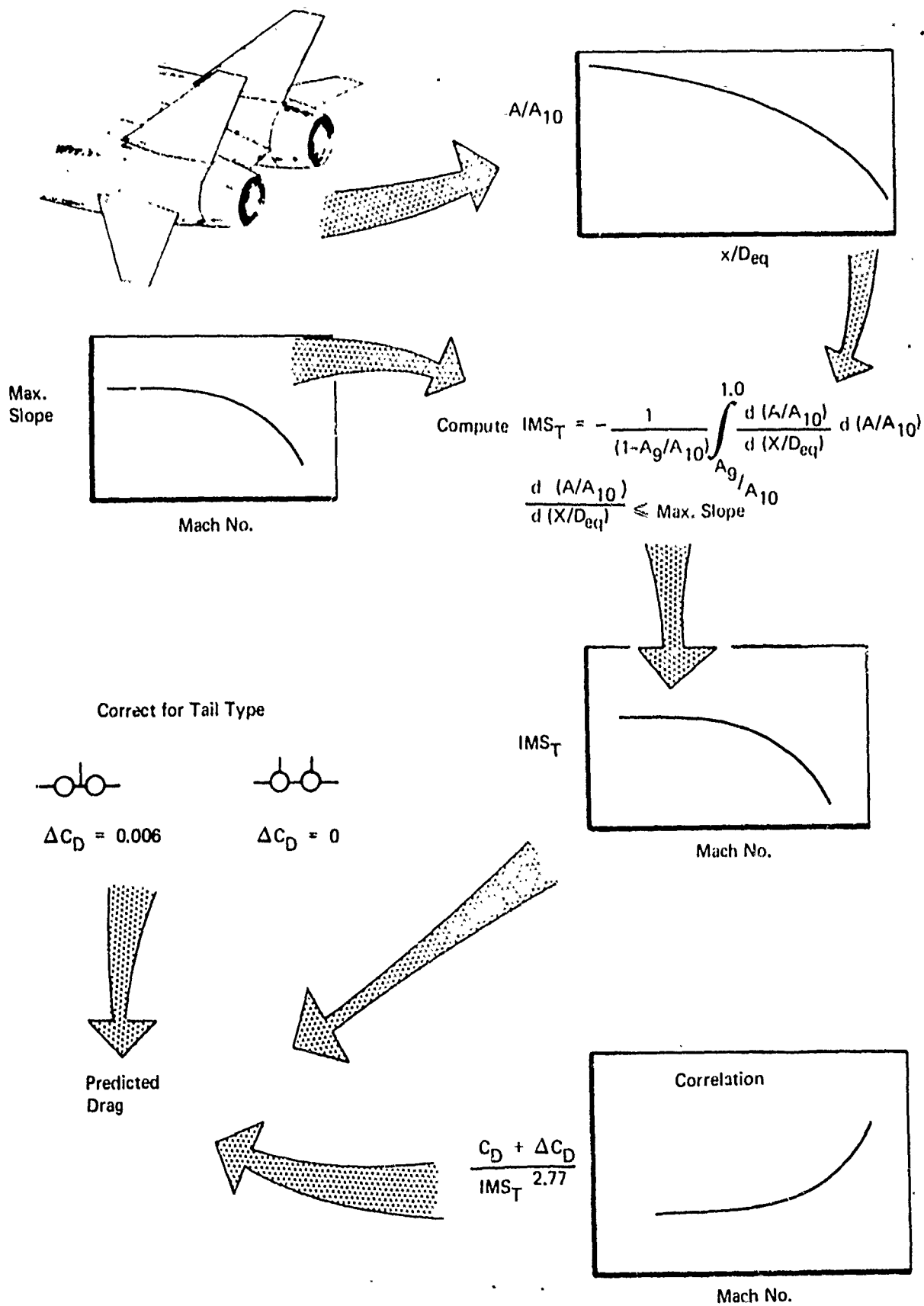
Figure 63 :   DRAG PREDICTION PROCEDURE

89

SECTION IV

DATA FOR SPECIFIC CONFIGURATIONS

4.1 INLET DATA

This section contains a collection of data covering a wide
variety of configurations from subsonic inlets through
supersonic designs. The purpose of this section is to
provide a source of data that can be readily used to develop
the inputs required to use the PITAP procedure. It can also
be used as a handy reference source for general inlet
geometrical and performance characteristics.

The data are arranged in the order of design Mach number.
Within each data group, a sketch of a typical inlet geometry
is presented first, followed by the recovery characteristics,
then drag. As much information as possible is presented, but
complete sets of data are not available for all configurations.
Some of the data sets are complete in the format used by PITAP
and can be used to make installed performance calculations.
Data can readily be added to this section as it becomes available.

4.1.1 NORMAL SHOCK INLETS

A sketch of the normal shock inlet is shown in Figure 68. This
inlet model and several other variations of it, were tested
extensively for drag and recovery characteristics during the
development of the North American F-100 aircraft (Reference 37).
Except for the fact that a LWF normal shock inlet would be
mounted under the fuselage, and have a boundary layer diverter,
the normal shock inlet configuration shown here and its
performance are probably representative of the configuration
and performance levels applicable to LWF at small angles-of-
attack. No boundary layer bleed or bypass are used in the
inlet. The capture area size is based on the transonic airflow
demand of the engine. The decrease in total pressure recovery
at free-stream Mach numbers above 1.50 makes this capture
area adequate to provide all the airflow required to match
engine demand up to Mach 2.0. In fact, spilling a significant
amount of airflow is required above Mach 1.5, which accounts
for its high drag at engine matched condition.

Test results up to M_O = 1.5 were used as a basis for the
performance data.   Above Mach 1.50, total pressure recovery
was calculated from normal shock total pressure losses and
subsonic diffuser losses for a duct loss coefficient of ε =.12.
This was found to correlate well with test results up to Mach
1.50; therefore, it offered a reasonable approach to extend
the recovery data to Mach 2.0.
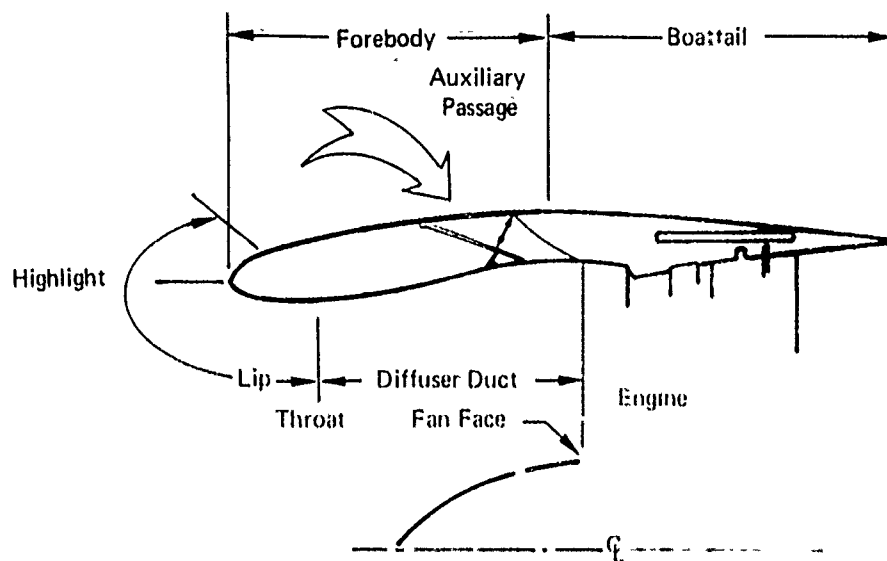
Figure 64 :   *SUBSONIC INLET DESIGN*
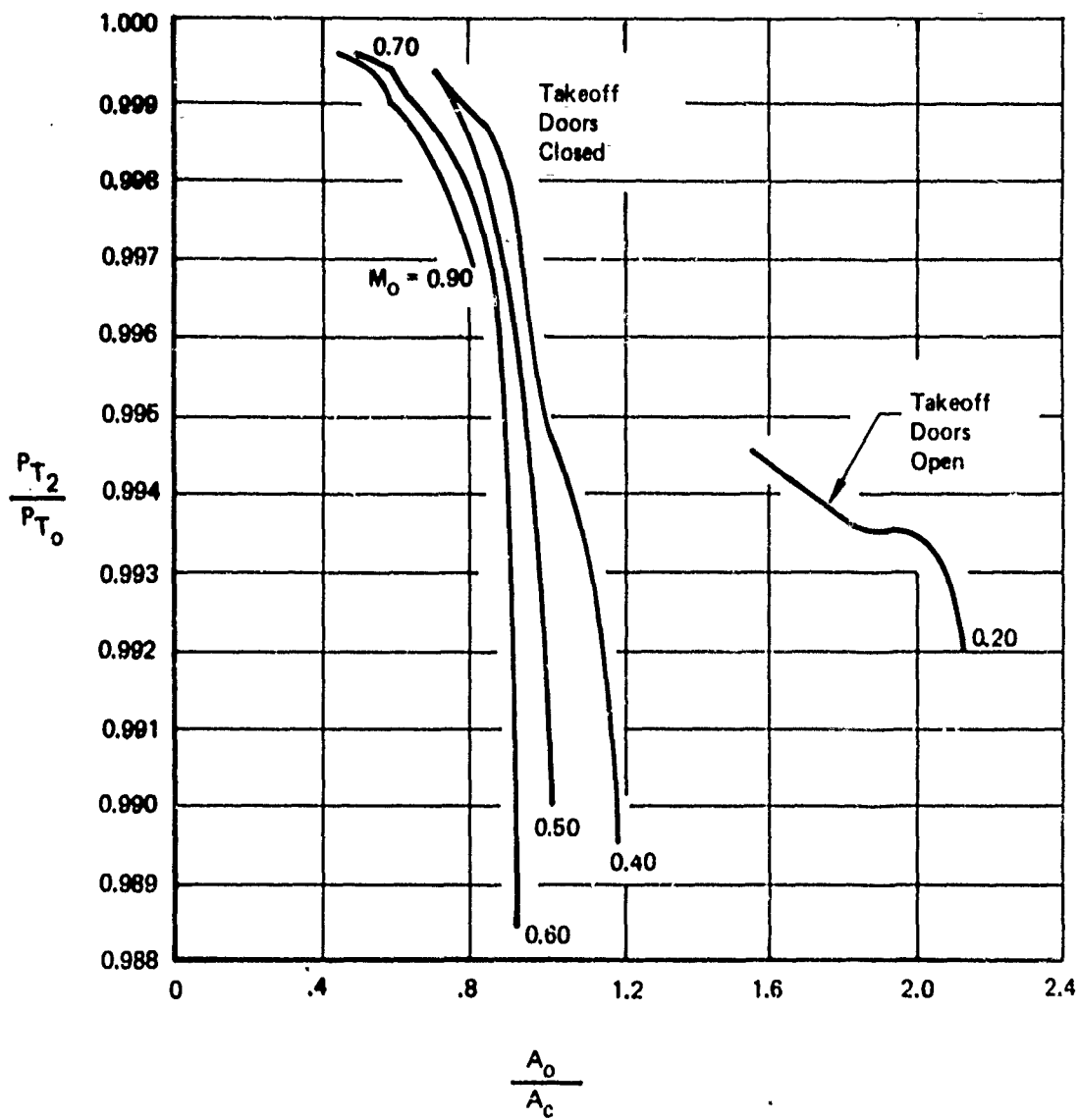
Figure 65 : SUBSONIC INLET PERFORMANCE DATA

92

$$C_{D_{Spill}} = \frac{D_{Spill}}{\frac{\gamma}{2} P_o M_o^2 A_1}$$
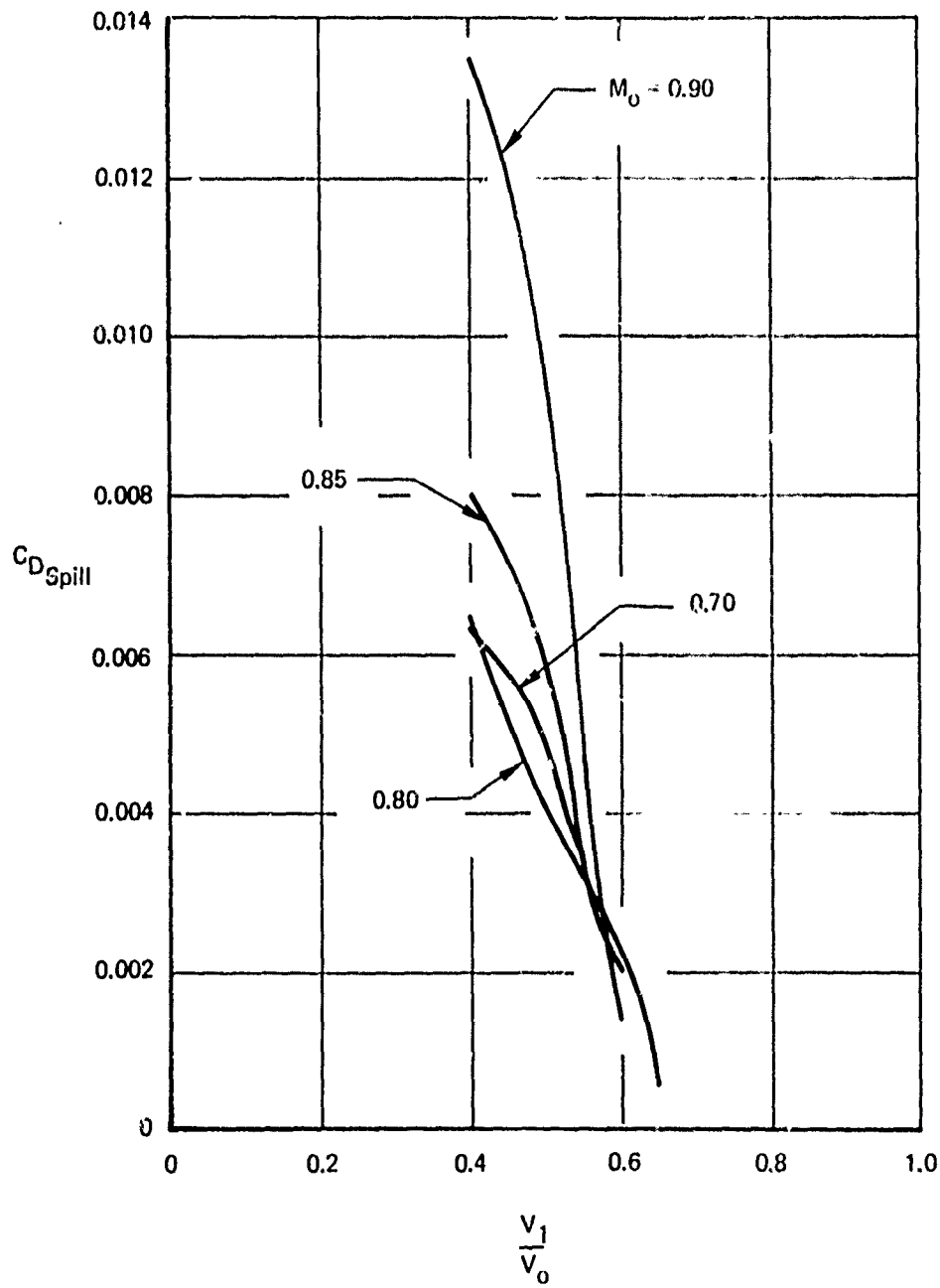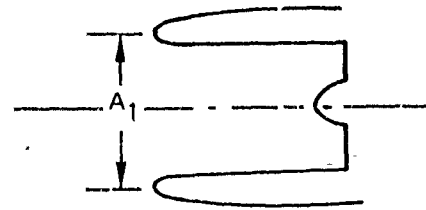
Figure 66 :   SUBSONIC INLET SPILLAGE DRAG DATA

93

ARC: $r/D_{LE} = 0.118$

Ellipse $r_i/D_{LE} = 0.0785$

$r_2/r_1 = 2$

$M_0 = 0.85$

$d/D = 0.908$

$X/D = 0.16$

K_{ADD}

MFR
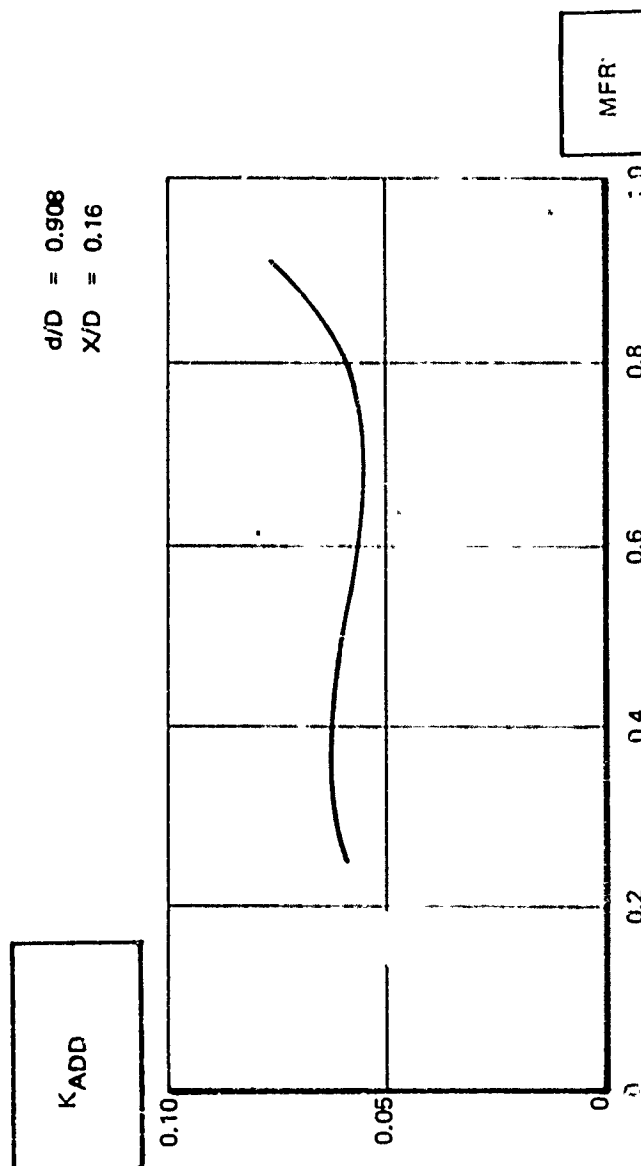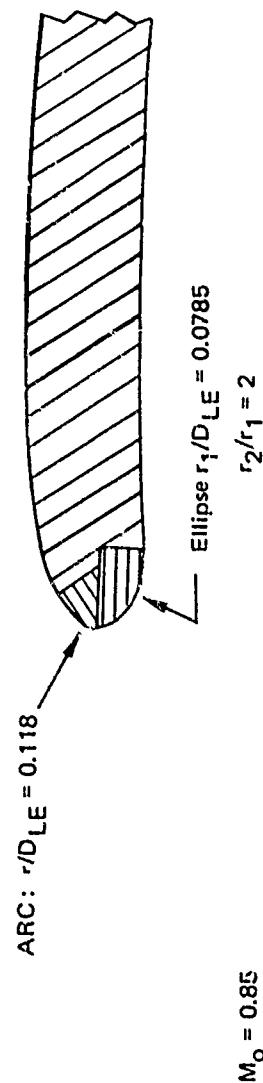
Figure 67 : K_{ADD} FOR SHORT THIN COWL, MODIFIED NACA-1 CONTOUR

94
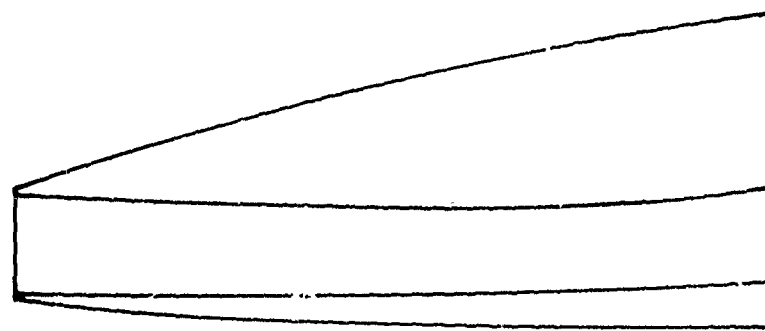
(a)   Nose Inlet
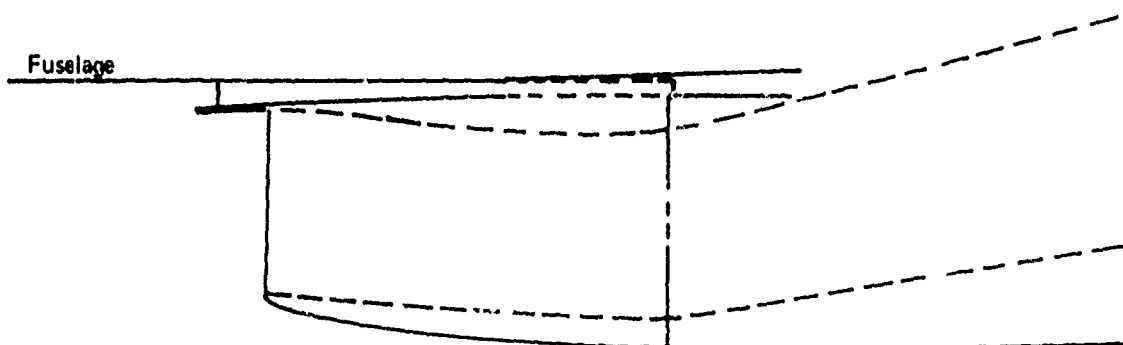
Fuselage

(b)   Under Fuselage

Figure 68 :   NORMAL SHOCK INLET

95

The recovery-mass flow plots are presented in Figures 69 & 70
and the corresponding matched recovery and mass flow as a
function of local Mach number are shown in Figures 78 and 79,
respectively.

The distortion limit is shown in Figure 80. No buzz limit
is required for the normal shock inlet.

Spillage drag is presented in Figure 81. Test data from wind
tunnel tests were used to obtain the shapes of the spillage
drag curves for Mach number up to 1.50. For Mach 1.8 and
2.0, the spillage drag slope correspond to the slopes obtained
from additive drag calculations for open nose inlets. For
the normal shock inlet, a reference mass flow ratio of 1.0
was used.

4.1.2   FIXED GEOMETRY, TWO-SHOCK INLETS

4.1.2.1   TWO-DIMENSIONAL

The configuration is shown in Figure 94. It is designed for
shock-on-lip at $M_O=2.0$. The inlet is basically designed
for Mach 1.60 operation with a capability to go to Mach
2 without having shock ingestion problems. A throat bleed
slot is provided to remove the boundary layer near the normal
shock interaction region. Bleed air is dumped overboard
through a fixed geometry choked convergent exit.

The throat bleed slot was added to improve inlet recovery,
distortion, and flow stability characteristics at Mach
numbers above 1.50. For these higher Mach numbers, the normal
shock strength will separate the turbulent boundary layer.
layer and improve entrance conditions to the subsonic
diffuser.

Figure 95 presents the recovery versus mass flow ratio
characteristics for the inlet from low-speed up to Mach 2.0.
Max airflow match lines are also shown for reference. The
effect of takeoff doors on low-speed recovery is shown in
Figure 96 for $M_O=$ .20 and .40.

Matched inlet recovery as a function of local Mach number is
presented in Figure 97. The effect of takeoff doors equal
in area to .235 A_C is shown to result in a 5% improvement
in static pressure recovery.

Figure 98 presents the matched inlet mass flow characteristics,
including the effect of boundary layer bleed flow through the
slot. The upper curve, labeled A_{O_I}/A_C represents the total
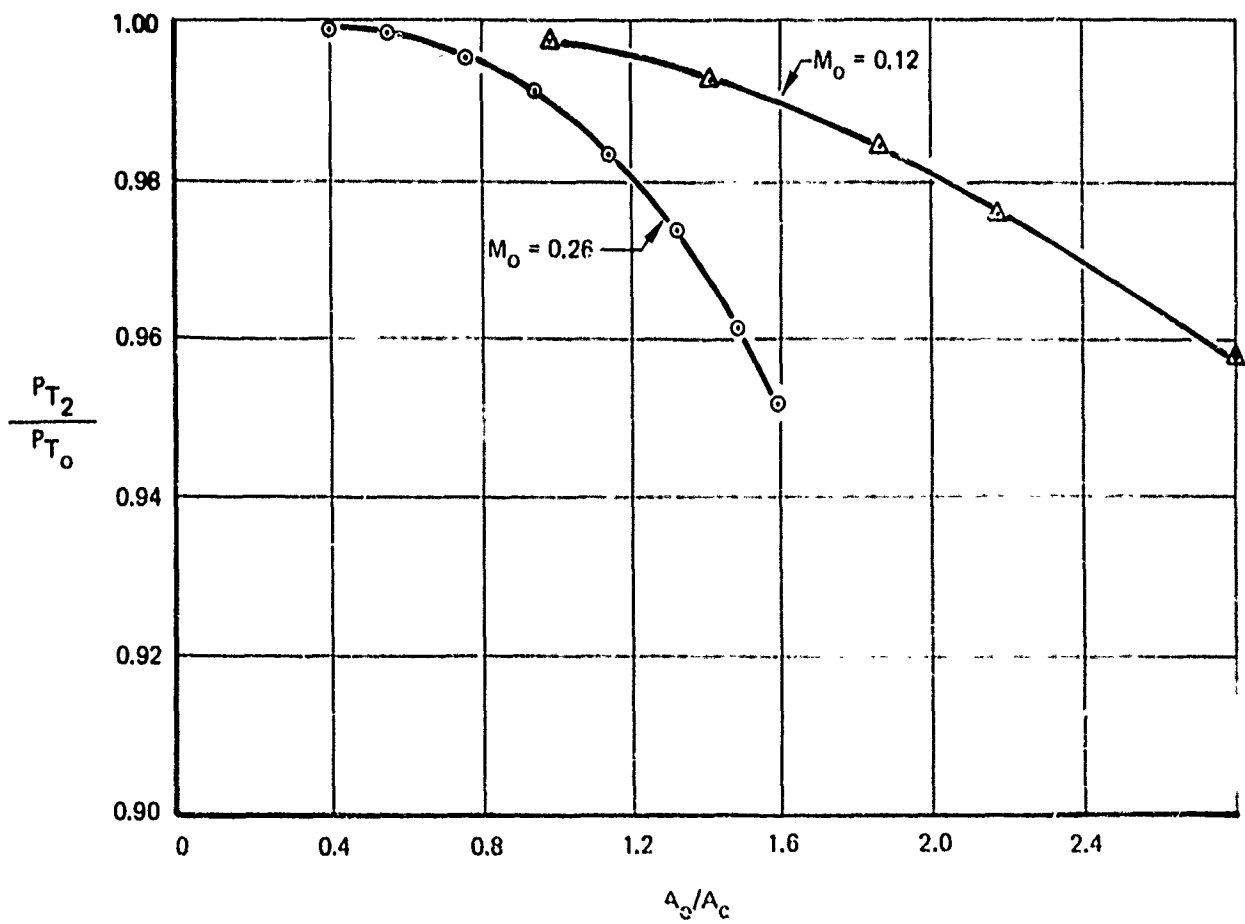
Figure 69 : NORMAL SHOCK INLET PERFORMANCE
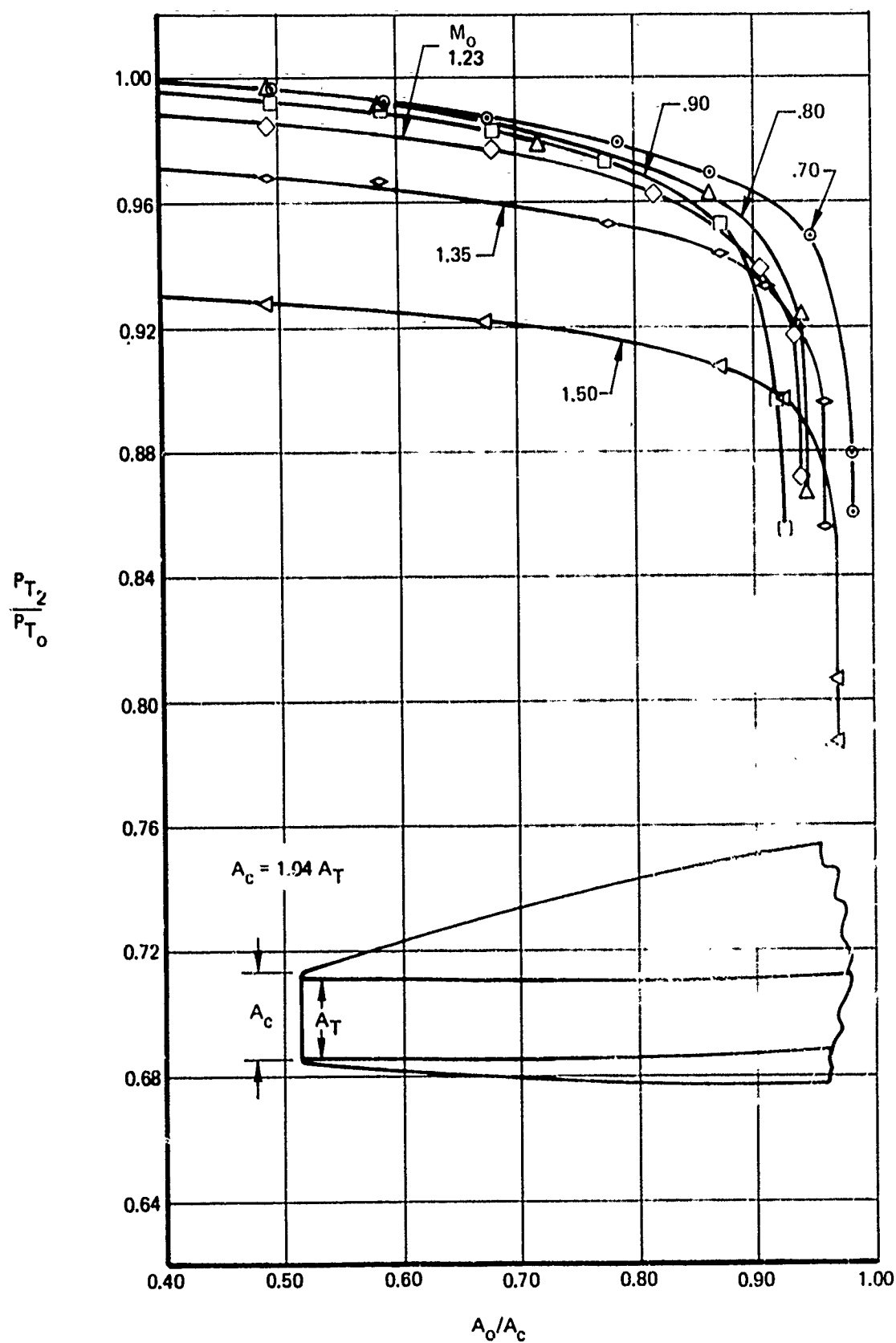
Figure 70: NORMAL SHOCK INLET PERFORMANCE
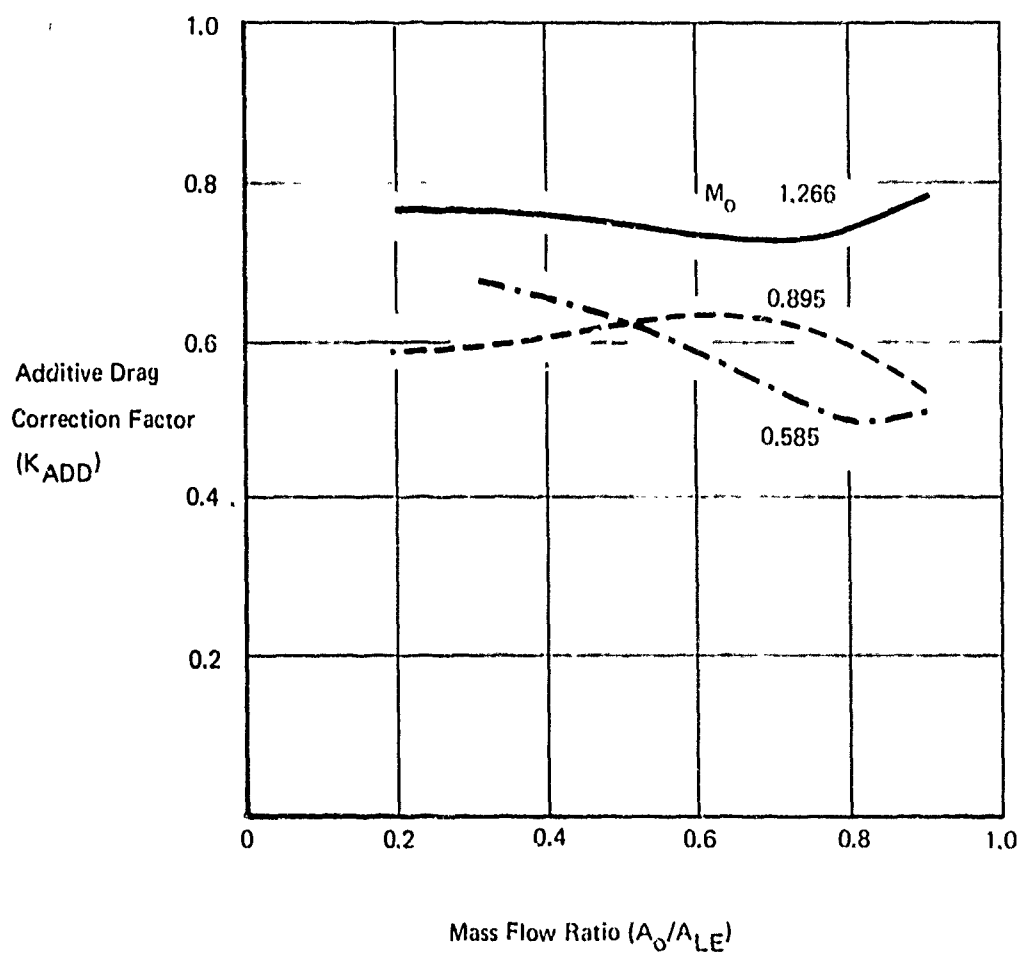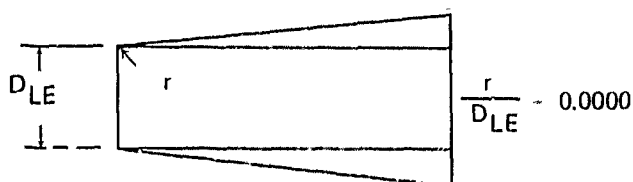
$$\frac{r}{D_{LE}} = 0.0000$$

Figure 71 : K_{ADD} FOR OPEN NOSE INLETS. STRAIGHT COWL (r/D_{LE} = 0.000)
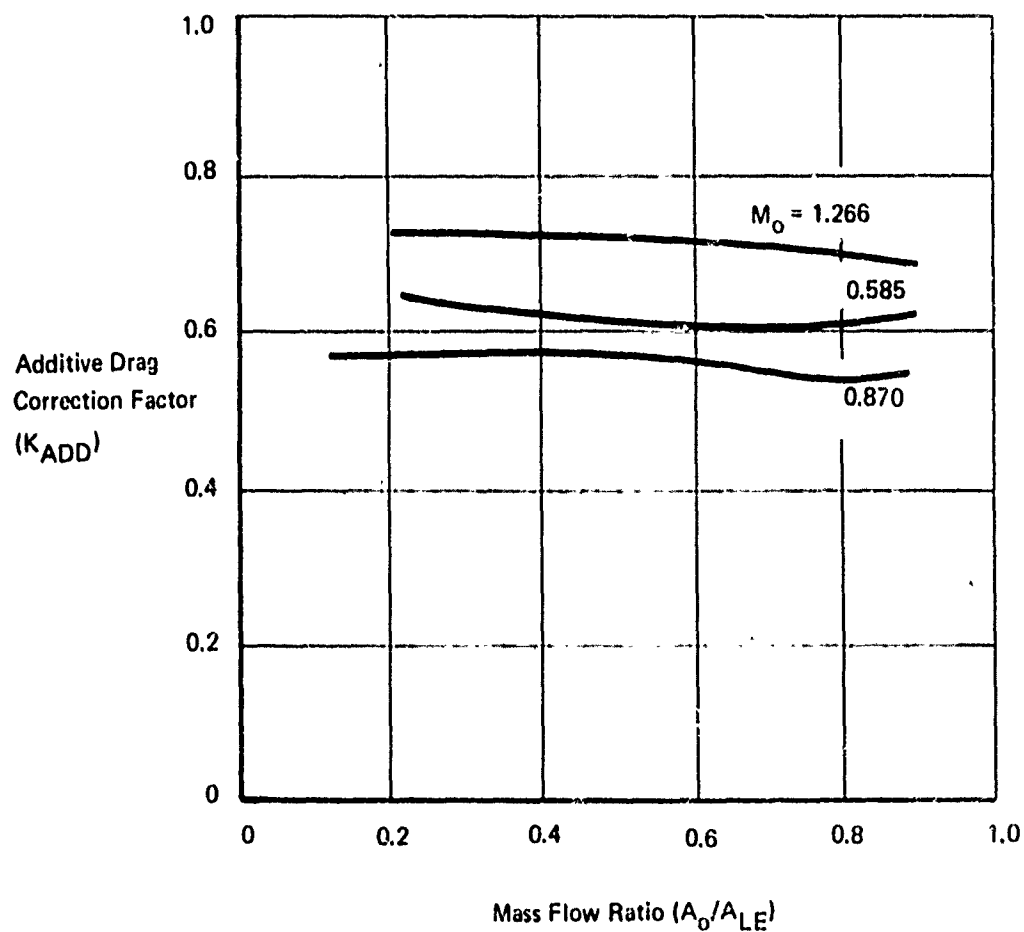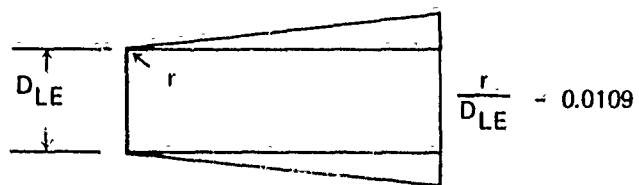
$$\frac{r}{D_{LE}} = 0.0109$$

Figure 72: K_{ADD} FOR OPEN NOSE INLETS. STRAIGHT COWL — r/D_{LE} 0.0109.
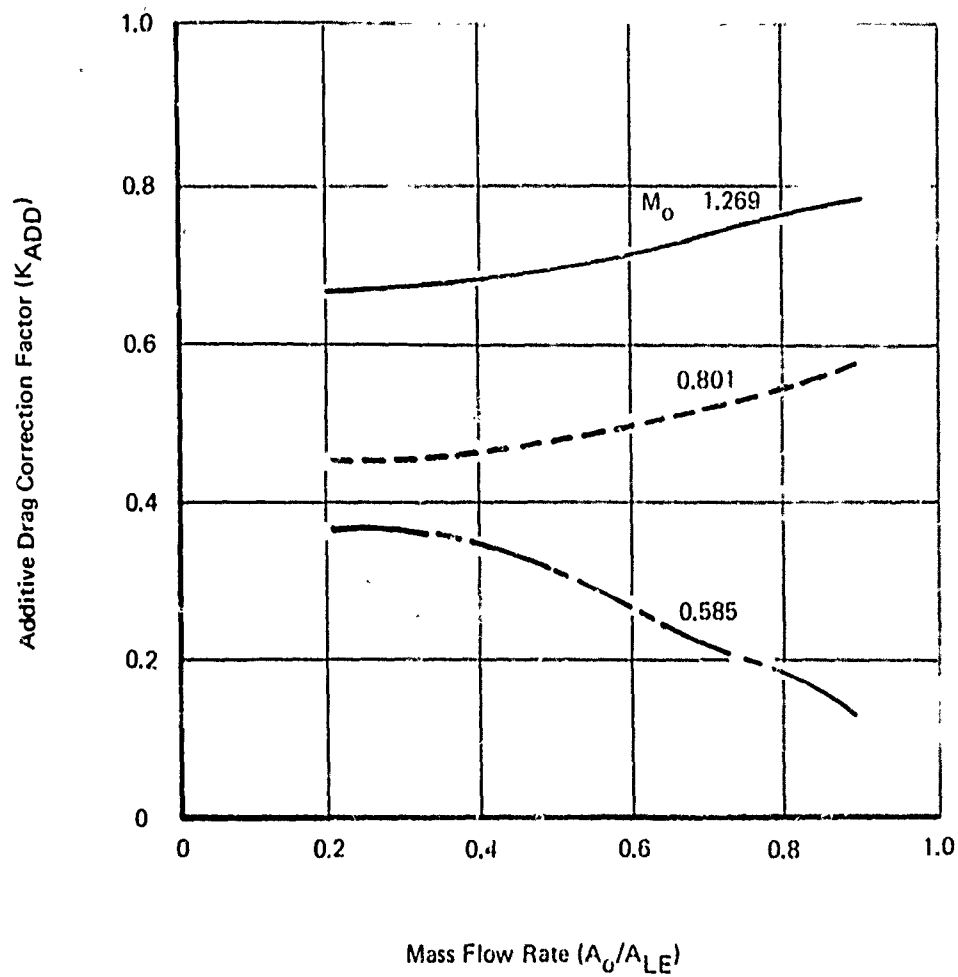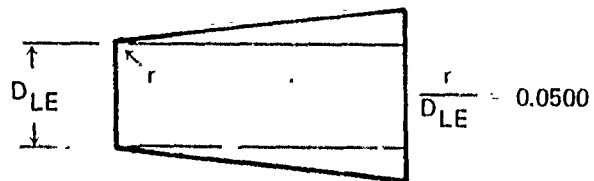
$$\frac{r}{D_{LE}} = 0.0500$$

Figure 73: K_{ADD} FOR OPEN NOSE INLETS, STRAIGHT COWL — $r/D_{LE} = 0.0500$.
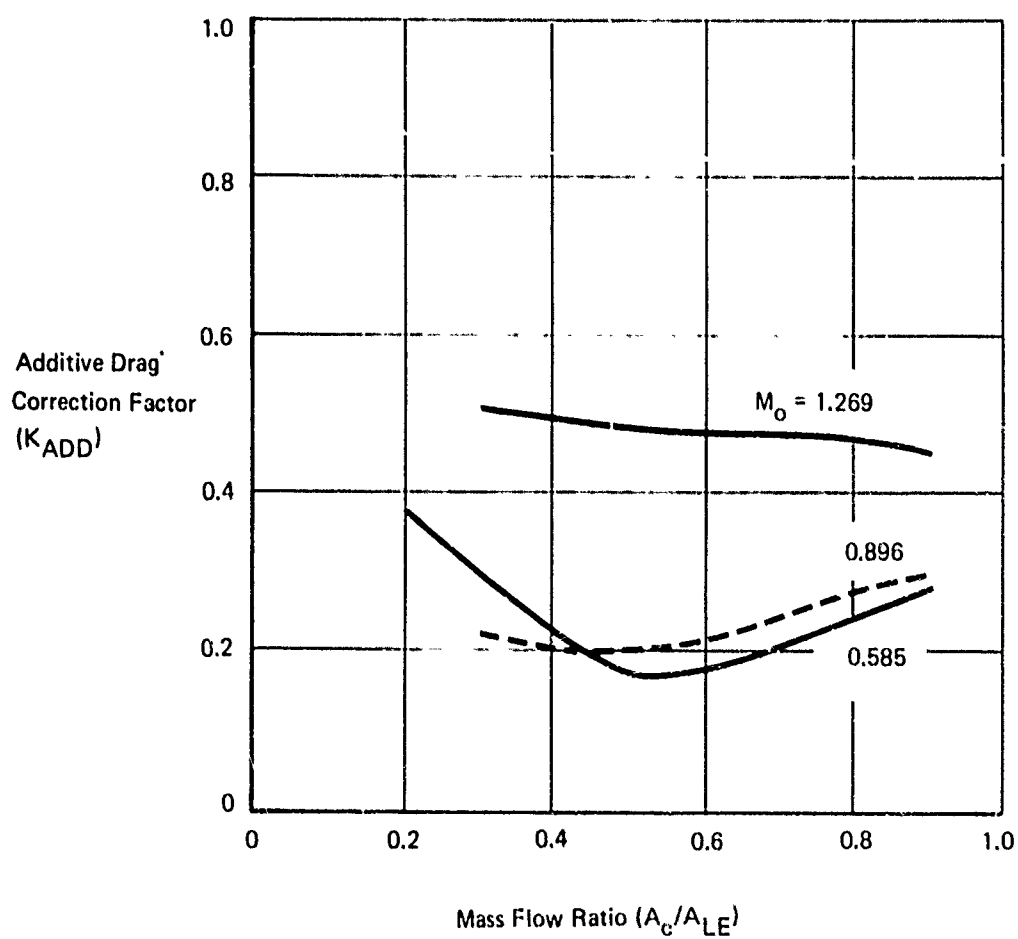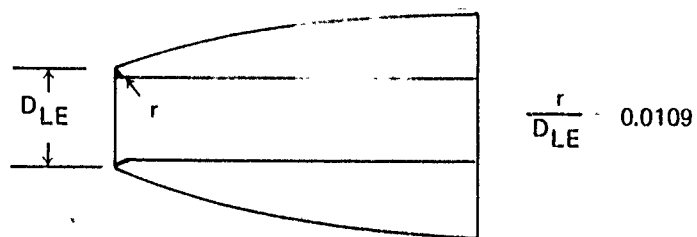
$$\frac{r}{D_{LE}} \quad 0.0109$$

Figure 74 : K_{ADD} FOR OPEN NOSE INLETS, CURVED COWL − $r/D_{LE} = 0.0109$

102

$\frac{r}{D_{LE}} = 0.0500$

Additive Drag Correction Factor (K_{ADD})

$M_0 = 1.269$

0.895

0.585

Mass Flow Ratio (A_0/A_{LE})
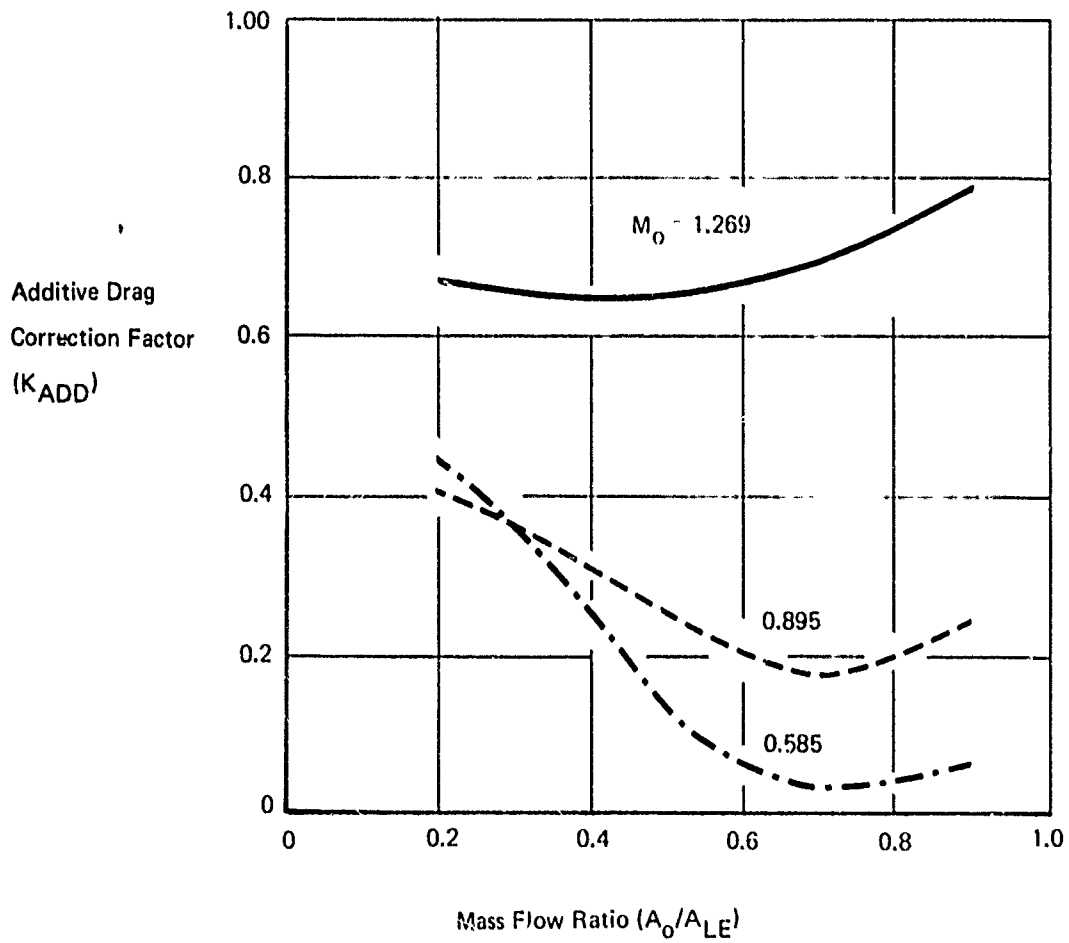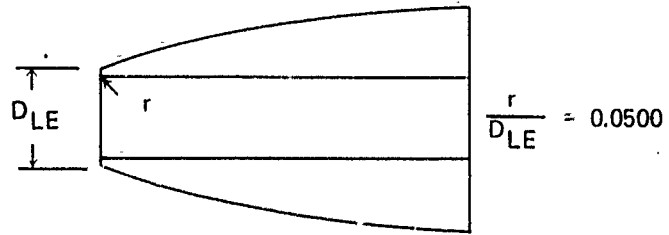
Figure 75: K_{ADD} FOR OPEN NOSE INLETS, CURVED COWL - $r/D_{LE} = 0.0500$.
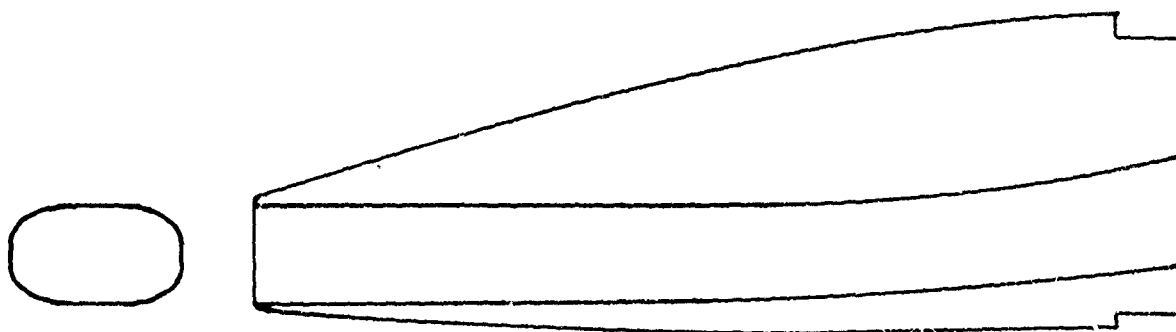
Figure 76 :   *NORMAL SHOCK INLET*

104
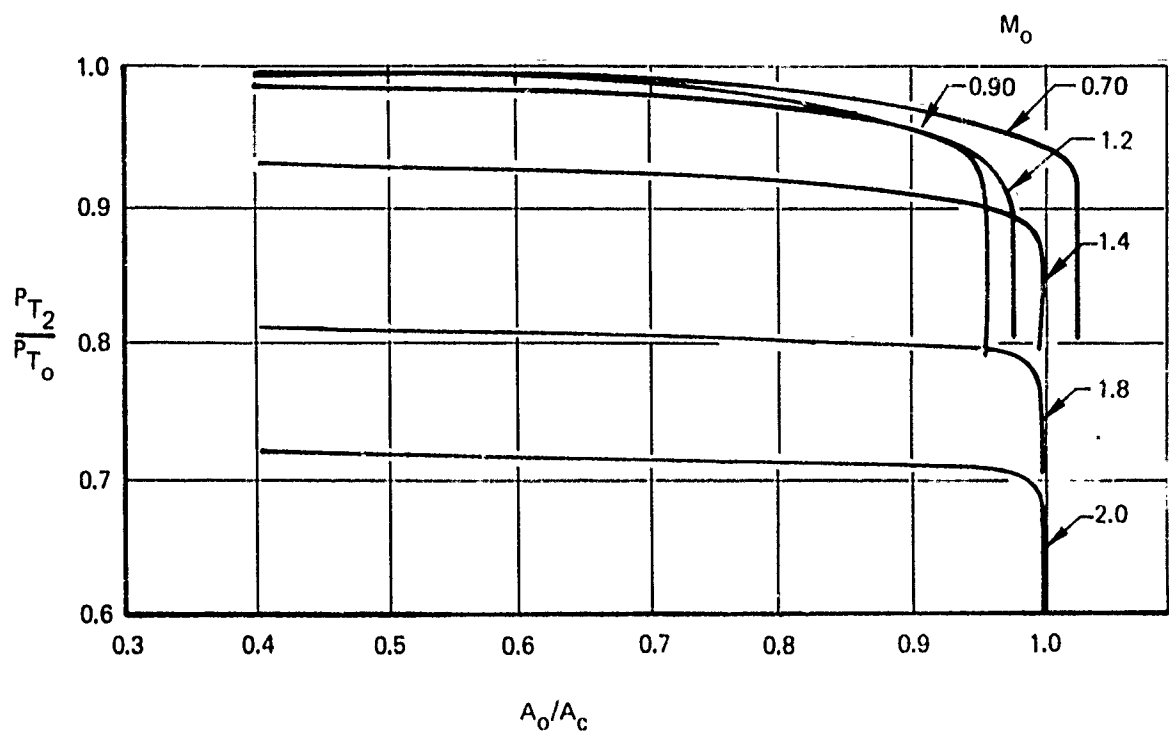
Figure 77 :   RECOVERY VERSUS MASS FLOW
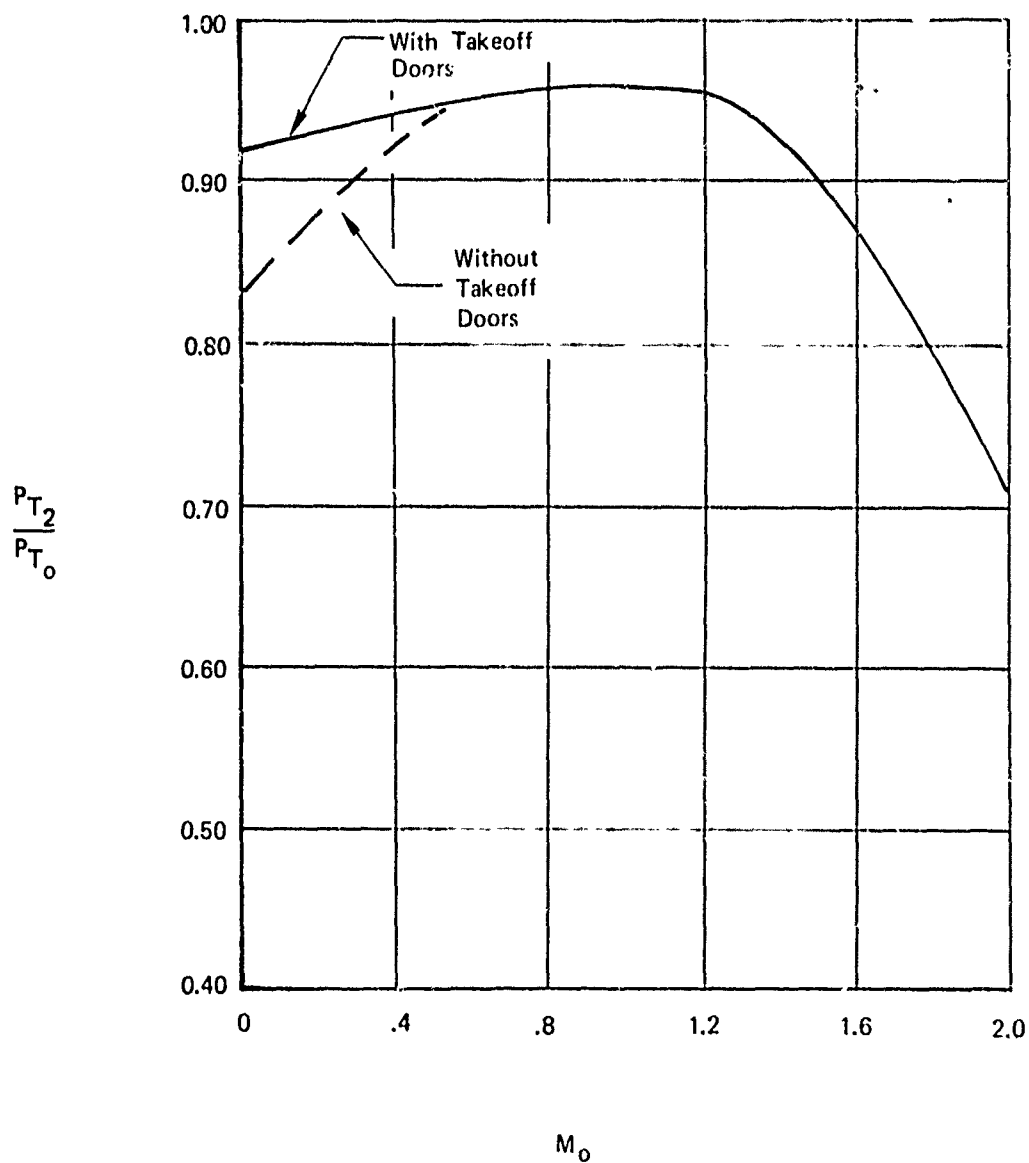
Figure 78 : MATCHED RECOVERY
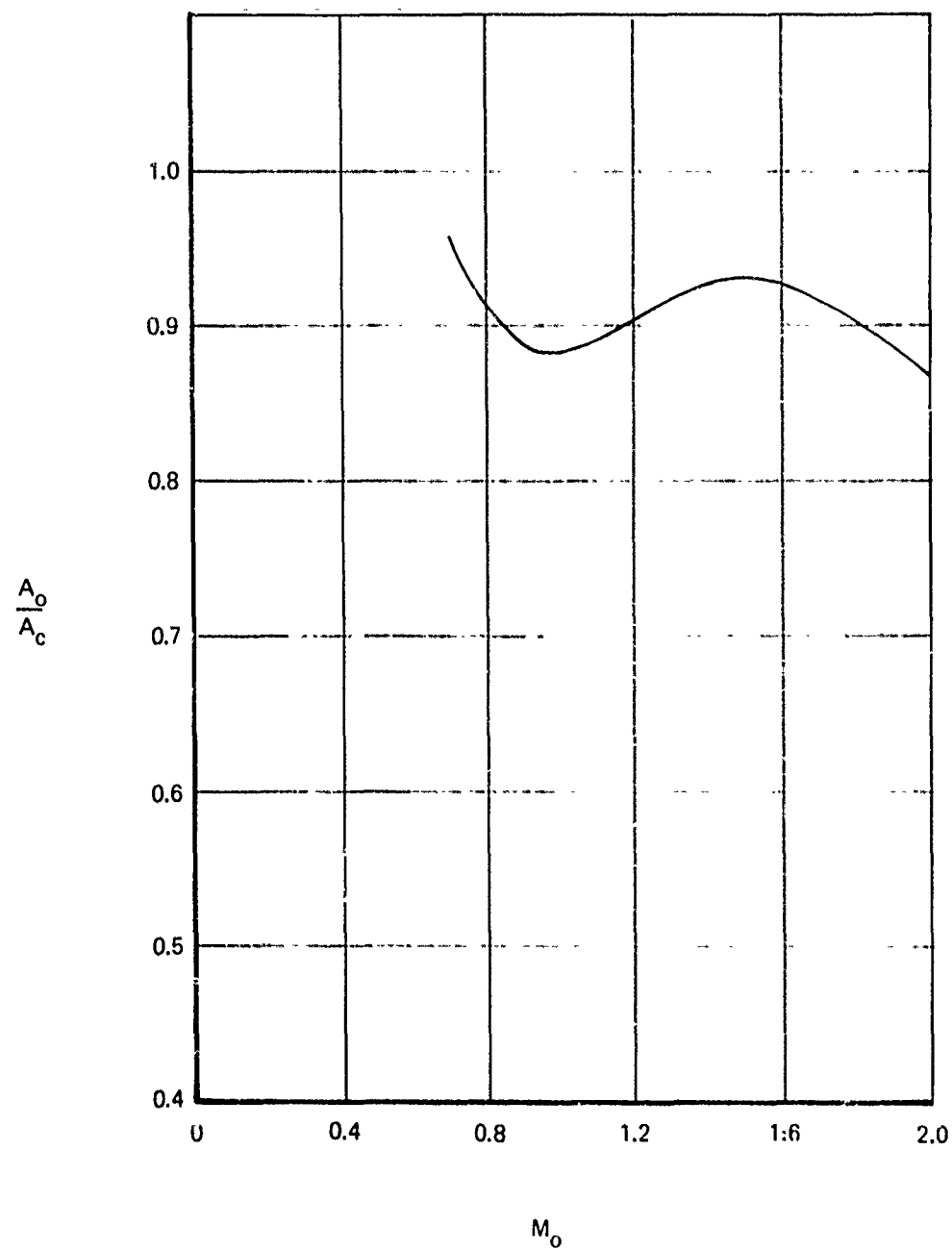
Figure 79 : MASS FLOW VERSUS M_O
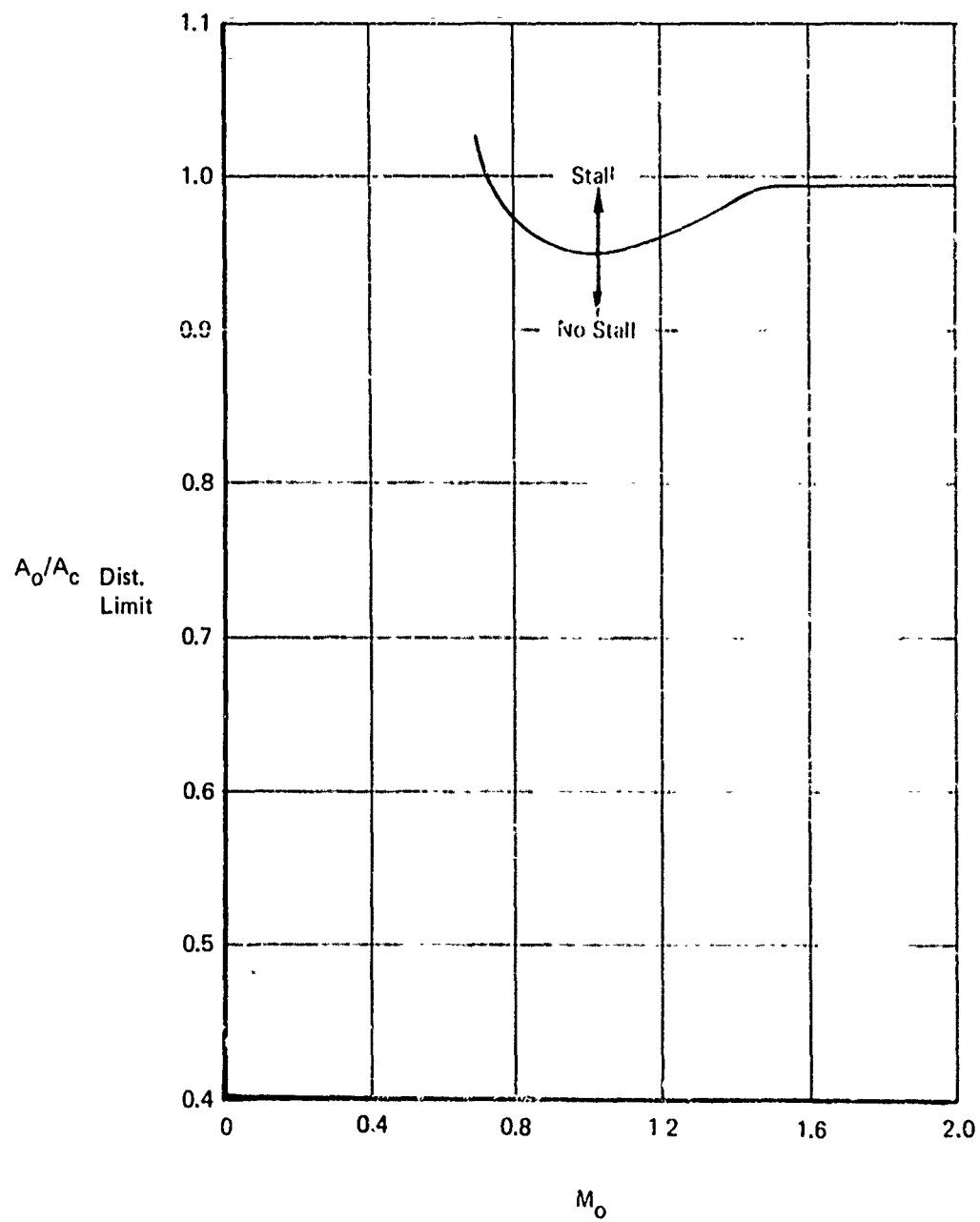
Figure 80 : DISTORTION LIMIT
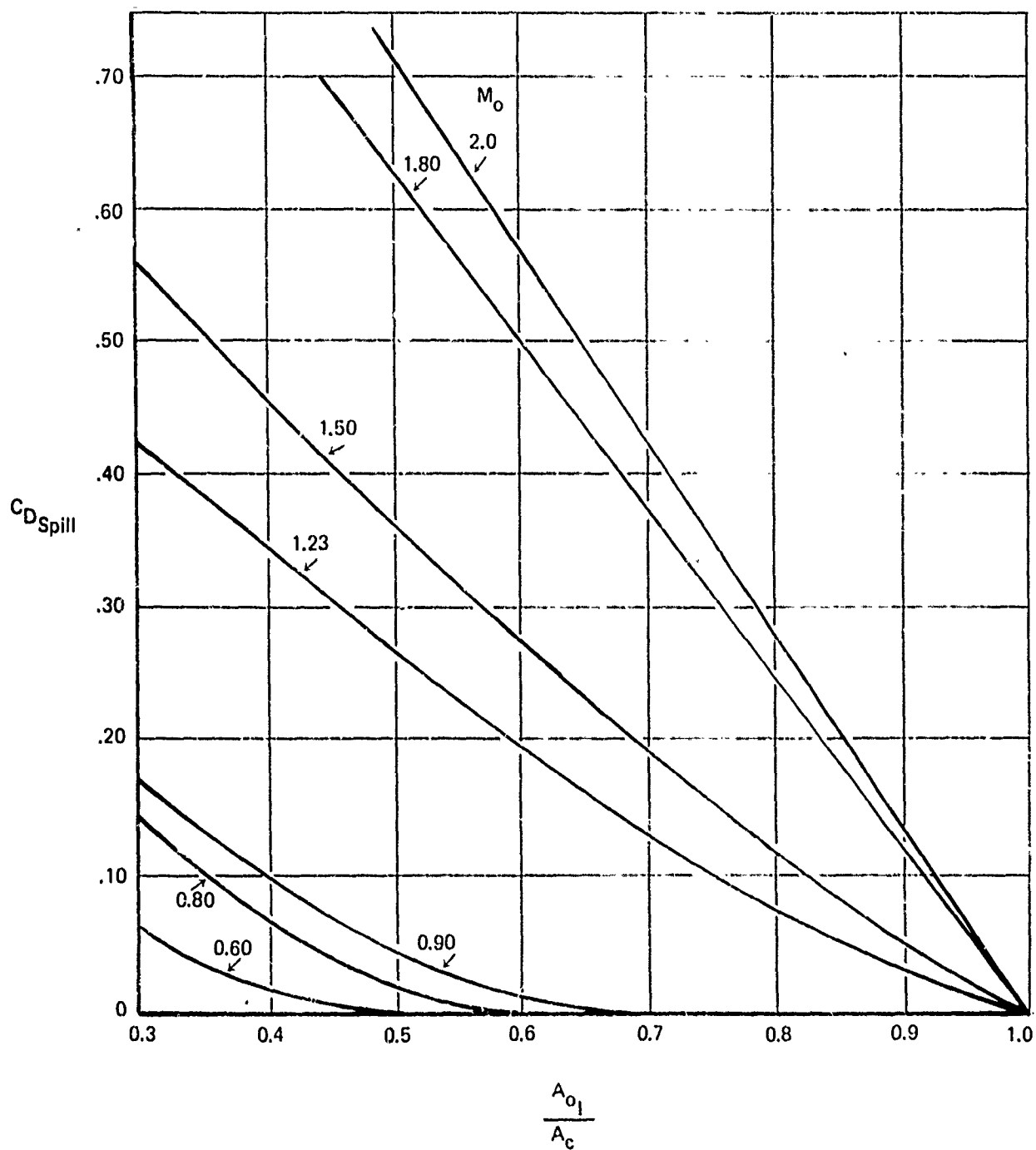
Figure 81 : SPiLLAGE DRAG

109
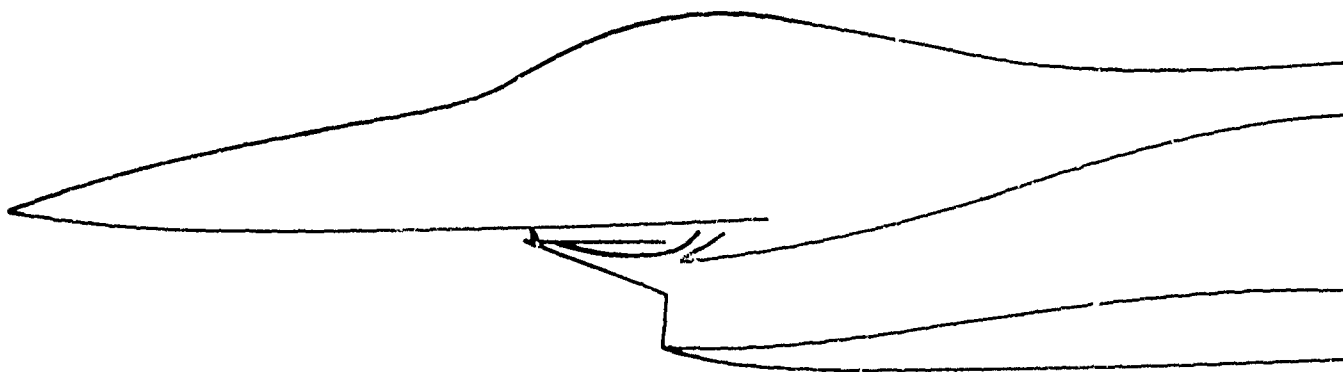
Figure 82: $M_0 = 1.60$ *FIXED GEOMETRY TWO-DIMENSIONAL INLET*

$M_O = 1.60$
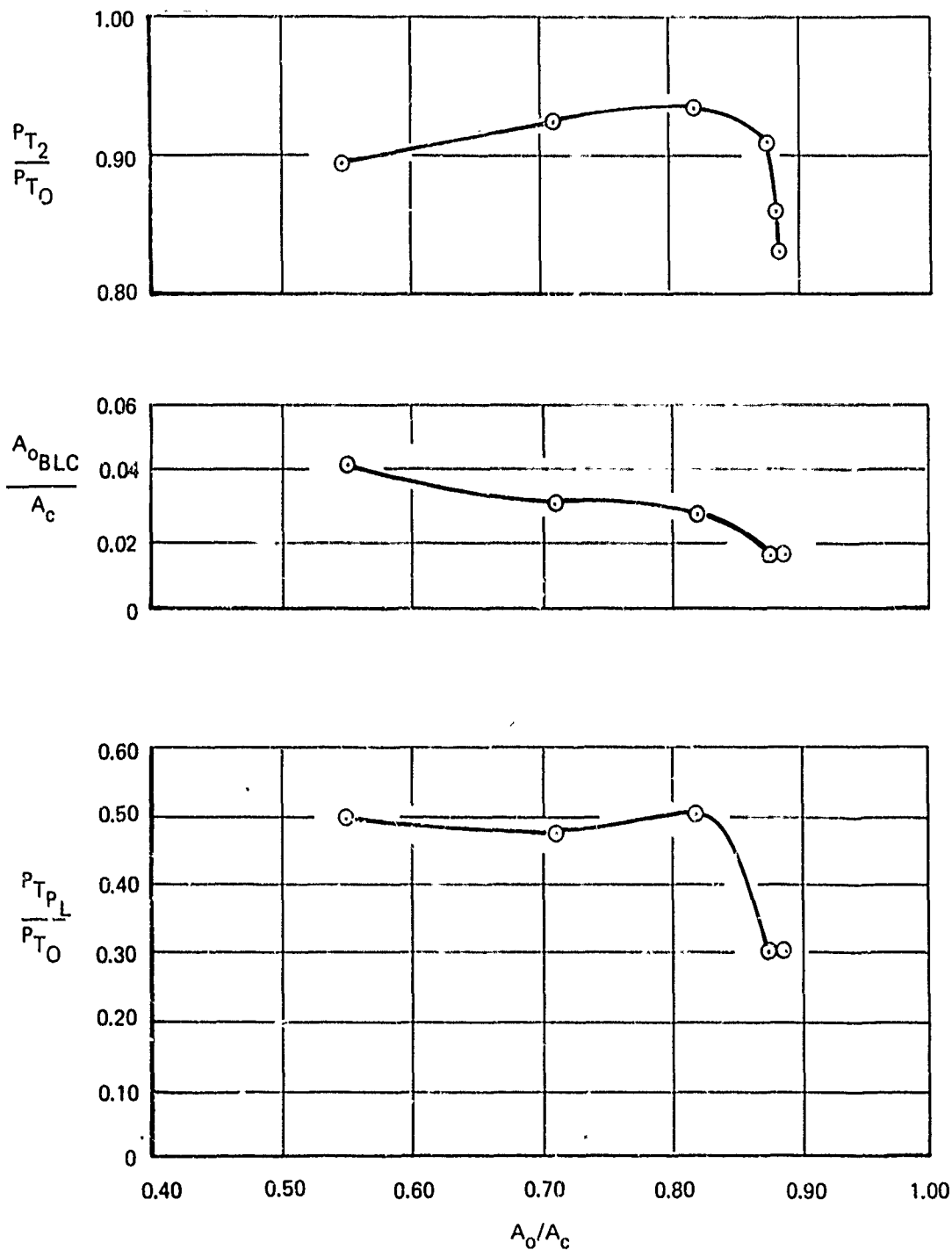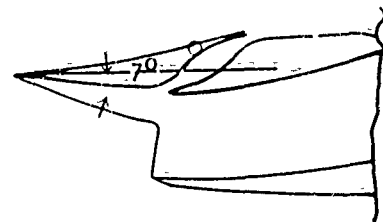
Figure 83: INLET PERFORMANCE DATA FOR A MACH 1.60
2-D, FIXED GEOMETRY INLET WITH SLOT BLEED

111

$\beta = 0$
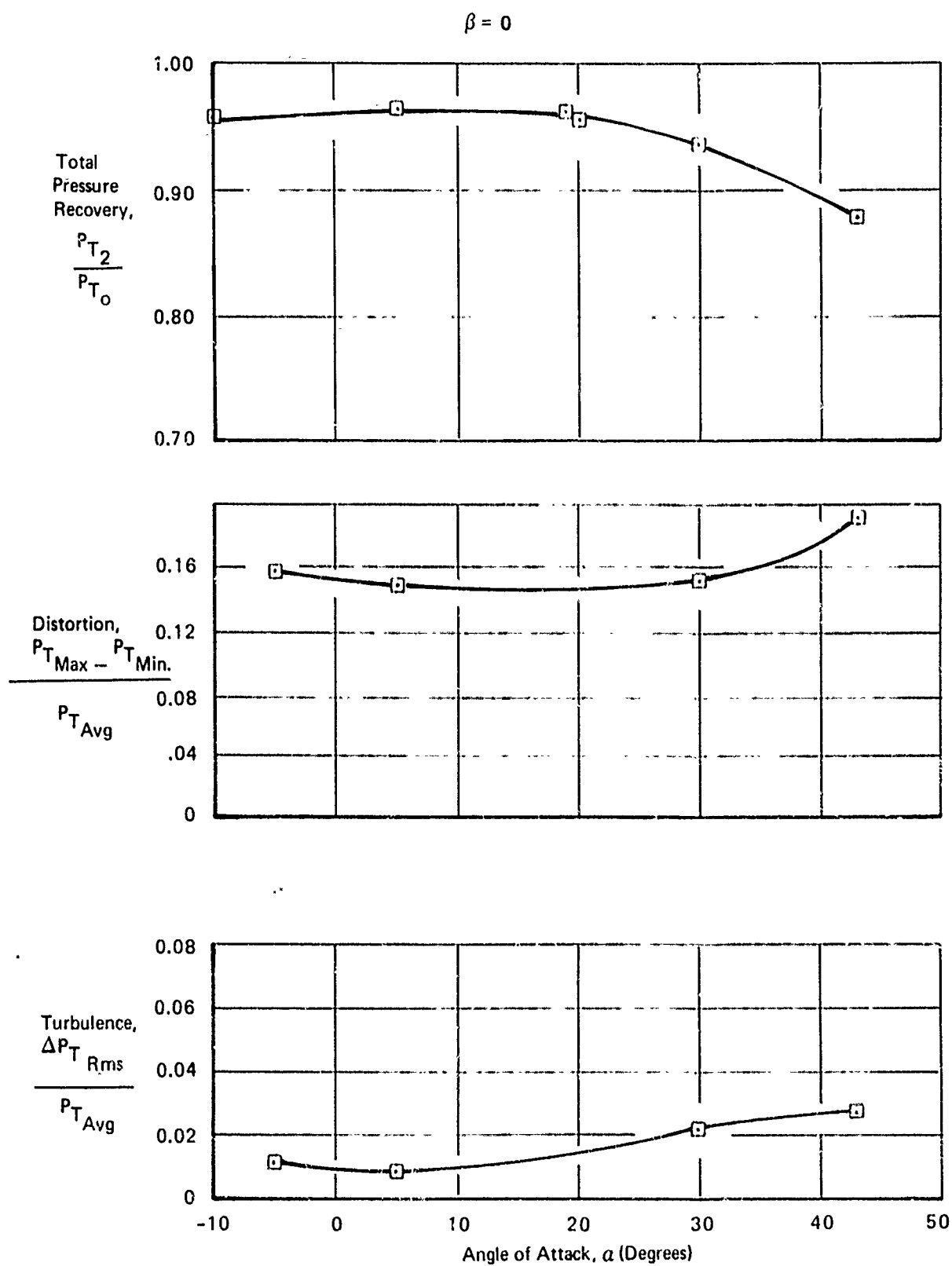
Figure 84: EFFECT OF ANGLE OF ATTACK ON INLET PERFORMANCE AT $M_0 = 0.90$ (UNDER FUSELAGE MOUNTED INLETS)

$\beta = 0$

Angle of Attack, a (Degrees)
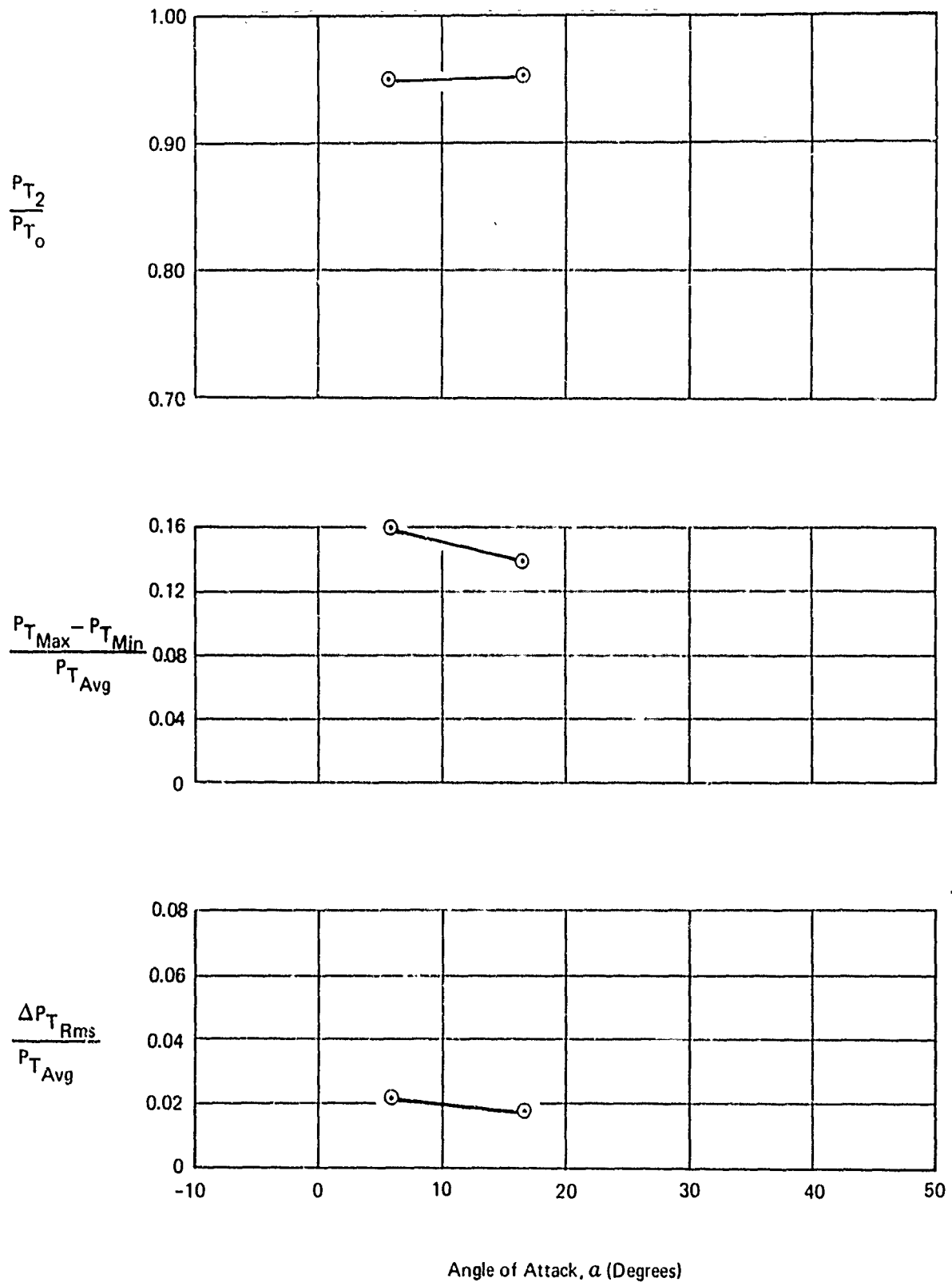
Figure 85 : EFFECT OF ANGLE-OF-ATTACK ON INLET PERFORMANCE AT $M_O = 1.10$
(UNDER FUSELAGE MOUNTED INLETS)

113
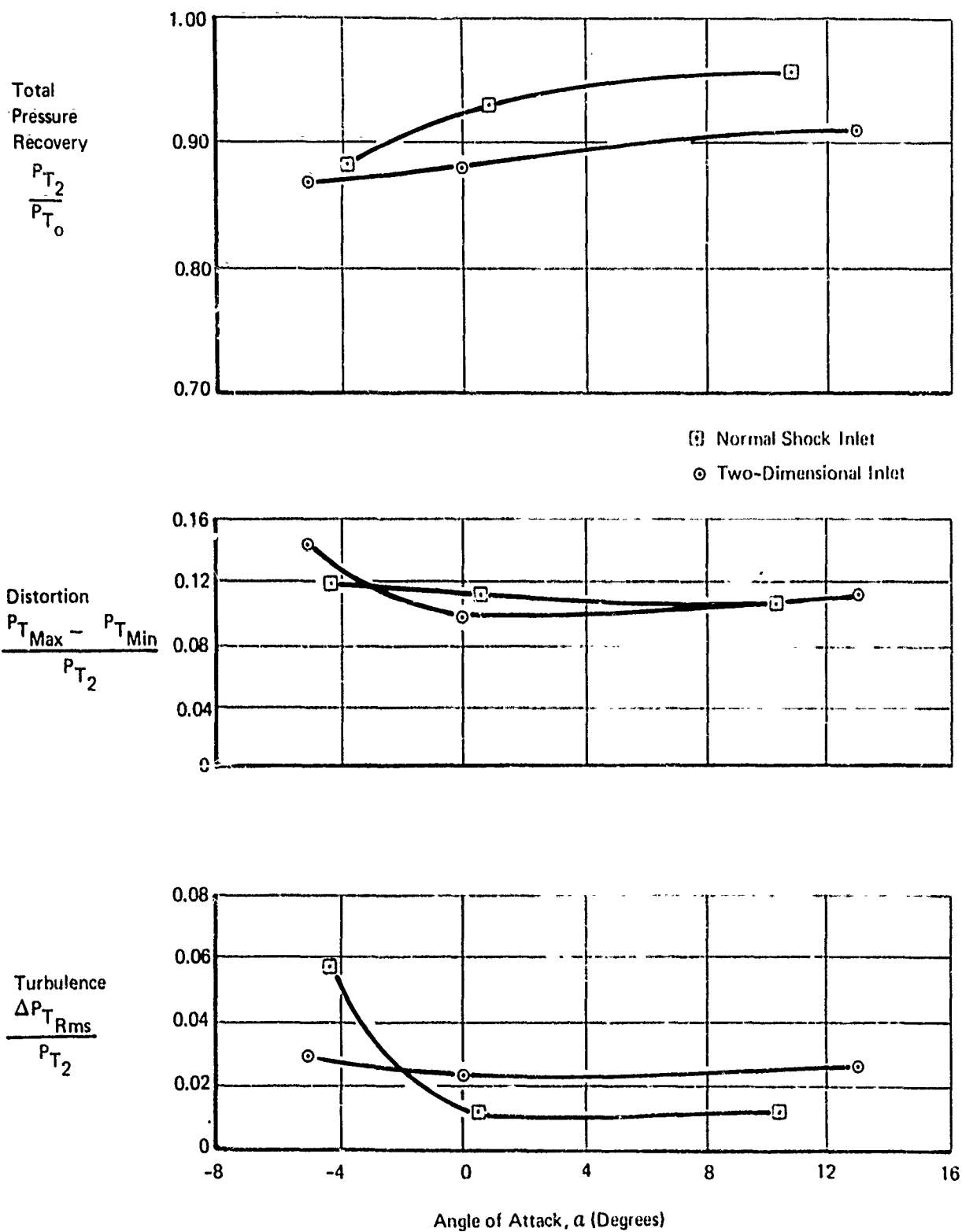
Figure 86: EFFECT OF ANGLE OF ATTACK ON INLET PERFORMANCE AT $M_o = 1.60$ (UNDER FUSELAGE MOUNTED INLETS)
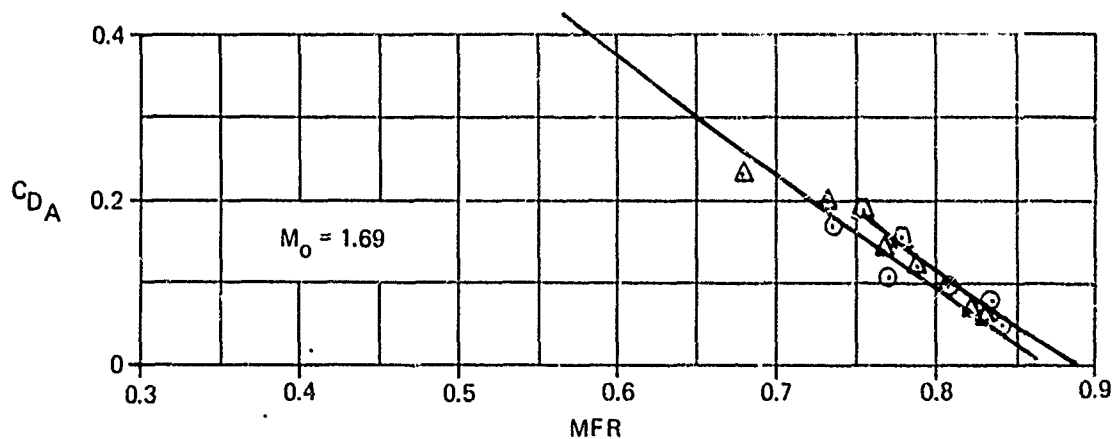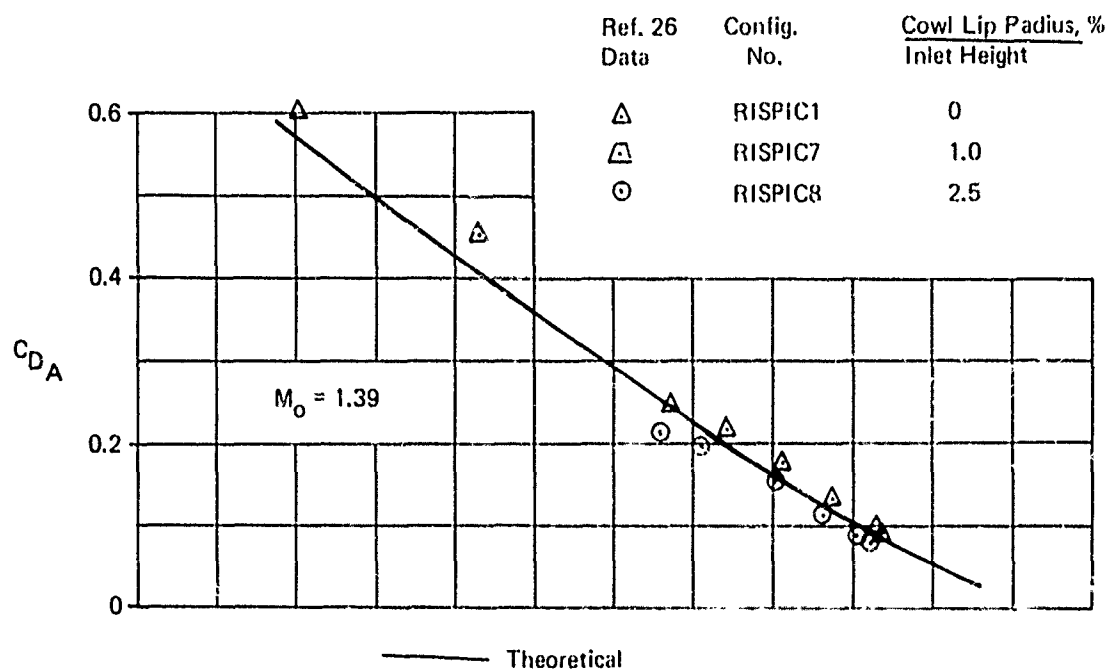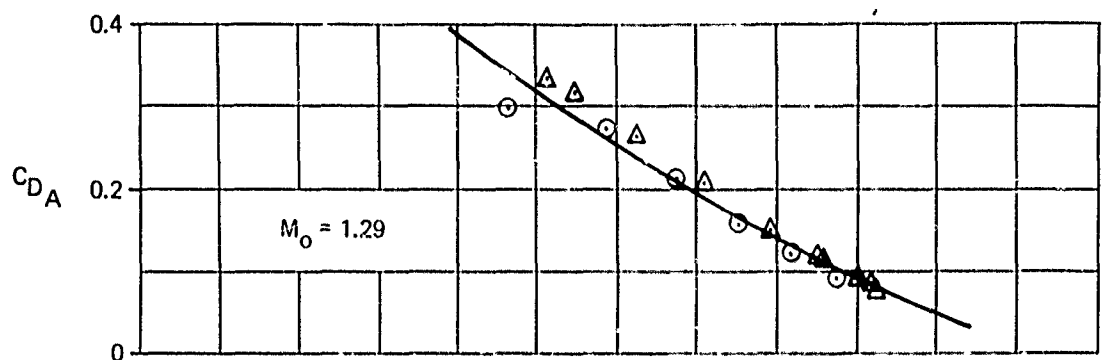
Figure 87 : COMPARISON OF THEORETICAL AND EXPERIMENTAL ADDITIVE DRAG
COEFFICIENTS, 2D INLETS, 5° RAMP, SWEPT SIDE PLATES

115
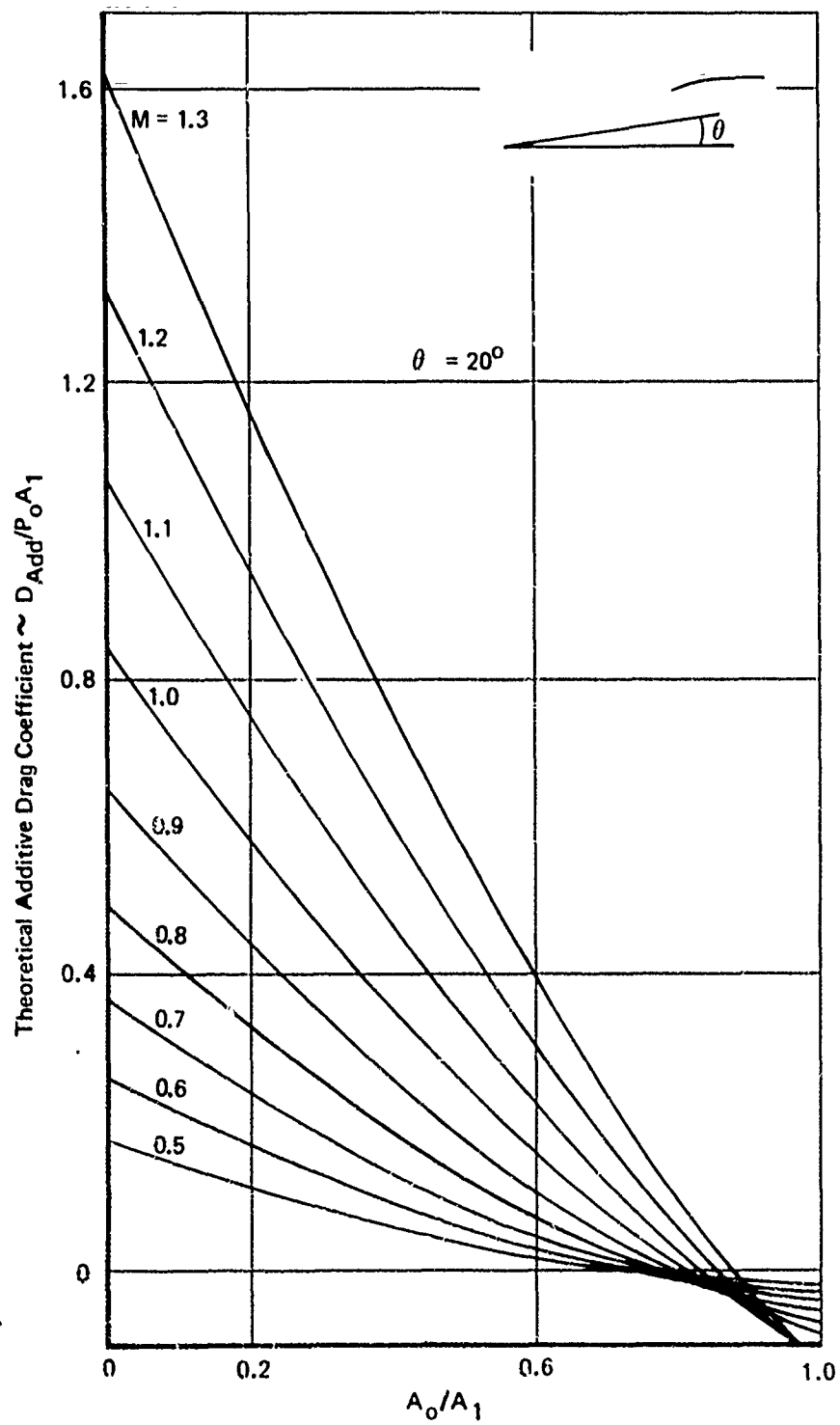
Figure 88: *THEORETICAL ADDITIVE DRAG OF 2-D INLETS WITH θ = 20°*

116
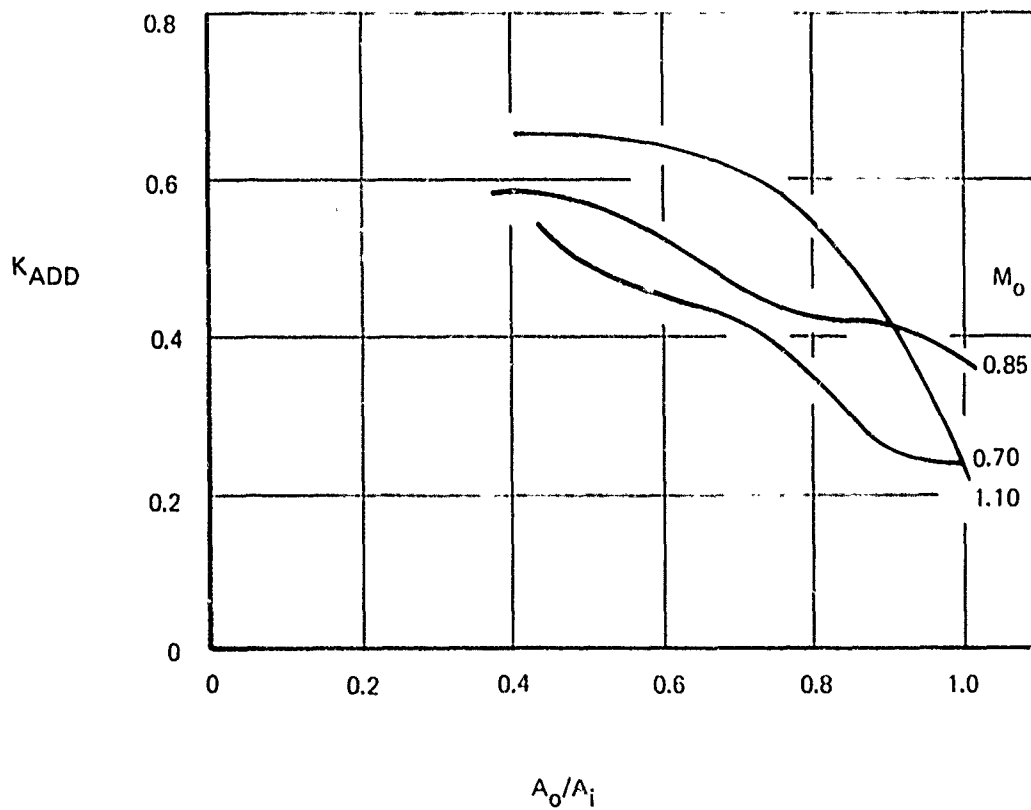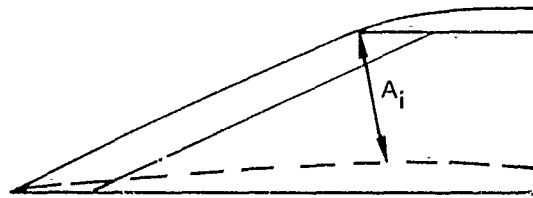
Figure 89 : K_{ADD} FACTORS FOR 2-D INLETS WITH FULL SIDEPLATES
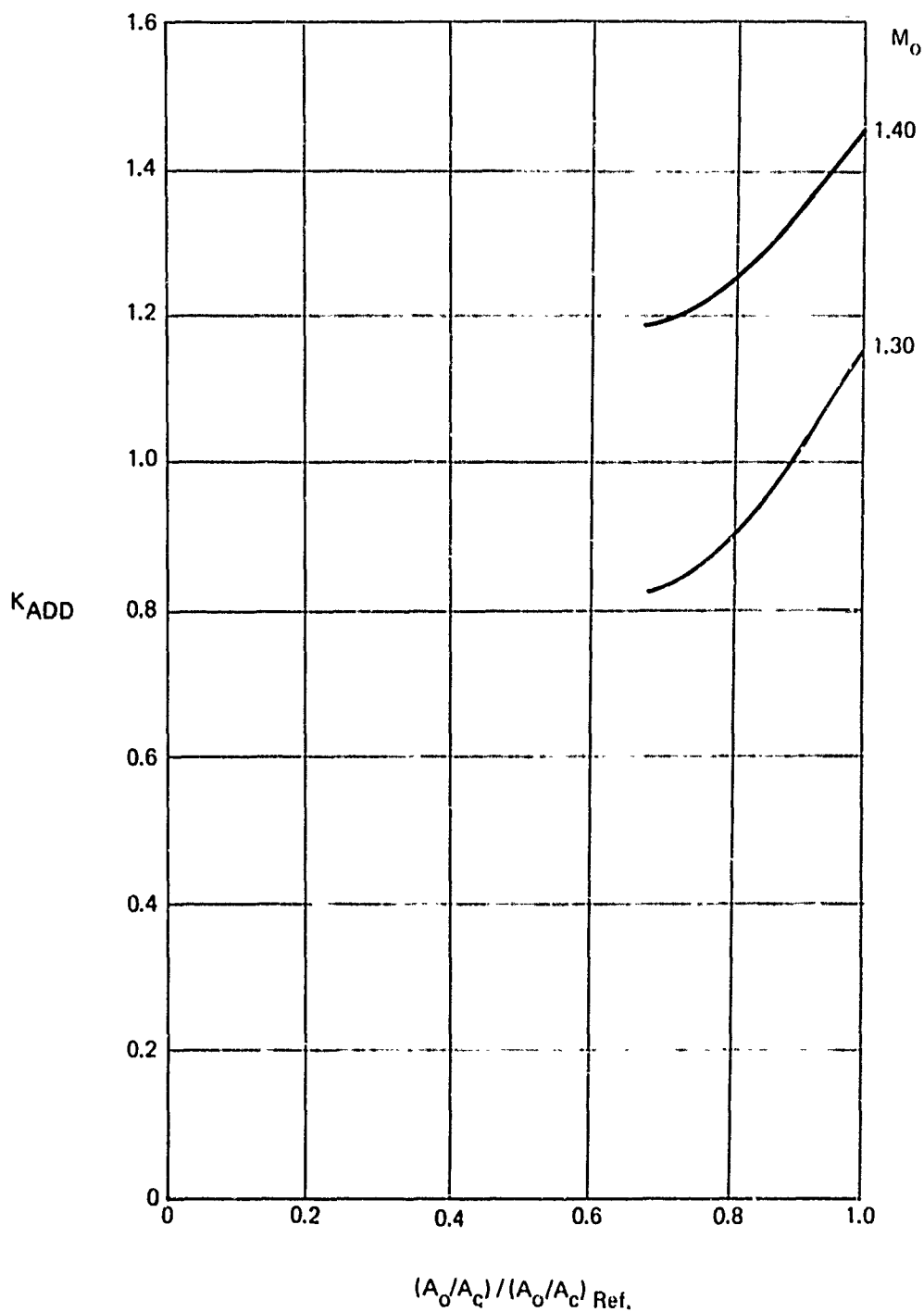
Figure 90 : K_{ADD} FACTORS FOR 2-D INLETS WITH FULL SIDEPLATES

118
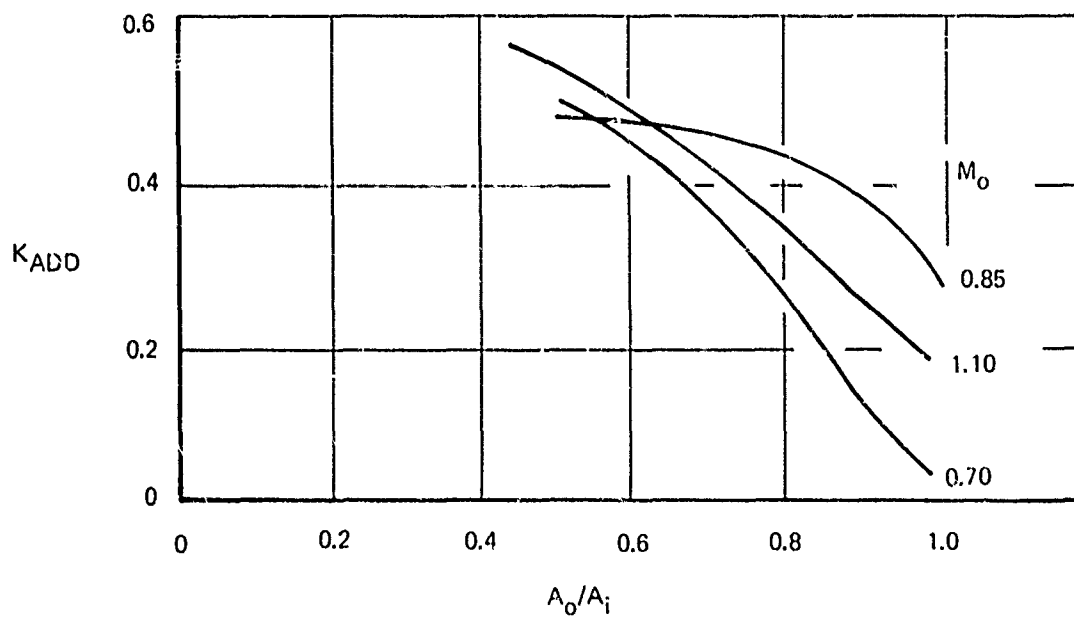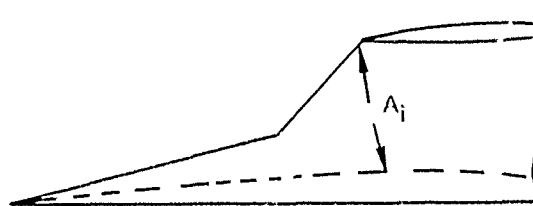
Figure 91 : K_{ADD} FACTORS FOR 2-D INLETS WITH CUTBACK SIDEPLATES

119
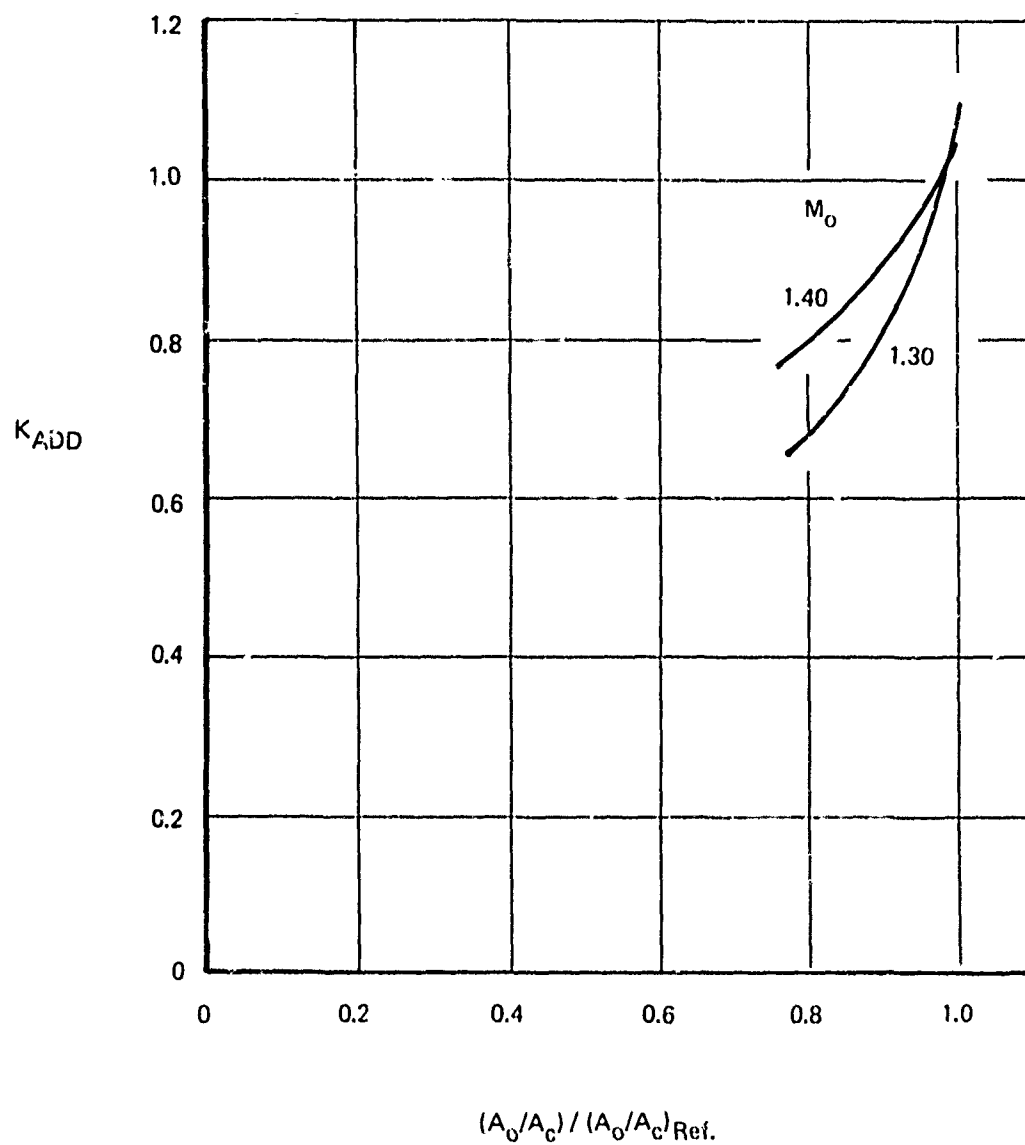
Figure 92: K_{ADD} FACTORS FOR 2-D INLETS WITH CUTBACK SIDEPLATES

120

Config	a^o	β^o	M_o	(Ao/Ac) Ref
RISPIC1	5°	5°	0.84	0.796
SP2	5°	5°	0.84	0.796
SP3	5°	5°	0.865	0.796
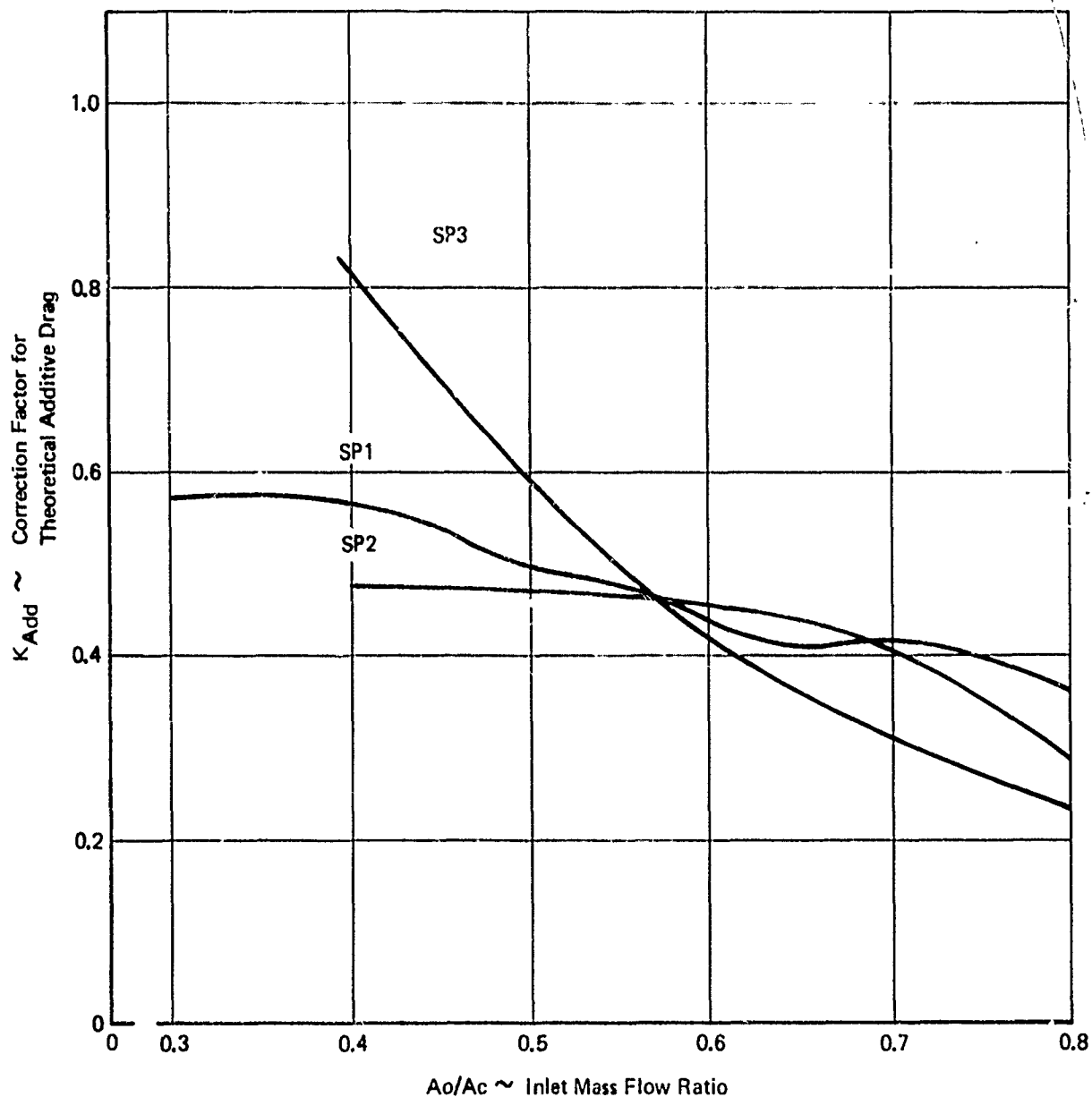
Figure 93: K_{ADD}, SEVERAL SIDE PLATES, M_o = 0.85

Fixed Bleed Exit

$$\frac{A_{\text{Bleed}}}{A_c} = 0.043$$

$$\frac{A_{\text{Slot}}}{A_c} = 0.07$$

$7°$

A_c
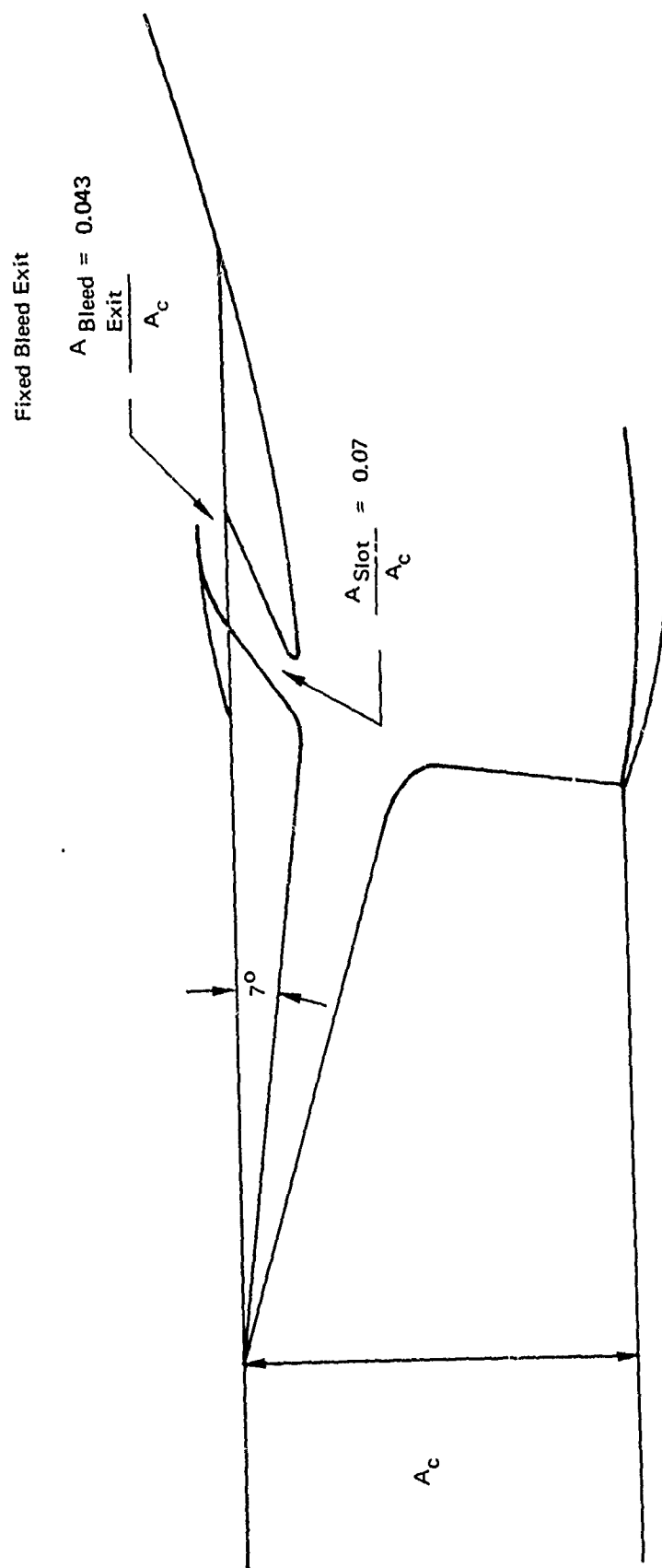
Figure 94: FIXED GEOMETRY INLET WITH THROAT SLOT BLEED
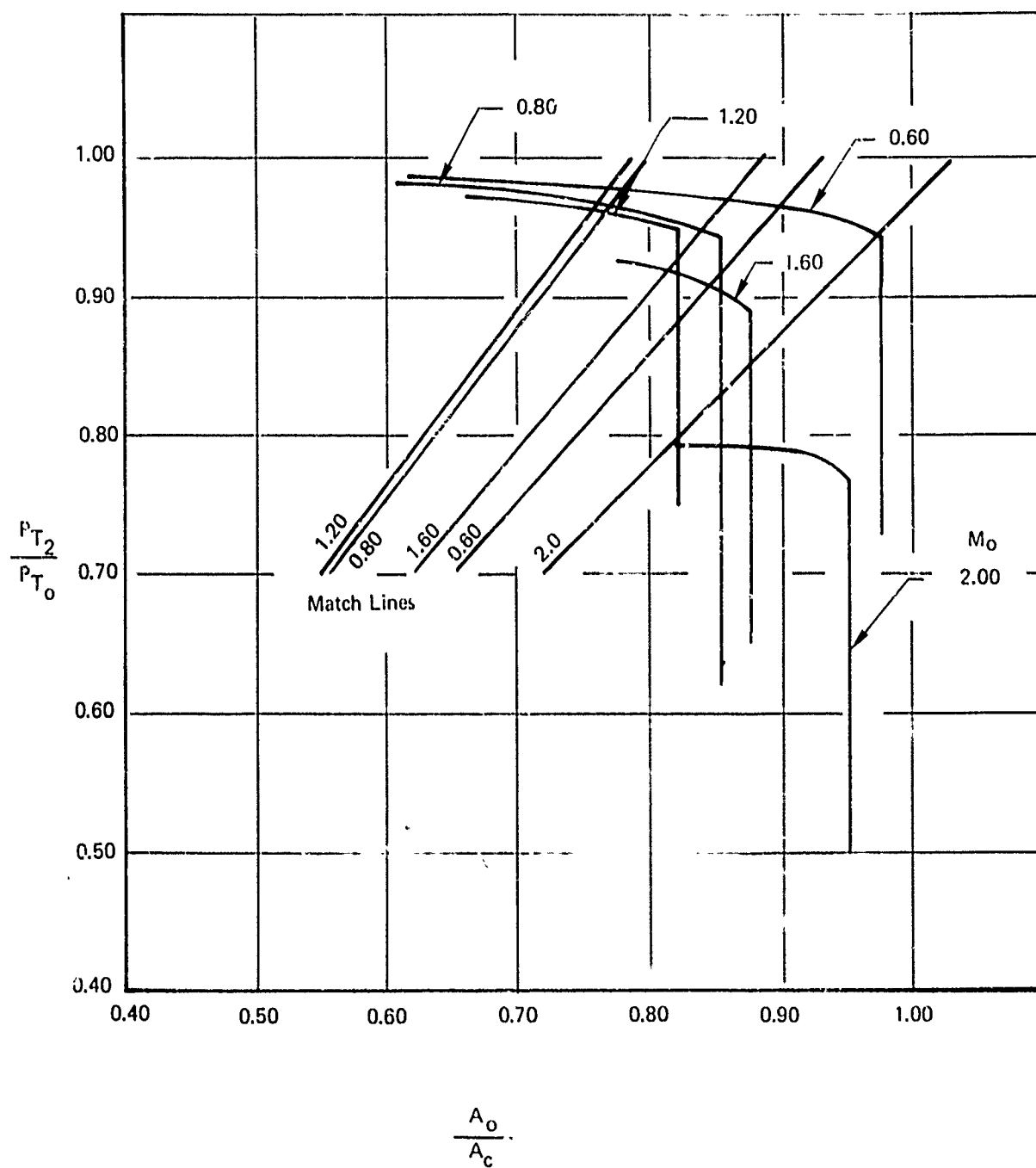
Figure 95 : RECOVERY VERSUS MASS FLOW

123
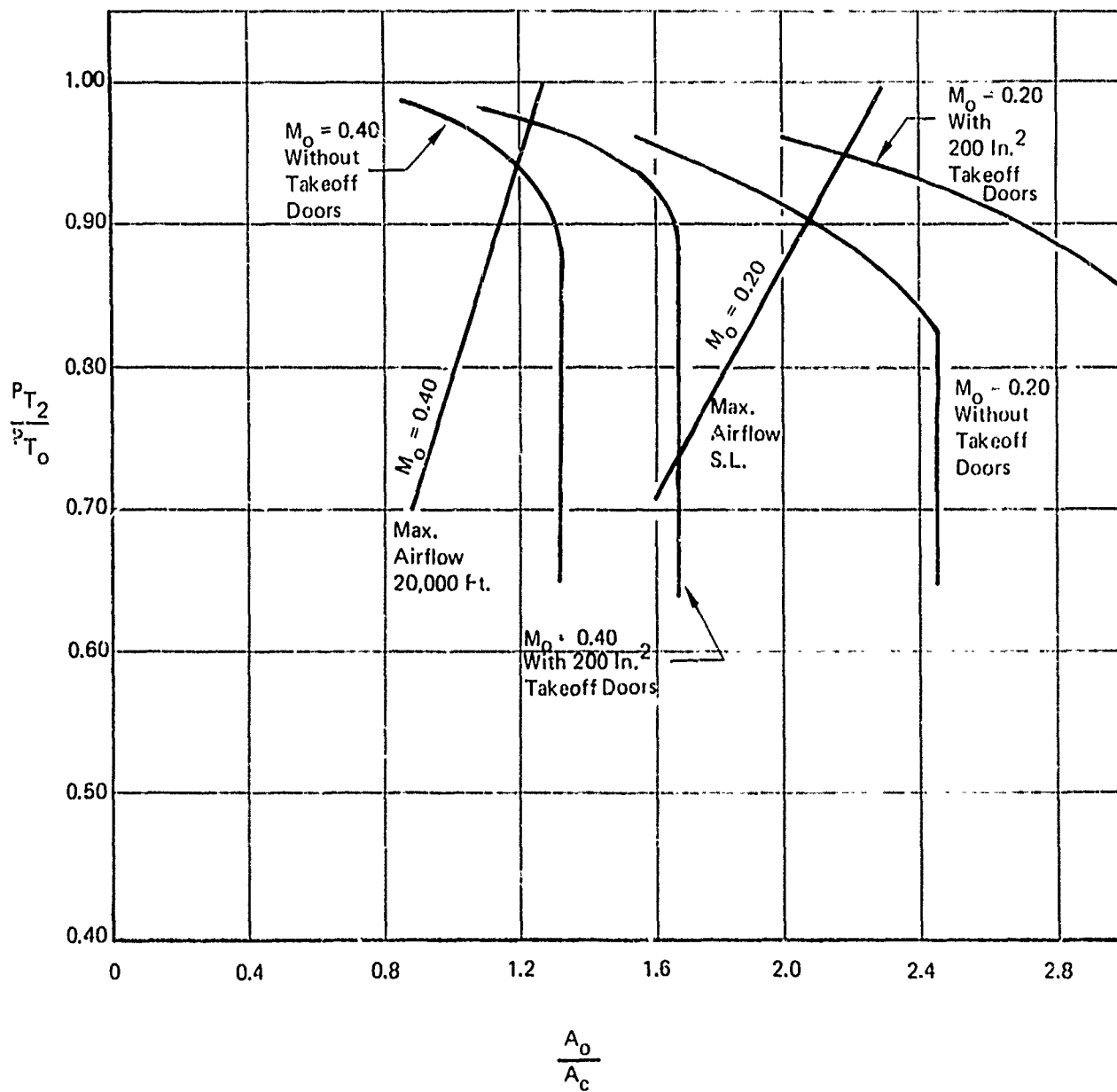
Figure 96 : RECOVERY VERSUS MASS FLOW (LOW SPEED)
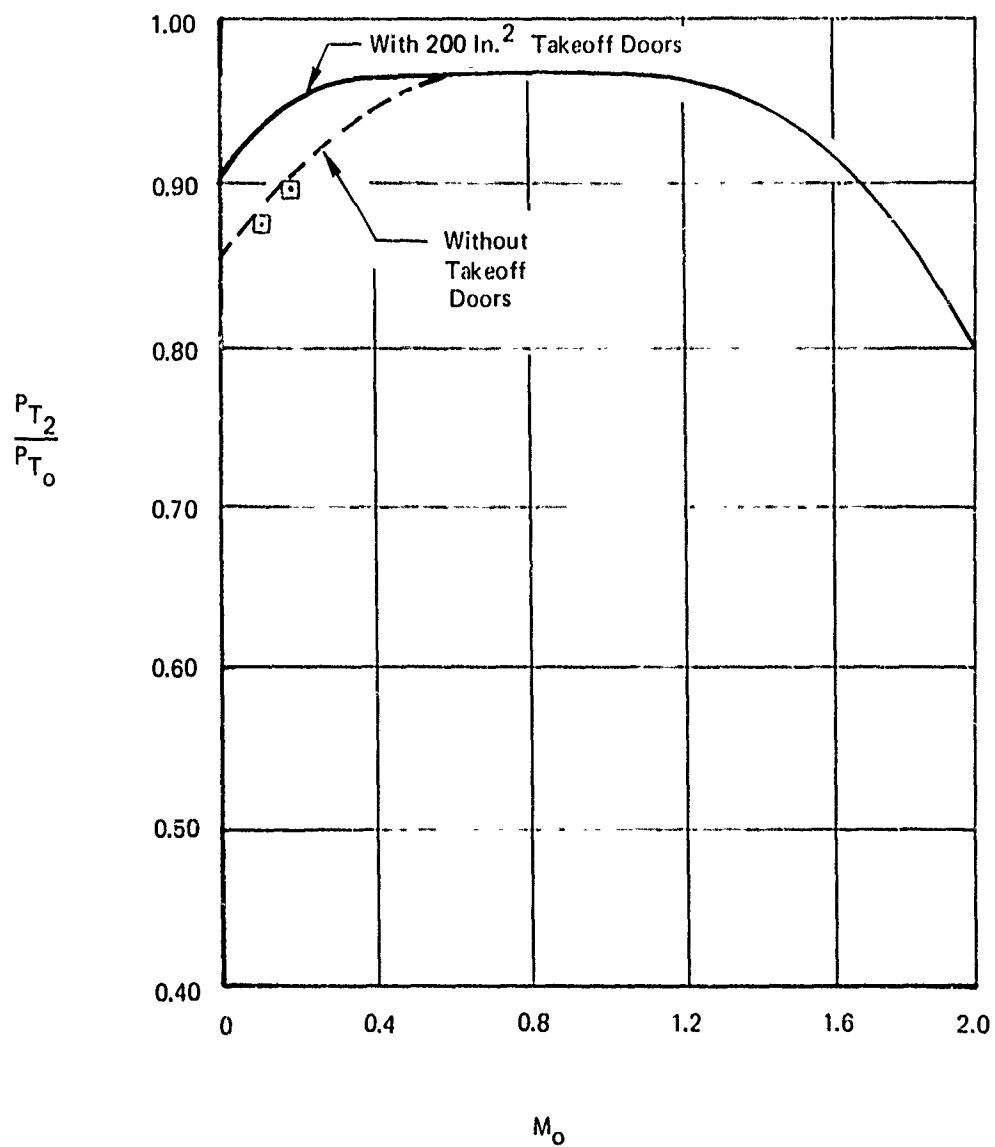
Figure 97 : MATCHED INLET RECOVERY

125
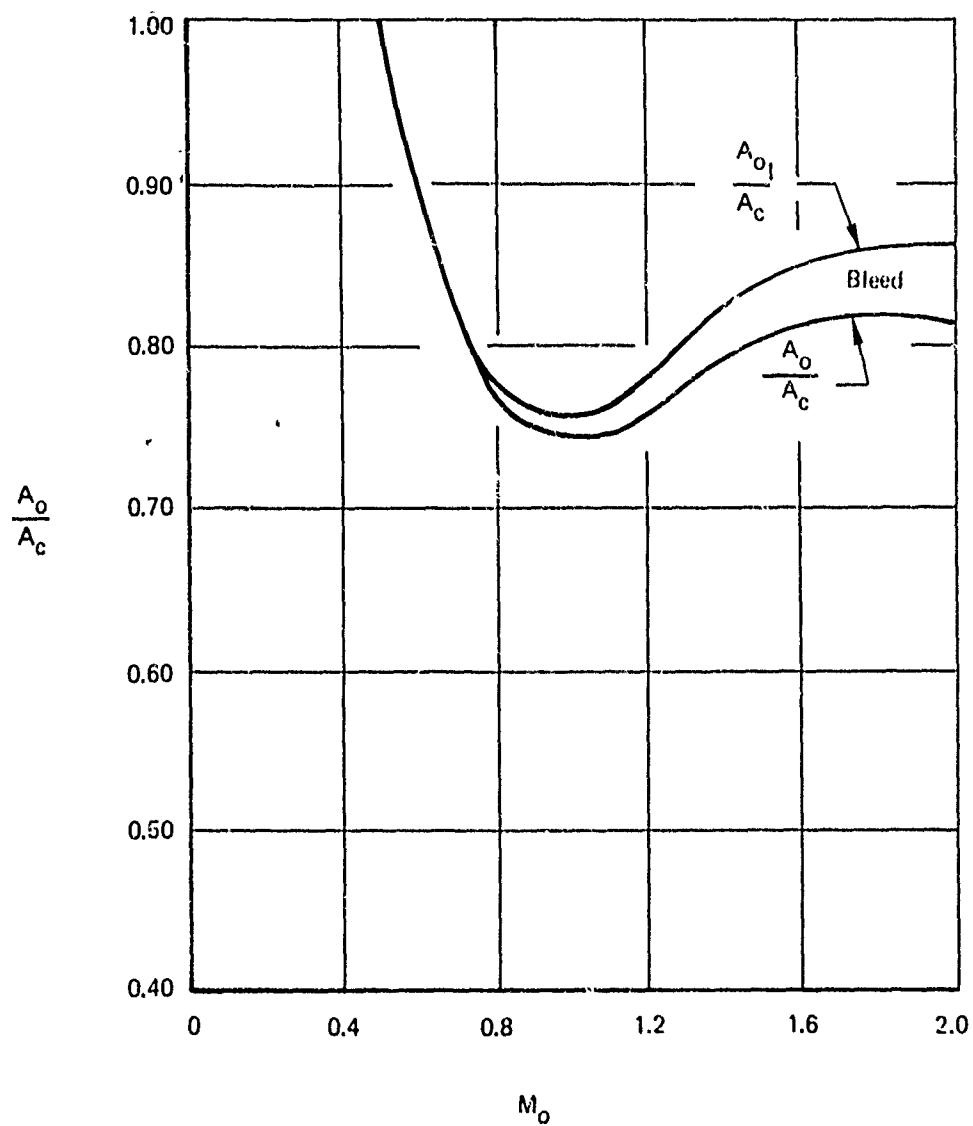
Figure 98 : MATCHED MASS FLOW

126

inlet airflow, and the lower curve, labeled A_0/A_C represents the net flow remaining after slot bleed is removed. The mass flow data shown are matched to the engine at max airflow condition. The matched bleed flow is also presented as a function of local Mach number in Figure 98. The variation of boundary layer bleed flow as a function of mass flow ratio is shown in Figure 105. The sharp drop-off in bleed flow that occurs at higher mass flow ratios for the $M_0 = 1.6$ and 2.0 conditions reflects the fact that the inlet is going supercritical (shock sucked downstream of the bleed slot). The gain in bleed flow as mass flow is decreased results from increased subsonic diffusion ahead of the bleed slot. This causes higher pressures and greater bleed flow. The effects of boundary layer on the pressure distributions have been accounted for in the analysis. These effects would cause the pressure distributions to propagate forward and would have a smoothing effect on the curves shown in Figure 105.

Figures 99 and 100 present the estimated buzz and distortion limits. The buzz mass flow ratio is based on data from F-107 tests. The F-107 inlet is roughly similar to the present design and was extensively tested for buzz.

Spillage drag data presented in Figure 101. The reference mass flow used is shown in Figure 102.

The bleed drag is presented in Figure 103. The variation in bleed flow, $A_{0_{BLC}}/A_C$, at each Mach number results from variations in main duct mass flow, which cause changes in inlet Mach number and in shock position. These changes result in increased pressures in the bleed slot as main duct mass flow is reduced and reduced pressure as mass flow is increased.

The increased total pressure recovery in the bleed slot reduces the bleed drag for a given amount of airflow. This effect causes the bleed drag coefficient to level off and decrease slightly as bleed flow increases.

4.1.2.2 AXISYMMETRIC

The basic features of the inlet configuration are shown in Figure 111. The side mounted half-round inlets have translating 25 degrees half-angle cone centerbodies. The movable centerbody is used to provide a large throat area (1740 in.^{2}) for low speed operation and, by translating forward, can also provide shock-on-lip for high recovery, low drag supersonic operation at Mach 1.60 ($A_C = 1860$ in.^{2}).
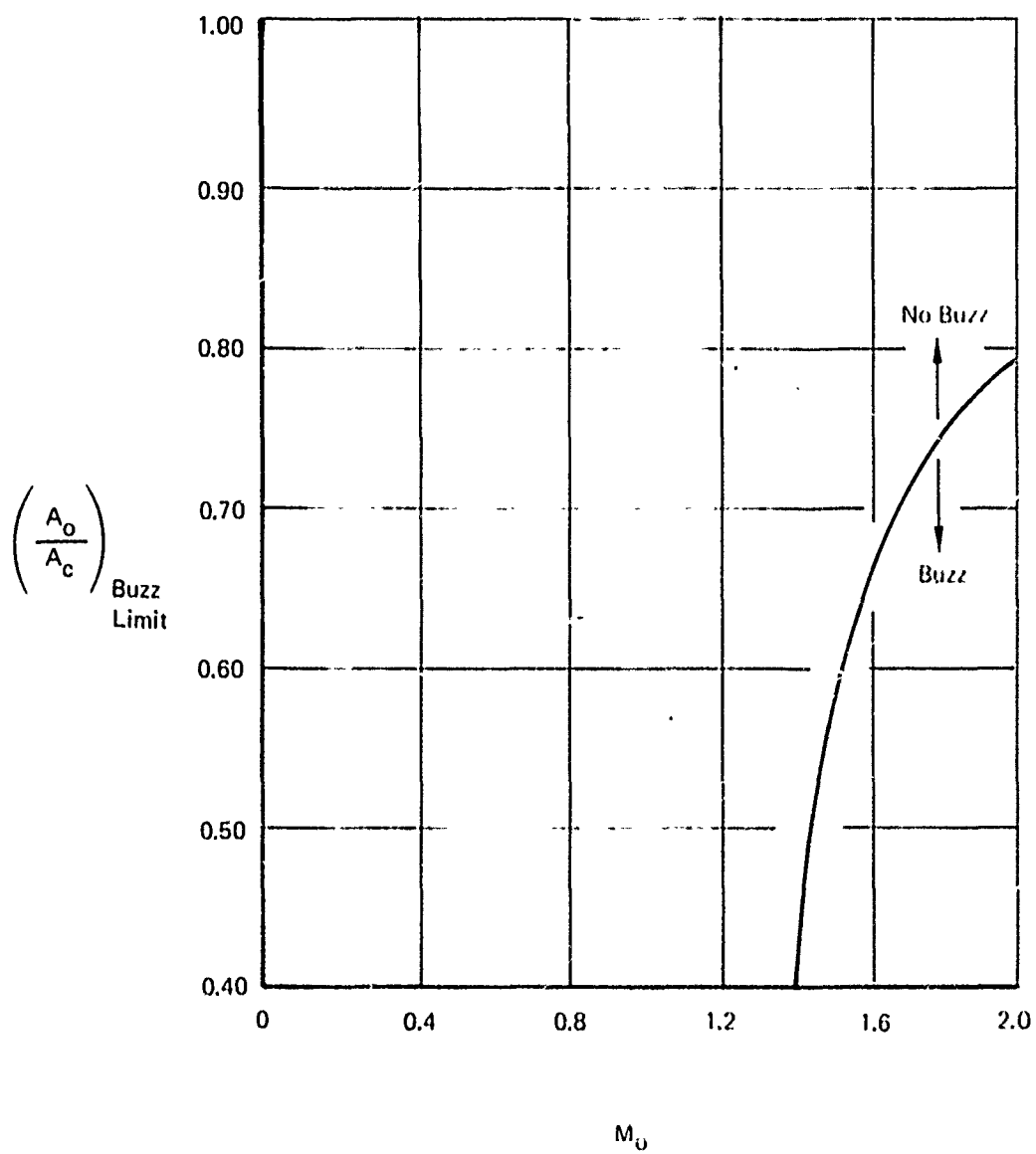
Figure 99 : BUZZ LIMIT

128
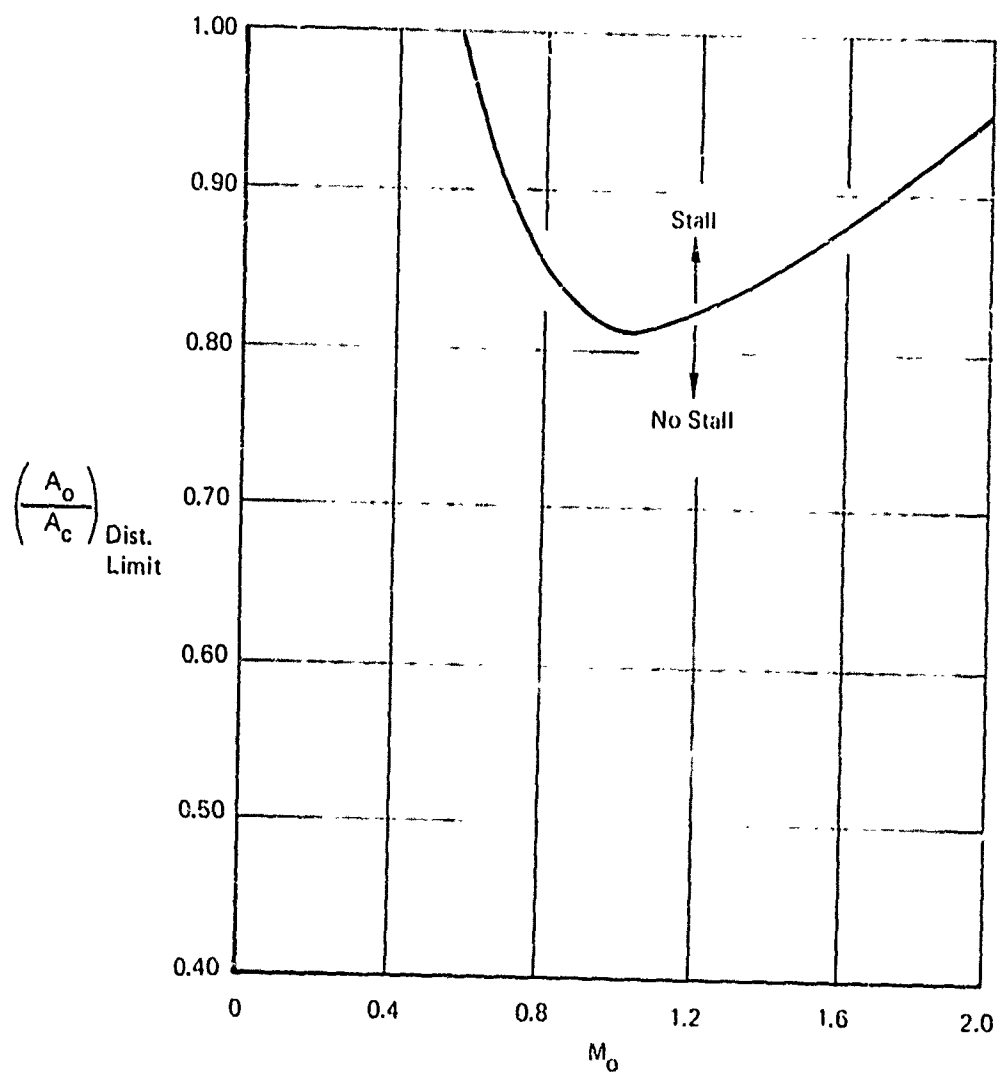
Figure 100 : DISTORTION LIMIT

129
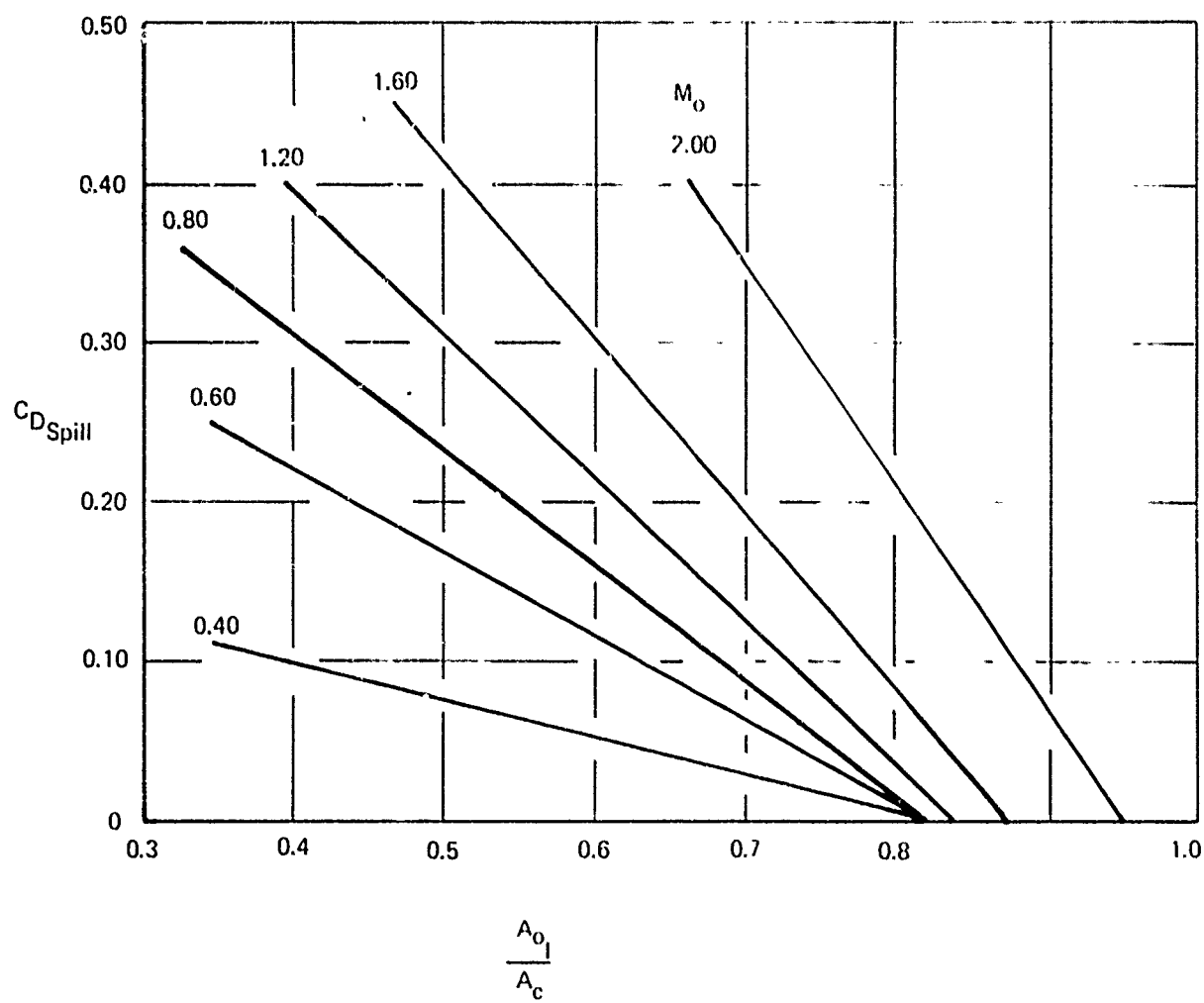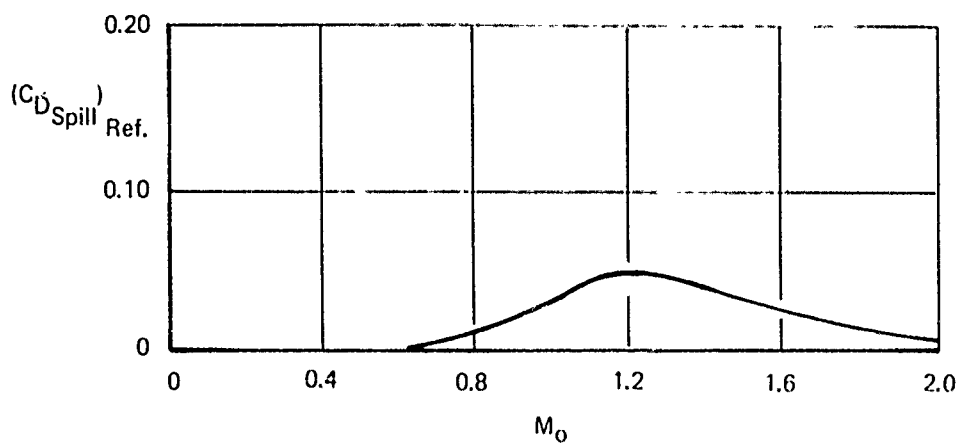
Figure 101 : SPILLAGE DRAG

130
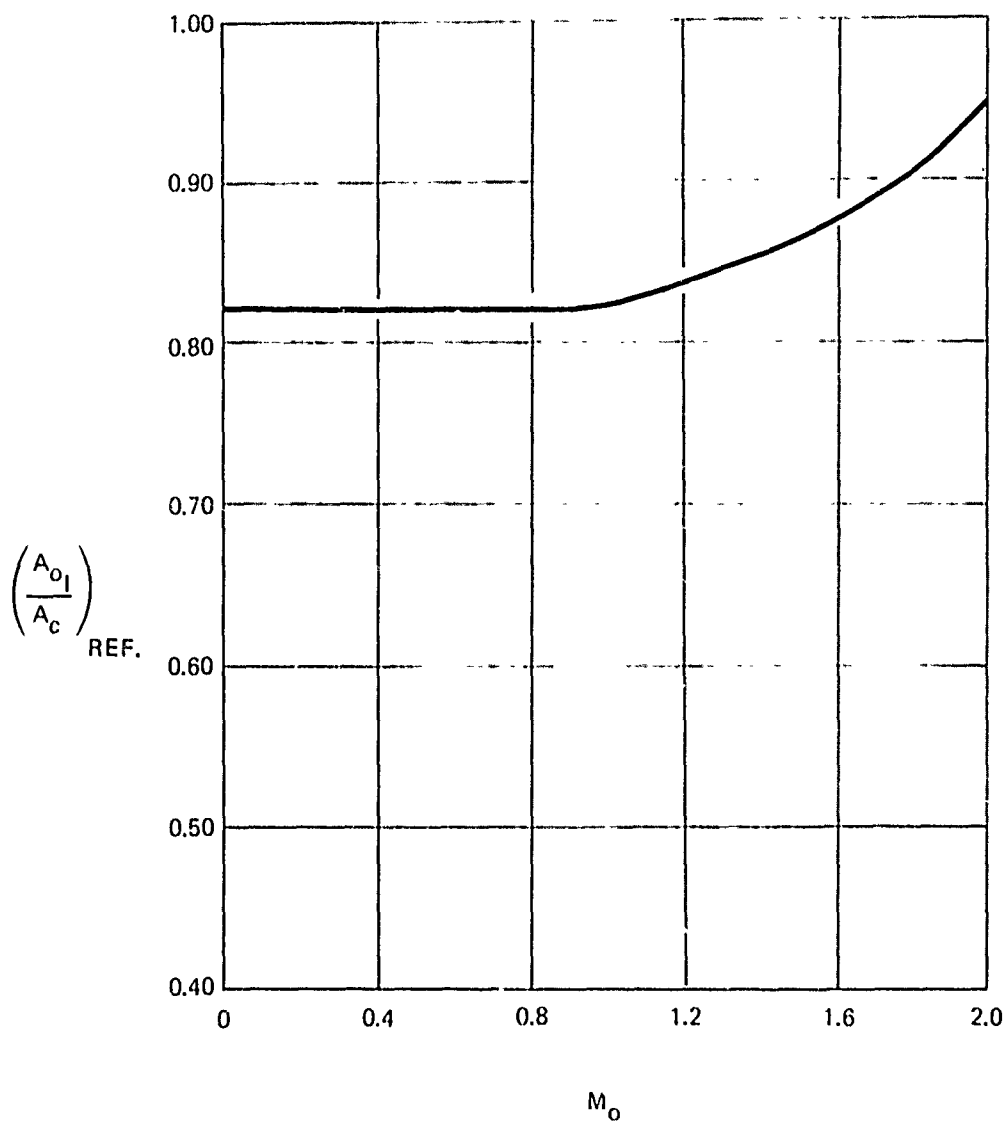
Figure 102 : REFERENCE MASS FLOW
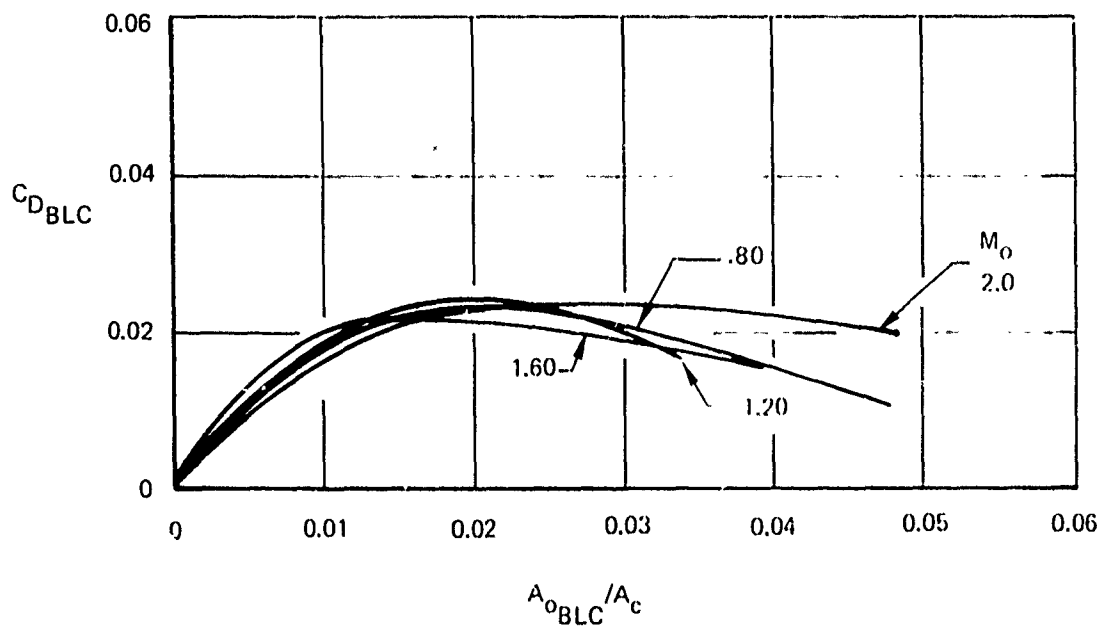
Figure 103:   BOUNDARY LAYER BLEED DRAG
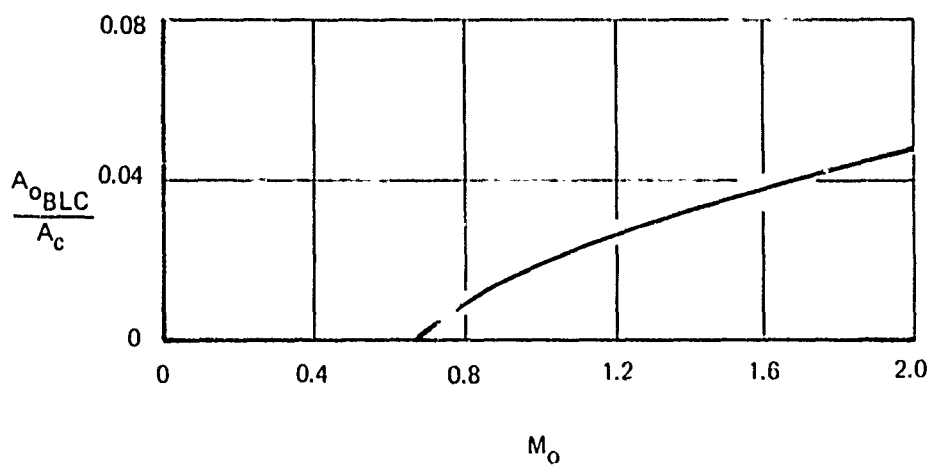
Figure 104:   BOUNDARY LAYER MASS FLOW

132
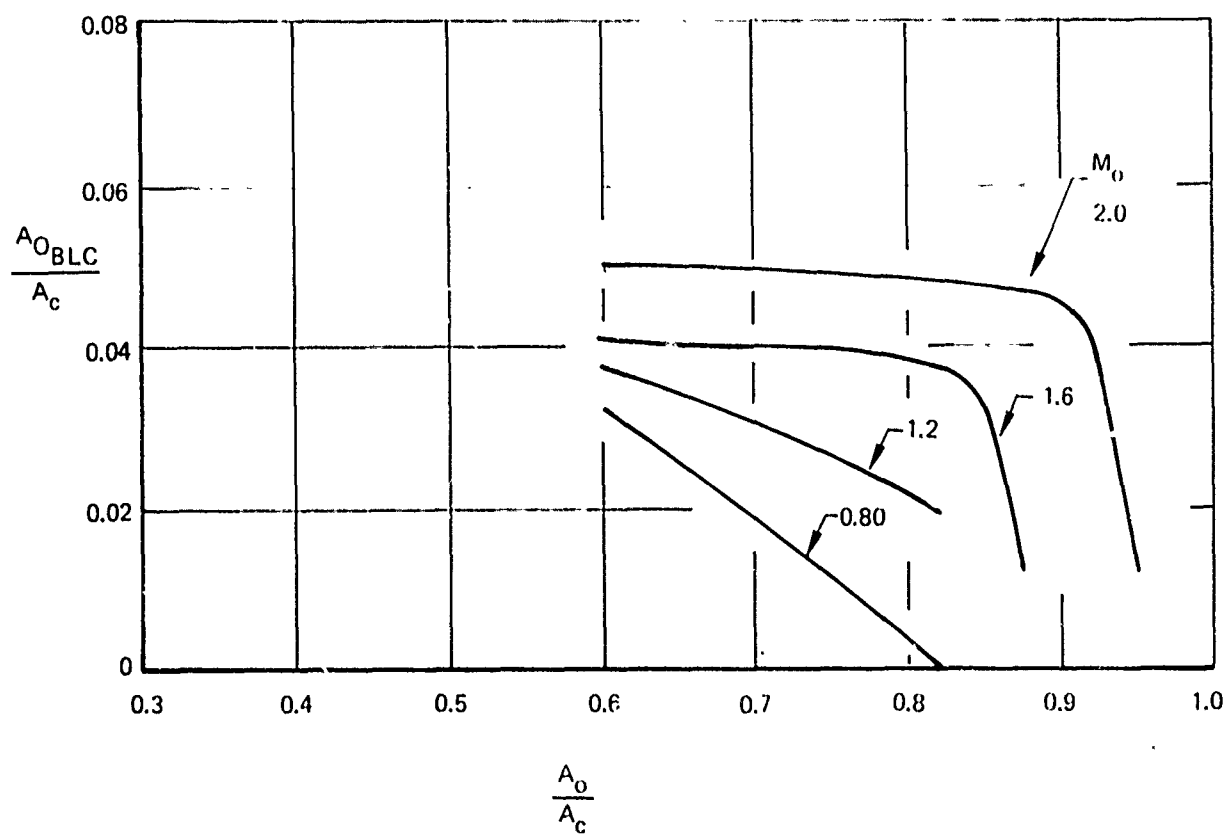
Figure 105 :   BLEED MASS FLOW

133
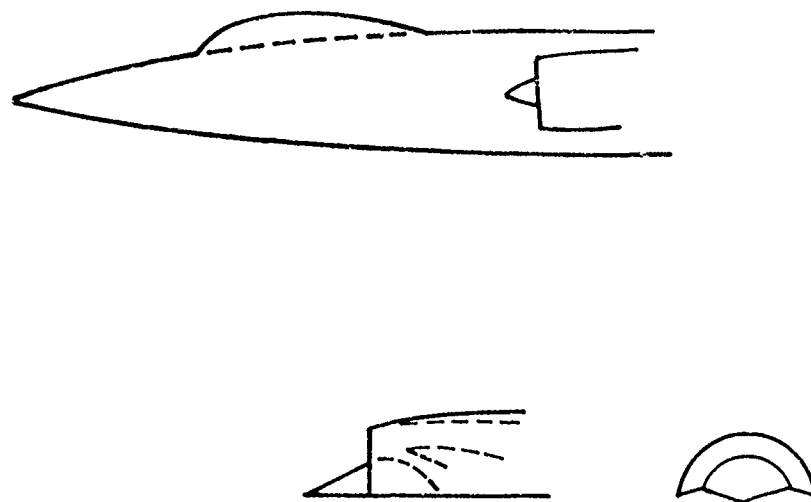
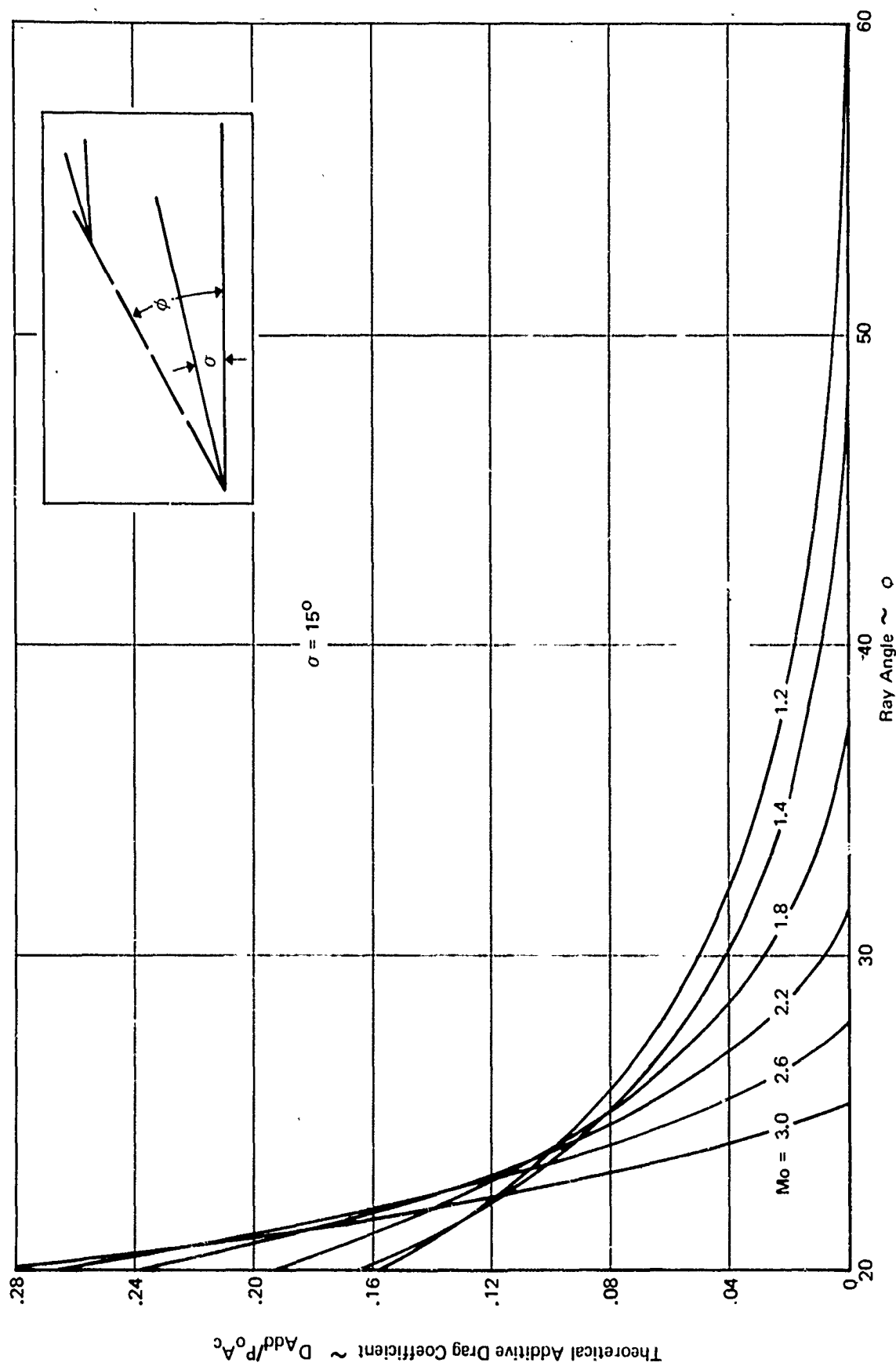Figure 106: TWO-SHOCK, EXTERNAL COMPRESSION, FIXED GEOMETRY INLET

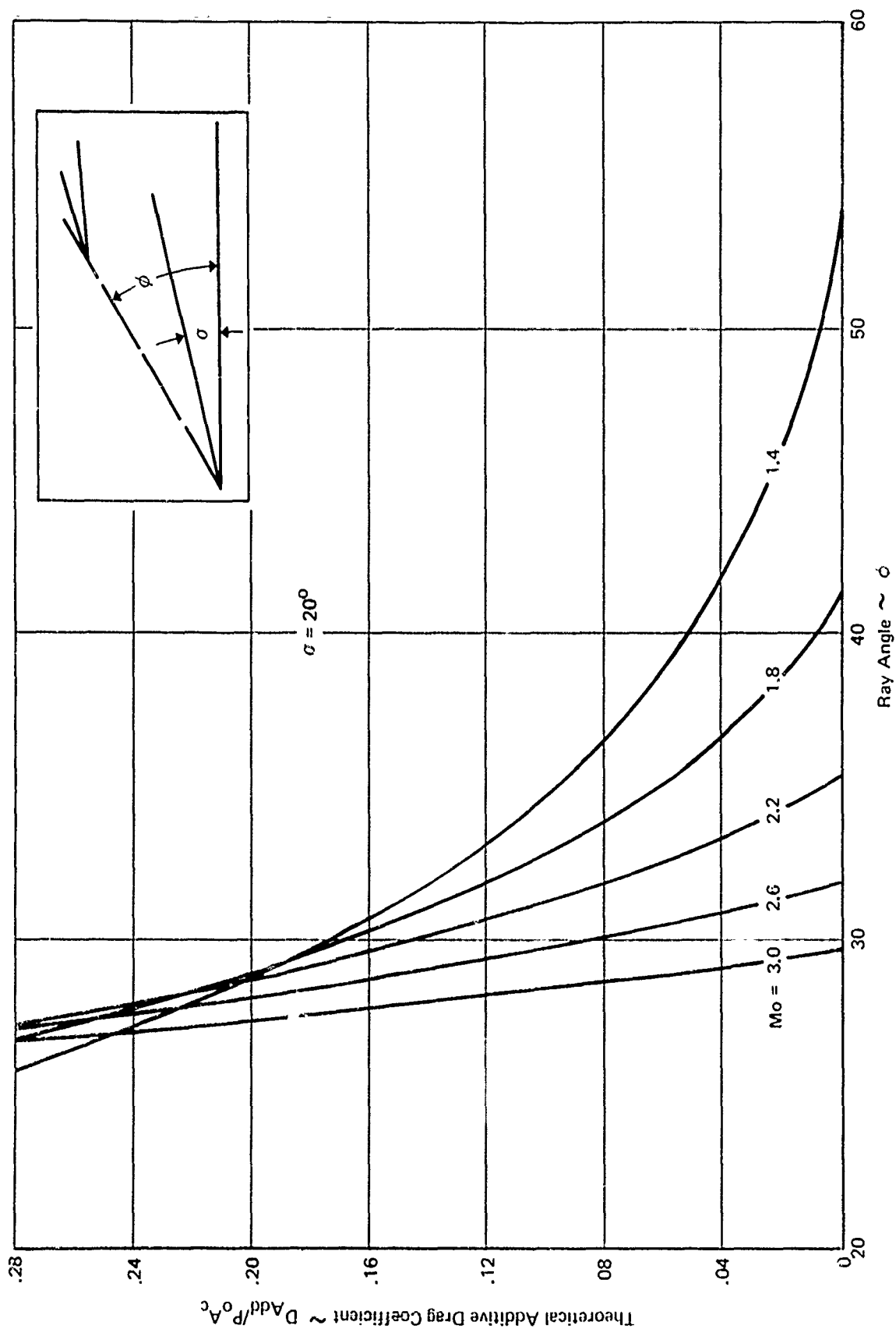Figure 107: THEORETICAL ADDITIVE DRAG OF SPIKE INLETS — CONE HALF ANGLE = 15°

135

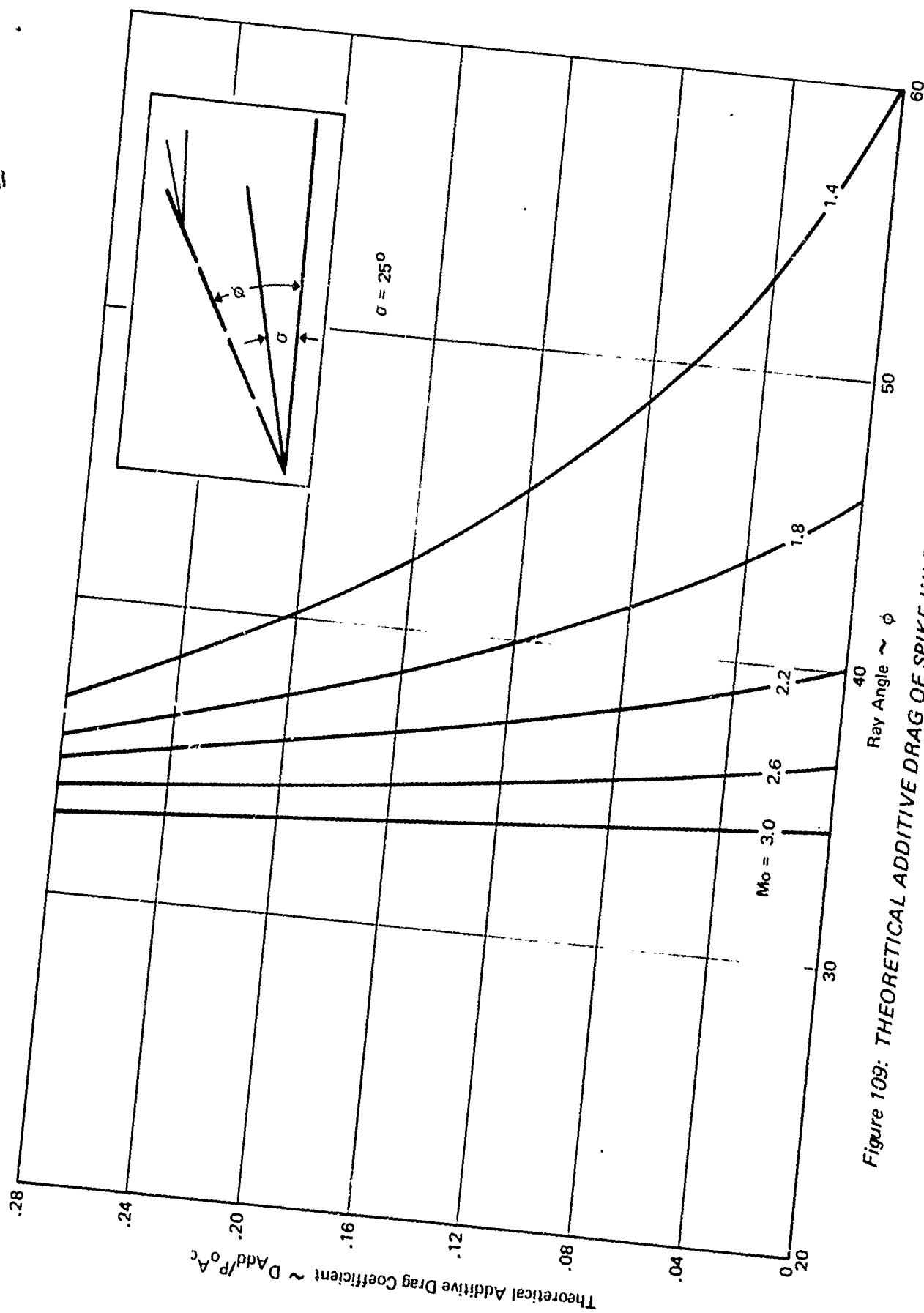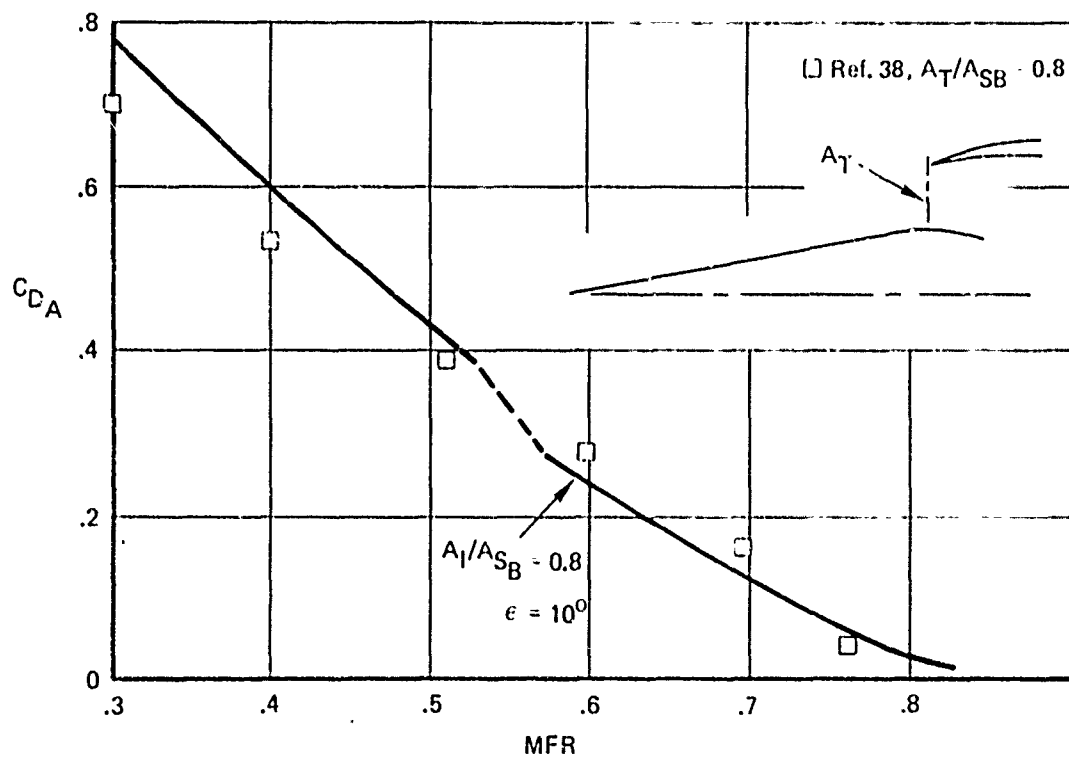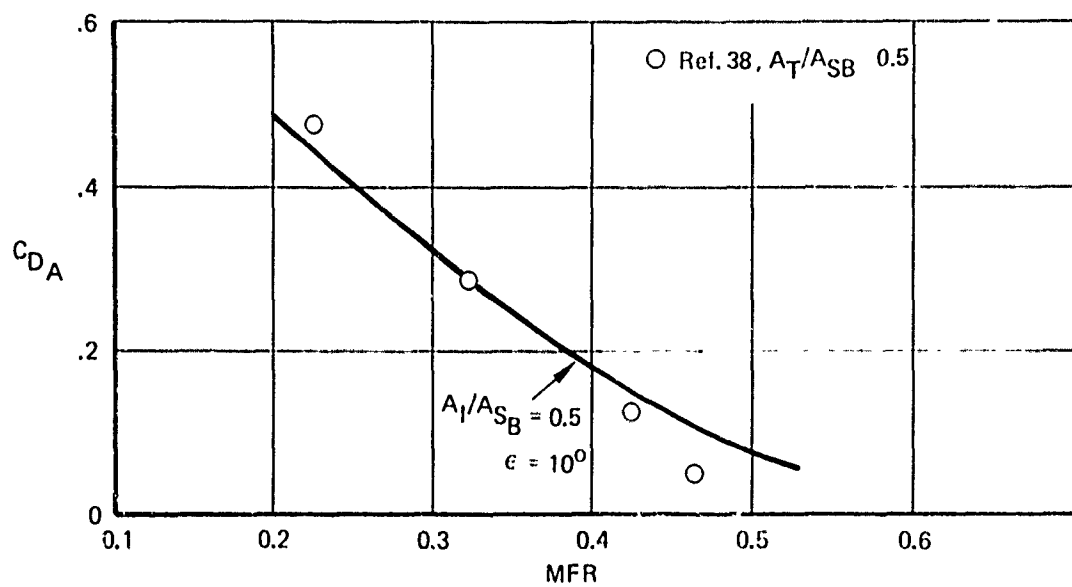Figure 108: THEORETICAL ADDITIVE DRAG OF SPIKE INLETS ~ CONE HALF ANGLE = 20°

136

Figure 109: THEORETICAL ADDITIVE DRAG OF SPIKE INLETS ~ CONE HALF ANGLE = 25°

Figure 110: COMPARISON OF THEORETICAL AND EXPERIMENTAL ADDITIVE DRAG COEFFICIENTS, $M_0 = 1.26$, CONE HALF-ANGLE = 10^0

A moderately blunted, fixed cowl lip and large (860 in.^{2})
blow-in doors are used to achieve high total pressure
recovery and low distortion at static and low-speed
conditions.

No boundary layer bleed or bypass are used. In the normal
process of developing an inlet of this type, wind tunnel
tests would be conducted to optimize the inlet configuration.
If these tests show that the addition of internal boundary
layer bleed is necessary, no more than 1 - 2% of inlet air
would be required for bleed. The addition of this bleed
would not significantly change the configuration.

Estimated inlet performance characteristics are presented in
Figures 111 through 125 in the format required by the PITAP
program. Each data map shown is entered into the computer
program as a Table.

As shown in Figure 112, the local Mach number was assumed to
be equal to free stream Mach number.

The recovery-mass flow "canes" are presented in Figure 113
for a range of Mach numbers from .60 to 1.60.

Matched recovery as a function of local inlet Mach number
is presented in Figure 114 and the corresponding inlet mass
flow is presented in Figure 115.

Buzz and distortion limits for this inlet configuration
are shown in Figure 116 and 117.

Spillage drag as a function of inlet mass flow ratio and
local Mach number are shown in Figure 118. The reference
mass flow of Figure 120 was used in calculating the spillage
drags of Figure 118. The spillage drag shown in Figure 118
represents the drag at mass flow ratios less than the
reference mass flow is shown in Figure 119. This reference
drag normally is included in the airplane drag.

Figures 121, 122, 123, 124 and 125 are included for the sake
of completeness only. Since no bypass or bleed are used,
the drag and mass flow of these items are zero for all flight
conditions.

4.1.3 VARIABLE-GEOMETRY, FOUR-SHOCK INLETS

4.1.3.1 EXTERNAL COMPRESSION

The inlet geometry details are shown in Figure 137. The
inlet is designed to have shock-on-lip at Mach 2.5 but its
capture area is sized to match engine demand at Mach 2.2,

$A_c = 1,860$ In.^{2} Total for 2 Sides

$A_{T_{Max}} = 1,740$ IN.^{2} Total for 2 Sides In.^{2}

Take-Off
Doors (Throat Area = 860 In.^{2} Total)

25° Half-Angle Cone
Translating Spike

Top View

Side View
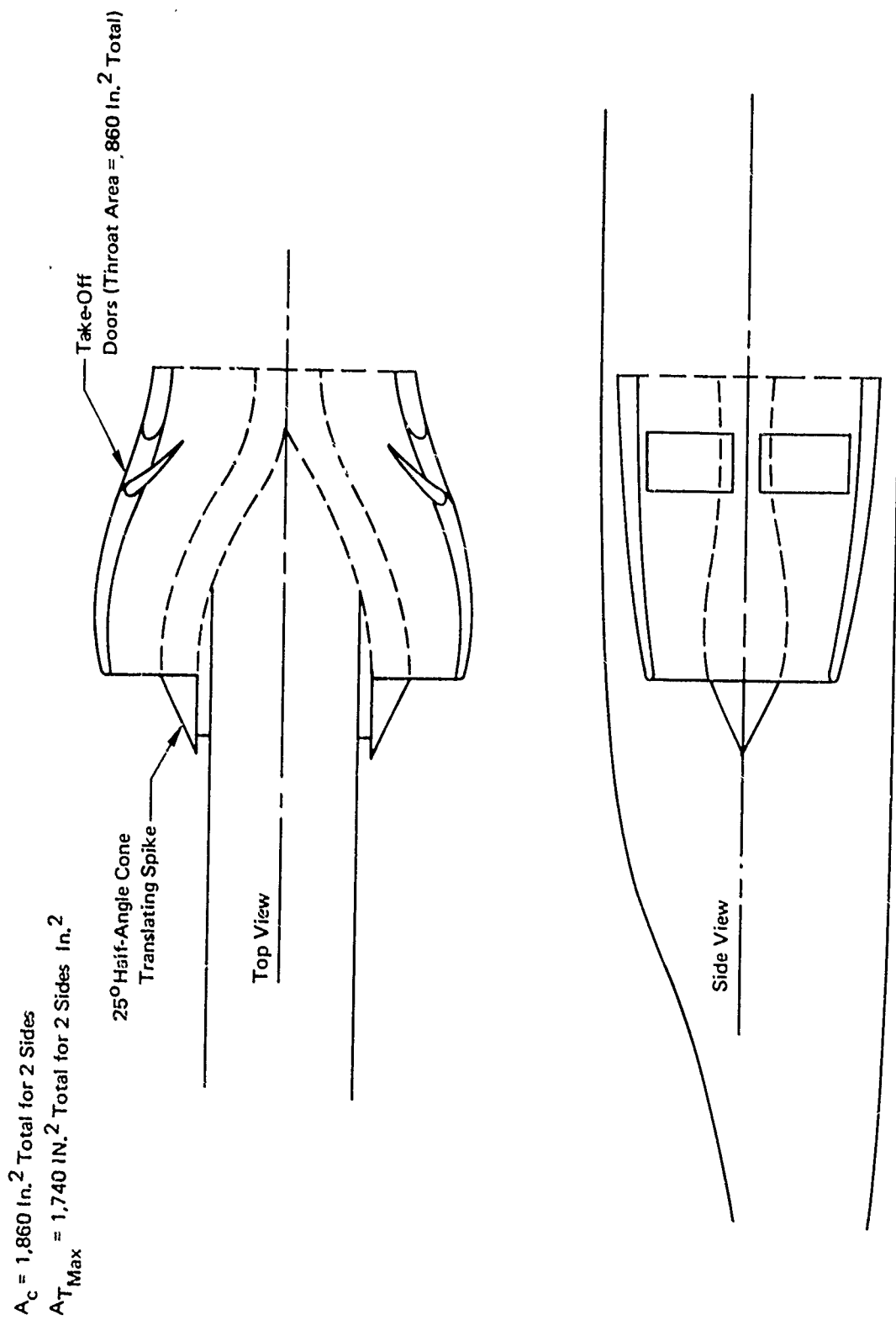
Figure 111: SUPERSONIC (M = 1.60) V/STOL INLET

140
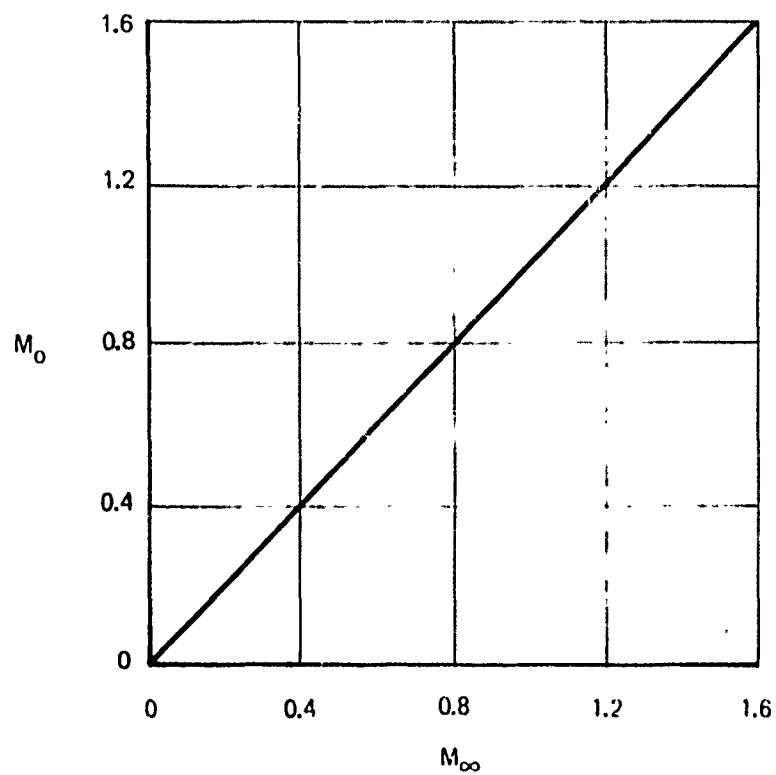
Figure 112: LOCAL MACH NUMBER

141
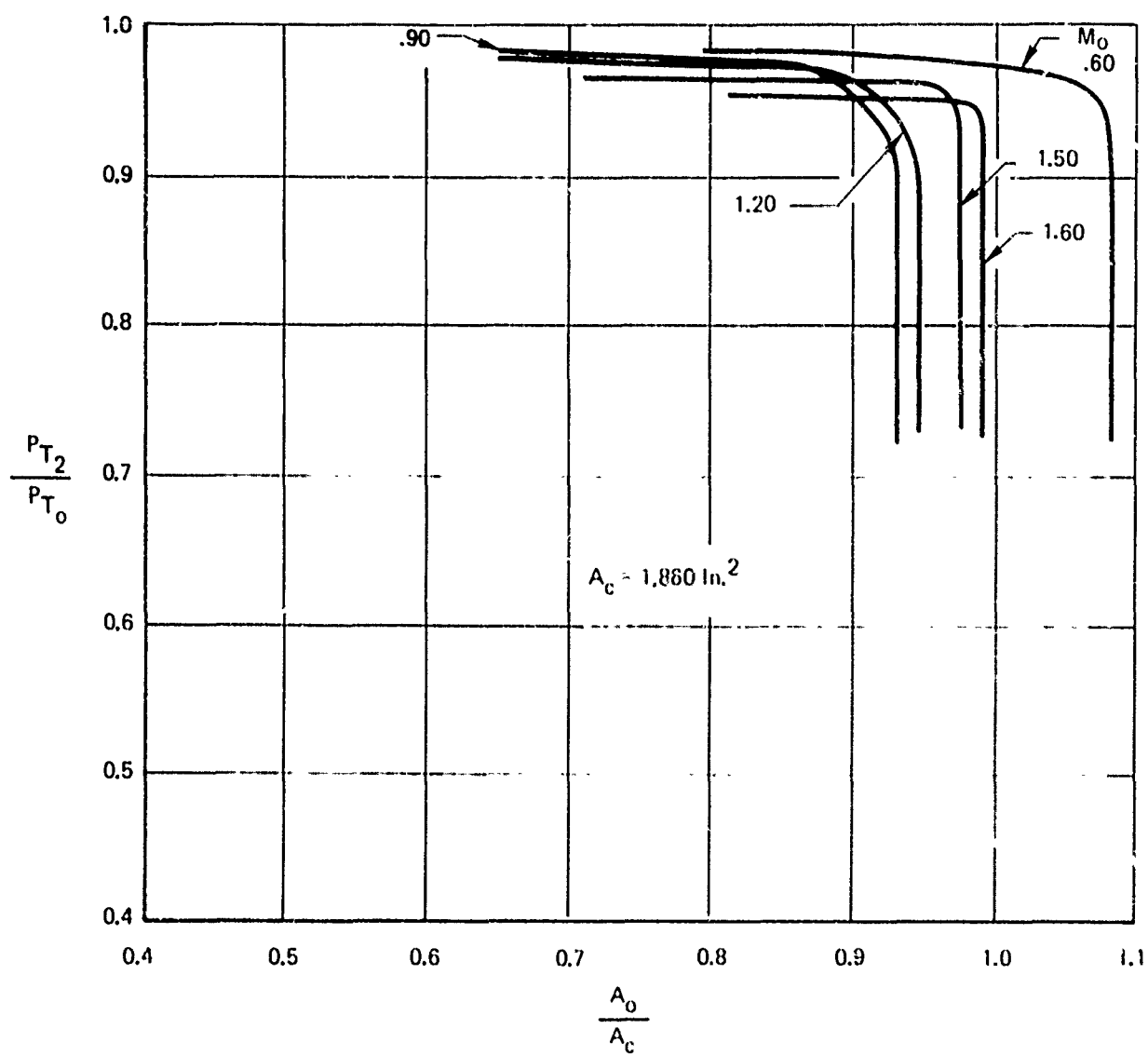
Figure 113: RECOVERY VS MASS FLOW
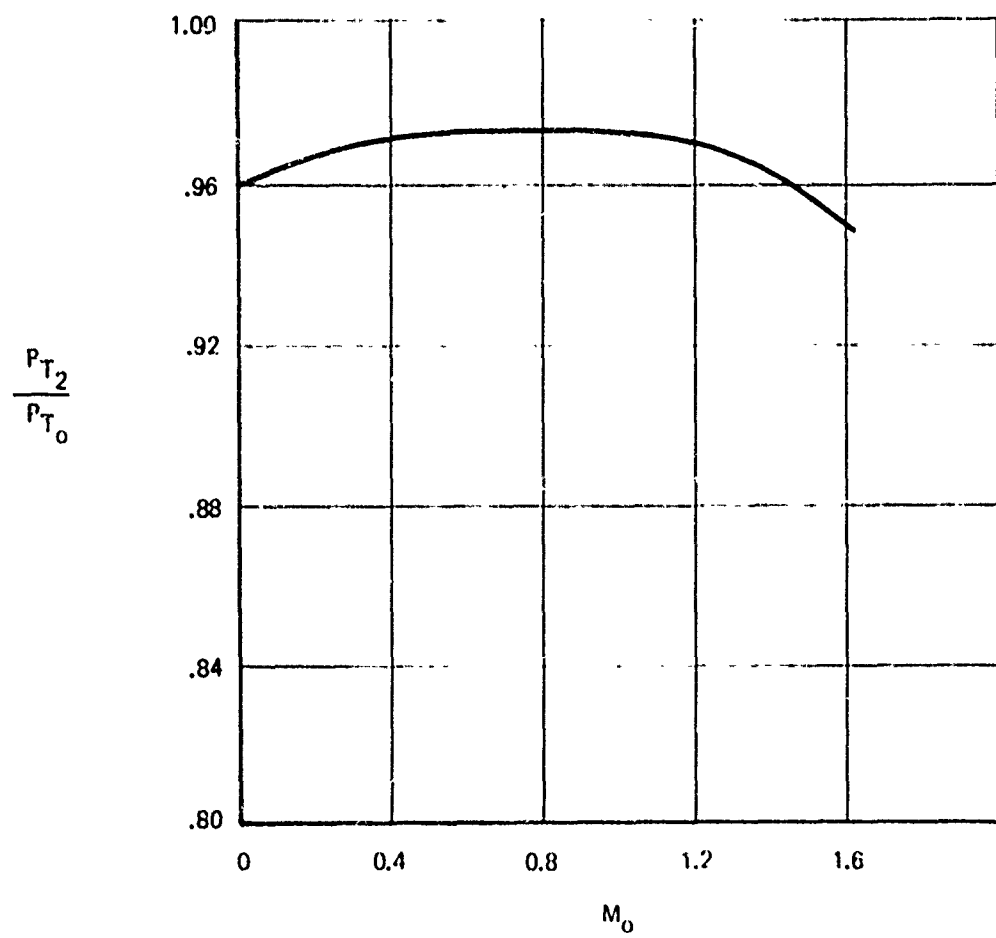
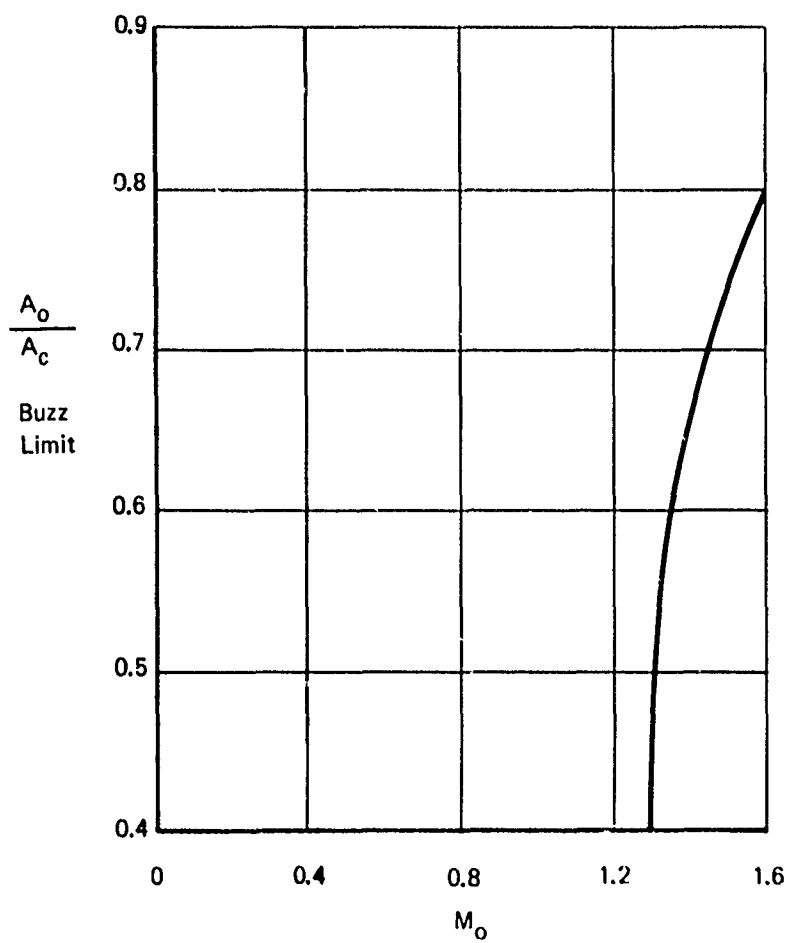Figure 114: RECOVERY VS M_O

143
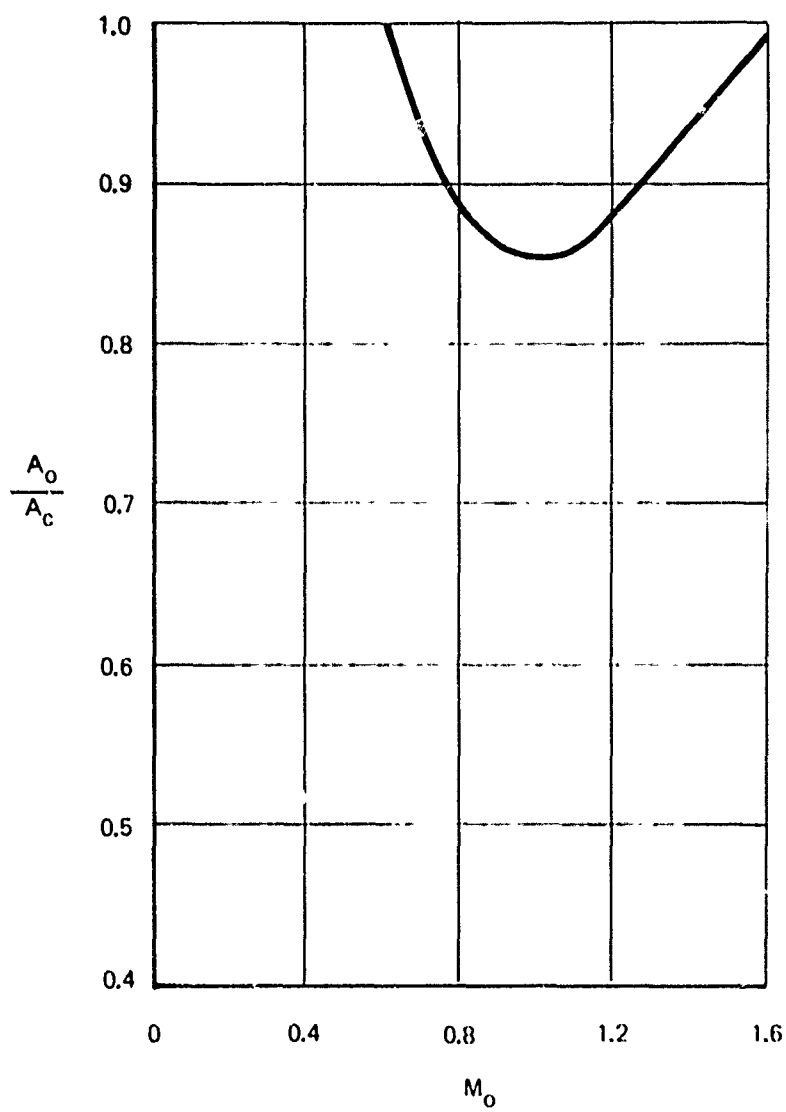
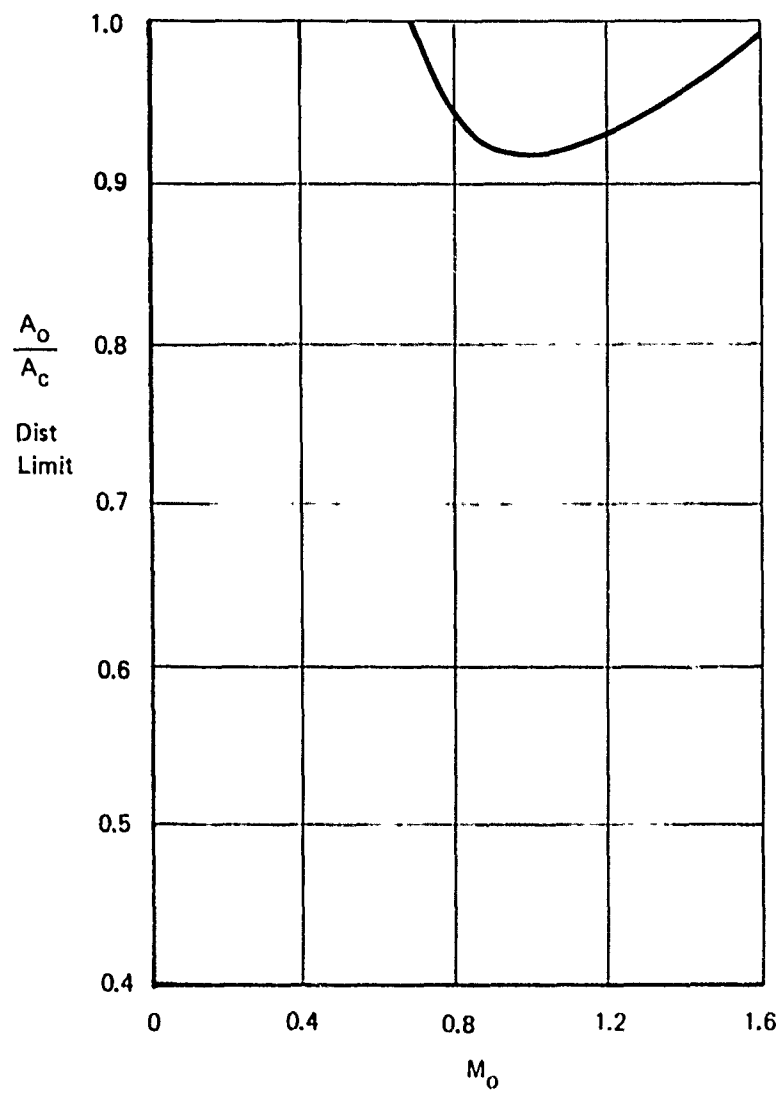Figure 115: MASS FLOW VS M_O

144
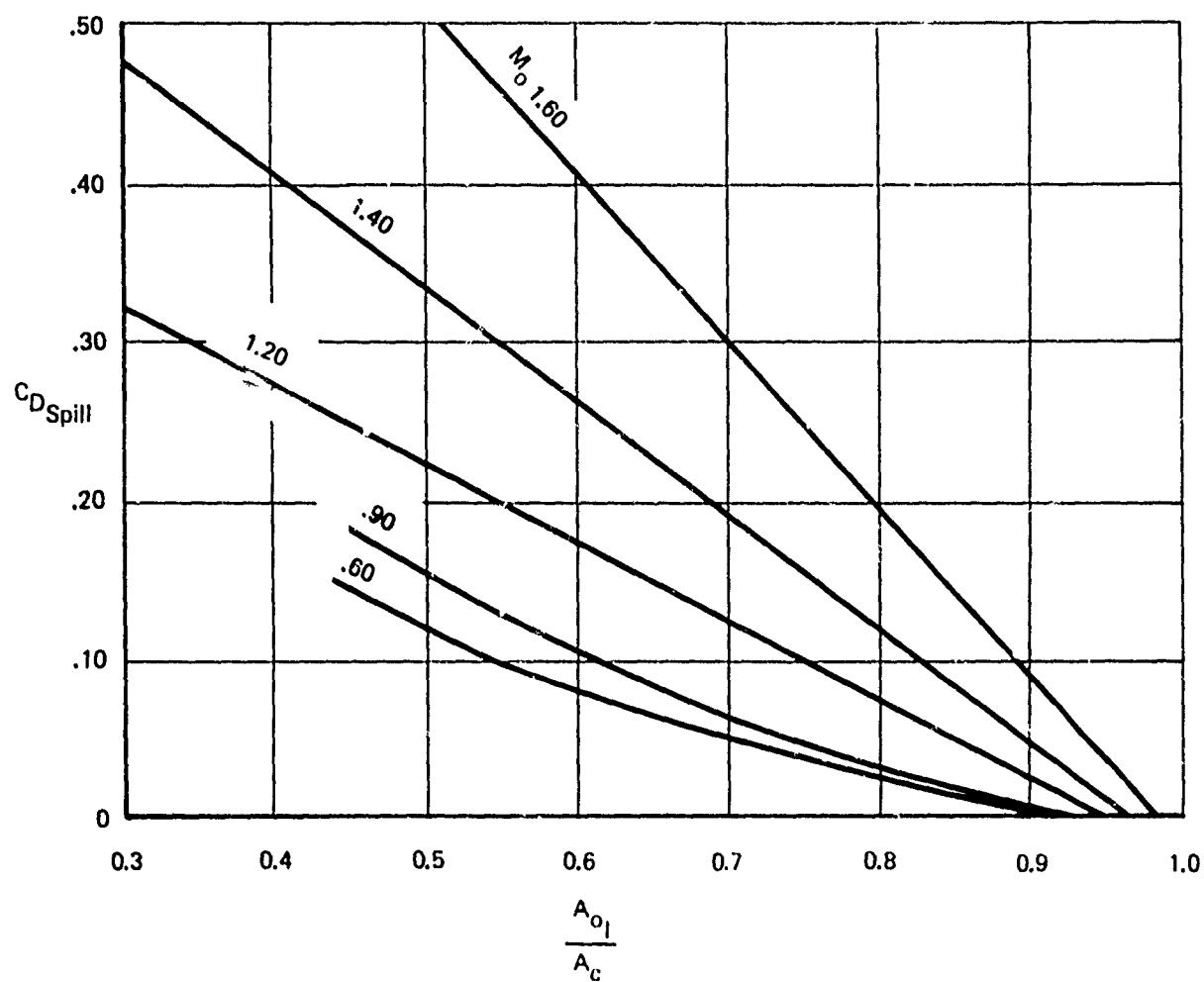
Figure 116: BUZZ LIMIT

145

Figure 117: DISTORTION LIMIT

146

Figure 118: SPILLAGE DRAG

147
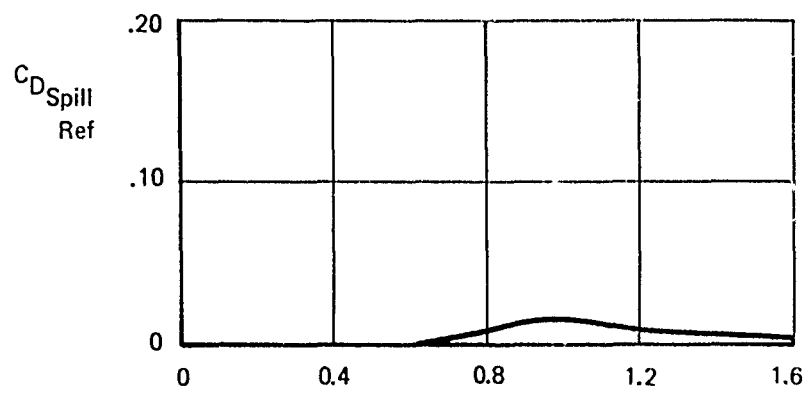
Figure 119: REFERENCE SPILLAGE DRAG
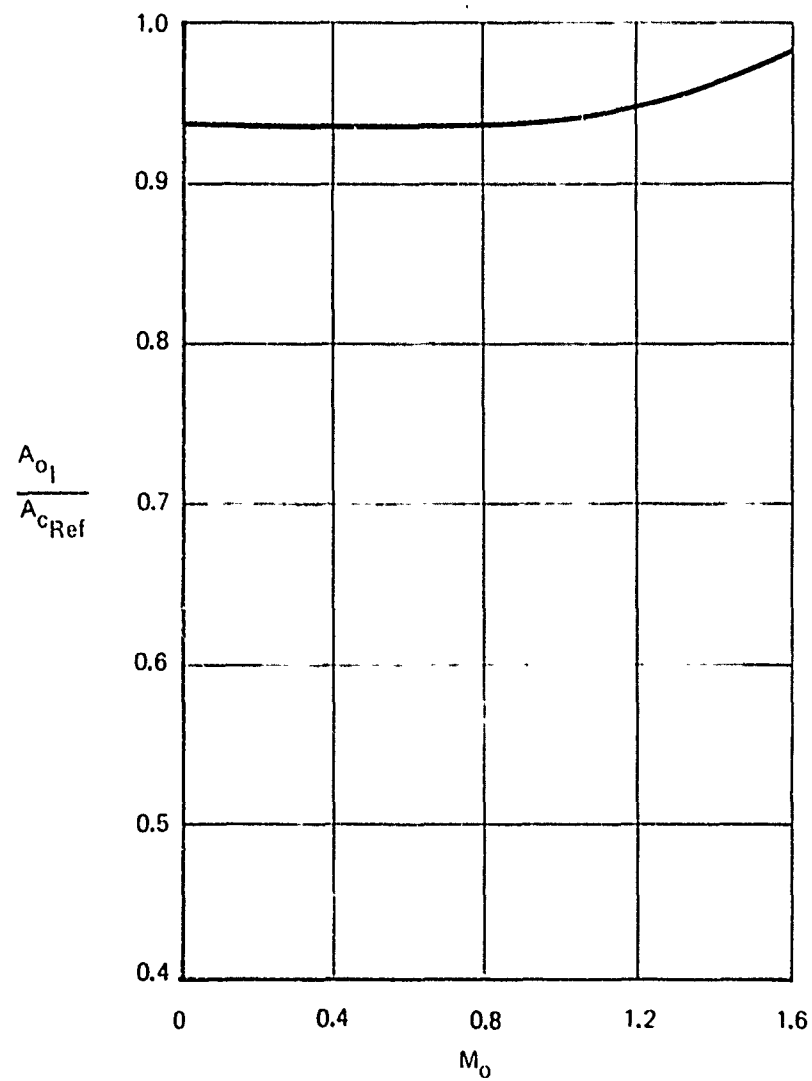
Figure 120: REFERENCE MASS FLOW

148

$C_{D_{BLC}}$

$C_{D_{BLC}}$ = 0 for All Conditions
(No Bleed)

$A_{O_{BLC}}/A_c$
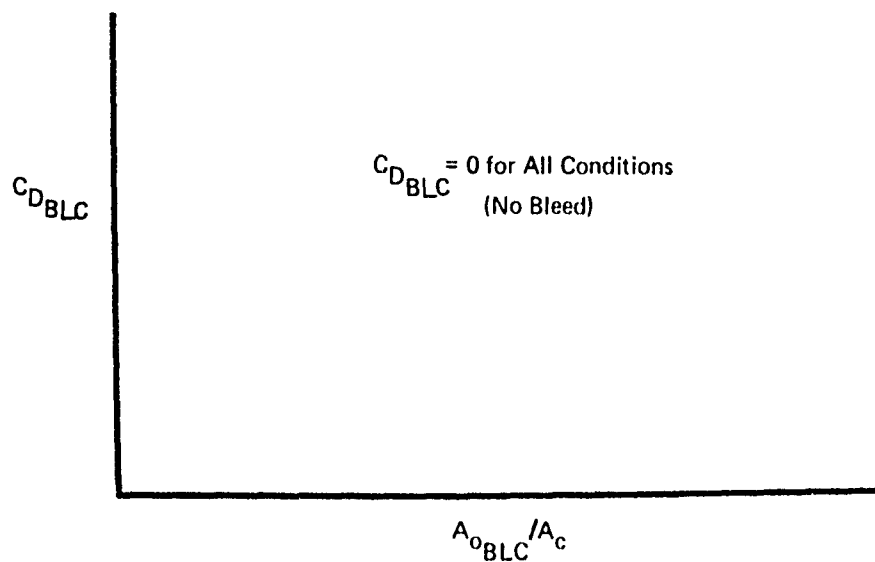
FIGURE 121: BLEED AND BYPASS DRAG

$C_{D_{BP}}$ = 0 for All Conditions
(No Bypass)

$C_{D_{BP}}$

$A_{O_{BP}}/A_c$
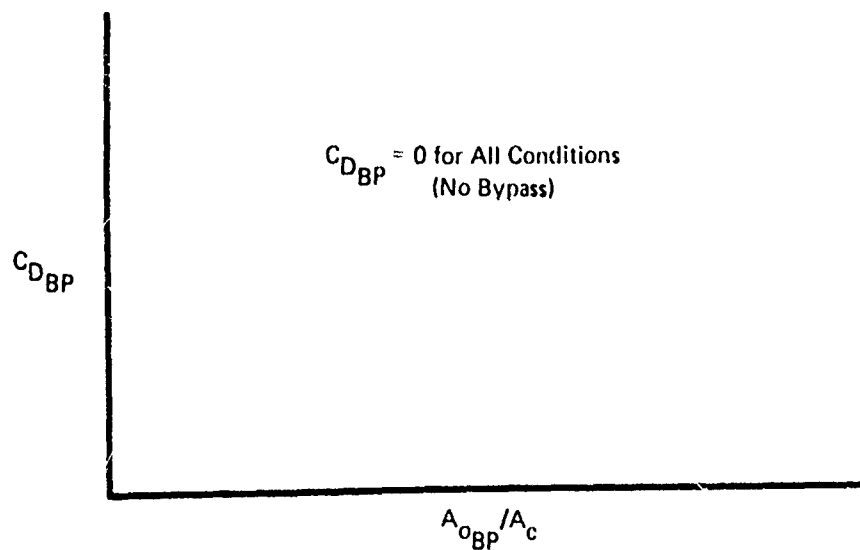
Figure 122: BLEED AND BYPASS DRAG

149

$$\frac{A_{0_{BLC}}}{A_c}$$

$$\frac{A_{0_{BLC}}}{A_c} = 0 \text{ for All Conditions}$$
(No Bleed)

A_0/A_c
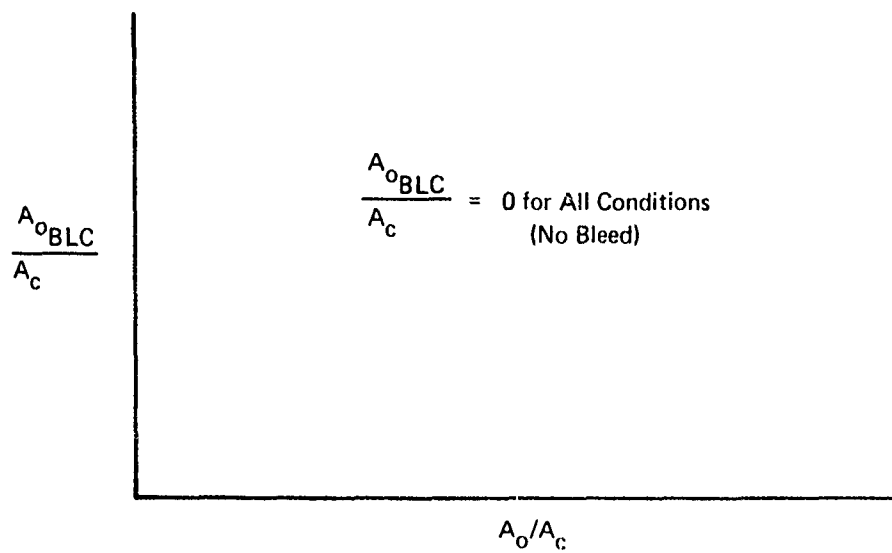
Figure 123: BLEED MASS FLOW VS A_0/A_c

$$\frac{A_{0_{BLC}}}{A_c}$$

$$\frac{A_{0_{BLC}}}{A_c} = 0 \text{ for All Conditions}$$
(No Bleed)

M_0
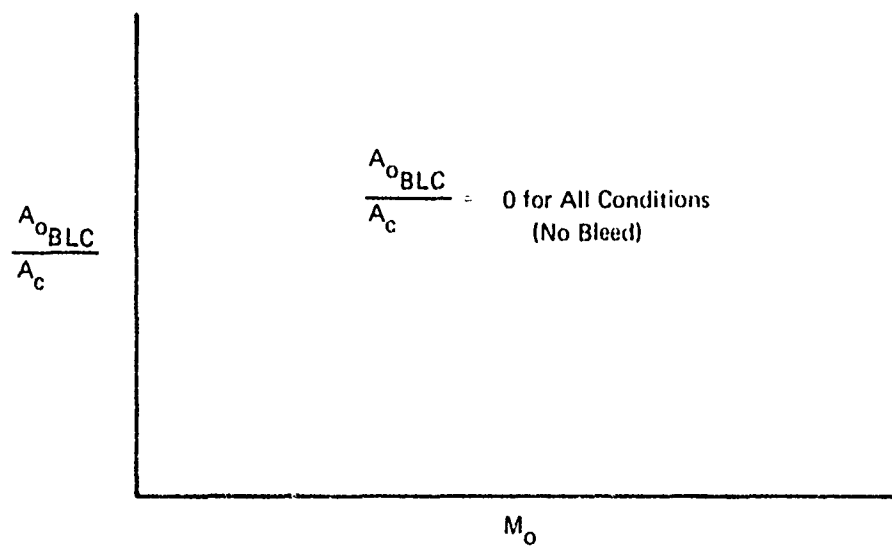
Figure 124: BLEED MASS FLOW VS M_0

150

$$\frac{A_{o_{BP}}}{A_c} = 0 \text{ for All Conditions (No Bypass)}$$
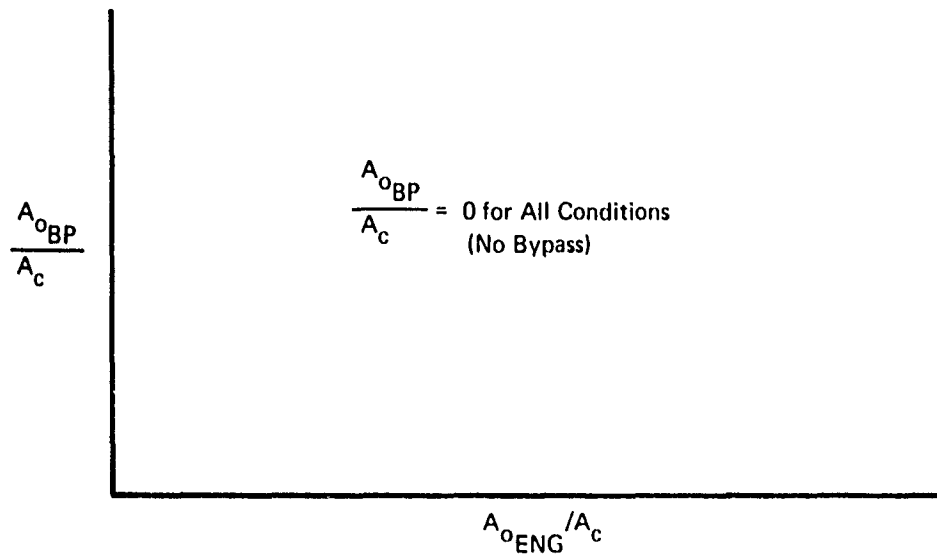
Figure 125: BYPASS MASS FLOW

Figure 126: M_O = 2.0, TWO-DIMENSIONAL VARIABLE GEOMETRY INLET

Porous Bleed
on Compression
Surfaces

Plow

Subinlet

Plow

153
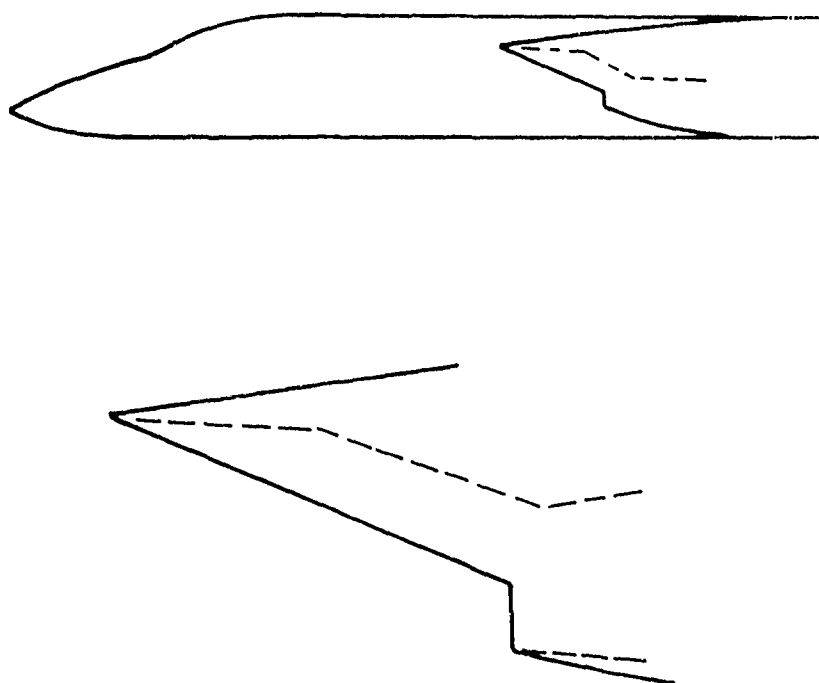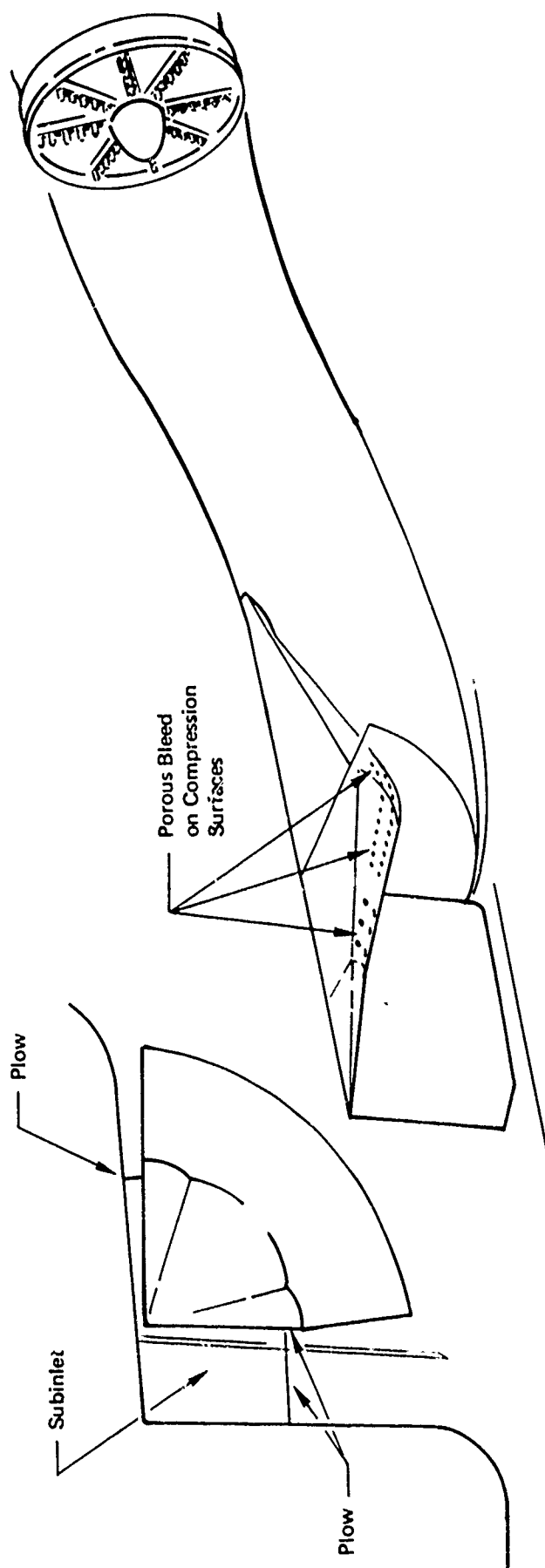
Figure 127: THREE-SHOCK, EXTERNAL COMPRESSION, VARIABLE GEOMETRY INLET
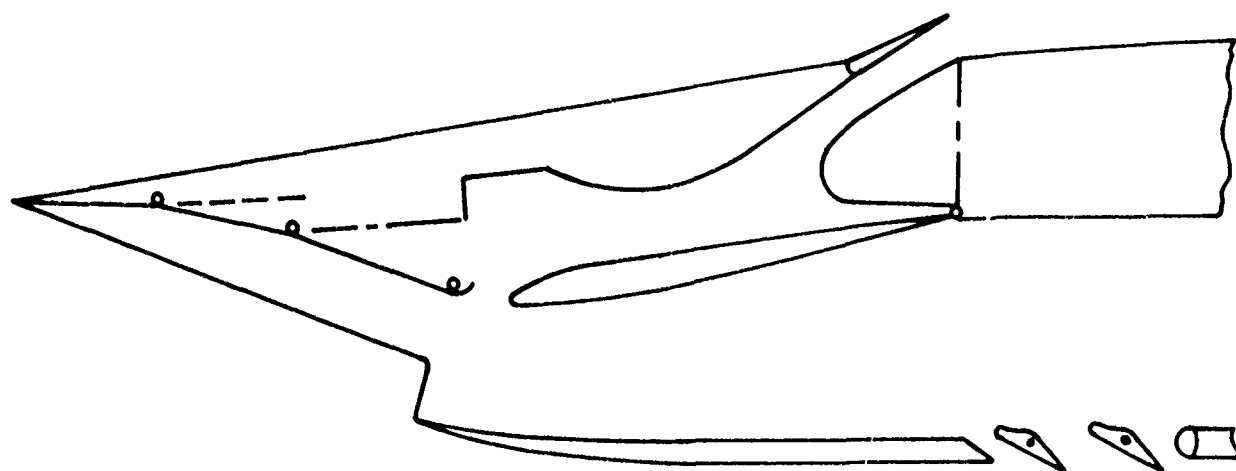
Figure 128: M_0 = 2.20, EXTERNAL COMPRESSION, VARIABLE GEOMETRY INLET
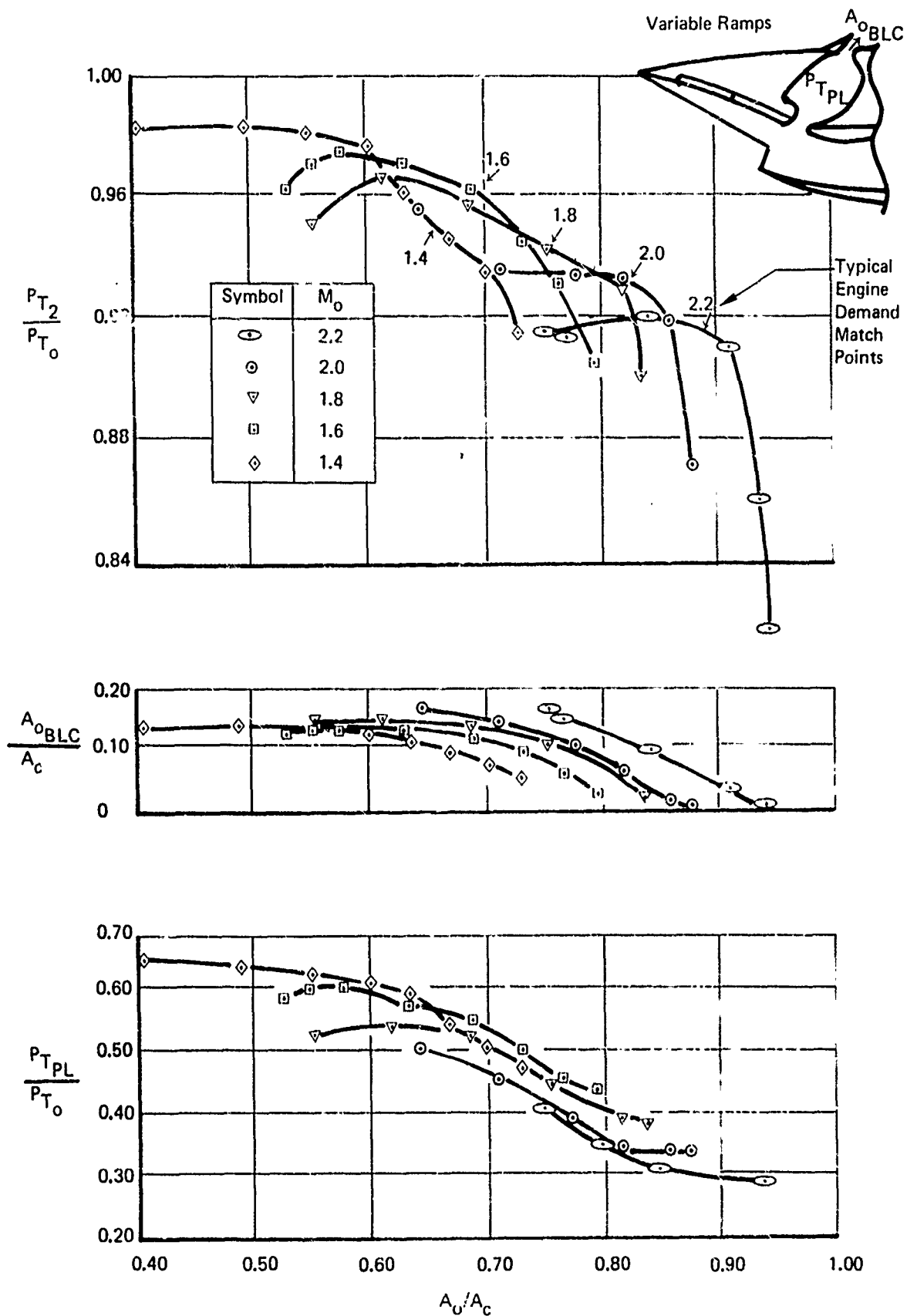
Figure 129 : EFFECT OF MACH NUMBER ON PERFORMANCE OF A
2-D INLET WITH THROAT SLOT BLEED

$M_{\infty} = 2.2$
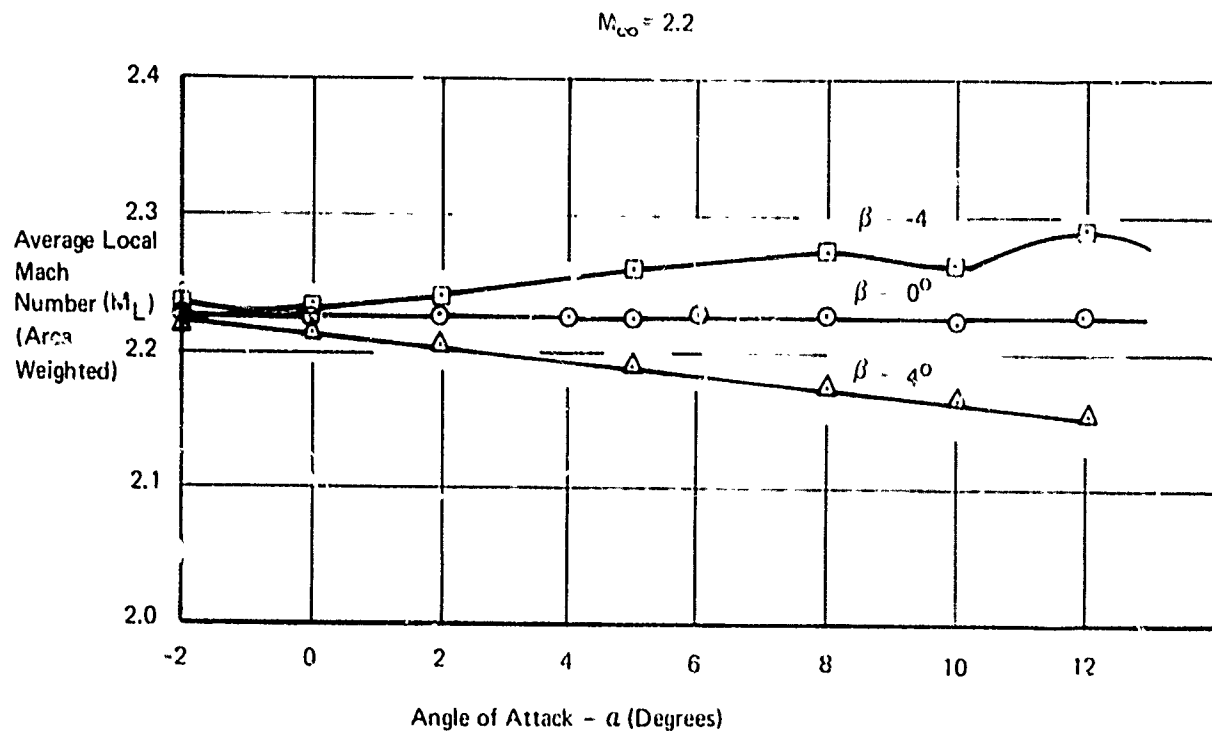
Figure 130 : EFFECT OF ANGLE-OF-ATTACK ON FLOWFIELD
MACH NUMBER FOR SIDE-MOUNTED INLETS

156

$$M_o = 1.3$$
$$a = 2^o$$
$$\psi = 0^o$$
$$R_c = 10^o$$

Forebody On

$$\frac{P_{T_2}}{P_{T_0}}$$

Forebody Off

$$\frac{P_{T2}}{P_{T_0}}$$

Engine Mass Flow Ratio $\frac{A_{O_E}}{A_C}$
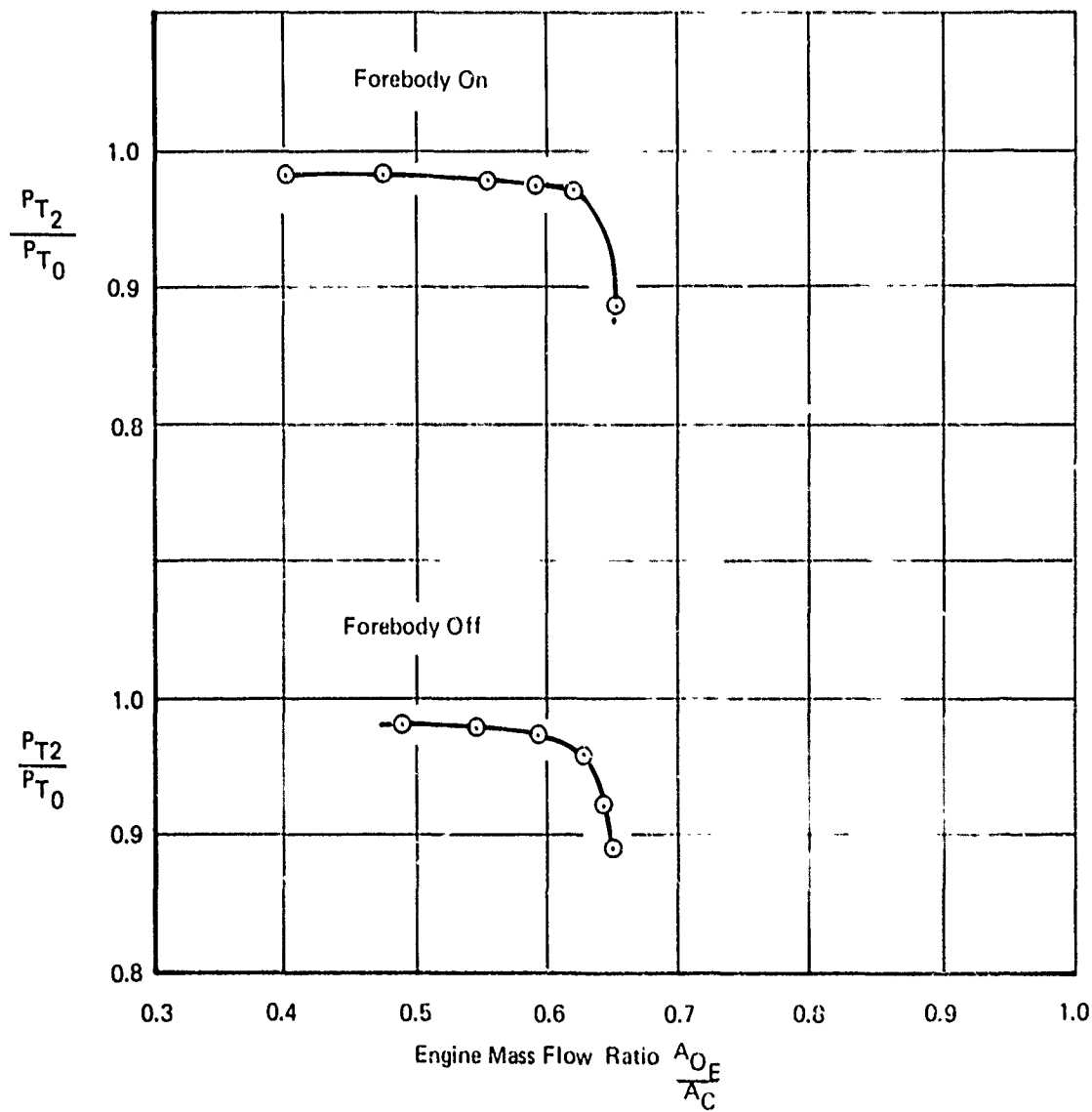
Figure 131 :   *TOTAL PRESSURE RECOVERY, FOREBODY ON AND OFF, $M_o = 1.3$*

157

Rectangular Installed Inlet Model 1160I-1
Force Balance Test Data
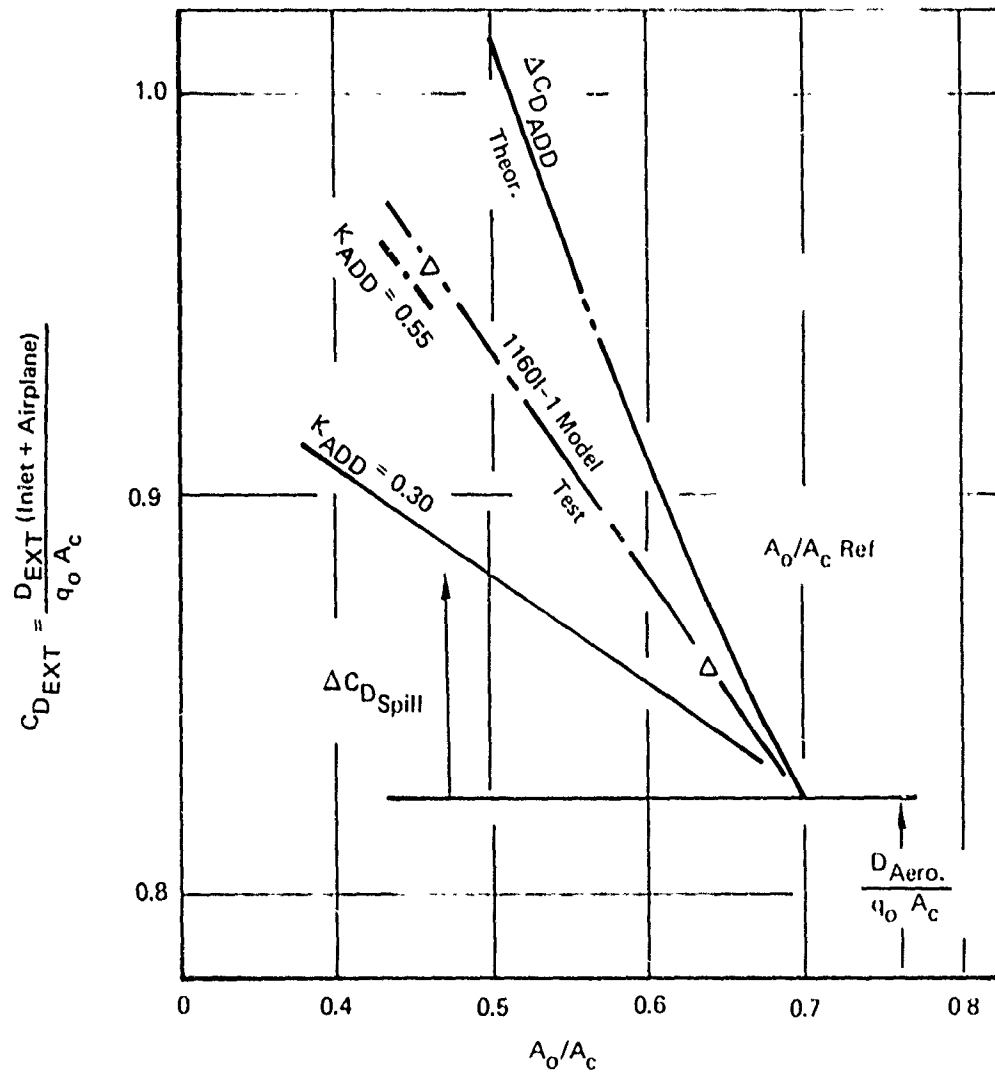
Figure 132 : COMPARISON OF SOME MODEL . .· ..· ..·.TA WITH PREDICTED DATA
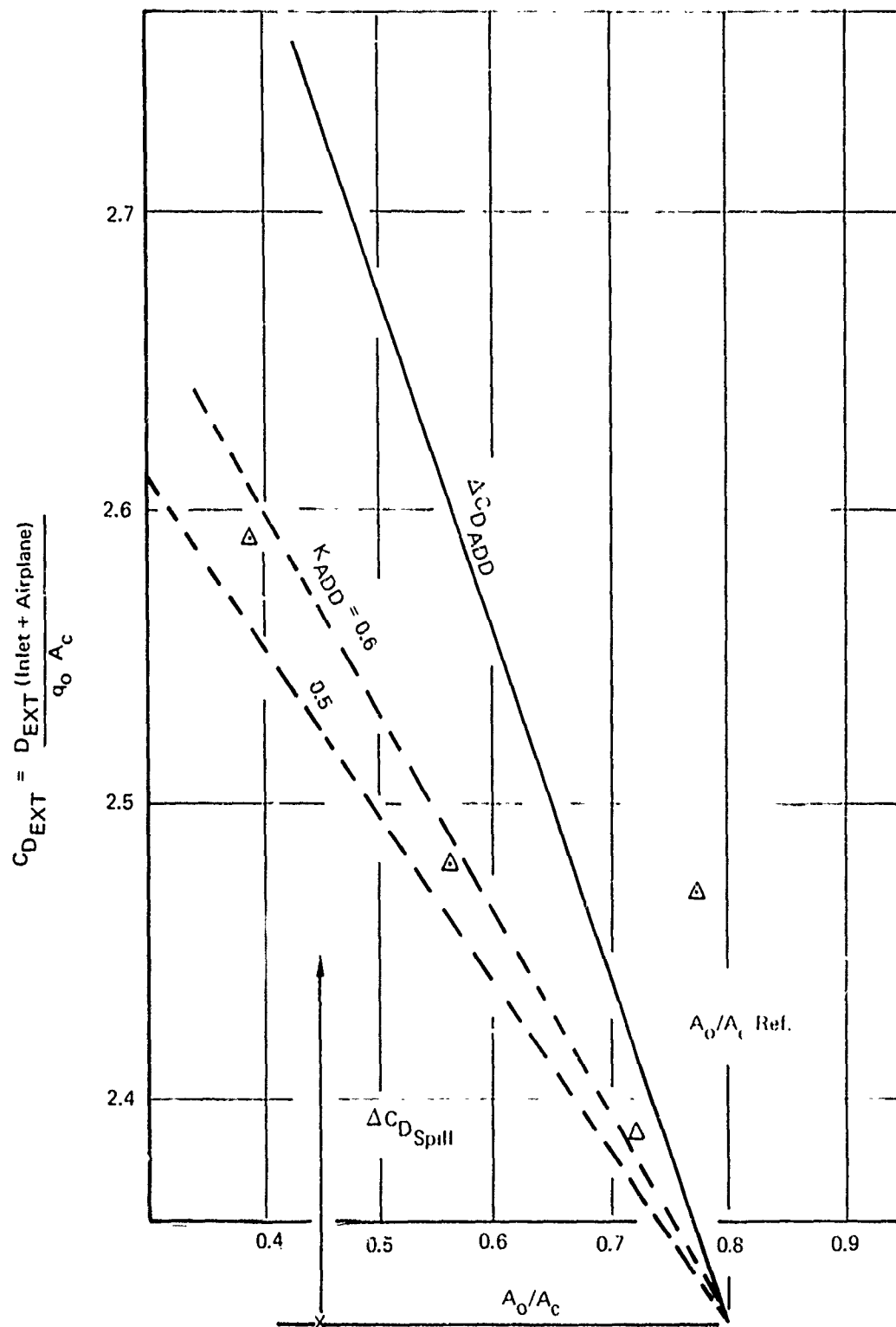
Figure 133 : FORCE BALANCE TEST DATA
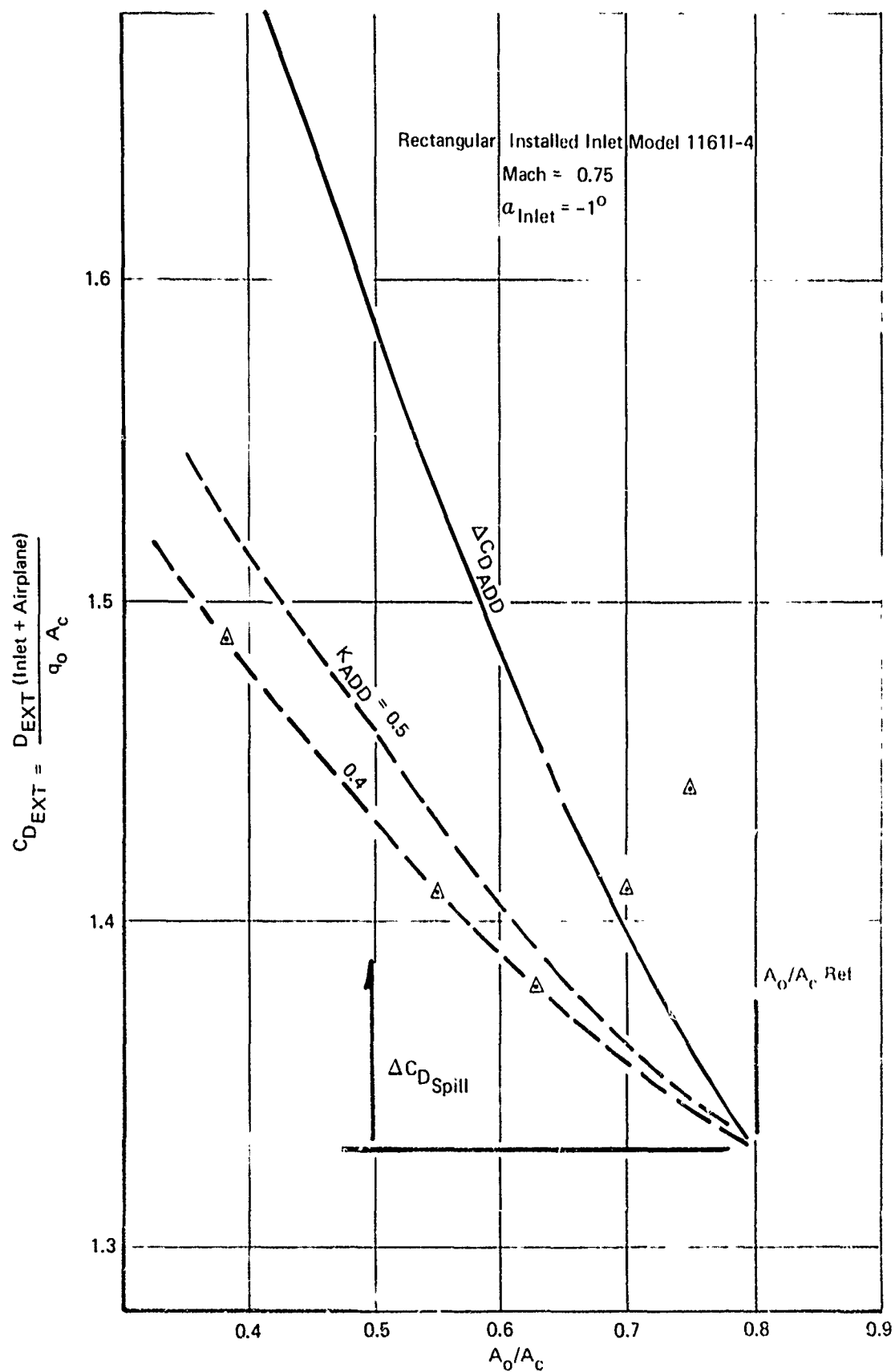
Figure 134: FORCE BALANCE TEST DATA
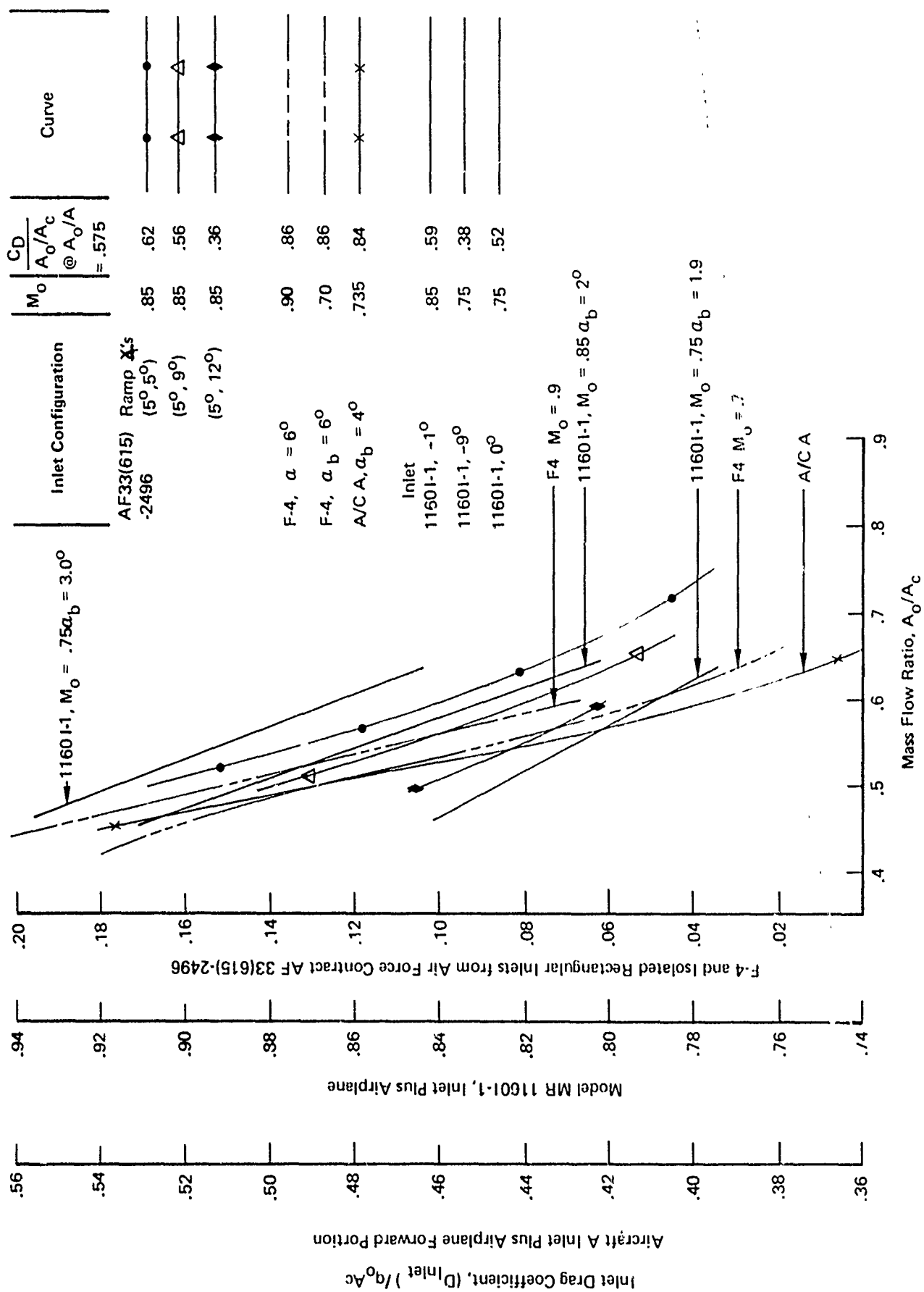
Figure 135: CORRELATION OF INLET DRAG DATA

161

Takeoff
• Ramp Collapsed
• Throat Collapsed
• Auxiliary Inlet Open

Mach 0.85
• Ramp 9°
• Throat at 24 Inches
• Cowl Drooped

Mach 1.2
• Ramp Collapsed
• Throat Collapsed
• Bypass Activated (Open)
• Cowl Normal

Mach 2.2
• Ramp 11°
• Throat at 16 Inches
• Bypass Activated (Closed)
• Cowl Normal
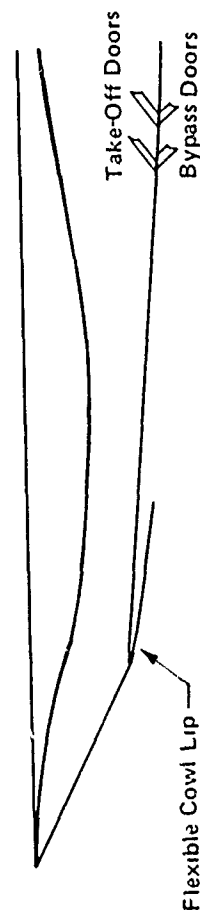
Take-Off Doors

Bypass Doors

Flexible Cowl Lip

Figure 136: MACH 2.20, MIXED COMPRESSION TWO-DIMENSIONAL INLET
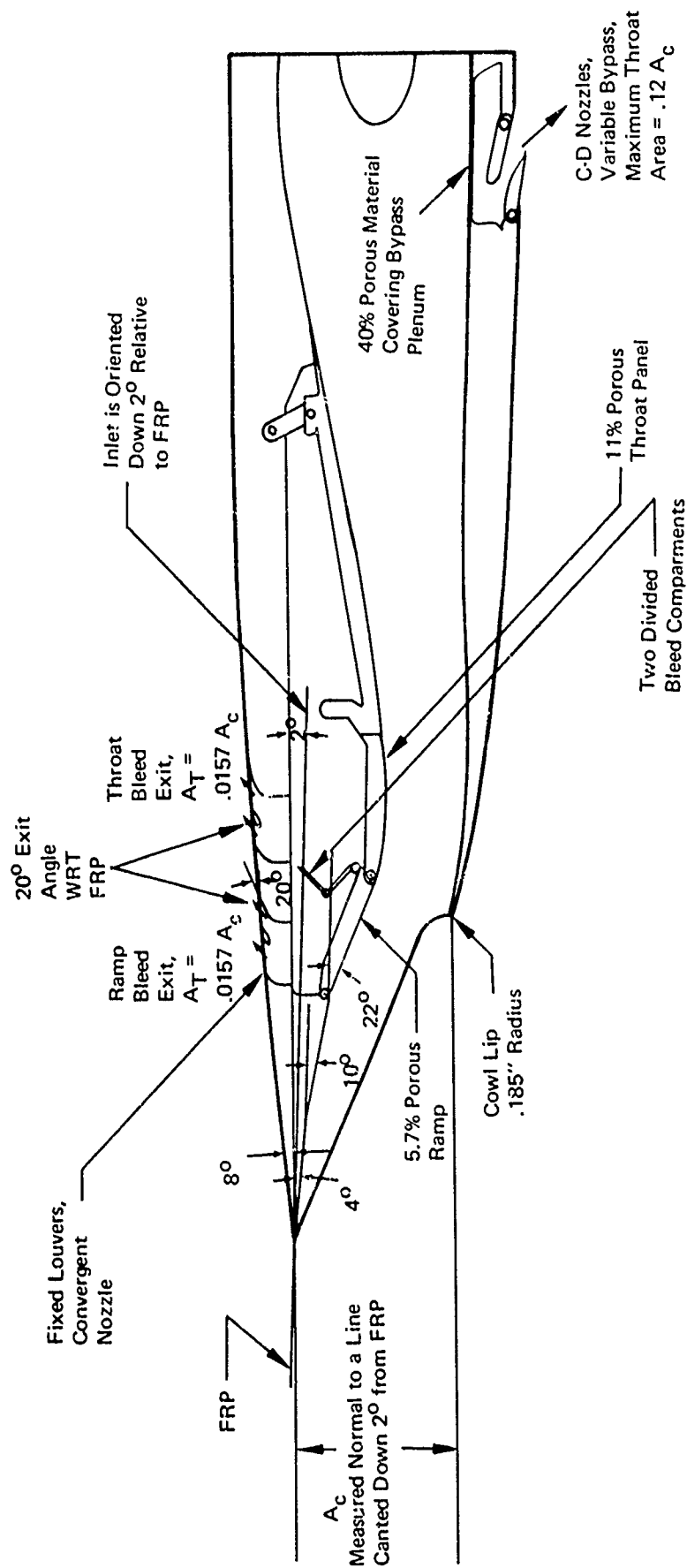
162

Figure 137: MACH 2.5 EXTERNAL COMPRESSION INLET

36,089 feet altitude. The inlet is an external compression, horizontal ramp design. It has internal boundary layer bleed through a porous third ramp panel and a throat panel. The bleed from each of these panels is collected in separate, divided plenum compartments and then is exited overboard through convergent nozzles provided by exit louvers. The bleed flow is exited at an angle of 20 degrees relative to the fuselage reference line. The inlet is oriented down at an angle of 2 degrees relative to the F.R.P. so that the initial fixed ramp angle of 4 degrees (relative to the F.R.P.) will provide 6 degrees of compression at the +2 degrees angle of attack flight attitude.

The first two ramps are fixed, but the third ramp and throat panel are movable. This provides capability to vary shock geometry and throat area. The maximum throat area corresponds to $A_{throat}/A_C = .70$. This is obtainable by collapsing the third ramp to the 6-degree position.

A bypass system is provided forward of the engine entrance to dump excess inlet air overboard. The bypass doors are convergent-divergent nozzles provided by movable doors. The bypass air is collected through porous material into a plenum chamber surrounding the duct, then is exited through the doors.

To achieve high performance at takeoff (M = .20), either the maximum throat area would have to be increased to 840 in^2 per engine (by further collapsing the ramps), or takeoff doors of 112 in^2 per engine could be added.

The estimated inlet performance characteristics are presented in Figures 138 through 150. The data are presented in the format required by PITAP.

Figure 138 shows the variation of local inlet Mach number with free-stream Mach number. For the horizontal ramp inlet location ahead of the wing, it is assumed that local and free-stream Mach numbers are the same.

Figure 139 presents the variation of inlet total pressure recovery as a function of mass flow for a range of Mach numbers from 0.60 to 2.50. These data are based largely on results from previous wind tunnel tests conducted under Air Force contracts.

Figures 140 and 141 show the variation of "recommended" (Matched) pressure recovery and mass flow as a function of free-stream Mach number. The inlet is designed to operate at Mach 2.50, therefore the position of the initial ramp angle was located so that shocks would not be ingested at Mach 2.50.
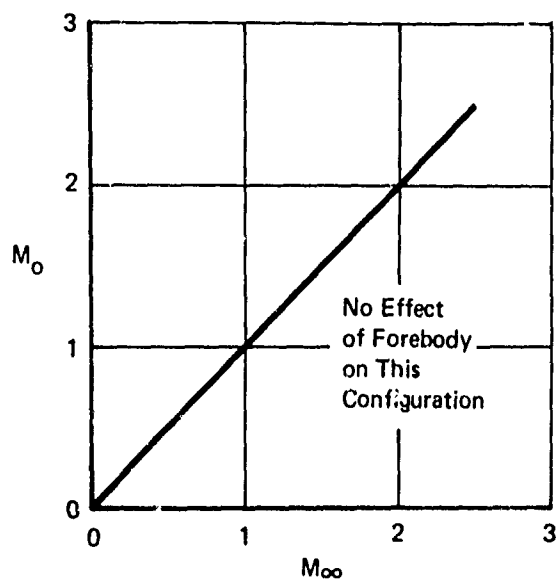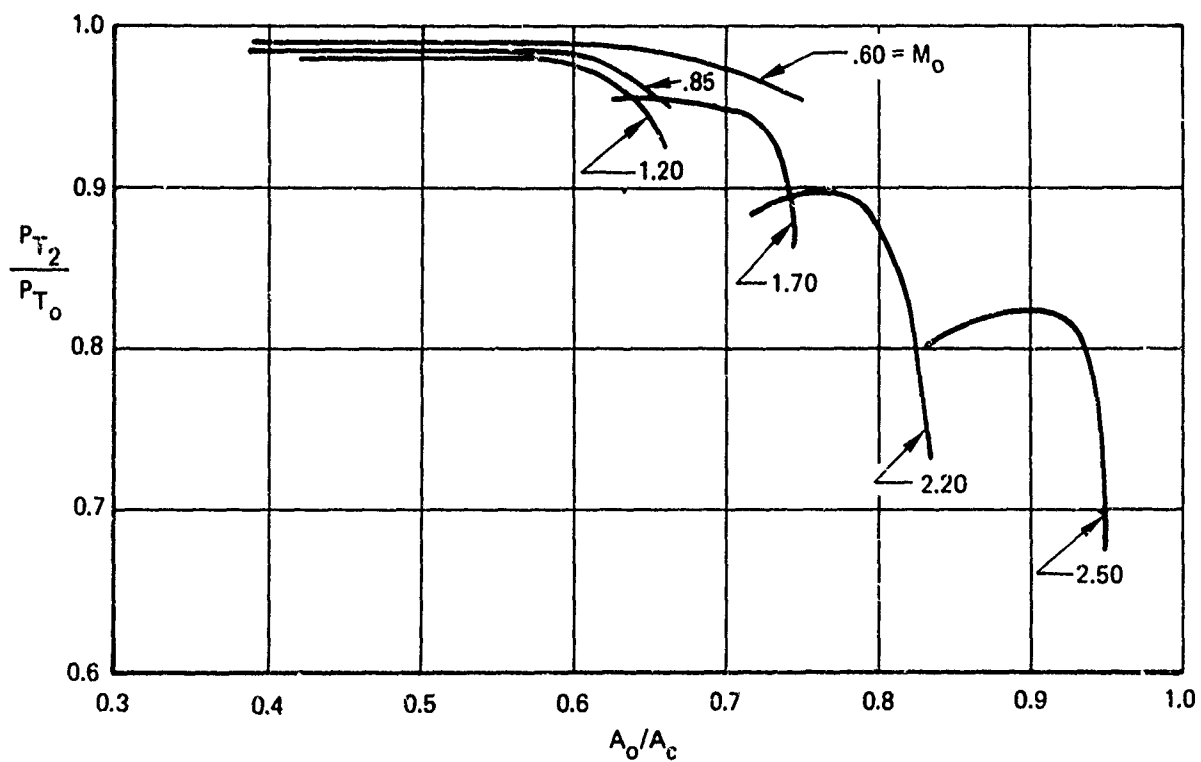
Figure 138: LOCAL MACH NUMBER
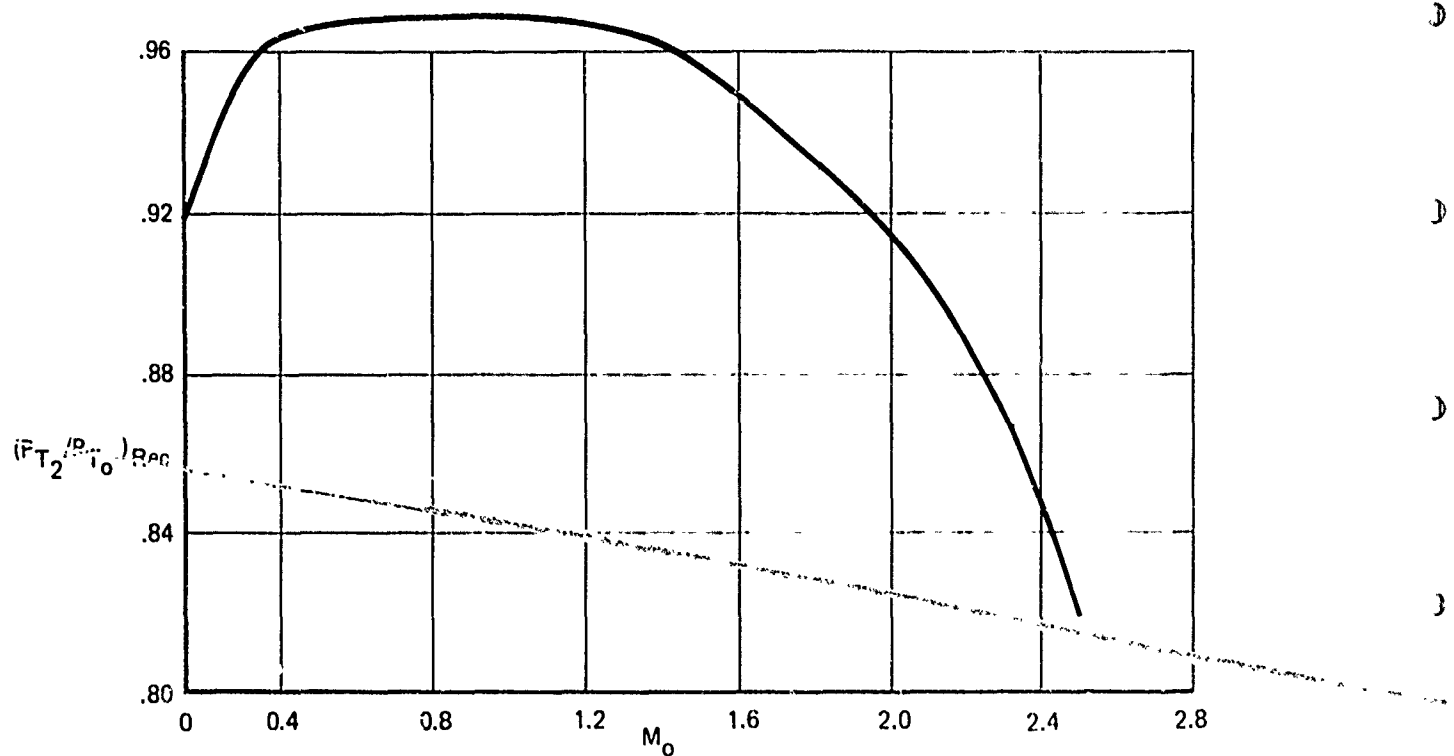

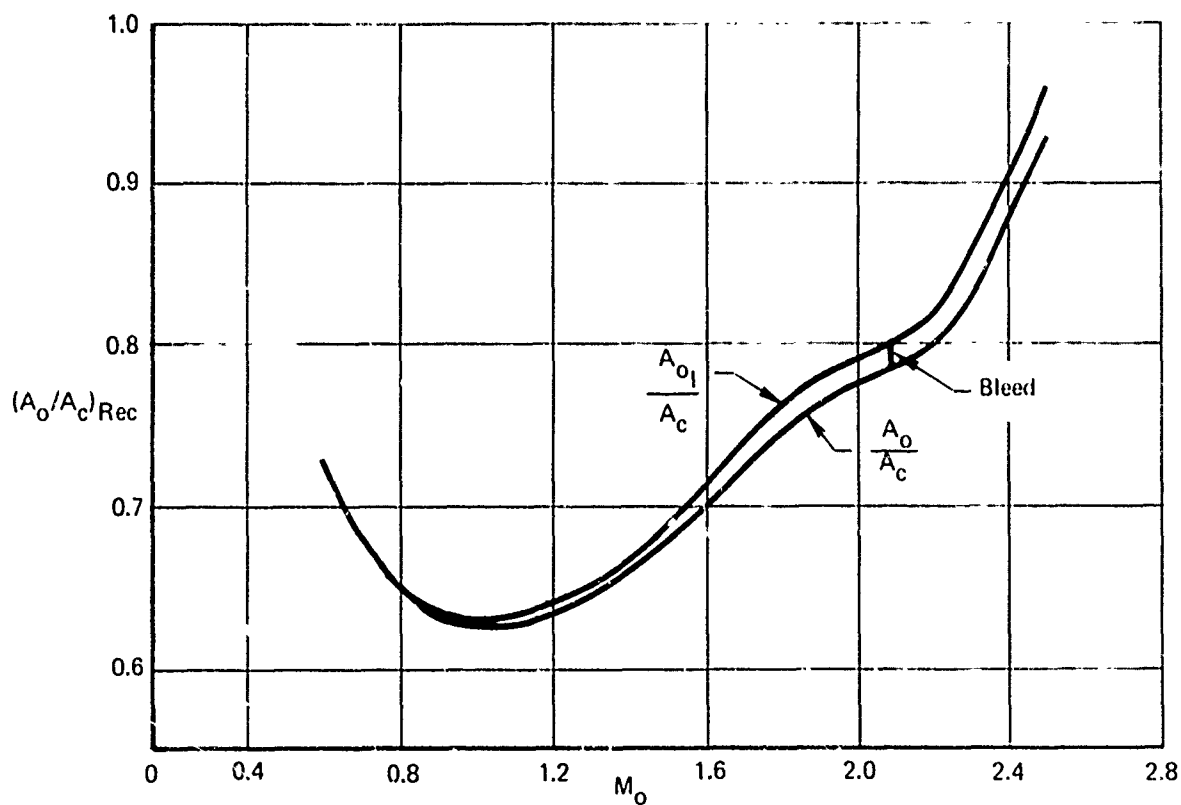Figure 139: RECOVERY VS MASS FLOW

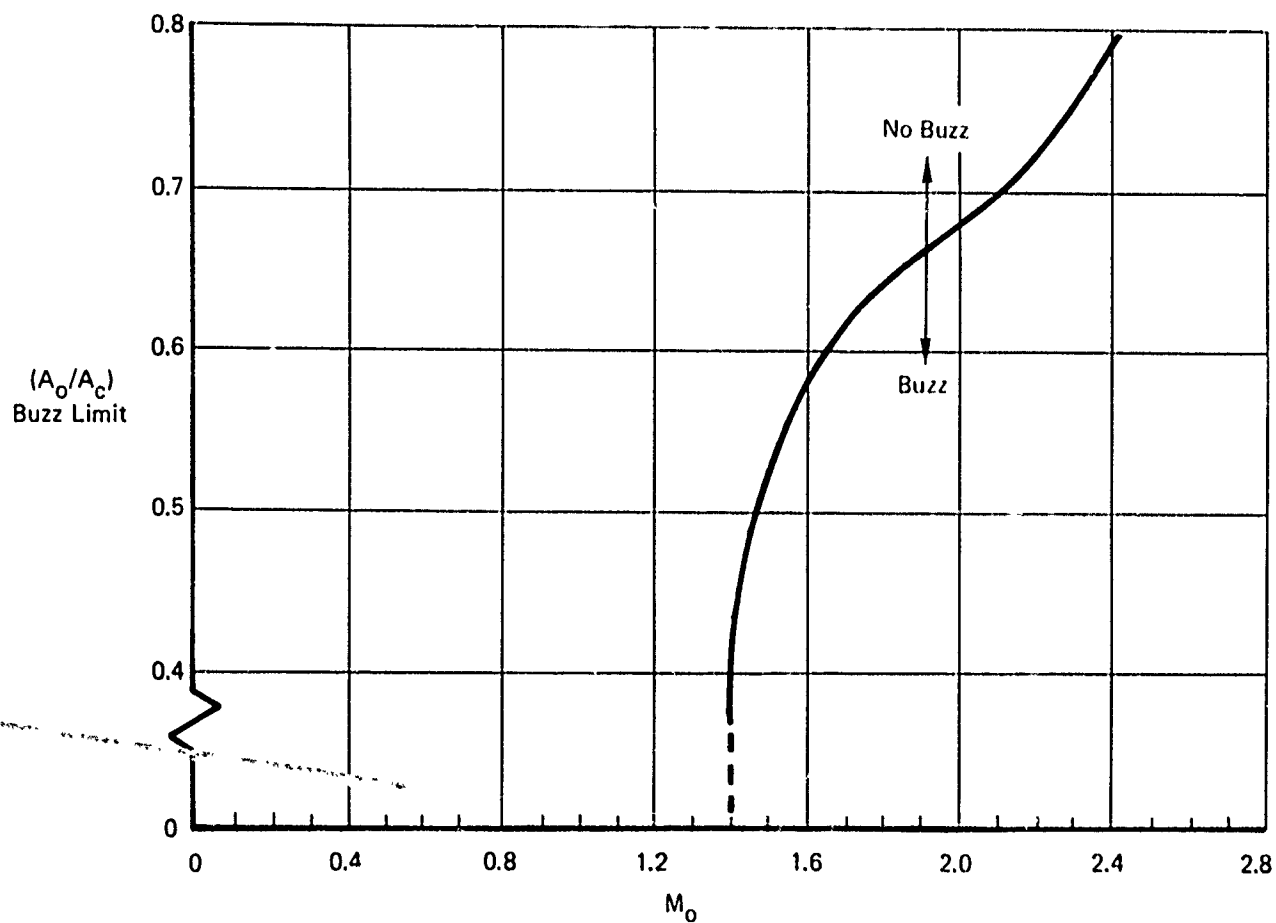Figure 140: RECOVERY VS M_o

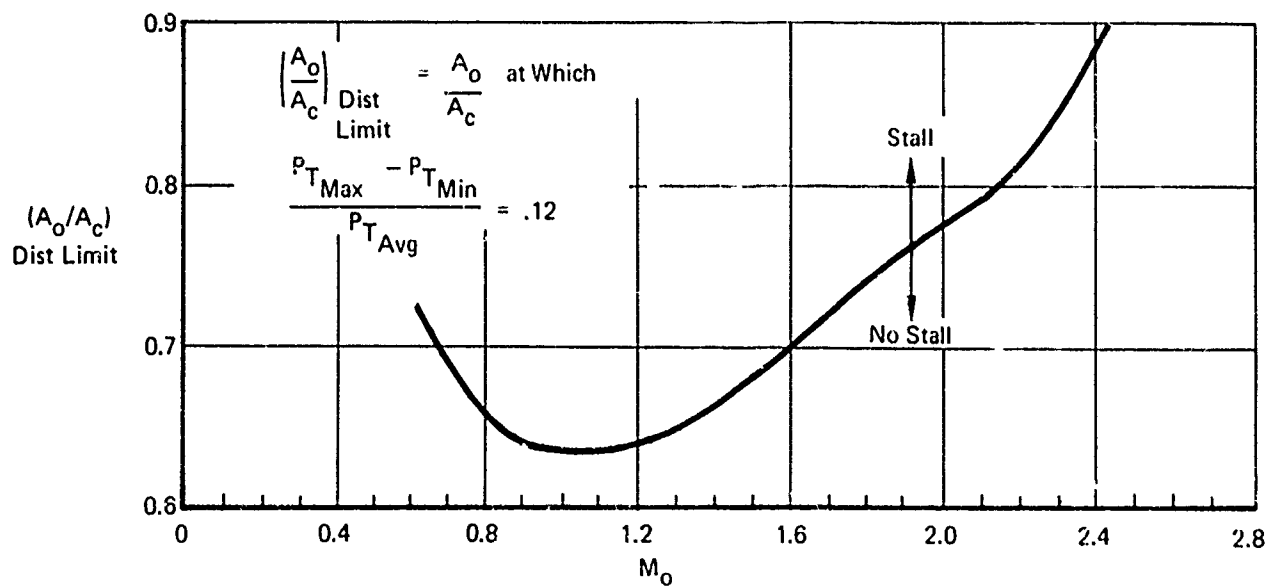Figure 141: MASS FLOW VS M_o

Figure 142: BUZZ LIMIT

$$\left(\frac{A_o}{A_c}\right)_{\substack{Dist \\ Limit}} = \frac{A_o}{A_c} \text{ at Which}$$

$$\frac{P_{T_{Max}} - P_{T_{Min}}}{P_{T_{Avg}}} = .12$$
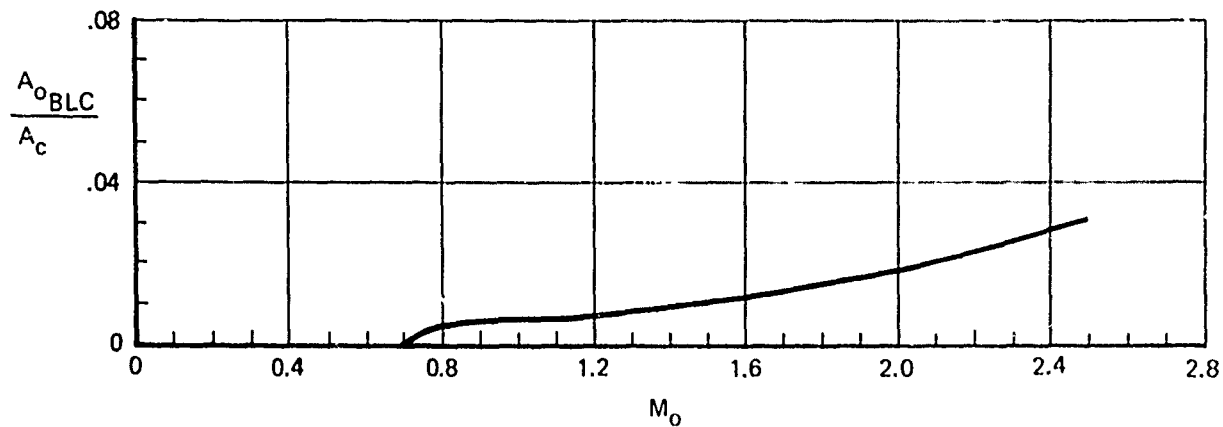
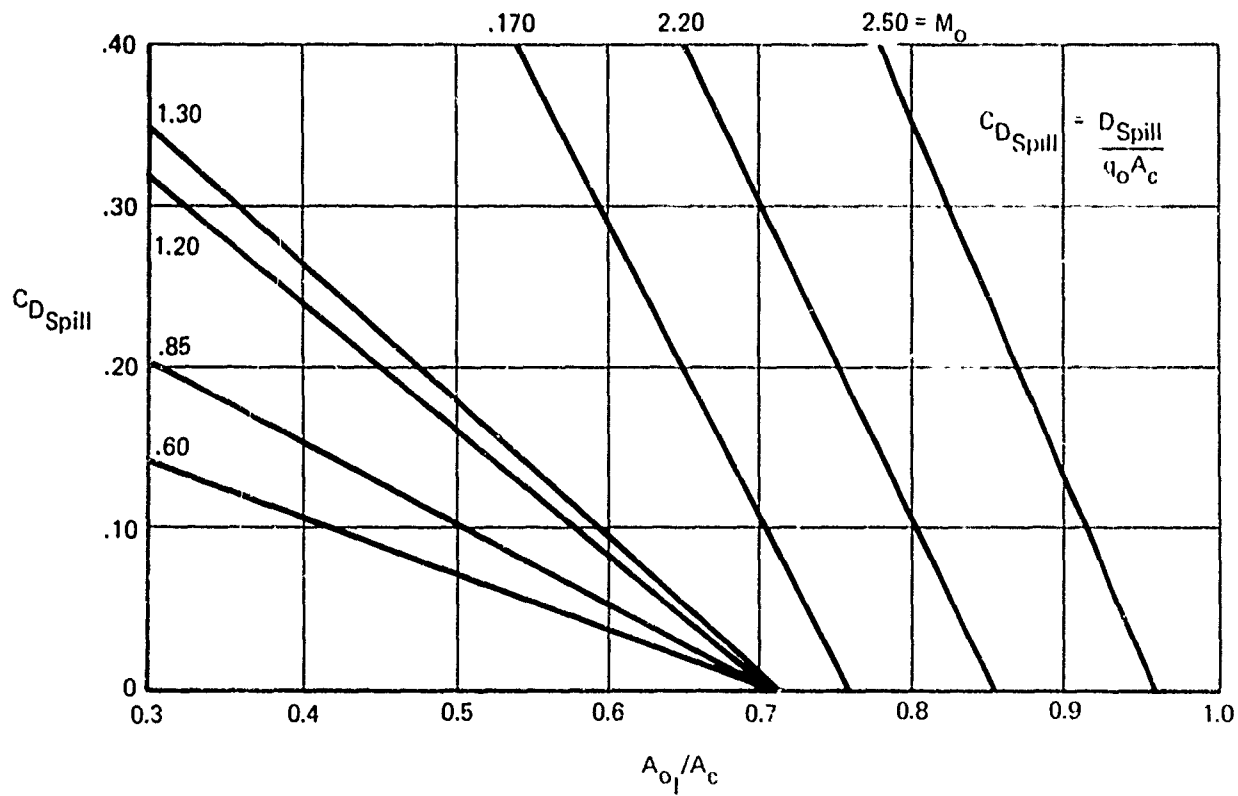*Figure 143: DISTORTION LIMIT*
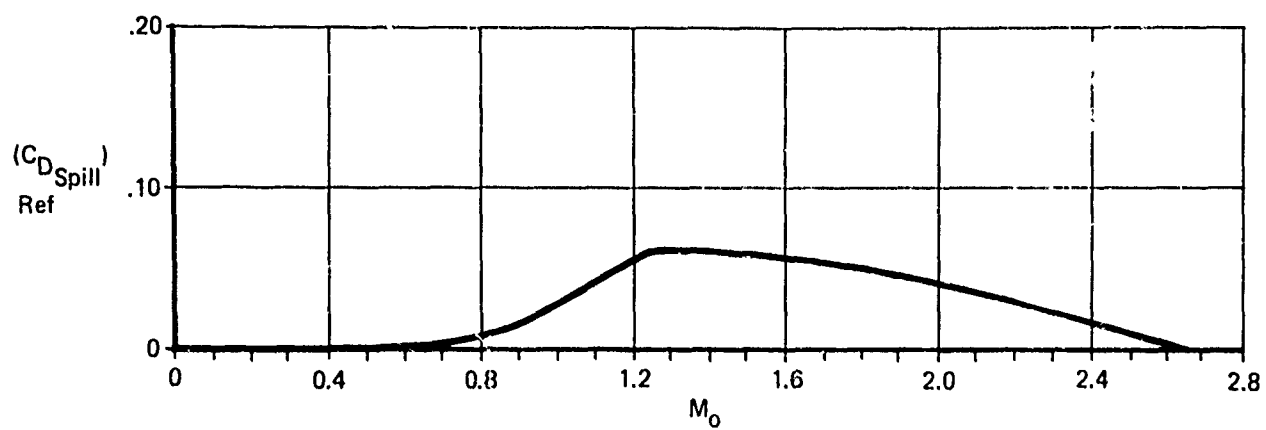
Figure 144: BLEED VS M_o

Figure 145: SPILLAGE DRAG
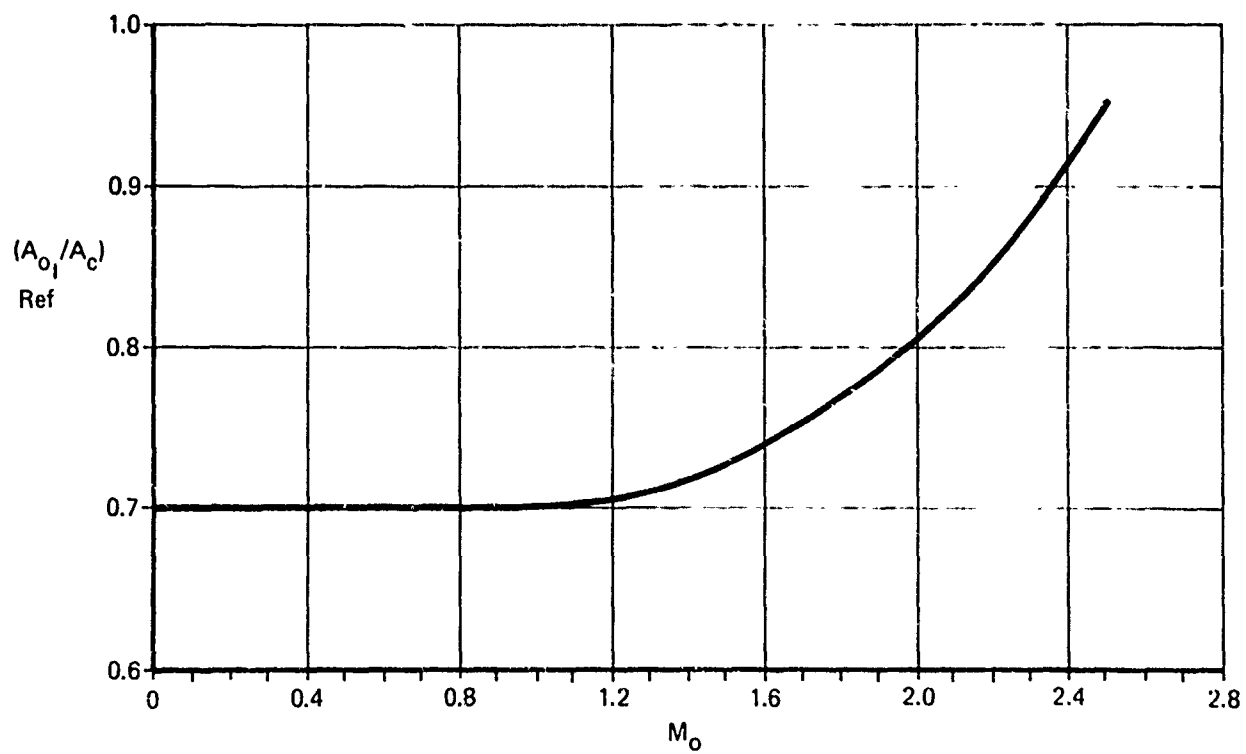
168

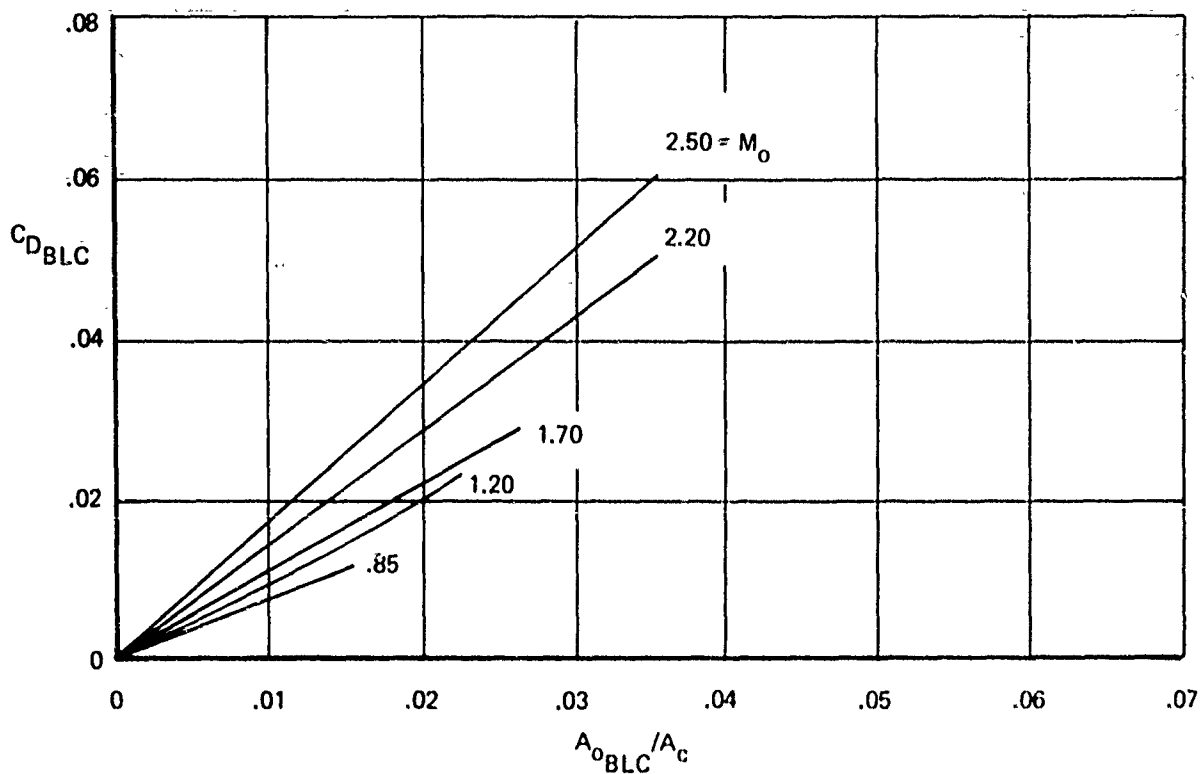Figure 146: REFERENCE SPILLAGE DRAG

Figure 147: REFERENCE MASS FLOW RATIO
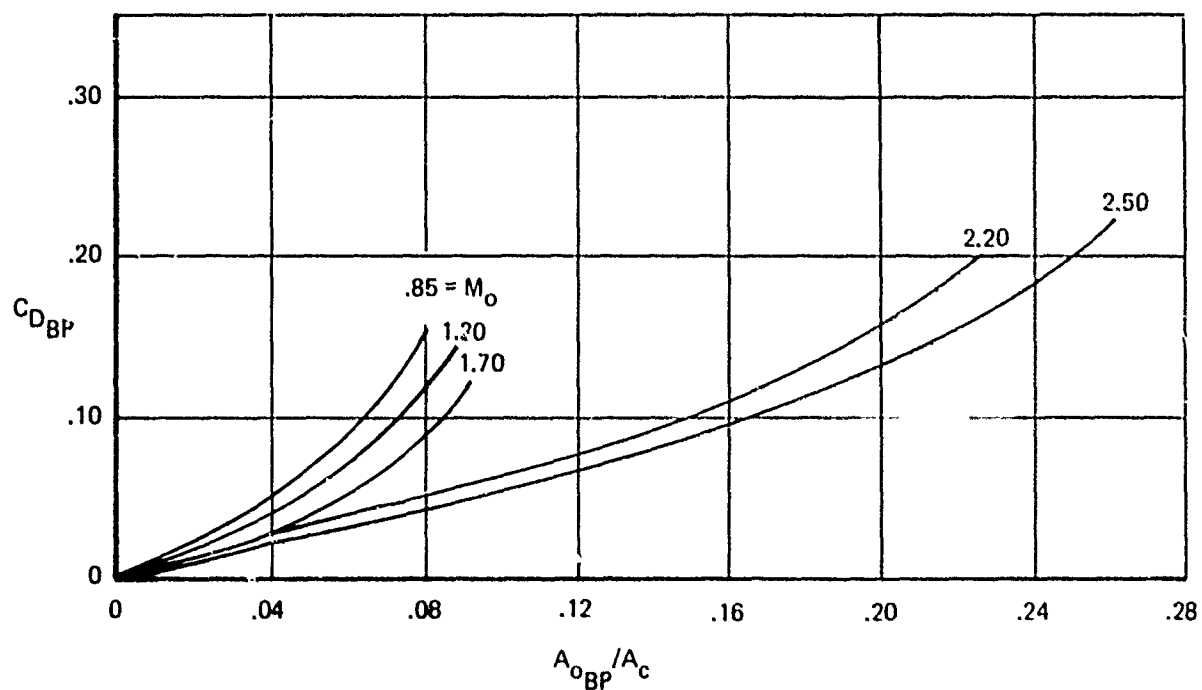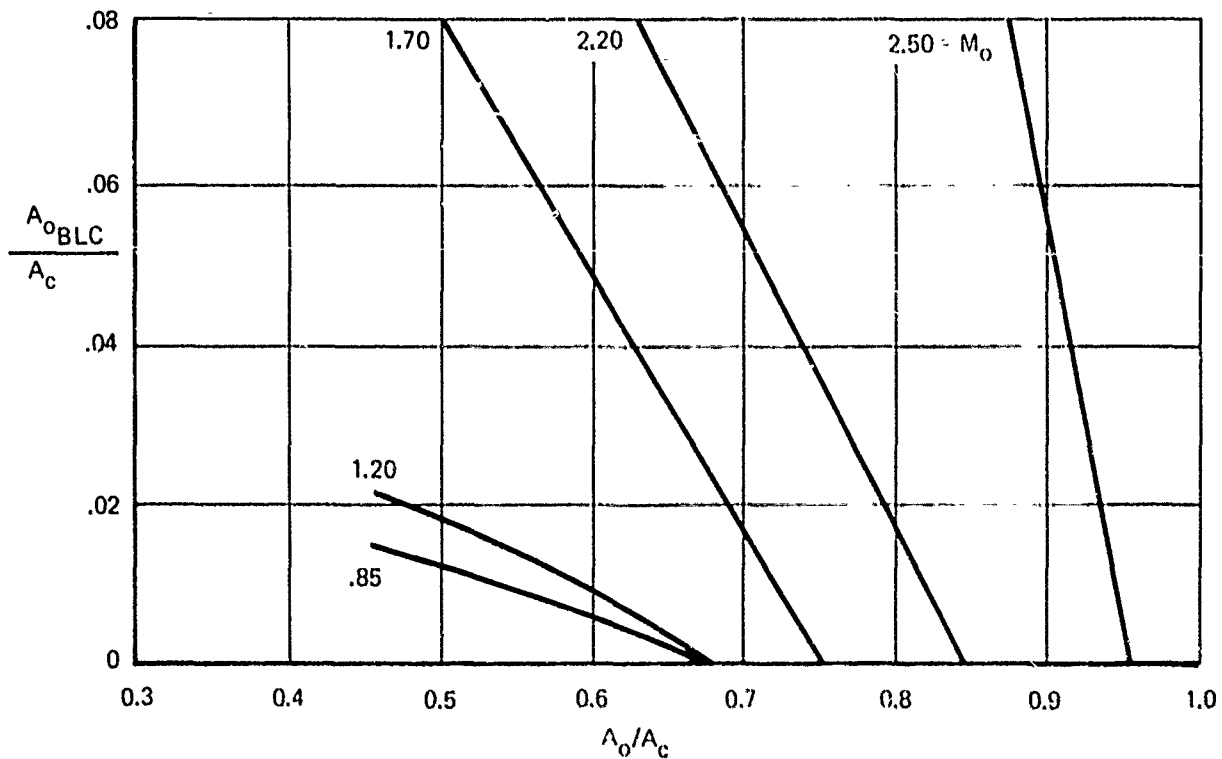
Figure 148: BLEED DRAG

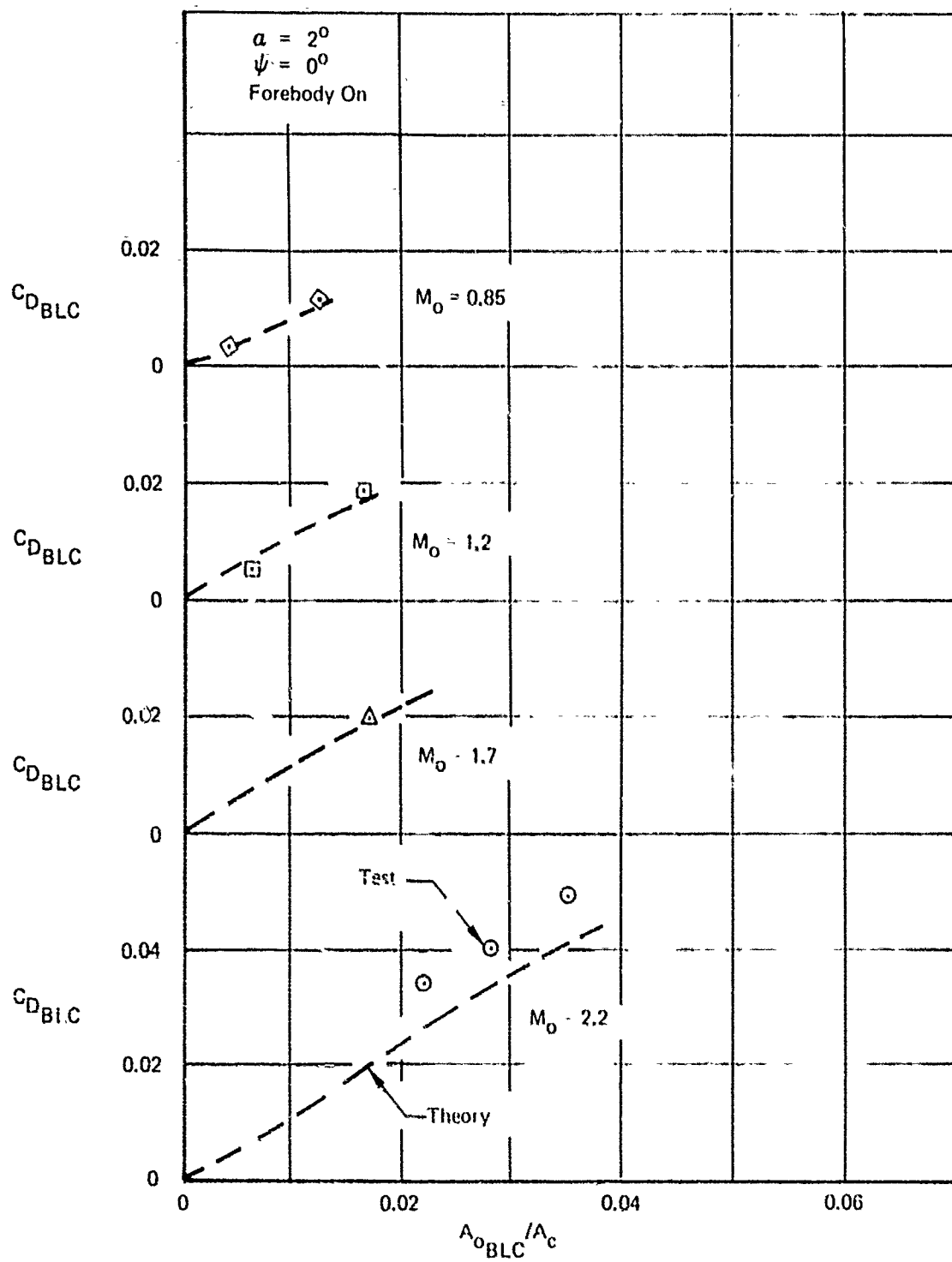
Figure 149: BYPASS DRAG

Figure 150: BLEED MASS FLOW

171

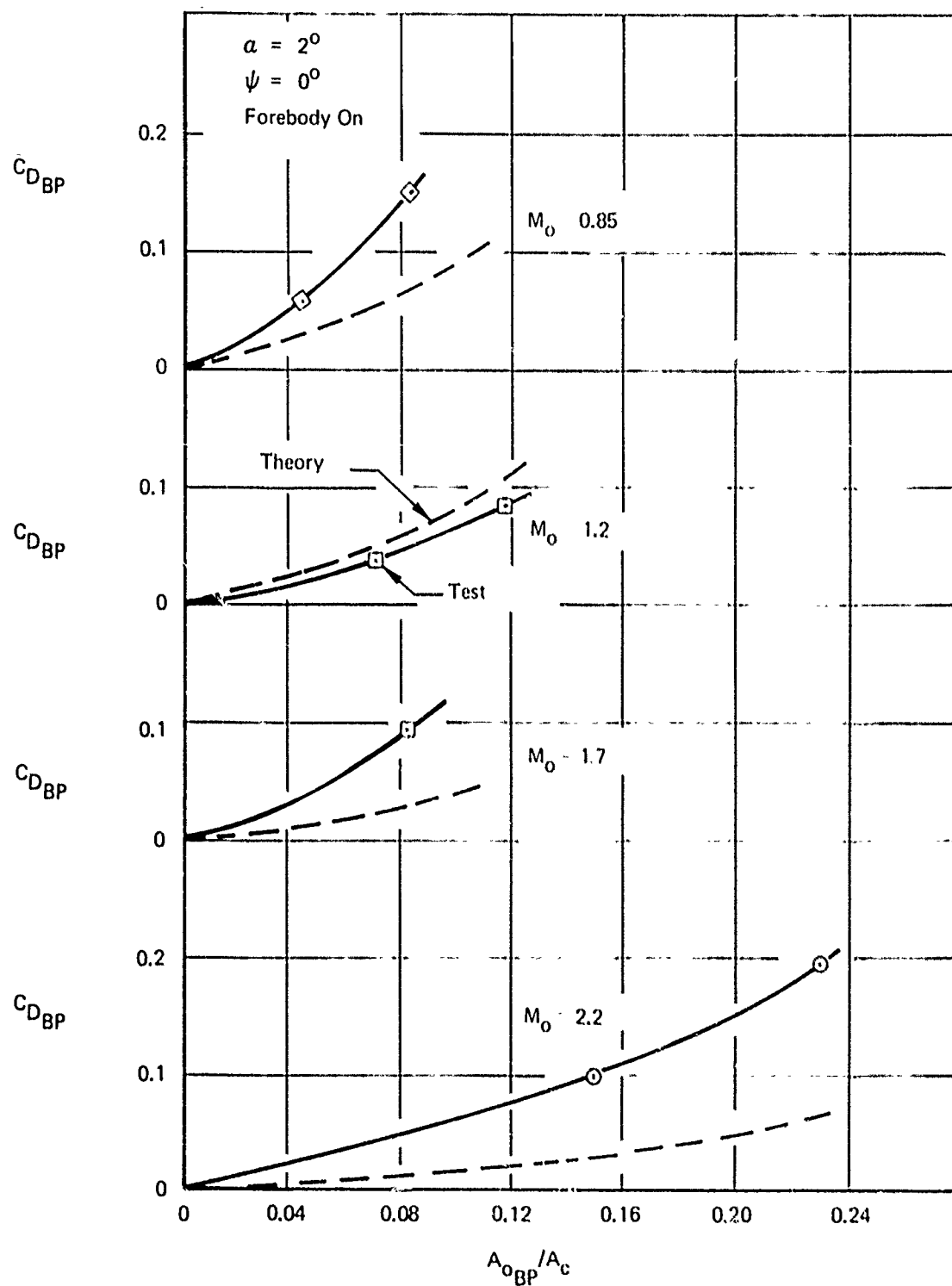Figure 151: COMPARISON BETWEEN THEORETICAL AND TEST BLC SYSTEM DRAGS

172

Figure 152: COMPARISON BETWEEN THEORETICAL AND TEST BYPASS SYSTEM DRAGS

173

The size of the capture area was determined by the Mach 2.20 condition however, since matching the engine corrected airflow demand at this point resulted in a larger capture area requirement. The result of these design constraints is shown by the mass flow data of Figure 141. A fairly large amount of airflow is spilled thru the oblique shock system at Mach 2.20, while at Mach 2.50, a significant amount of air must be bypassed. The required boundary layer bleed flow is shown by the difference between the A_{O_I}/A_C and the A_O/A_C curves of Figure 141.

Figure 142 and 143 show the buzz and distortion limits which are used by PITAP for this inlet design to indicate when inlet operation is approaching a region of questionable engine compatibility. These limits are based on the best available data or estimates. They are not intended to represent exact limits, but should be viewed as indications that problems are likely to be encountered that should either be studied in greater detail or avoided.

The nominal boundary layer bleed schedule is shown in Figure 144 for the airflow schedule of Figure 141. Figure 145 presents the variation of inlet spillage drag as a function of inlet mass flow ratio and local Mach number. The spillage drag shown in the plot is the drag associated with the air spilled externally due to operating at inlet mass flow ratios less than the reference mass flow shown in Figure 147. The spillage drag due to the spilled airflow at the reference mass flow is shown in Figure 146. This part of the spillage drag is normally included in the airplane drag, according to the bookkeeping system discussed in Section II of this report.

Figures 148 and 149 present boundary layer bleed drag and bypass drag as functions of bleed and bypass airflow for a range of local Mach numbers from 0.85 to 2.50.

Figure 150 presents bleed mass flow as a function of duct mass flow,

$$A_O/A_C; \quad (A_O/A_C = \frac{A_{O_{ENG}}}{A_C} + \frac{A_{O_{BYPASS}}}{A_C}).$$

Bypass mass flow is scheduled as a function of engine mass flow, $\frac{A_{O_{ENG}}}{A_C}$. This schedule has been selected to bypass the airflow increment between engine demand and the nominal $(A_O/A_C)_{rec}$ mass

174

flow schedule shown in Figure 141. No bypass is used below
Mach 0.85, however, since it is less drag to spill the excess
airflow externally around the inlet.

4.1.3.2 MIXED COMPRESSION

The inlet geometry is shown in Figure 153. A mixed compression,
horizontal ramp, two-dimensional variable geometry inlet
concept is used. The mixed compression inlet was selected
for the fighter/bomber mission instead of an external compres-
sion inlet because it offers the potential for higher pressure
recovery, lower drag, and better matching characteristics
for the sustained Mach 2.5 high speed flight condition. Also,
it does not have to meet the same requirements for extremely
high maneuverability (high angles-of-attack) which would be
difficult to control for the mixed compression inlet. Boundary
layer bleed is accomplished by use of porous ramps, cowl,
and sideplates. Bleed air is collected in divided plenum
chambers behind the porous walls and is then dumped overboard
through choked convergent nozzles as near the plenum chamber
as possible. Divided plenums are used to provide optimum
bleed capability at lowest drag penalty. Movable ramp and
throat panels are used to achieve the best inlet geometry over
a wide range of flight Mach numbers.

A bypass system is also used (not shown in Figure 153) to
dump excess inlet air overboard and maintain the terminal
shock in its design location just downstream of the geometric
throat during started operation and just forward of the lip
during external compression operation (M > 2.0). Bypass doors
are assumed to be variable geometry C-D nozzles.

For takeoff and low speed operation, the ramp system is
collapsed to provide a maximum throat area equal to $0.765A_C$.
Takeoff doors having a throat area equal to .12 A_C per
engine will also be required. These should be located near
the aft end of the subsonic diffuser near the engine.

The capture area size was determined by the engine maximum
airflow demand at Mach 2.20. The ramp geometry was selected
to provide shock on lip operation at Mach 2.60. This provides
a small margin for angle-of-attack transients and overspeed
at Mach 2.50.

The estimated inlet performrnce characteristics are presented
in Figures 154 through 167.

As shown in Figure 154, the local inlet Mach number was
assumed to be the same as free-stream.

Figure 155 shows the variations of total pressure recovery
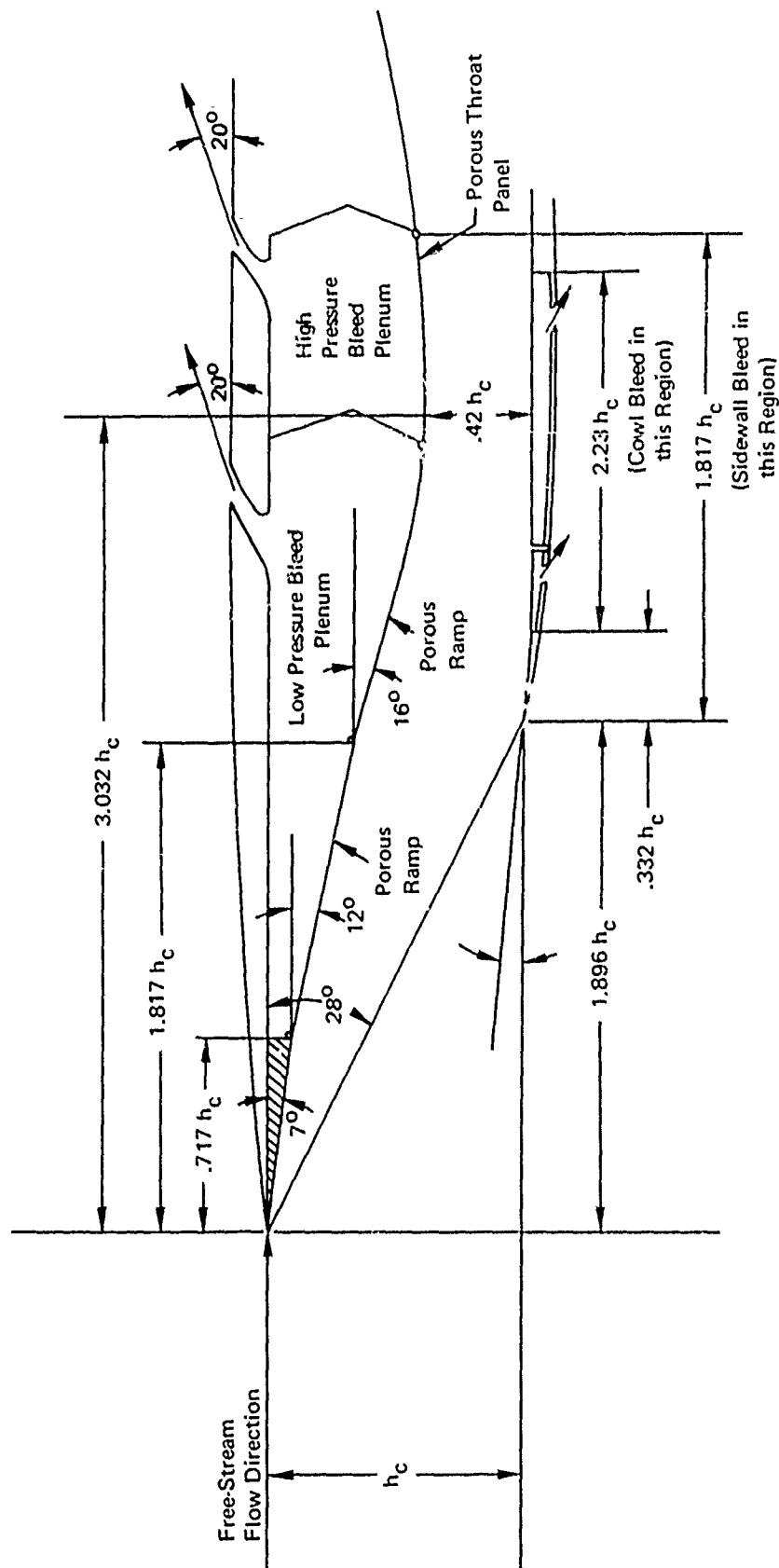with mass flow ratio used to obtain off-design matched
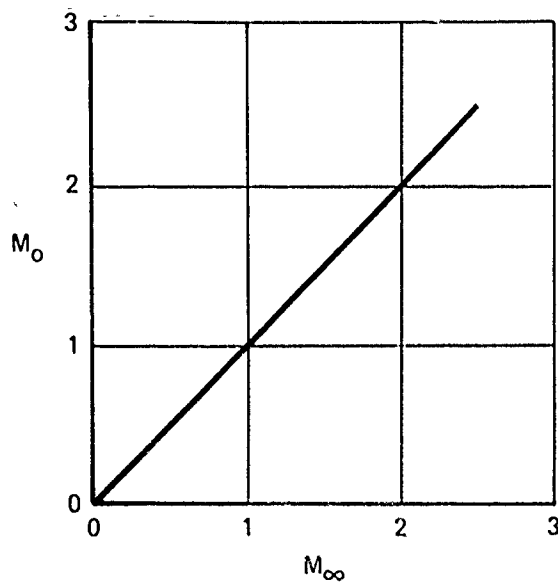
Figure 153: MACH 2.5 MIXED COMPRESSION INLET
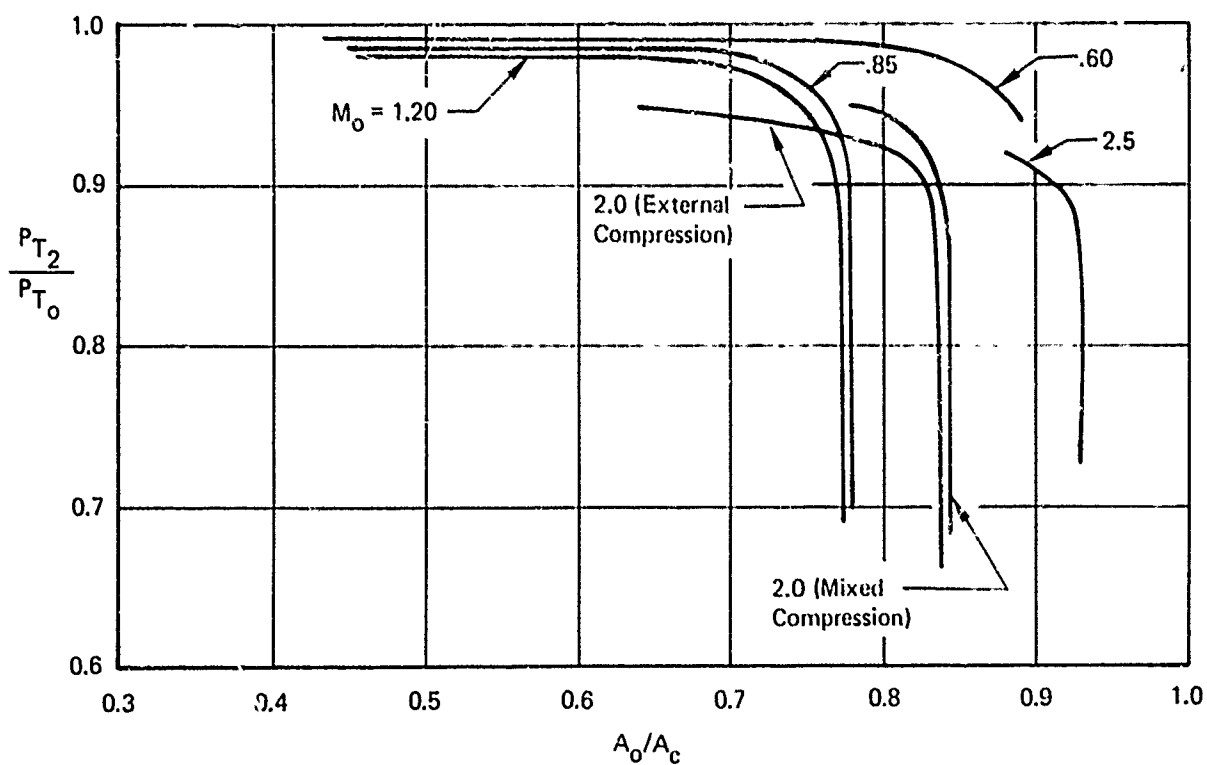
Figure 154: LOCAL MACH NUMBER

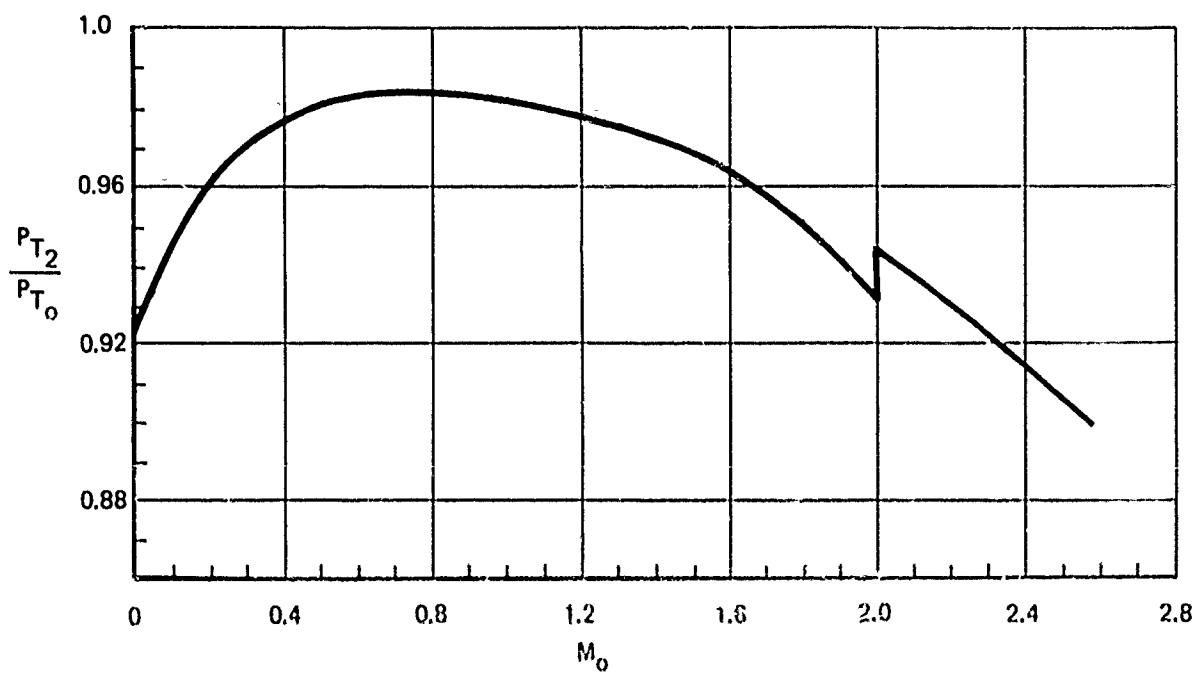

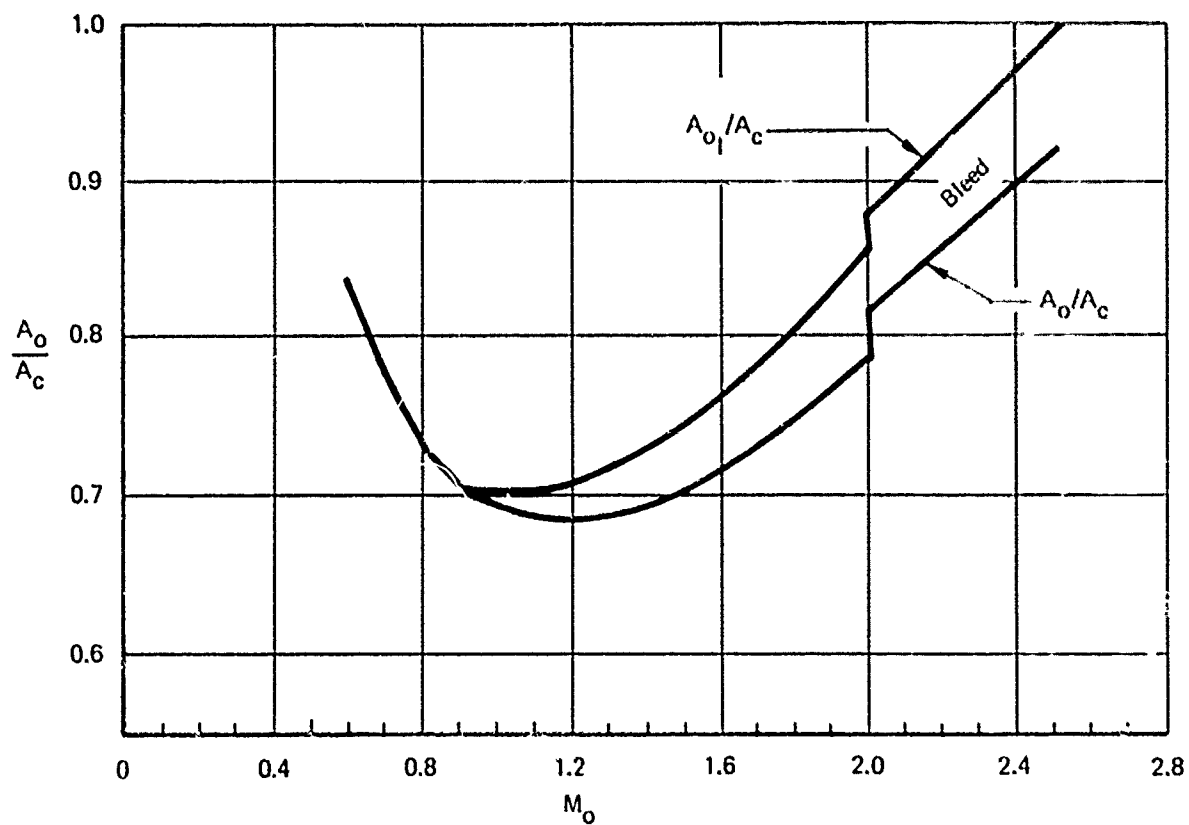Figure 155: RECOVERY VS MASS FLOW

Figure 156: PRESSURE RECOVERY VS M_o
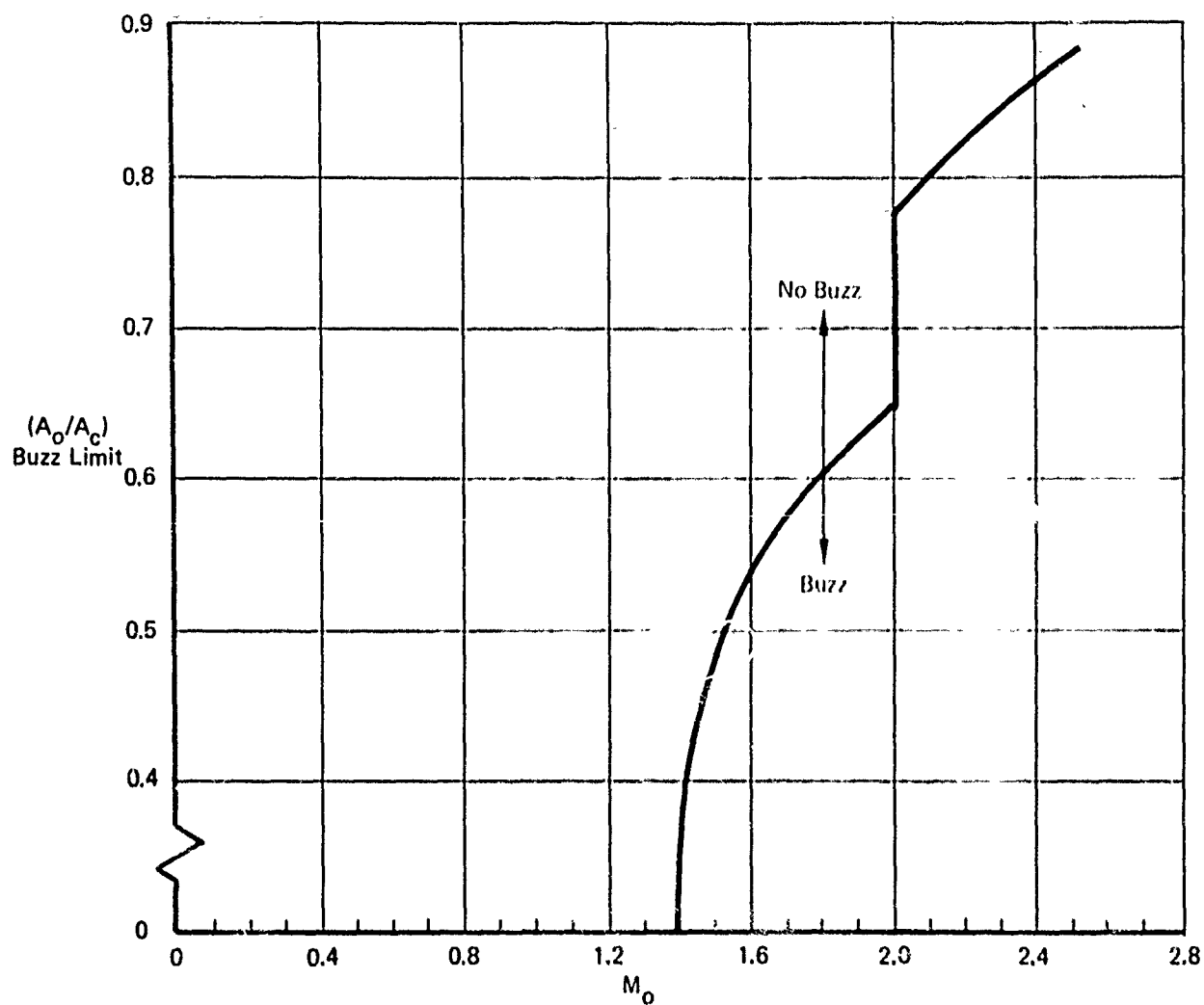

Figure 157: FLOW VS M_o

178
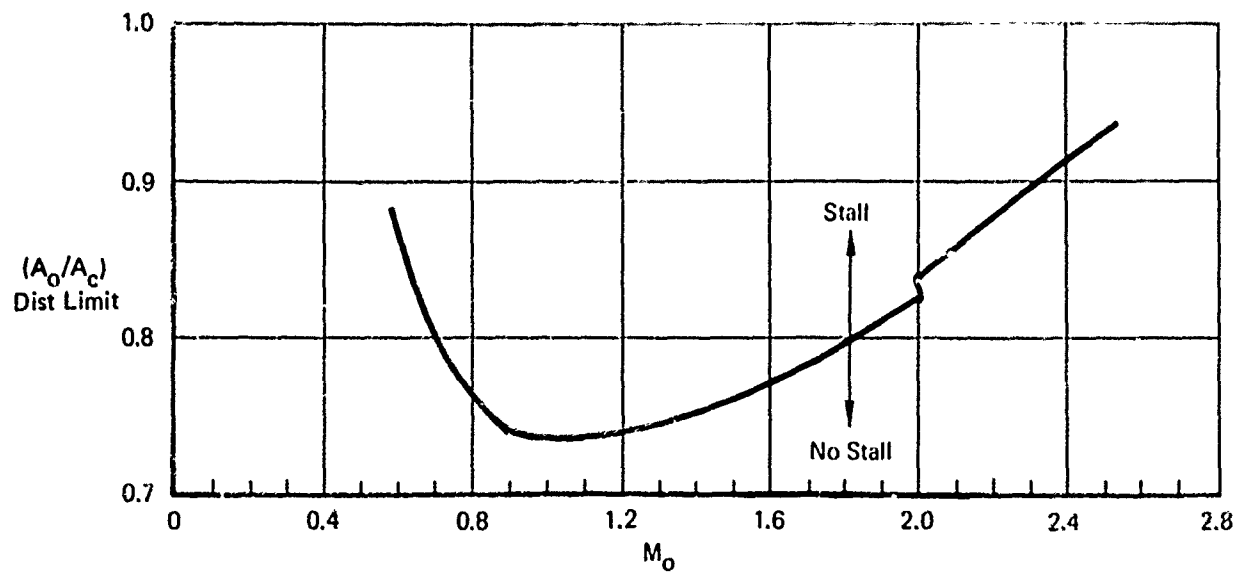
Figure 158: BUZZ LIMIT
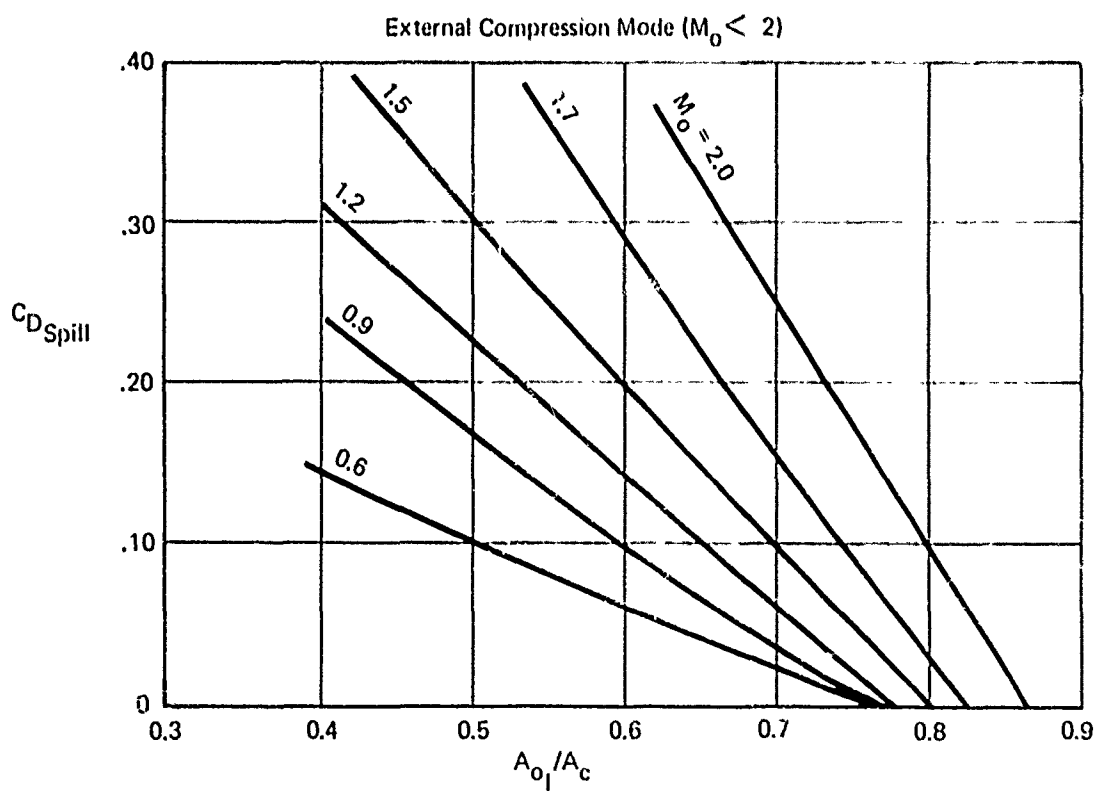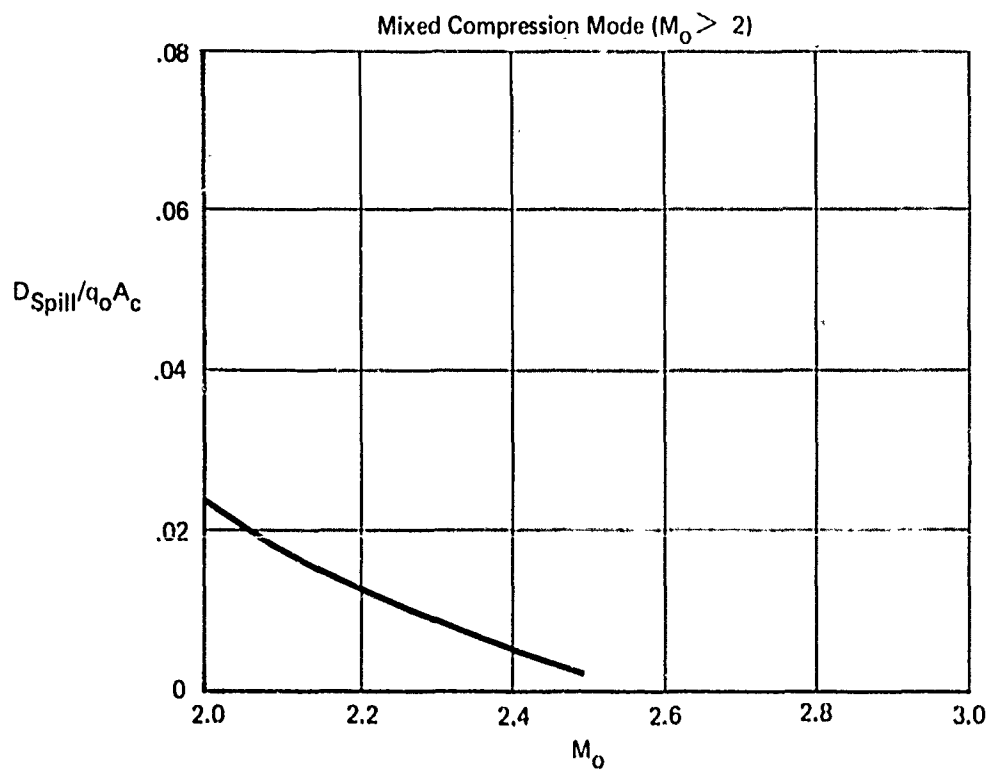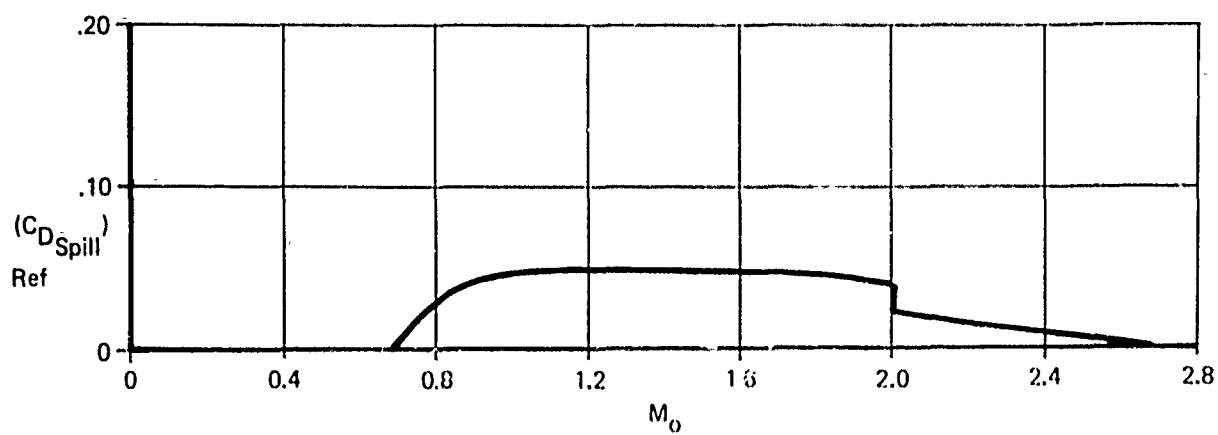

Figure 159: DISTORTION LIMIT

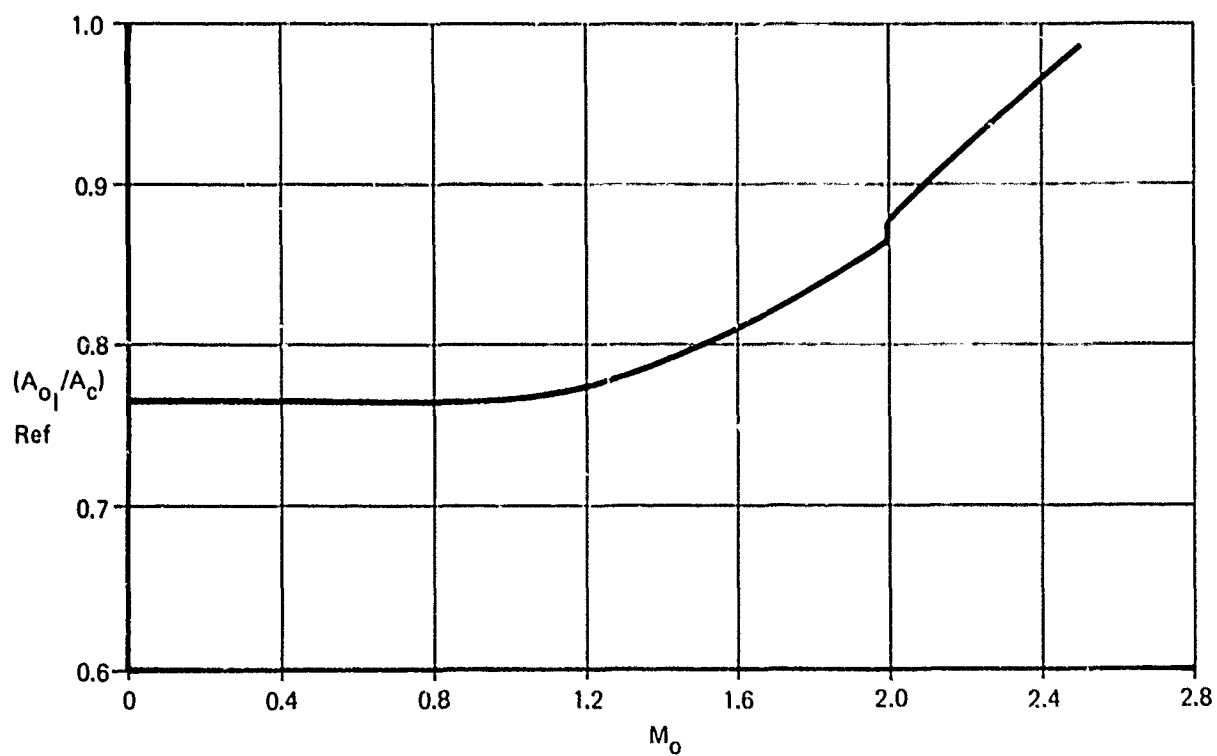Figure 160: SPILLAGE DRAG

Figure 161: REFERENCE SPILLAGE DRAG

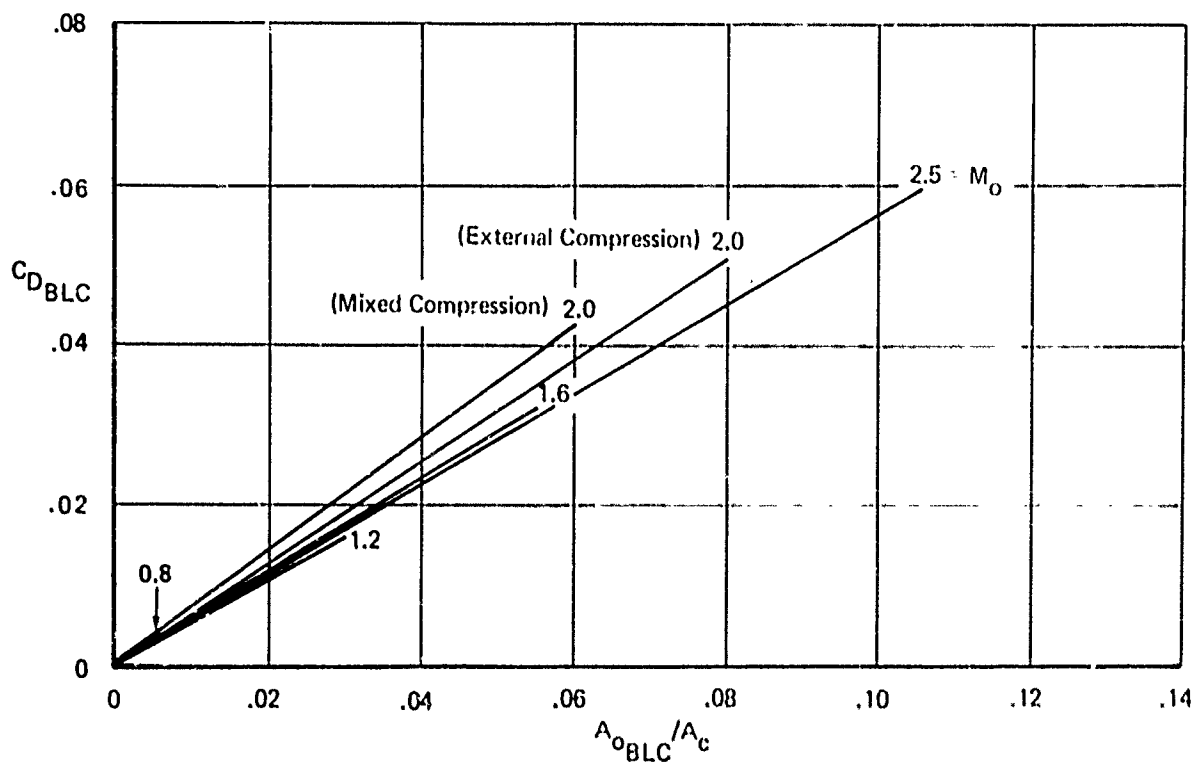*Figure 162: REFERENCE MASS FLOW RATIO*

181

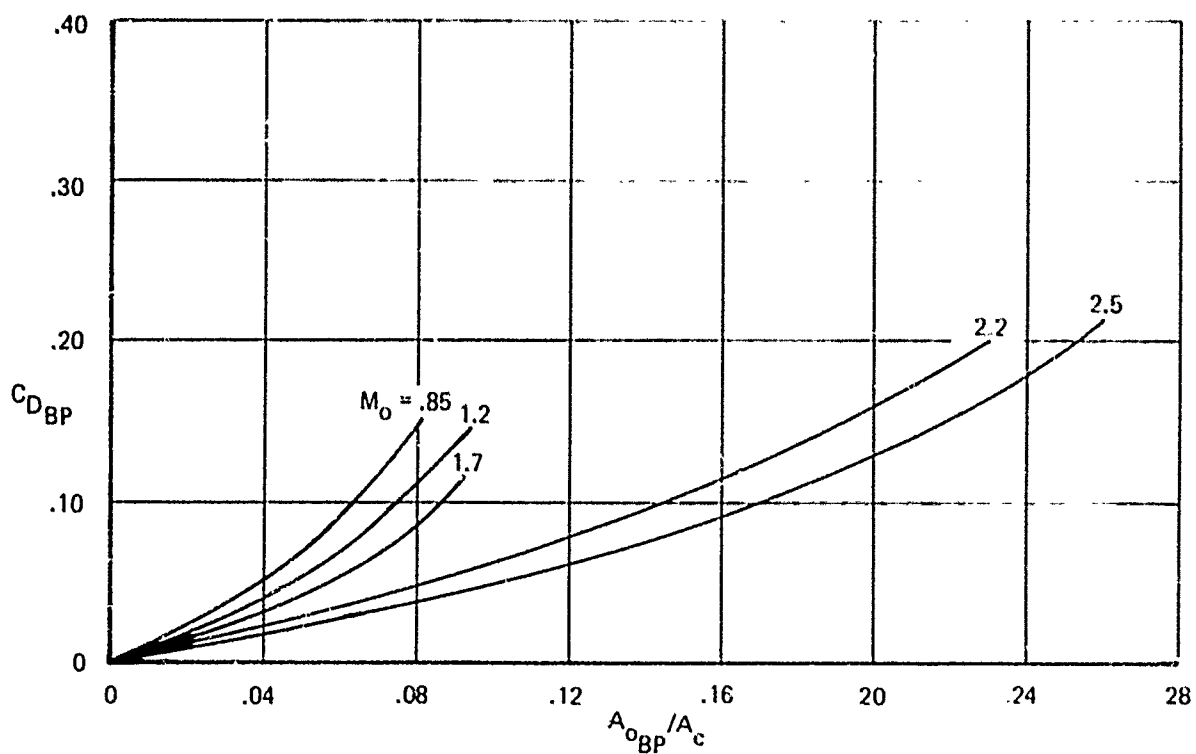*Figure 163: BLEED DRAG*

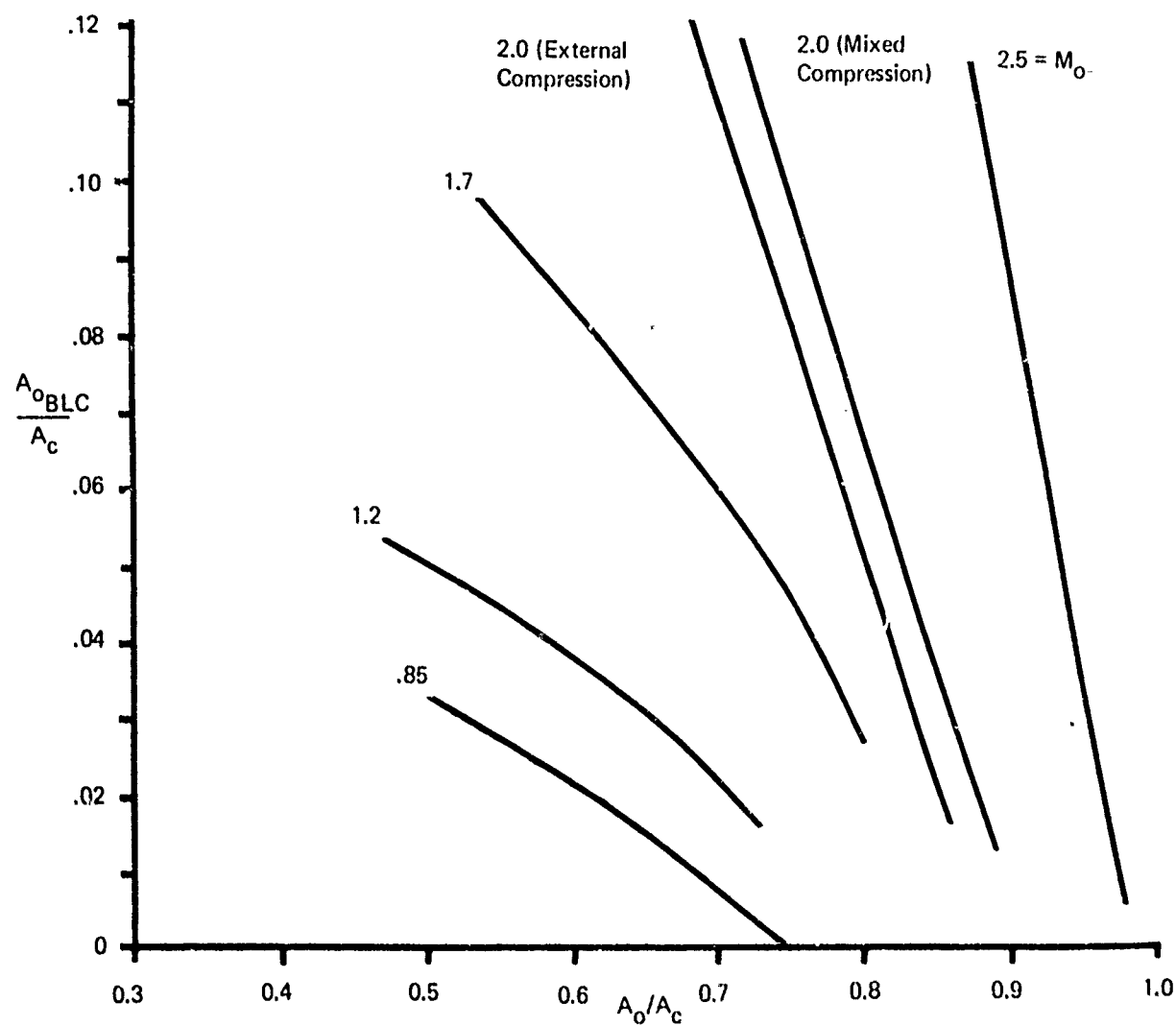*Figure 164: BYPASS DRAG*

182

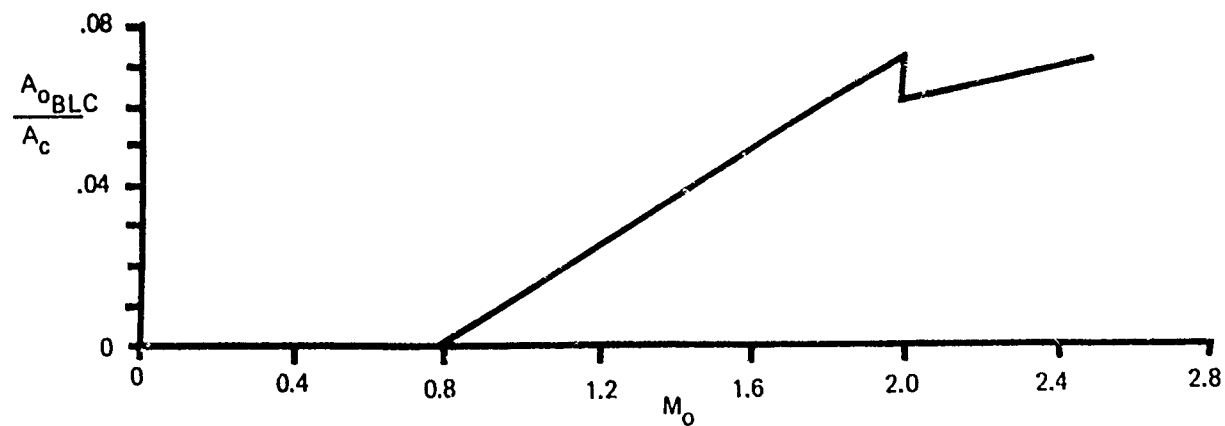Figure 165: BOUNDARY LAYER BLEED

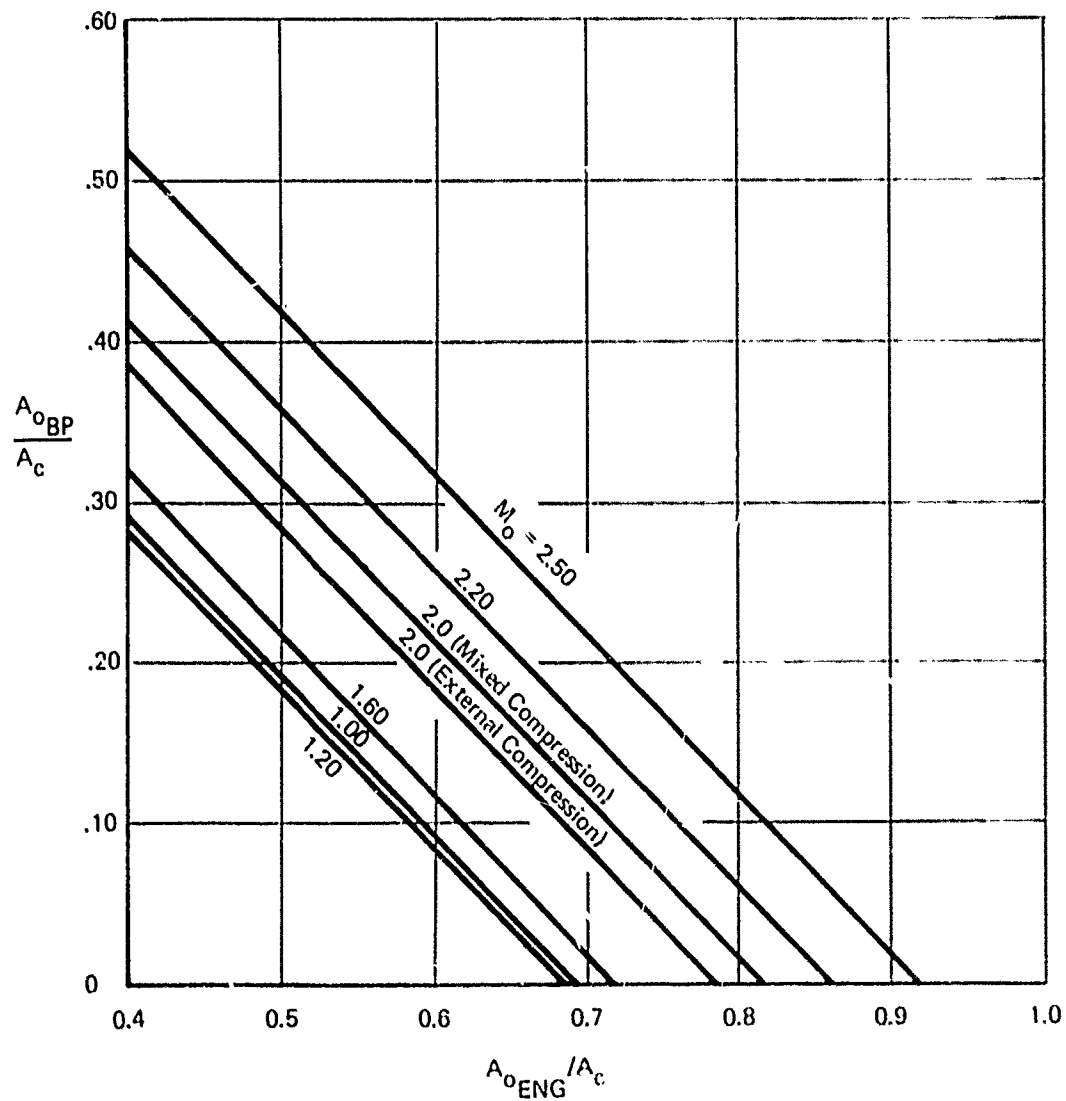
Figure 166: BLEED VS M_o

Figure 167:   BYPASS MASS FLOW

184

performance. The data are presented for a range of Mach numbers from 0.60 to 2.50. For the Mach 2.0 condition, recovery-mass flow variations are presented for both external compression and mixed-compression operating modes.

Figures 156 and 157 present the nominal (engine-matched) recovery and mass flow schedules as a function of Mach number. These schedules are based on maximum engine airflow demand. Figure 157 also shows the inlet boundary layer bleed flow required at each Mach number for the maximum airflow condition. (This is also plotted in Figure 166). At other than maximum airflow condition, the bleed airflow can be determined from Figure 165 which shows bleed airflow as a function of duct airflow.

Figures 158 and 159 show the estimated buzz and stall limits used to indicate probable conditions where stability problems are likely to be encountered. The inlet spillage drag is presented in Figure 160. For the mixed compression mode ($M_0 > 2$), the spillage drag is shown only as a function of Mach number, since the inlet will be started and excess airflow will be bypassed instead of spilled. The spillage drag shown in Figure 160 for started operation ($M_0 > 2$) is included in the reference drag of Figure 161 and does not need to be included separately in the engine-installed performance calculation. For external compression mode operation, spillage drag is presented as a function of both Mach number and inlet airflow since internal spillage is possible in addition to bypassed airflow.

The spillage drag presented in Figure 160 is the spillage drag in excess of the reference drag shown in Figure 161 which is included in the aerodynamic drag polar, rather than being included in the engine-installed thrust calculation. This is in accordance with the bookkeeping system described in Section II.

The reference mass flow used to calculate the reference spillage drag is presented in Figure 162.

Figures 163 and 164 present the performance maps used to estimate boundary layer bleed drag and bypass drag as a function of the amount of bleed or bypass airflow for each Mach number. Although bypass drag data (as a function of bypass airflow) are shown for $M_0 = 0.85$, no bypass is used below $M_0 = 1.20$, because trade studies for this configuration showed that a higher drag penalty would be incurred by bypassing air below $M_0 = 1.20$ than by spilling it around the inlet.

Figure 167 presents the bypass airflow schedule used during the performance calculation. Again, though, it should be noted that no bypass is used below $M_O = 1.20$, although the variation for $M_O = 1.0$ is shown in the plotted data.

4.1.4 VARIABLE-GEOMETRY, MIXED-COMPRESSION INLETS

The inlet geometry details are shown in Figure 184. The inlet is a mixed-compression type, with inlet "starting" occurring at Mach 2.0. Below Mach 2.0, the inlet operates in the external compression mode. Extensive boundary layer bleed is used on the inlet internal ramps, sideplates, and cowl to avoid problems with shock-boundary layer interactions. Three separate plenum chambers are used for collecting the boundary layer bleed air before it is exited overboard through choked convergent exit nozzles. The use of three separate plenums makes it possible to operate with a relatively high plenum pressure and hence, less drag.

The inlet ramp system is designed to provide shock-on-lip operation at Mach 3.0. Approximately 1% supersonic spillage is allowed to help insure that shocks are not ingested at inadvertent overspeed conditions or transient angle-of-attack maneuvers. Full sideplates are provided to minimize sideplate spillage.

A variable bypass system is provided ahead of the engine to bypass excess inlet airflow and help restart the inlet. The maximum bypass door throat area is 0.50 A_C. It is assumed that a maximum inlet throat area equal to at least 0.70 A_C can be achieved by retracting the ramps. The requirement for take-off doors to provide good recovery and low distortion during take-off will be examined when engine airflow demand characteristics are known.

The estimated inlet performance characteristics are shown in Figures 185 through 198.

Figure 185 shows the variation of inlet local Mach number with free-stream Mach number. Since the airplane design was not available, it has been assumed that the local and free-stream Mach numbers are the same.

The total pressure recovery versus mass flow plots presented in Figure 186 have been estimated by using the test results from XB-70, SST, Boeing in-house studies and tests and theory. The recommended operating (match point) recovery and mass flow as a function of free-stream Mach number are shown in Figures 187 and 188, respectively.
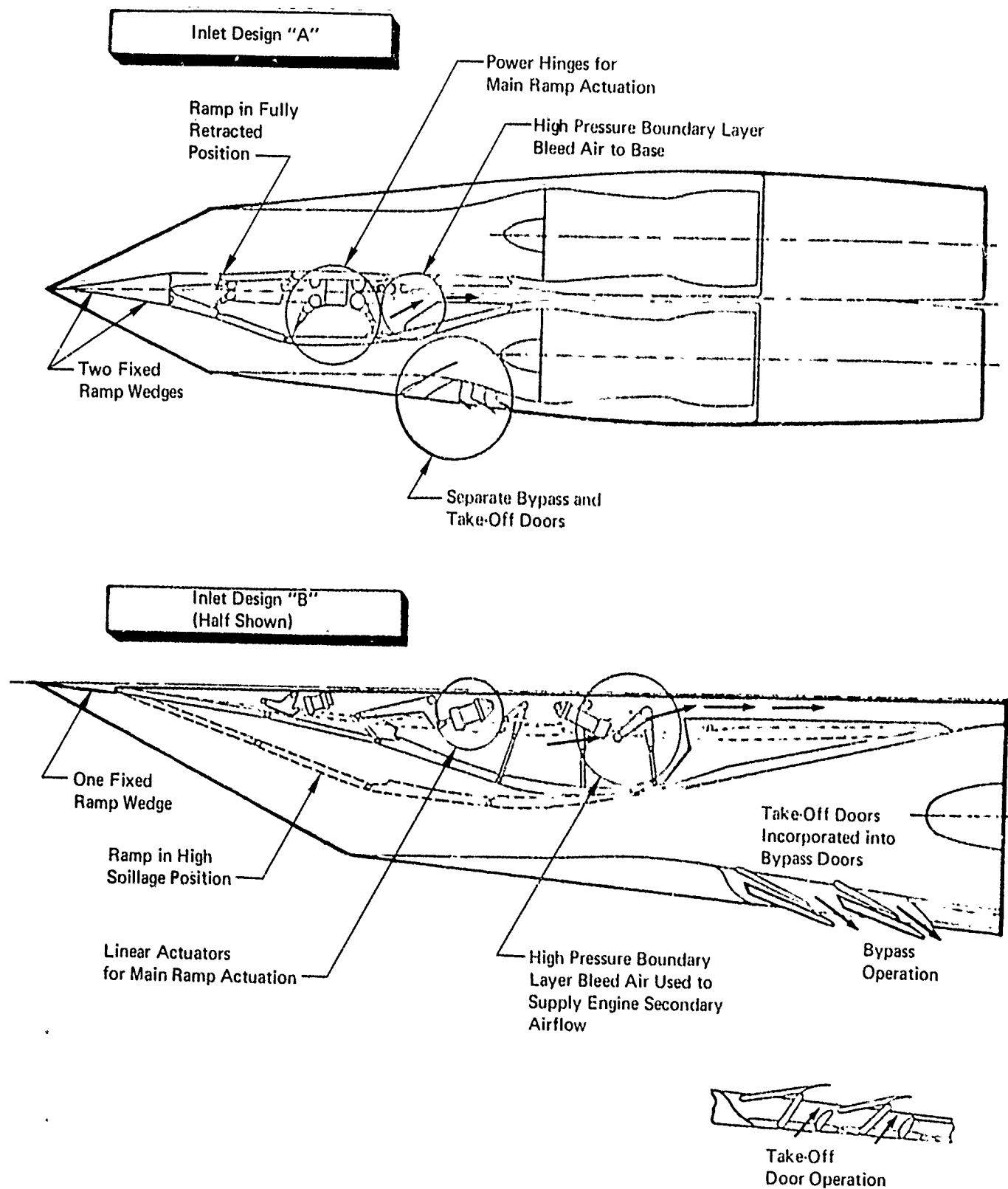
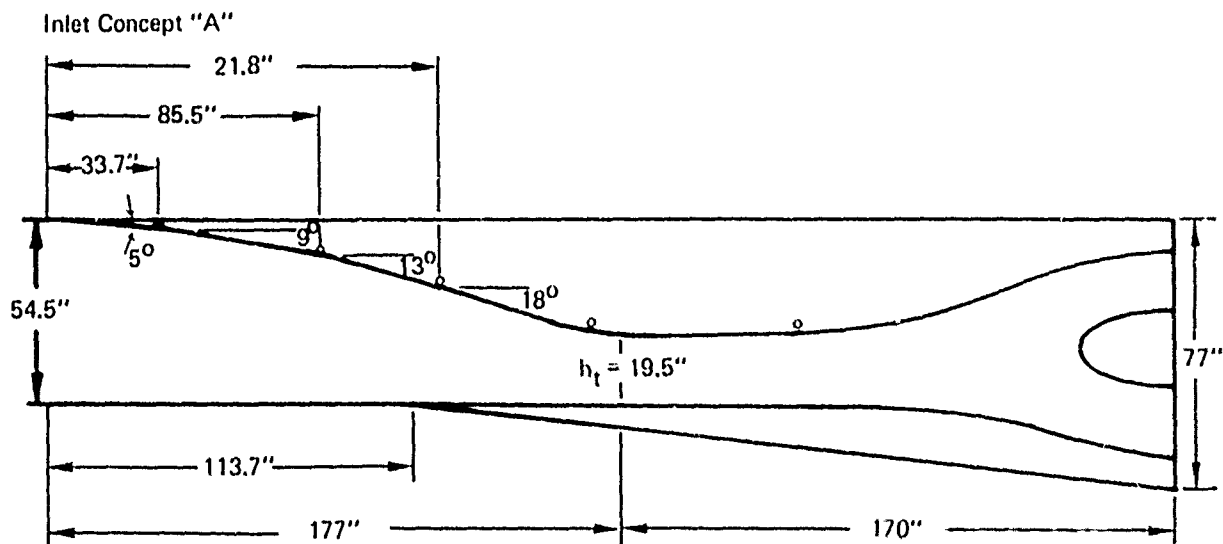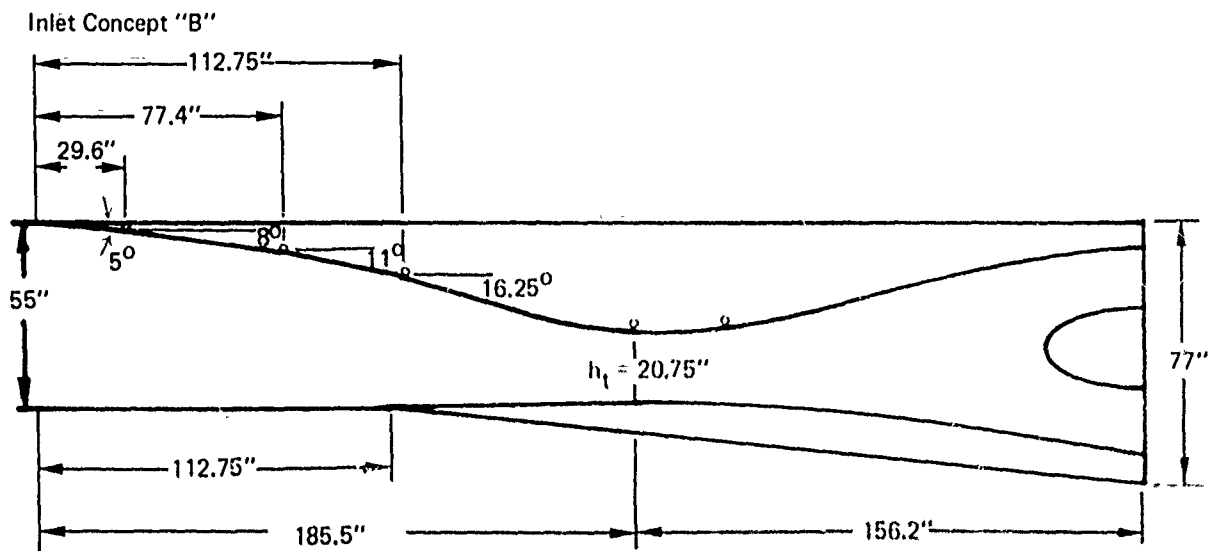Figure 168: *MACH 2.70 TWO-DIMENSIONAL, MIXED COMPRESSION INLET DESIGNS*
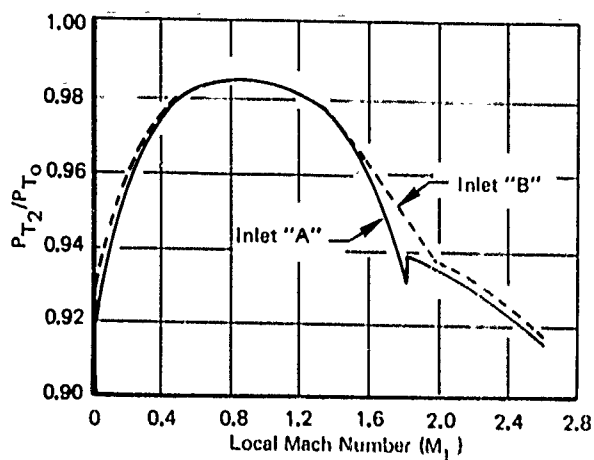
Figure 169 : *TWO-DIMENSIONAL INLET GEOMETRIES*

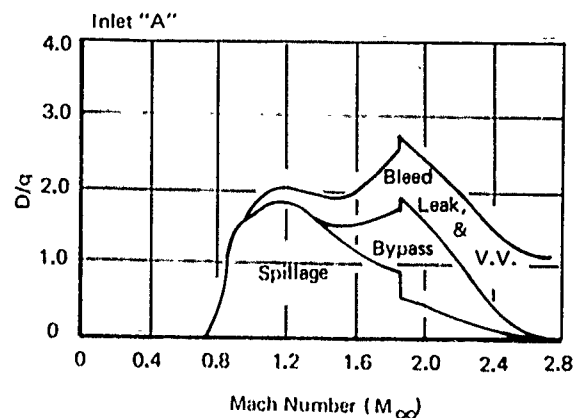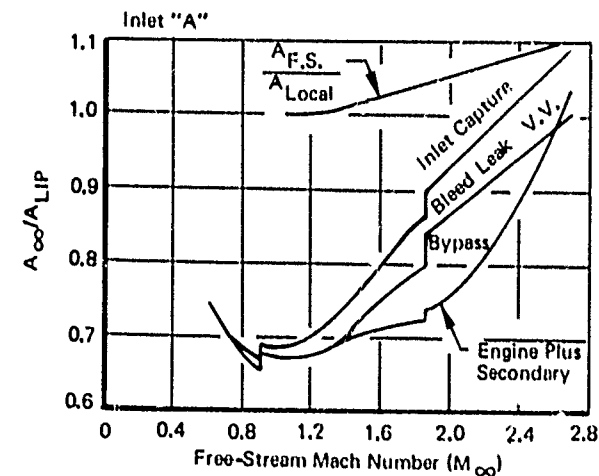188

Figure 170 : TOTAL PRESSURE
RECOVERY

Figure 171 : MASS FLOW
CHARACTERISTICS
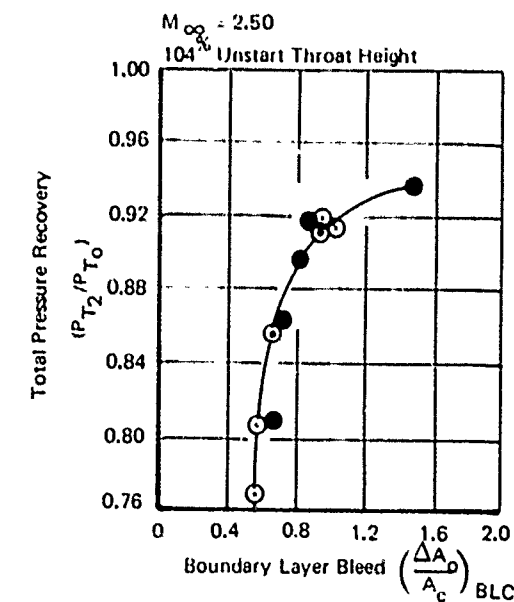

Figure 172 : INLET DRAG

Figure 173 : EXPERIMENTAL
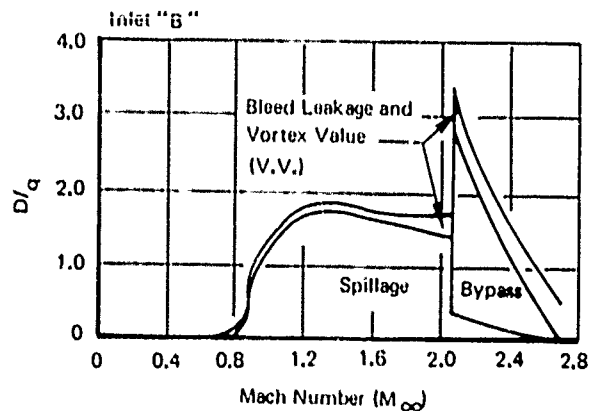PRESSURE RECOVERY
AND BLEED FLOW FROM
0.076 SCALE MODEL TEST

189
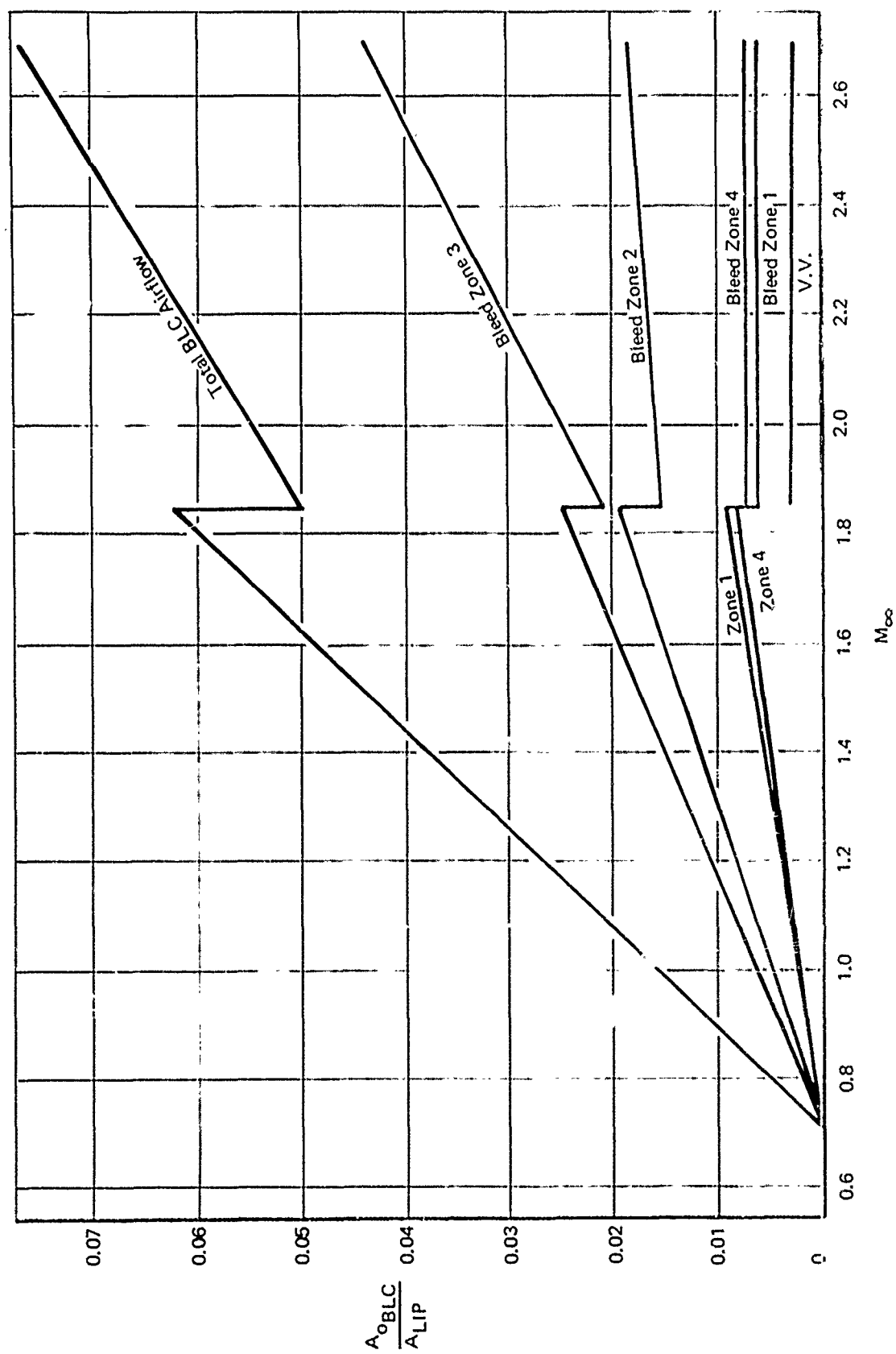
Figure 174. BLC SYSTEM BLEED AIRFLOW SCHEDULE – 2-D INLET
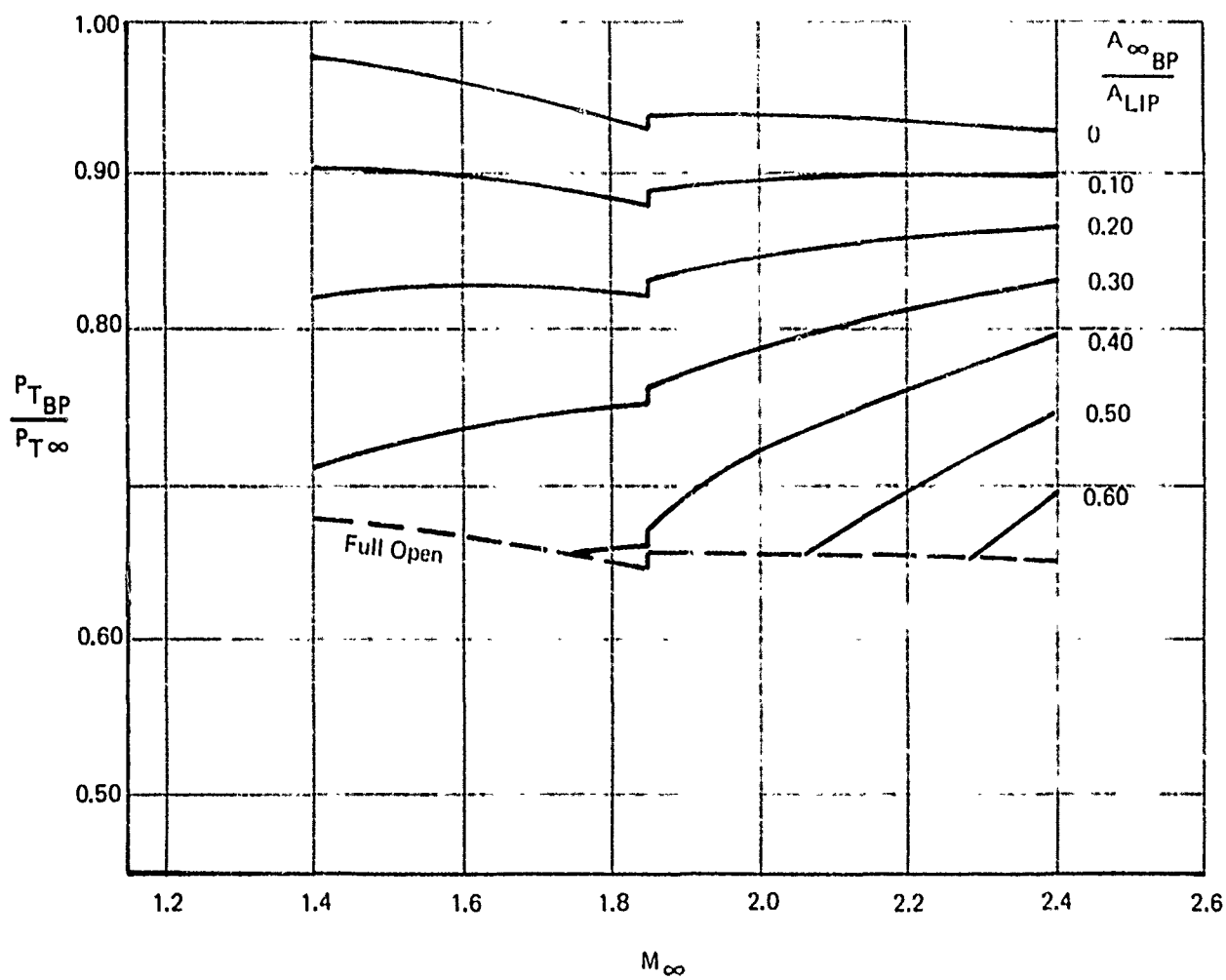
Figure 175 :   BYPASS TOTAL PRESSURE RECOVERY (2-D INLET)
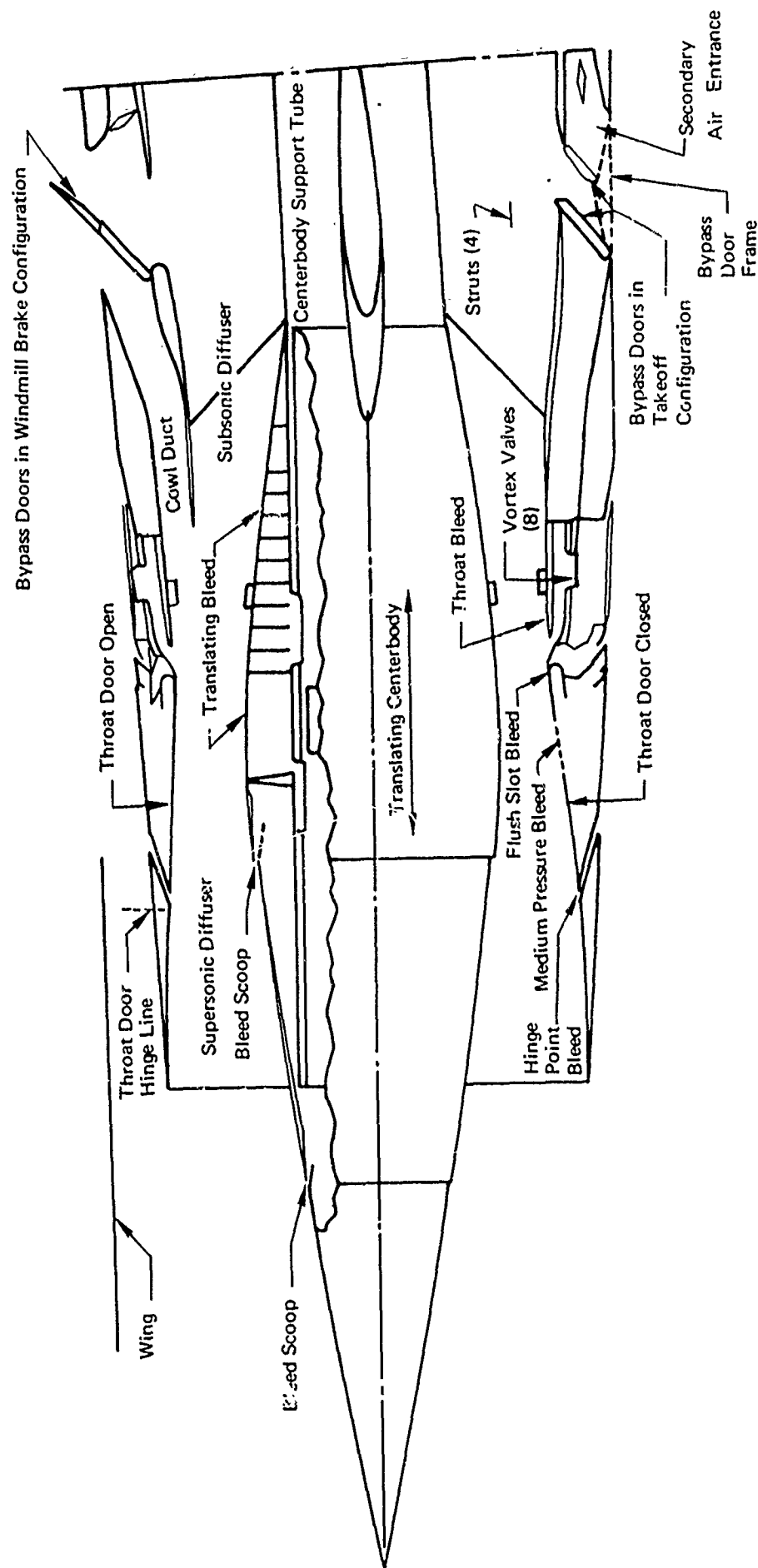
Figure 176: $M_o = 2.65$ AXISYMMETRIC-MIXED-COMPRESSION INLET
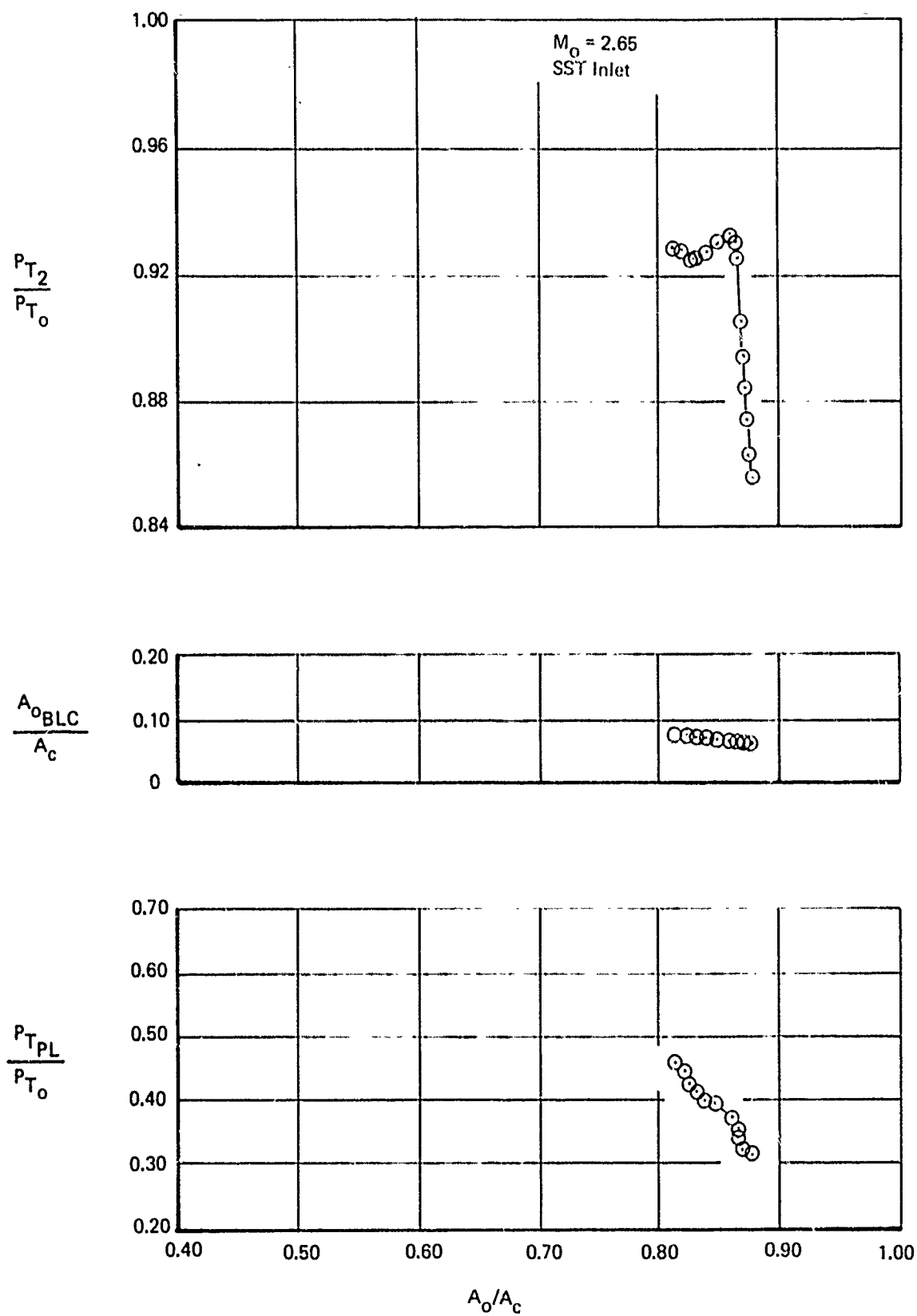
Figure 177 : *INLET PERFORMANCE FOR A MIXED COMPRESSION INLET*
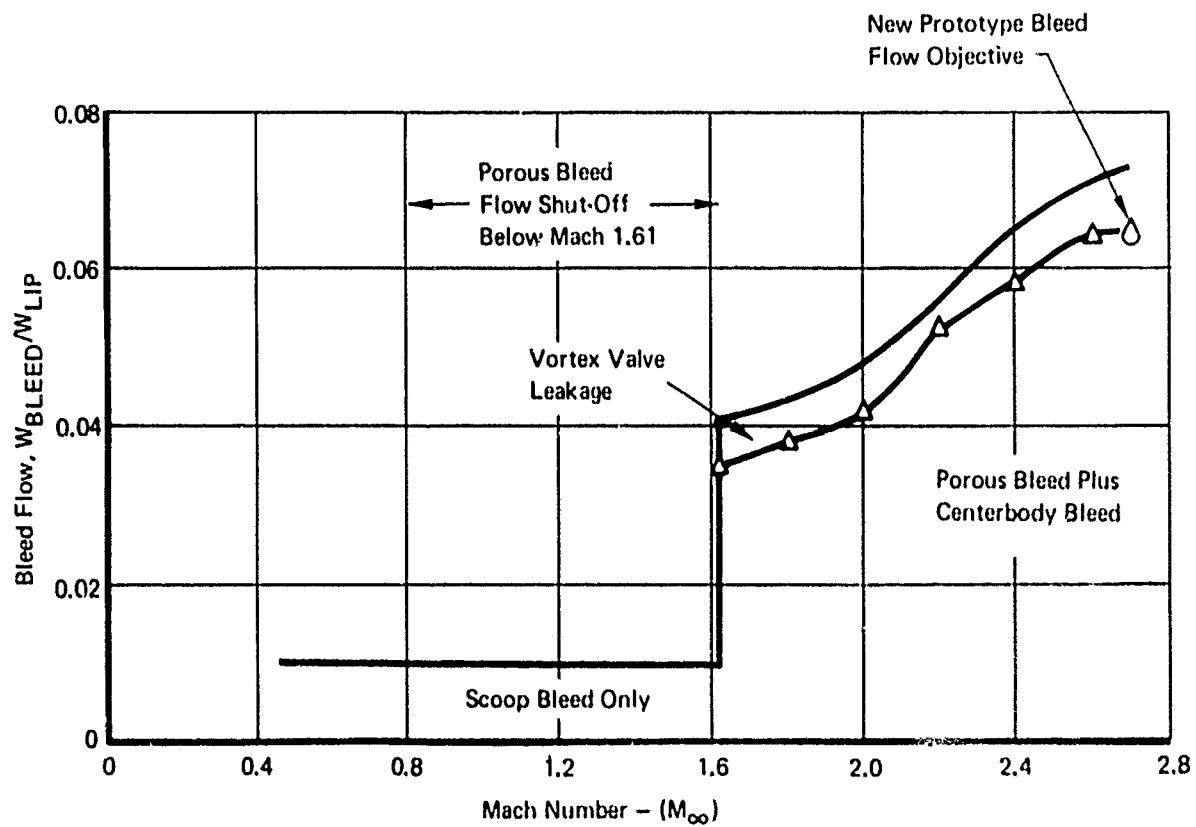
Figure 178: INTAKE BLEED FLOW SCHEDULE
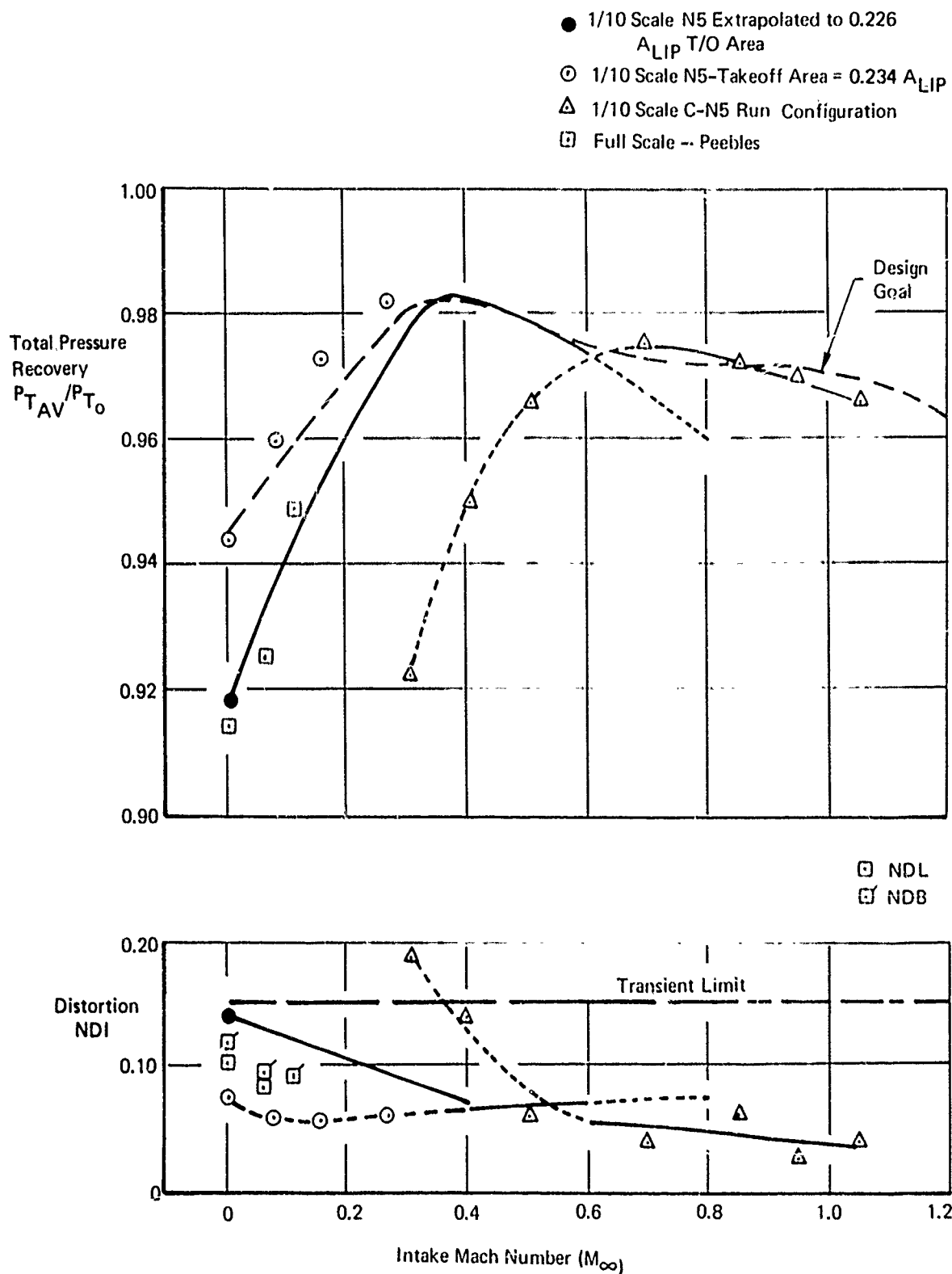
Figure 179: SUBSONIC INTAKE PERFORMANCE

195
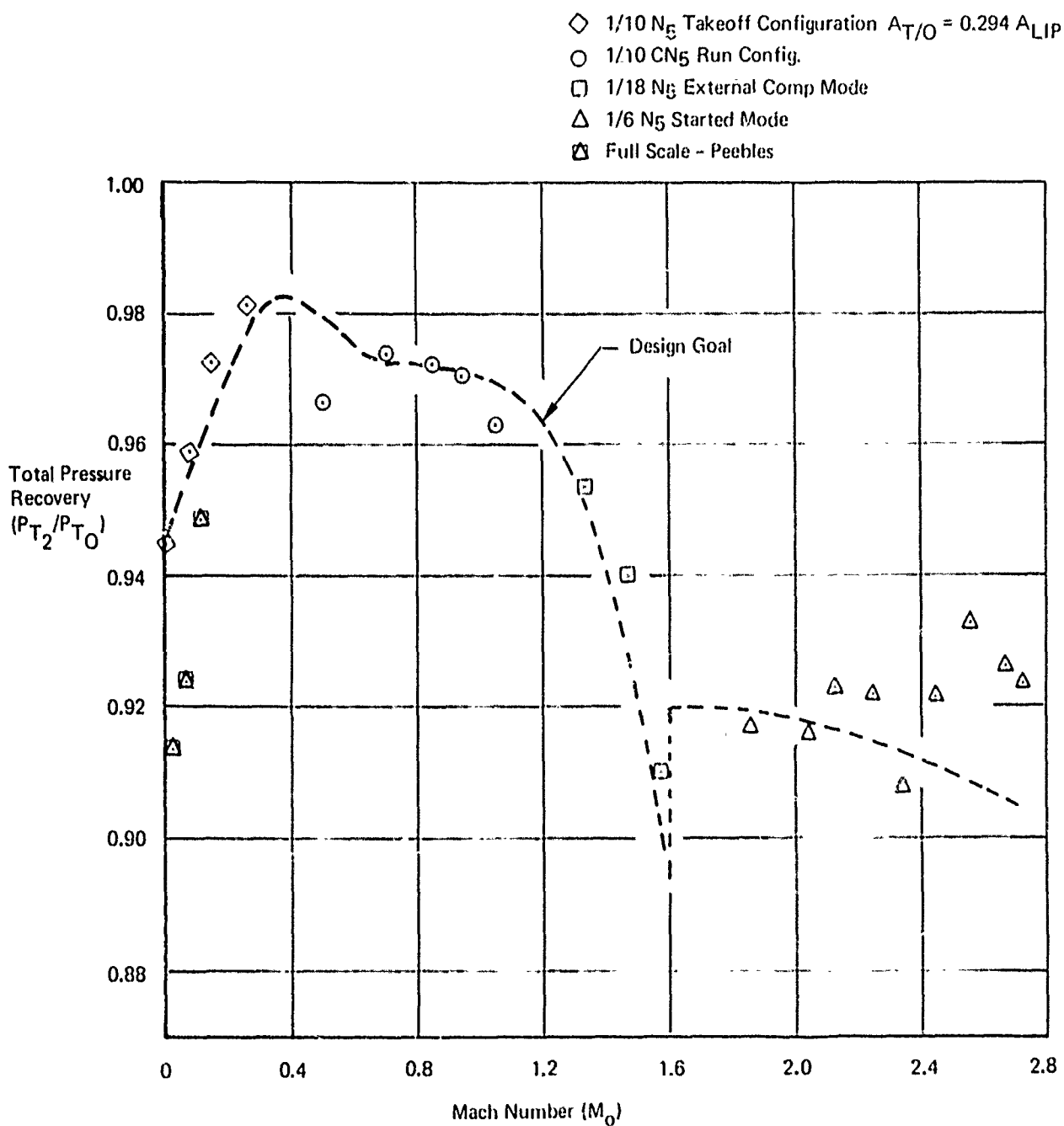
Figure 180: *MATCHED INTAKE TOTAL PRESSURE RECOVERY*
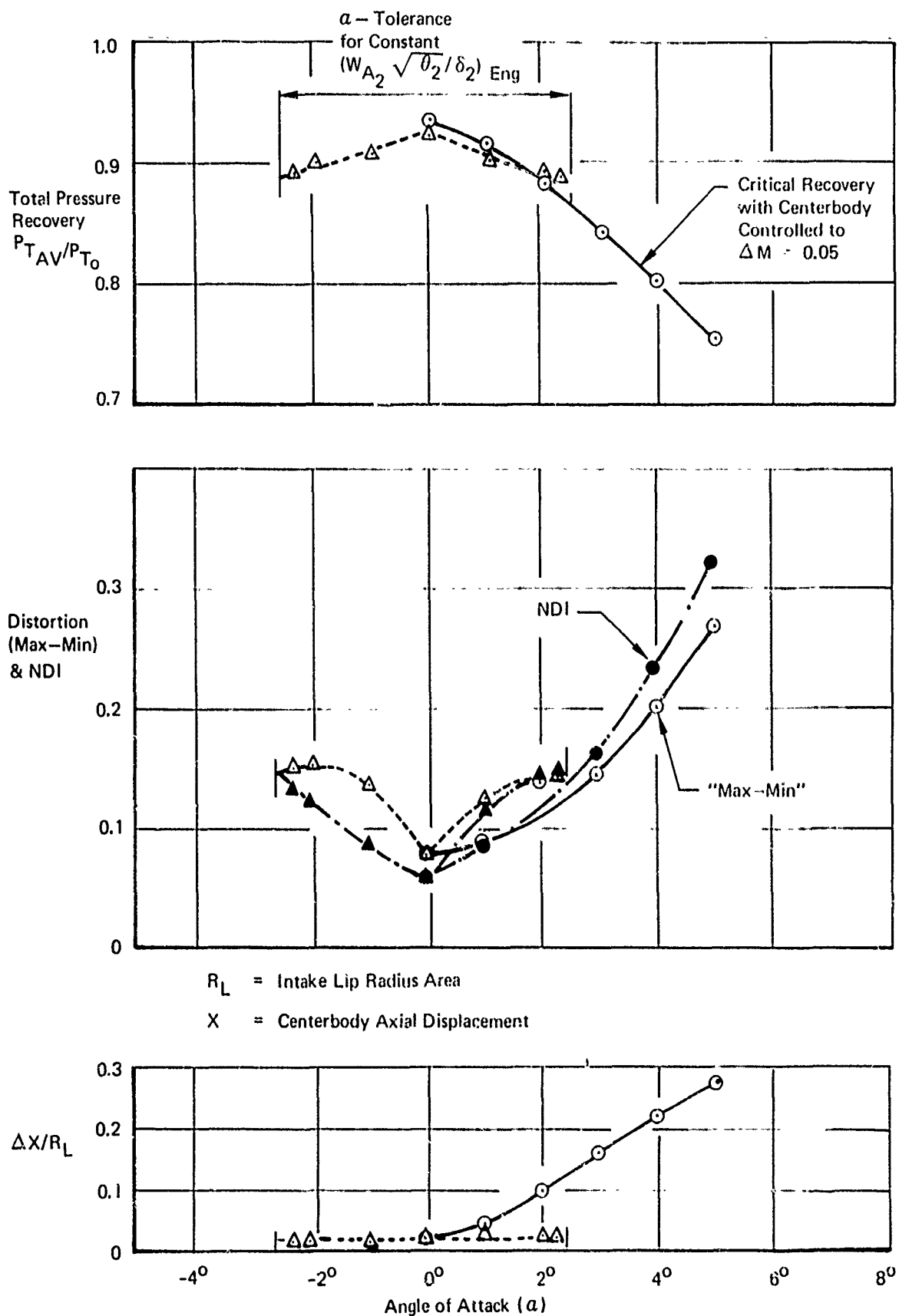
Figure 181 : ANGLE OF ATTACK PERFORMANCE 1/6 SCALE N_5 MODEL
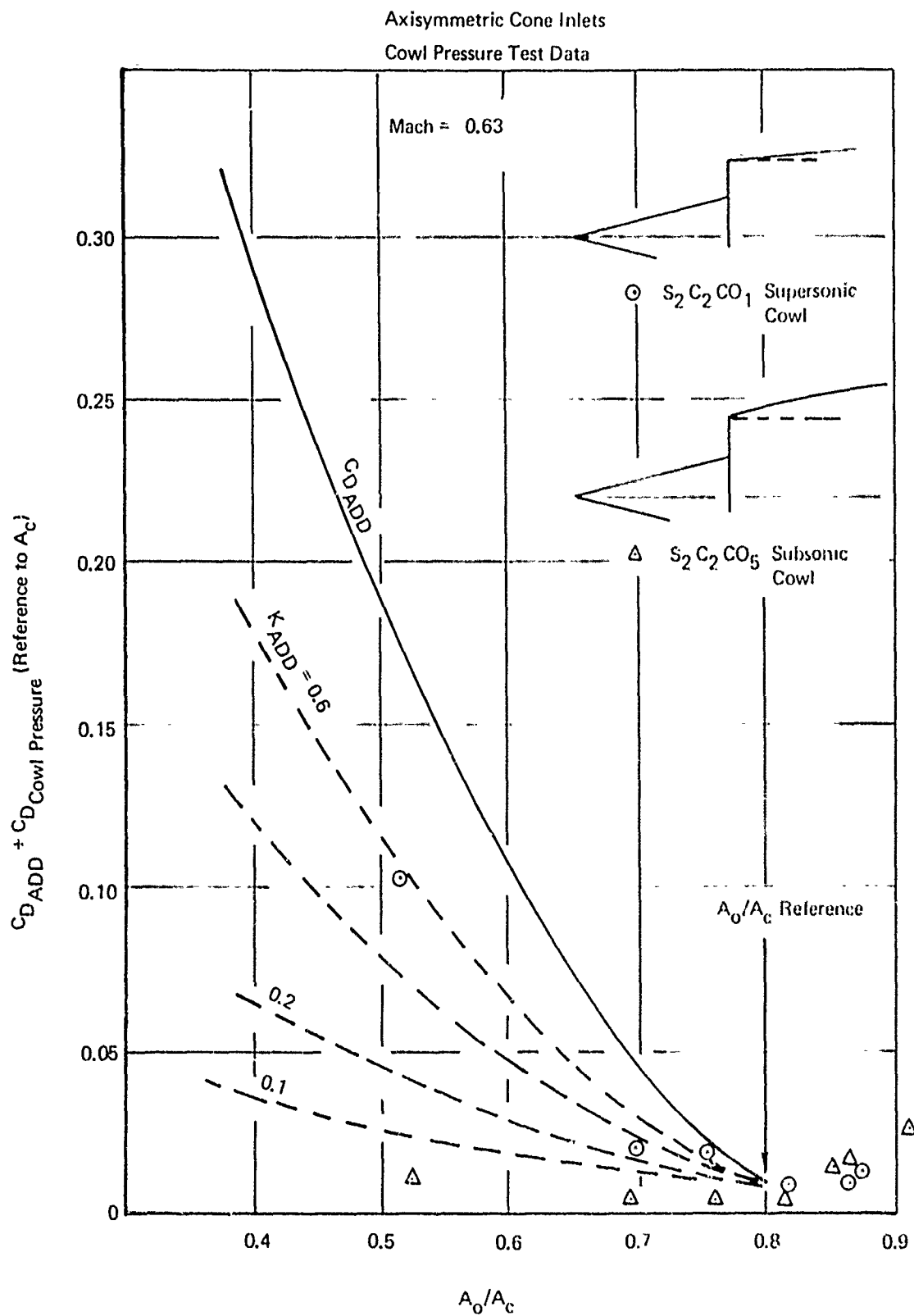
Figure 182 : COWL PRESSURE TEST DATA
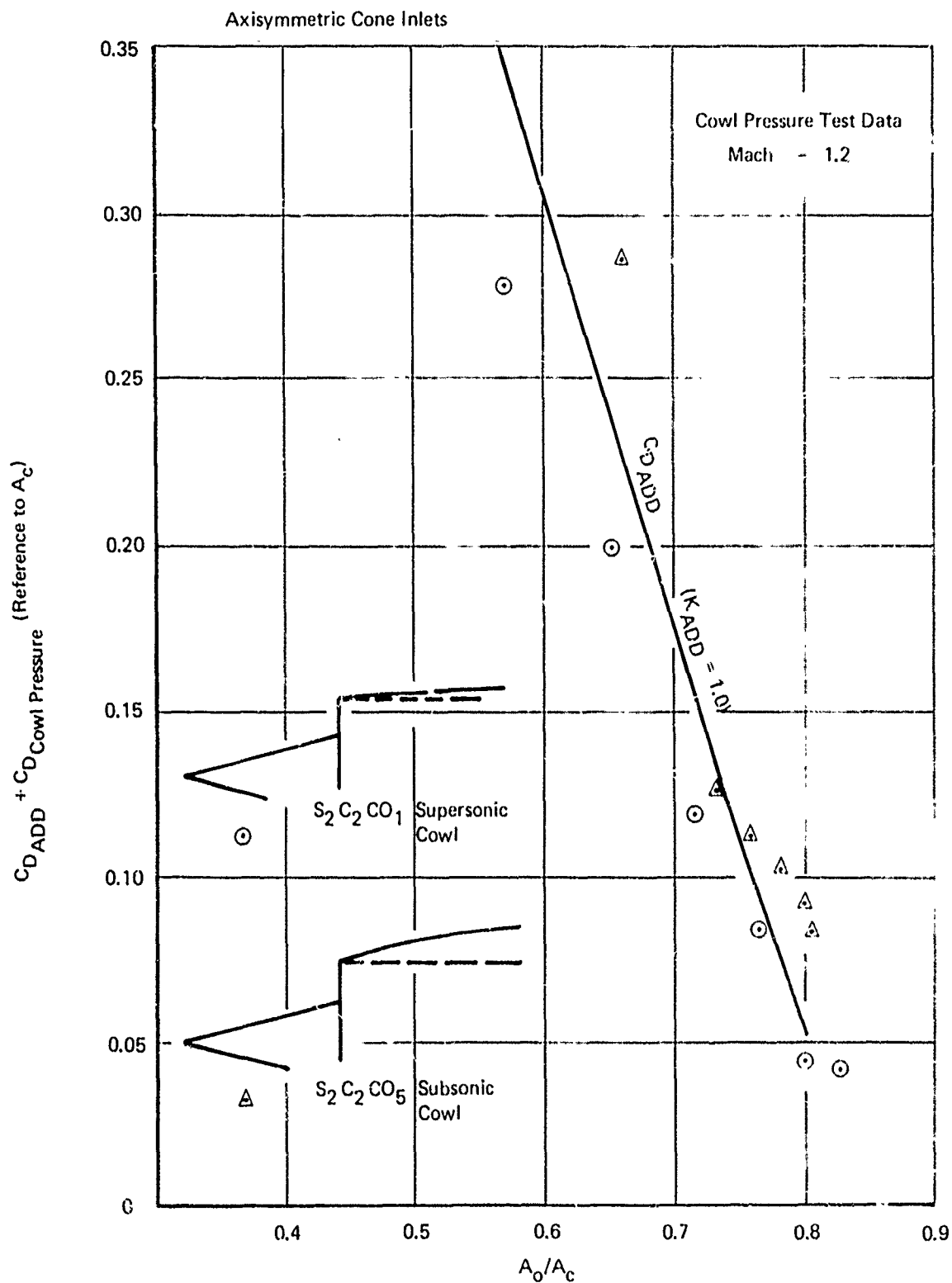
Figure 183: COWL PRESSURE TEST DATA
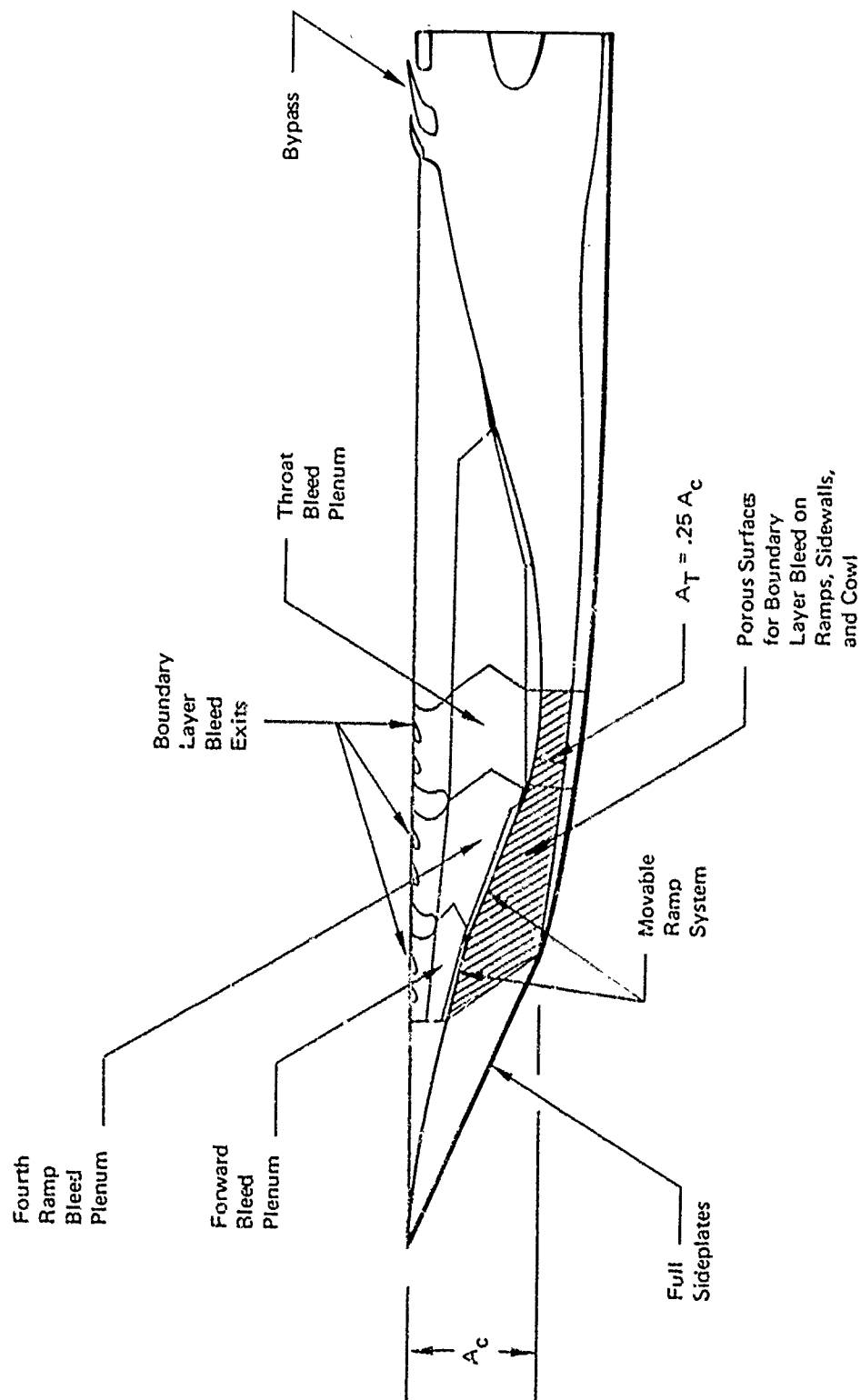
Figure 184: MACH 3 MIXED COMPRESSION INLET

Bypass

Throat
Bleed
Plenum

Boundary
Layer
Bleed
Exits

$A_T = .25 \, A_c$

Porous Surfaces
for Boundary
Layer Bleed on
Ramps, Sidewalls,
and Cowl

Fourth
Ramp
Bleed
Plenum

Forward
Bleed
Plenum

Movable
Ramp
System

Full
Sideplates

A_c
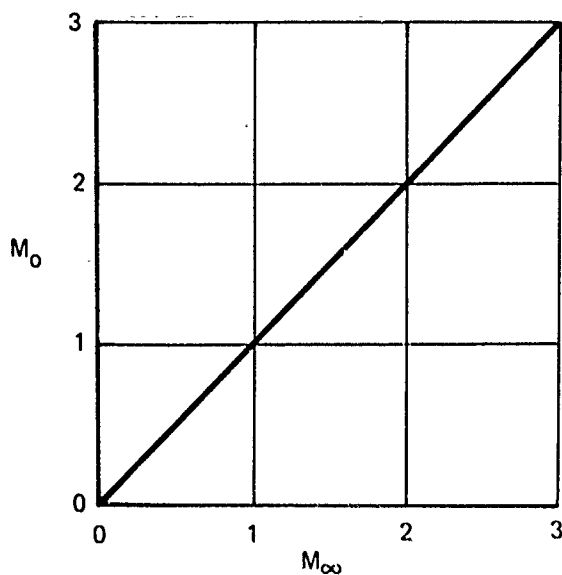
Figure 185: LOCAL MACH NUMBER
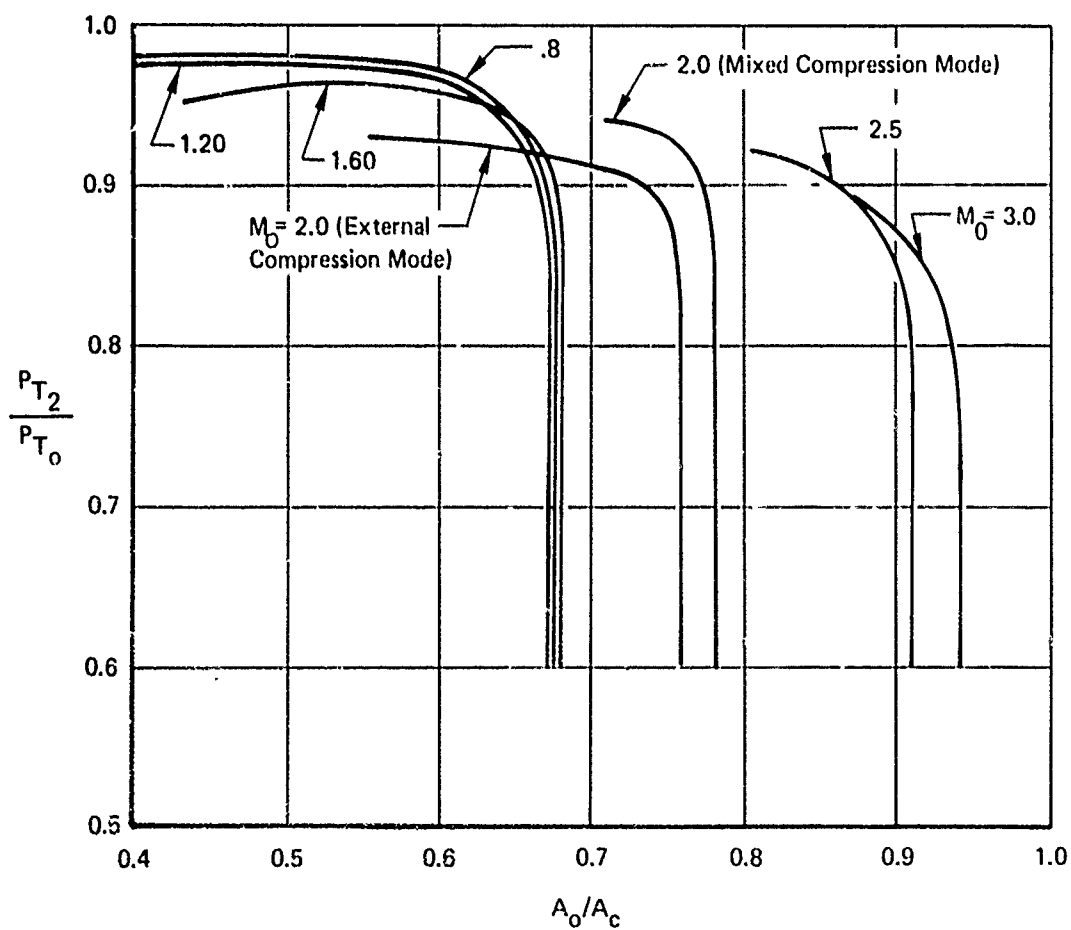
Figure 186: RECOVERY VS MASS FLOW
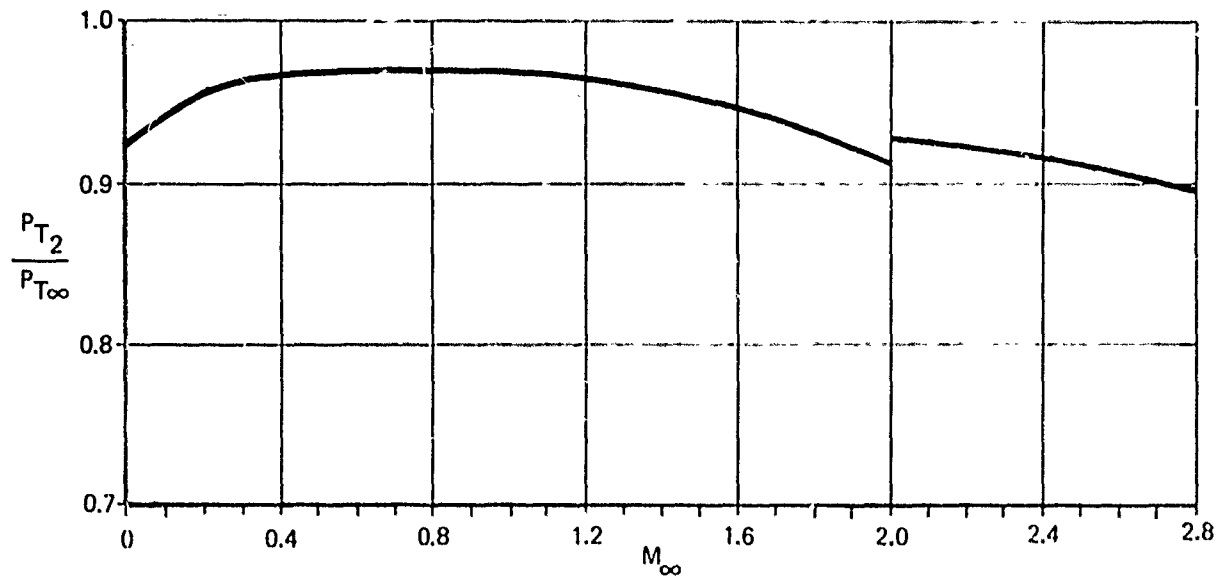
Figure 187: TOTAL PRESSURE RECOVERY
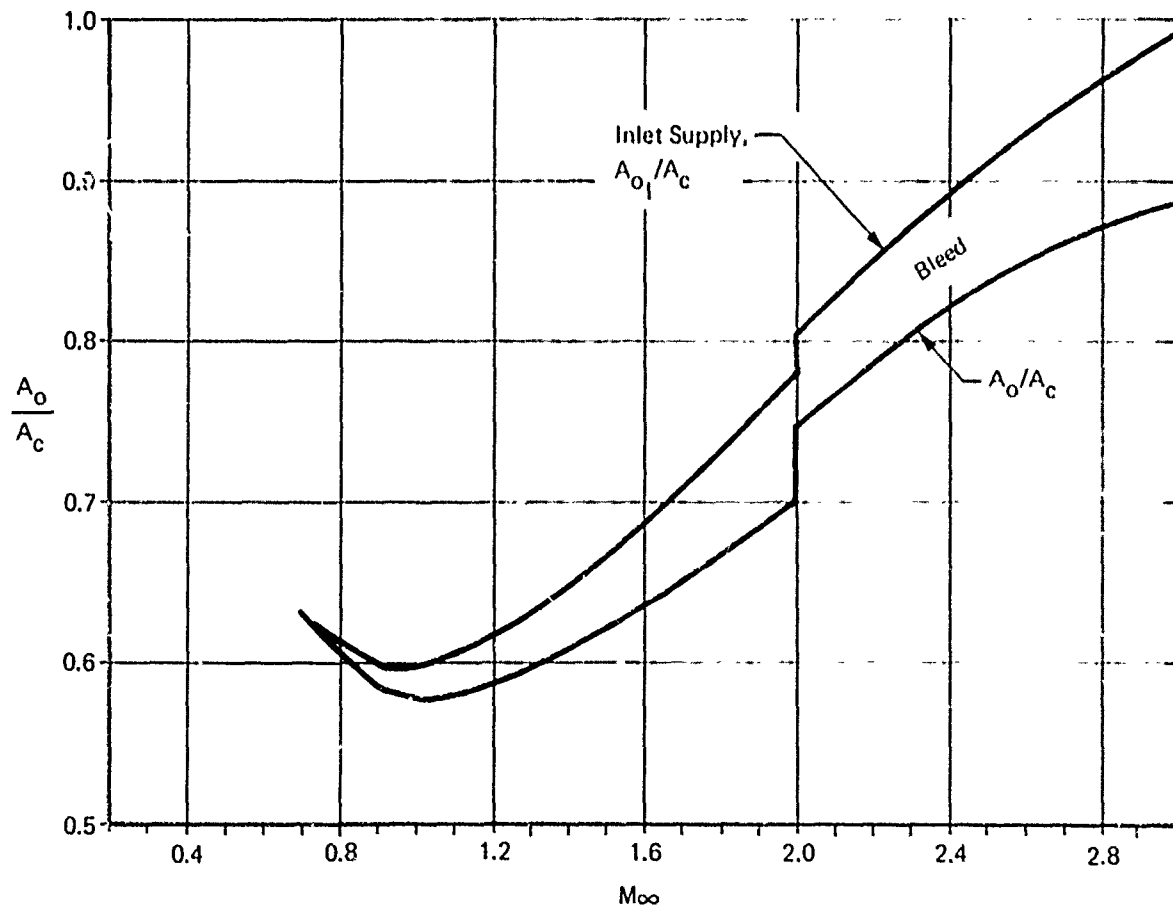
Figure 188:   MASS FLOW RATIO
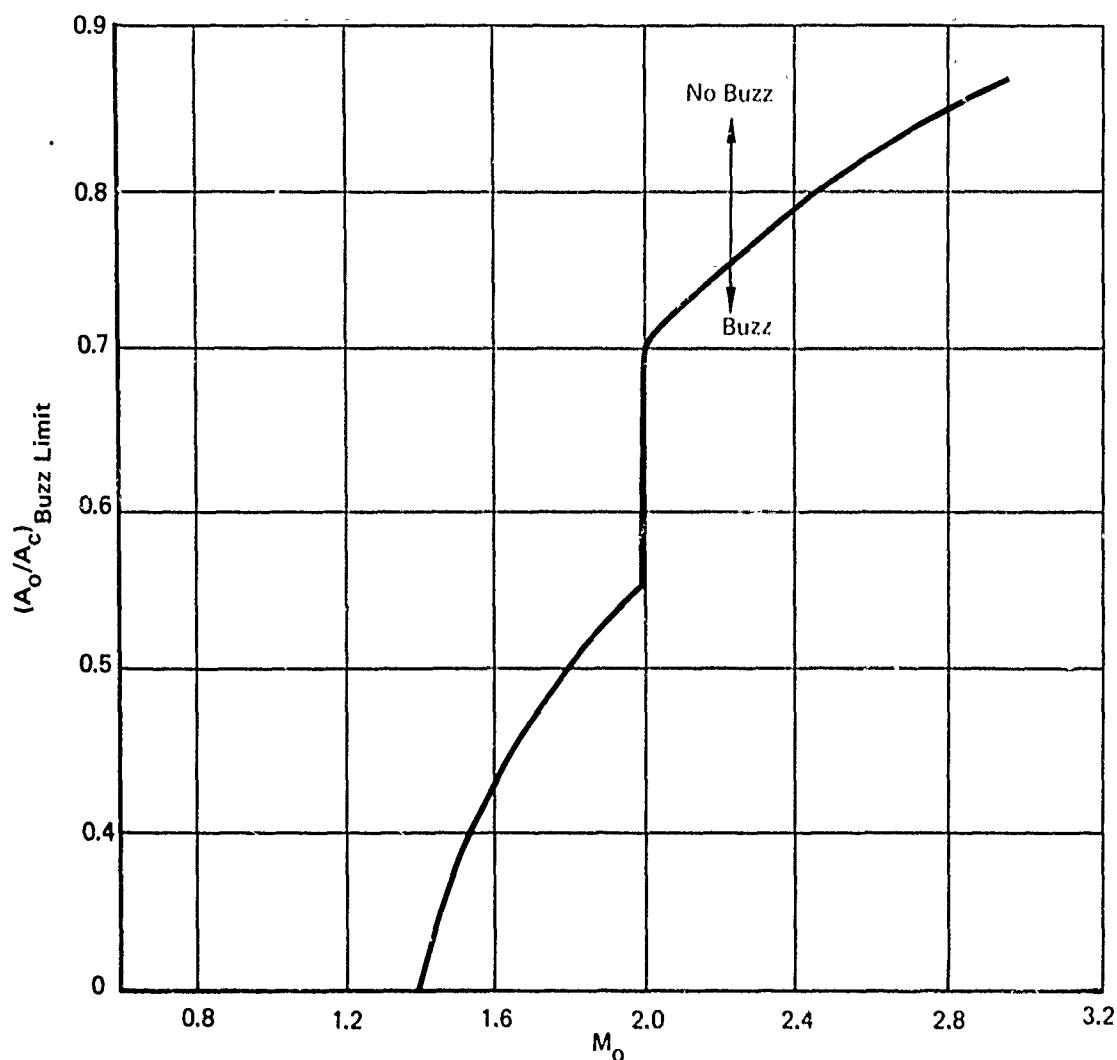
Figure 189: BUZZ LIMIT
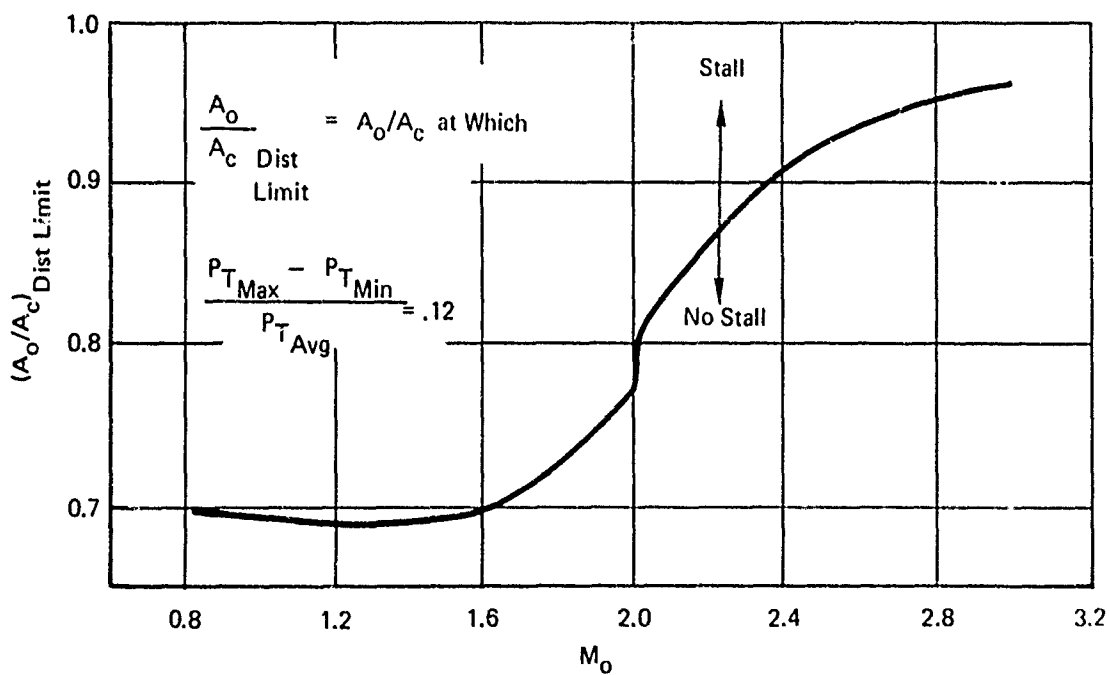
Figure 190: DISTORTION LIMIT

203
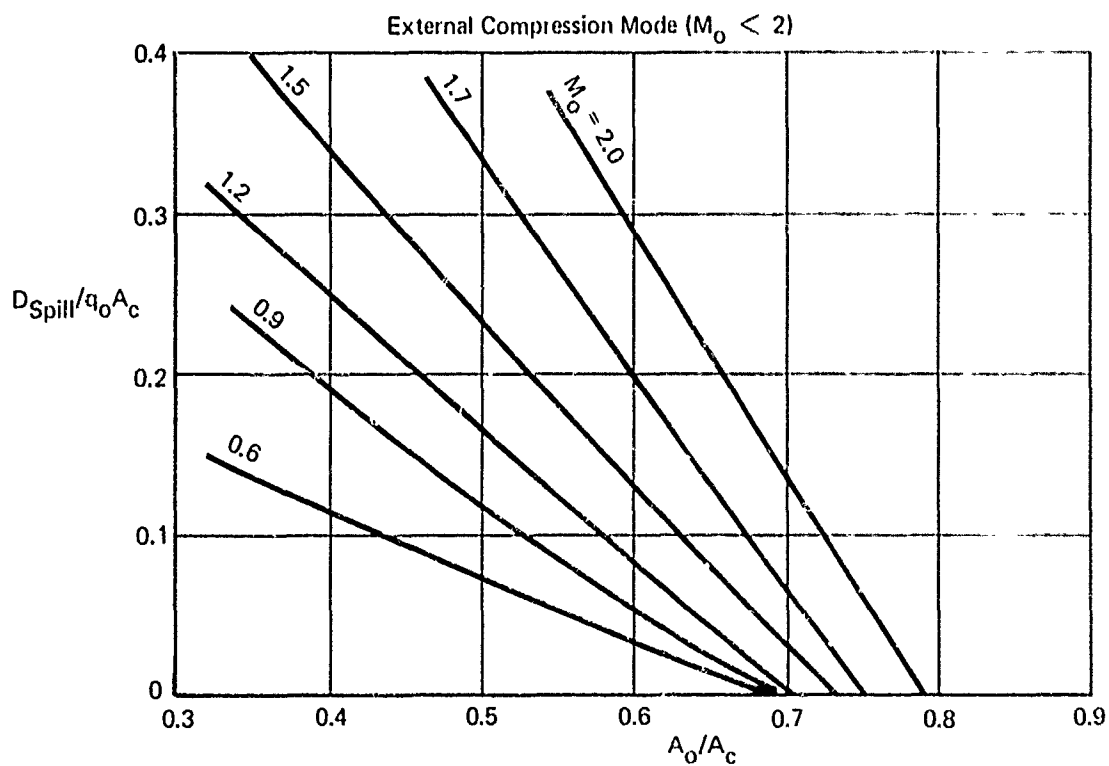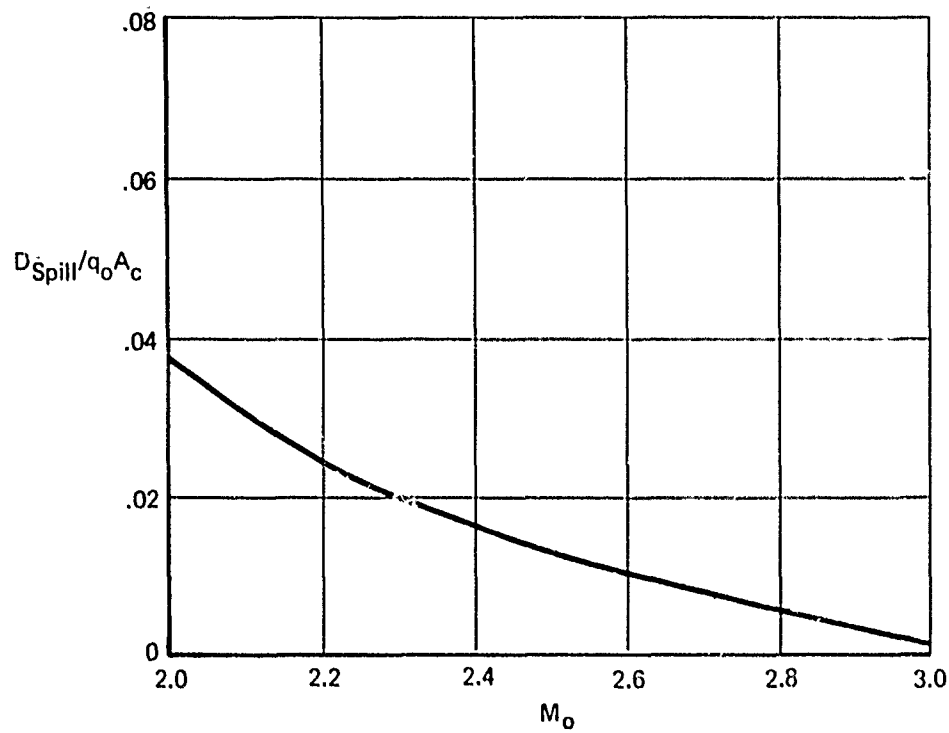
Figure 191: SPILLAGE DRAG
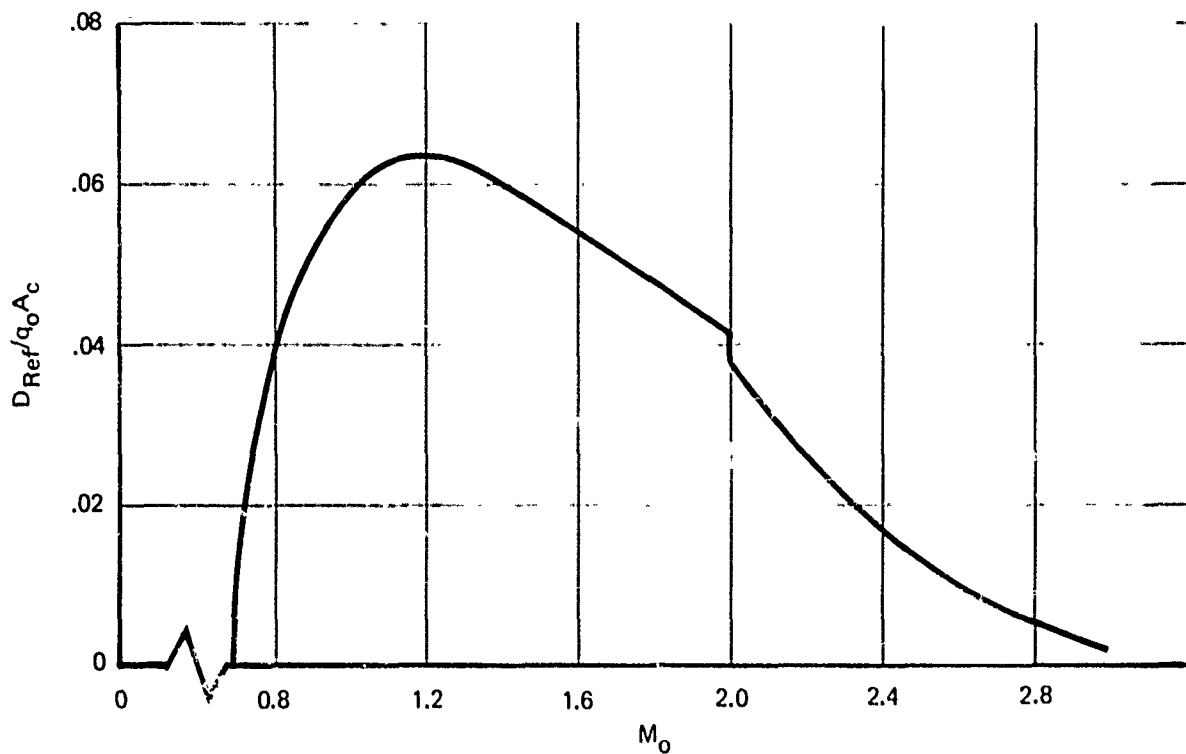
Figure 192:   INLET REFERENCE SPILLAGE DRAG
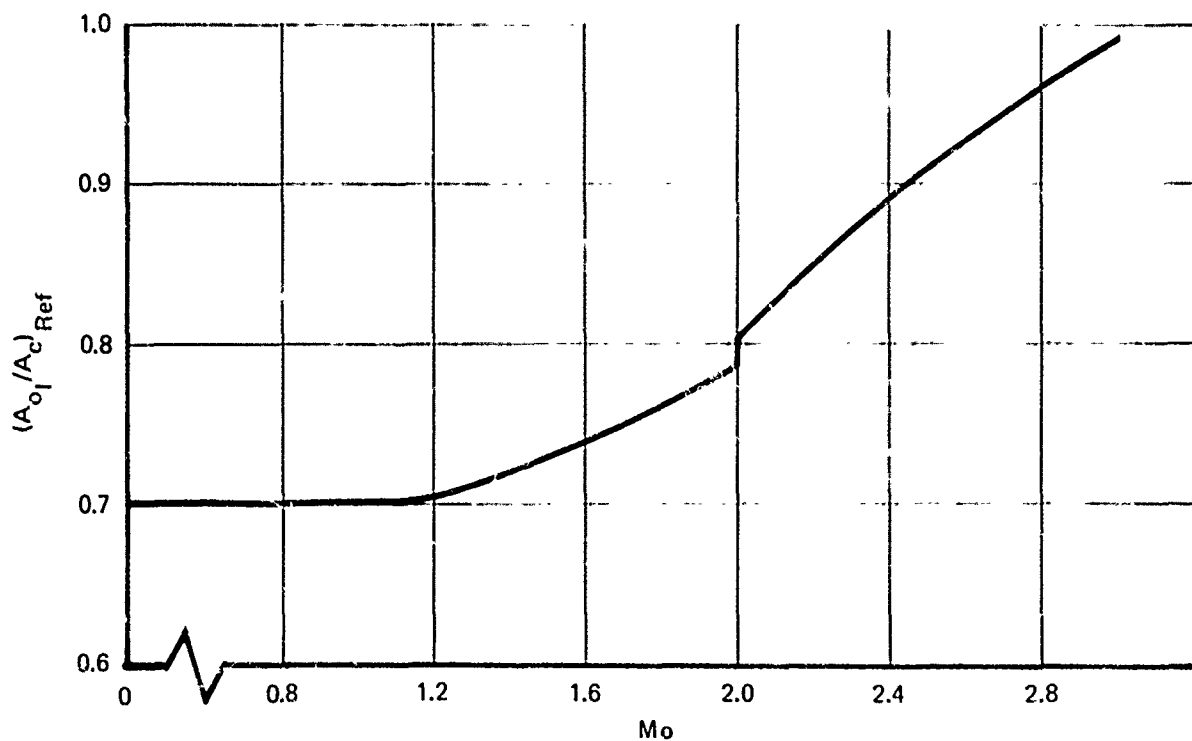
Figure 193:   REFERENCE MASS FLOW
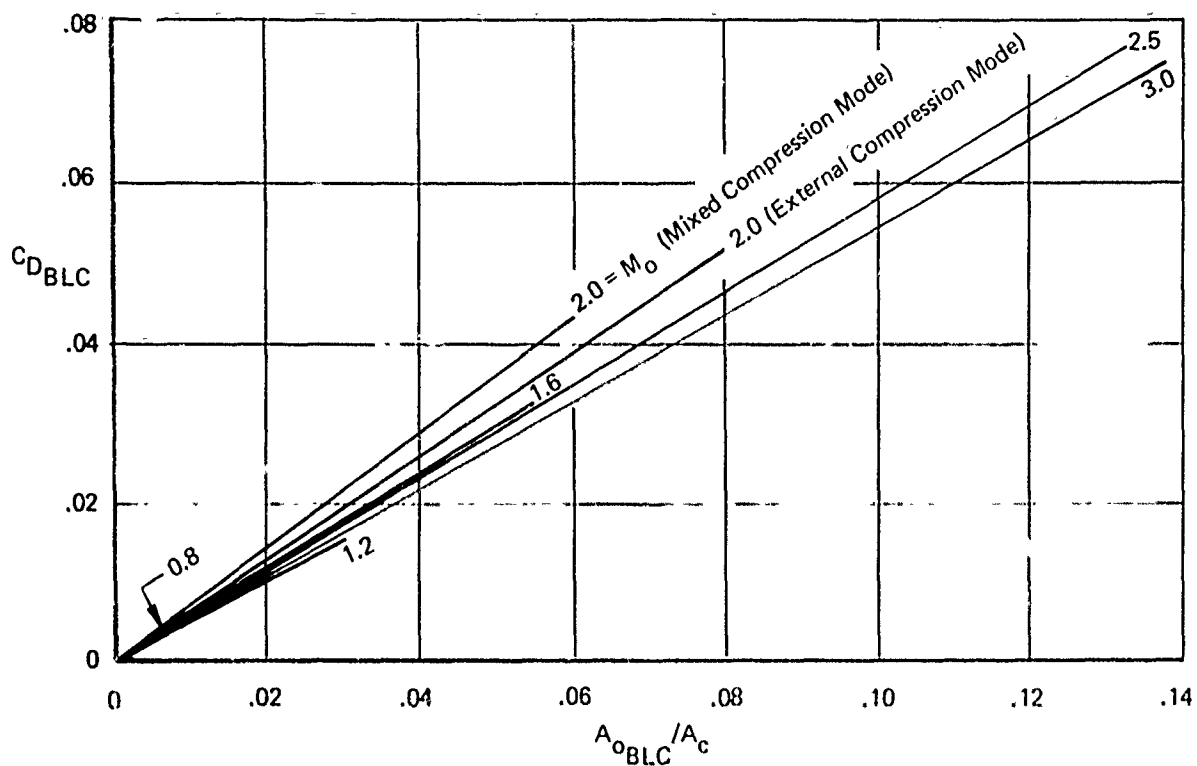
Figure 194:   BLEED DRAG
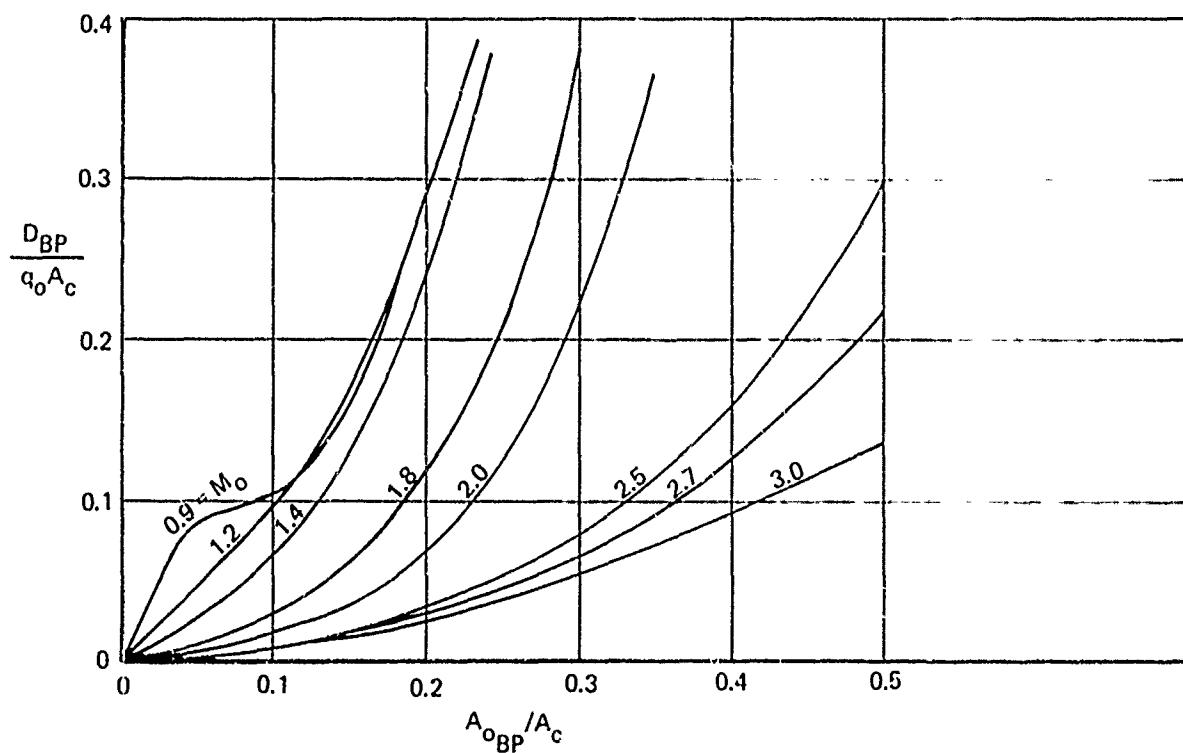
Figure 195:   BYPASS DRAG

206
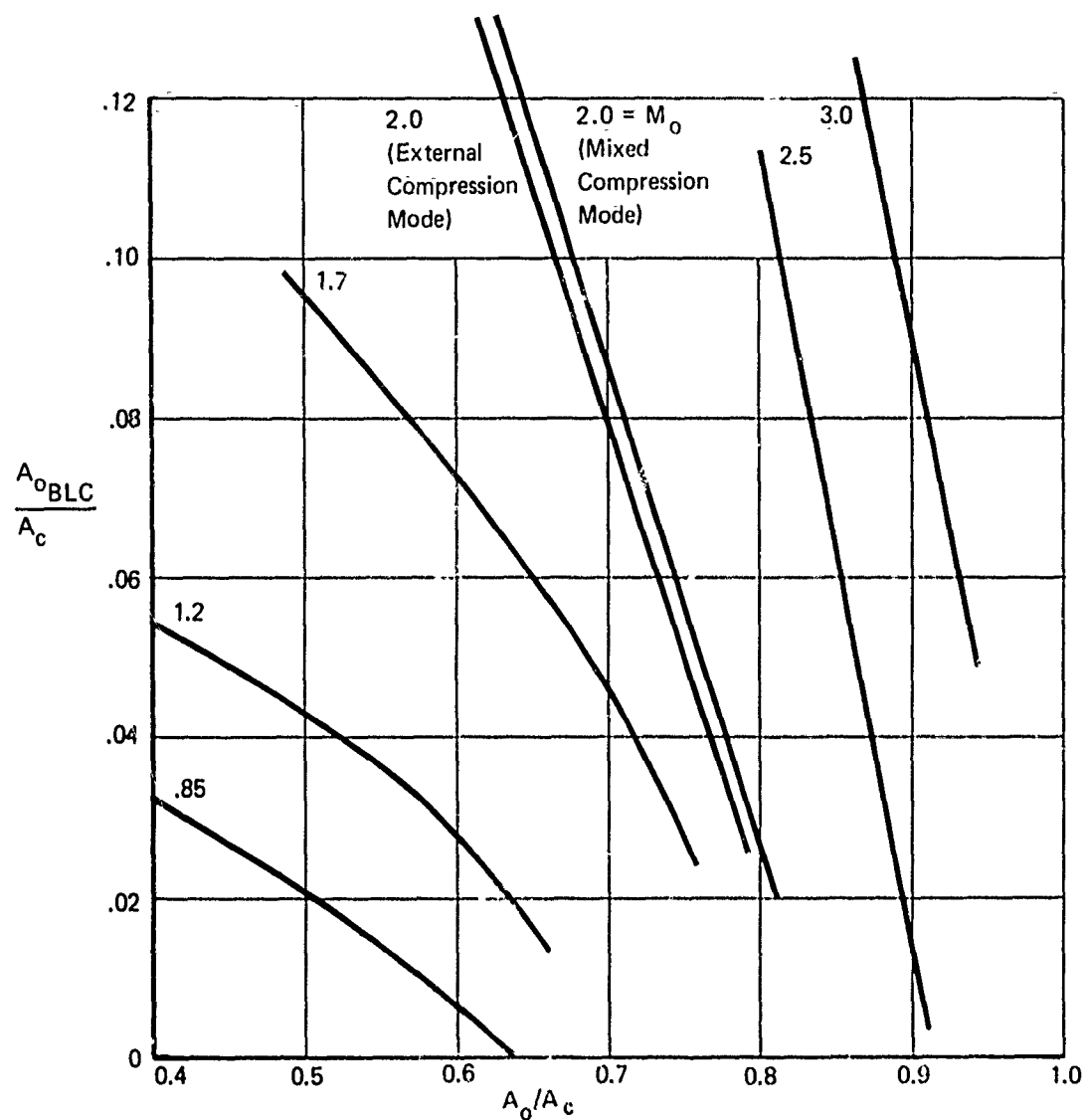
Figure 196: BOUNDARY LAYER BLEED SCHEDULE
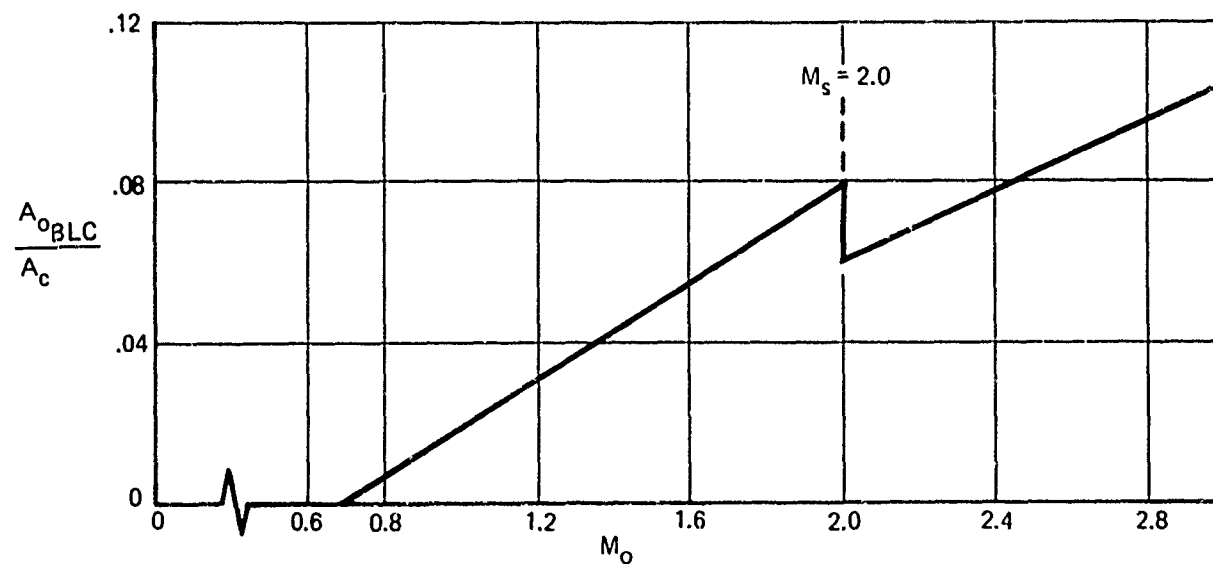
Figure 197: BOUNDARY LAYER BLEED VS M_o

207
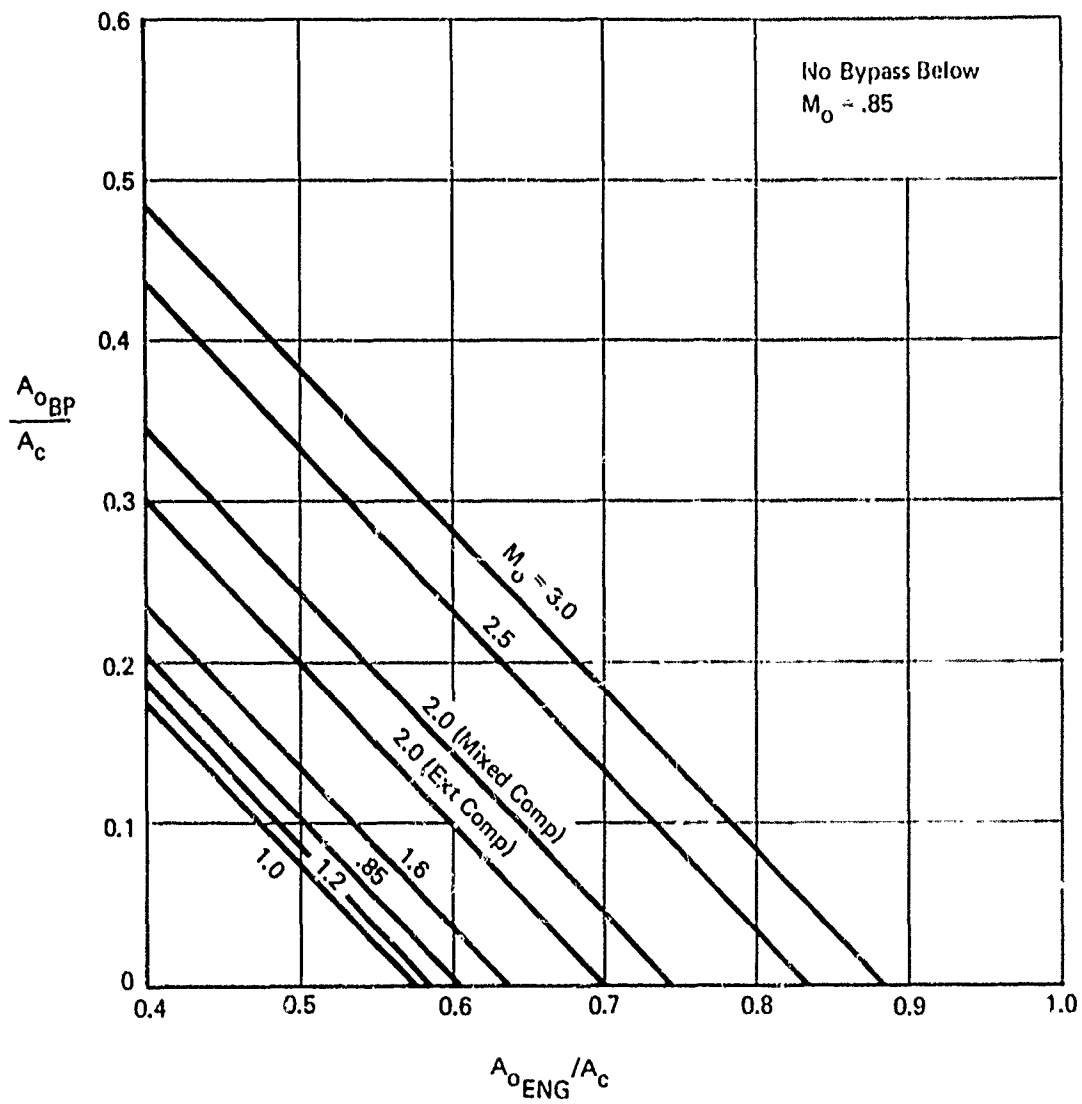
Figure 198: BYPASS MASS FLOW

208
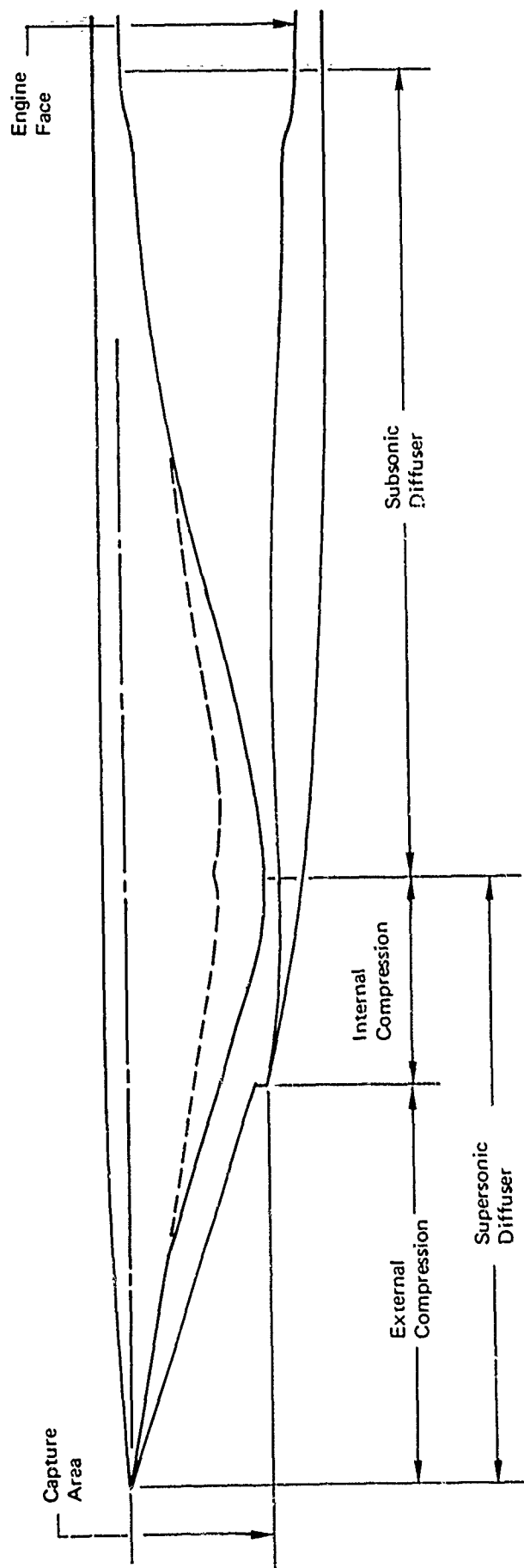
Figure 199: $M_O = 4.50$ MIXED COMPRESSION TWO-DIMENSIONAL INLET

209

The buzz and distortion limits for the recovery versus mass flow variations of Figure 186 were estimated to occur at the mass flows shown in Figures 189 and 190.. These limits are suitable for preliminary studies only, since they were selected largely from engineering judgment, based on trends in inlet buzz and distortion from past tests.

Figure 191 presents the estimated variation of spillage drag as a function of mass flow ratio and local Mach number. For the mixed-compression mode ($M_0 > 2$) spillage drag is shown as a function of Mach number only since it is assumed that that the inlet will be started and external spillage will not vary because the bypass system will handle the dumping of excess inlet airflow.

The spillage drag data in Figure 191 are based on the inlet reference mass flow ratio shown in Figure 193. The spillage drag for inlet mass flow ratios at or above the reference mass flow is shown in Figure 192. This part of the spillage drag is normally included in the airplane drag according to the bookkeeping system discussed in Section II.

Figures 194 and 195 show the variations of bleed and bypass drag as functions of the amount of bleed and bypass airflow for various free-stream Mach numbers.

Figure 196 presents the variation of inlet bleed as a function of mass flow ratio for various local Mach numbers. The nominal boundary layer bleed schedule at the recommended match points as a function of Mach number is shown in Figure 197. The bleed schedule above the "starting" Mach number of 2.0 remains relatively constant during normal operation because the bypass system will keep the throat shock in the design location.

The bypass schedule is shown in Figure 198. It is scheduled to bypass the difference between the engine demand and the A_0/A_C schedule shown in Figure 188. No bypass is used below $M_0 = 0.85$, however, since external spillage results in less drag.

The inlet performance characteristics can be modified a reasonable amount in a direction to help match the engine airflow demand after the engine demand is made available. Achieving the best engine/inlet matching involves an iteration process between engine manufacturer and inlet designer.

REFERENCES

1.   Johnson, R. H., et al., Propulsion System Integration
      and Test Program (Steady State) Summary: Part I,
      Integration Technique and Test Activities",
      AFAPL-TR-69-36, Part I, Air Force Aero Propulsion
      Laboratory, June 1969.

2.   Schreiber, L. H., "A Plan for Bookkeeping of the
      Propulsion and Aerodynamic Elements of Airplane
      Performance", presented at the Airframe Propulsion
      Compatibility Symposium at Miami Beach, June 24-26,
      1969.

3.   Anderson, R. D., Lee, C. C., and Martens, R. E.,
      A Thrust/Drag Accounting Procedure Applicable to
      Engine Cycle Selection Studies, MDC A1197, McDonnell
      Douglas Corporation, June 1971.

4.   Harner, P., (Naval Air Systems Command), Presentation
      at AIAA Sixth Propulsion Joint Specialist Conference,
      San Diego, June 15-19, 1970.

5.   Harner, P., Private Communication, August 20, 1970.

6.   Armstrong, R. S., and Miller, S. R., Subsonic Aerodynamic
      Performance of Nozzle Installations in Supersonic
      Airplanes, presented at the AIAA Third Propulsion Joint
      Specialist Conference, Washington D. C., July 1967.

7.   Migdal, D. , Miller, E. H. and Schnell, W. C., An
      Experimental Evaluation of Exhaust Nozzle/Airframe
      Interference, AIAA Paper No. 69-430, presented at
      the Fifth Propulsion Joint Specialist Conference,
      Colorado, June 9-13, 1969.

8.   Chamberlain, D., "Measurement of Drag from Interaction
      of Jet Exhaust and Airframe," Journal of Aircraft,
      Volume 6 No. 2, March-April, 1969.

9.   Migdal, D. and Greathouse, W. K., Optimizing Exhaust-
      Nozzle/Airframe Thrust Minus Drag, SAE Paper No. 680294,
      presented at Air Transportation Meeting, New York,
      April 29 - May 2, 1968.

10.   Ross, P. A., Inlet Development for Lightweight
      Fighter, D180-14475-1 TN, The Boeing Company,
      November 1972.

11.   Brajnikoff, G. B., Aero-Thermodynamics and Design
        Concepts of Air-Induction Systems, 1958.

12.   Miller, S. R., Experimental Determination of the Drag
        of a Series of Circular-Arc Boattails at Mach 0.4 to
        0.95, Boeing Document D6-23257, 1969.

13.   Shrewsbury, G. D., Effect of Boattail Juncture Shape
        on Pressure Drag Coefficients of Isolated Afterbodies,
        NASA TM X-1517, 1968.

14.   Compton, W. B. III, and Runkel, J. F.,   Jet Effects
        on the Boattail Axial Force of Conical Afterbodies
        at Subsonic and Transonic Speeds, NASA TM X-1960, 1970.

15.   Hiatt, D. L., Supersonic Boattail Wave Drag,
        Coordination Sheet ME-RES-593, The Boeing Co.,
        1969.

16.   McDonald, H., and Hughes, P. F., "A Correlation of
        High Subsonic Afterbody Drag in the Presence of a
        Propulsive Jet or Support Sting", Journal of Aircraft,
        Volume 2 No. 3, 1965.

17.   Miller, S. R., Prediction of Supersonic Axisymmetric
        Base Drag in the Presence of a Supersonic Jet , Memo
        METM 69-6, The Boeing Co., 1969.

18.   Nash, J. F., A Discussion of Two-Dimensional Turbulent
        Base Flows, NPL Aero Reprot 1162, 1965.

19.   Mercer, C. E., and Berrier, B. L., Effect of Afterbody
        Shape, Nozzle Type, and Engine Lateral Spacing on the
        Installed Performance of a Twin-Jet Afterbody Model,
        NASA TM X-1855, September 1969 (Confidential).

20.   Miller, S. R., and Salemann, V., Twin Engine Fighter
        Afterbody and Nozzle Tests, Mach 0.85 to 2.2, Report
        No. 1, Document D6-18088, The Boeing Company, 1966.

21.   Phase II Oral Review, Program for Experimental and
        Analytical Determination of Integrated Airframe-
        Nozzle Performance, Report LR 25153, Lockheed-California
        Company, February 29, 1972.

22.   Miller, S. R., Installation Effects on Plug Nozzle
        Performance at Subsonic Speeds, Document D162-10184-1,
        The Boeing Company, 1971.

23.   Misoda, P., SST Twin Engine Propulsion Pod Nozzle Study, Document D6A11701-1, The Boeing Co., 1971.

24.   Maiden, D. L., and Runckel, J. F., Effect of Nozzle Lateral Spacing on Afterbody Drag and Performance of Twin-Jet Afterbody Models with Convergent Nozzles at Mach numbers up to 2.2, NASA TM X-2099, 197.

25.   Salemann, V., Twin-Engine-Fighter Afterbody and Nozzle Wind Tunnel Tests, Mach 0.85 to 0.95, Report No. 2, Document D6-60033, The Boeing Co., 1966.

26.   Bergman, D., "Effects of Engine Exhaust Flow on Boattail Drag", Journal of Aircraft, Volume 8, No. 6, 1970.

27.   Duitsman, L. H., A Transonic Wind Tunnel Test on the MX-1149B-1 Model, BTWT Letter Report G-8355-142, The Boeing Co., December 1970.

28.   McClung, C. D., Test Data Report - Parametric Test of Conical Convergent Nozzles, Volume I, T6-5614-1, The Boeing Company, 1970.

29.   Hiatt, D. L., Propulsion Aerodynamics Handbook, Document D6-20394, The Boeing Company, 1968.

30.   Bresnahan, D. L., Experimental Investigation of a 10 Degree Conical Turbojet Plug Nozzle with Iris Primary and Translating Shroud at Mach Numbers from 0 to 2.0, NASA TM X-1709, 1968

31.   Armstrong, R. S., Mach 0 to 1.1 Thrust Minus Drag Tests of Several Exhaust Nozzles Designed for a Mach 2.7 Cruise Supersonic Transport, Document D6-9830-TN, The Boeing Company, 1965.

32.   Johns, A. L., and Steffan, F. W., Performance of an Auxiliary Inlet Ejector Nozzle with Fixed Inlet Doors and Triple-Hinge Trailing-Edge Flap, NASA TM X-2034, 1970.

33.   Johns, A. L., and Steffan, F. W., Performance of an Auxiliary Inlet Ejector Nozzle with Fixed Doors and Single-Hinge Trailing-Edge Flap, NASA TM X-2027, 1970.

34.   Steffan, F. W., and Johns, A. L., Performance of a Fixed-Geometry Wind Tunnel Model of an Auxiliary Inlet Ejector with a Clamshell Flow Diverter from Mach 0 to 1.2, NASA TM X-2037, 1970.

35. Bresnahan, D. L., Performance of an Aerodynamically Positioned Auxiliary Inlet Ejector Nozzle at Mach Numbers from 0 to 2.0, NASA TM X-2023, 1970.

36. Burley, R. R., and Mansour, A. H., Static Performance of an Auxiliary Inlet Ejector Nozzle Using an Afterburning Turbojet Gas Generator, NASA TM X-1999,

37. Randall, L. M., Haagenson, W. R., and Kavanagh, P., Experimental Investigation to Determine the Effect of Several Design Variables on the Performance of of the F-100 Duct Inlet, NA-53-26, North American Aviation, Inc., January 1953.

38. Muller, G. L., and Gasko, W. F., Subsonic-Transonic Drag of Supersonic Inlets, TDM-1973, Pratt and Whitney Aircraft, May 1966.

39. Herbert, M. V., Martlew, D. L., and Pinker, R. A., The Design Point Performance of Model Internal Expansion Propelling Nozzles with Area Ratios up to 4, Reports and Memoranda No. 3477, Royal Aircraft Establishment, 1963.

14 KEY WORDS	LINK A		LINK B		LINK C	
	ROLE	WT	ROLE	WT	ROLE	WT
Afterbody Drag						
Boattail Drag						
Bookkeeping Aero-Propulsion Forces						
Boundary Layer Bleed Drag						
Bypass Drag						
Inlet Performance						
Inlet Shock Losses						
Nozzle/Afterbody Installation Losses						
Nozzle Interference Drag						
Nozzle Thrust Coefficient						
Propulsion Installation Losses						
Spillage Drag						
Subsonic Diffuser Losses						
Supersonic Inlets						
Total Pressure Recovery						